# Quantifying the efficiency and stability potential of perovskite-based devices

Ph.D. Thesis, University of Amsterdam, January 2020

*Quantifying the efficiency and stability potential of perovskite-based devices*

Moritz Hieronymus Futscher

Cover image: artistic impression of a perovskite/silicon tandem solar cell with ion migration by Brigitte Futscher.

ISBN: 978-94-92323-33-0

The work described in this thesis was performed between December 2015 and January 2020 at AMOLF, Science Park 104, 1098 XG Amsterdam, The Netherlands.

This work is part of the Netherlands Organisation for Scientific Research (NWO).

A digital version of this thesis can be downloaded from http://www.amolf.nl.

# QUANTIFYING THE EFFICIENCY AND STABILITY POTENTIAL OF PEROVSKITE-BASED DEVICES

ACADEMISCH PROEFSCHRIFT

ter verkrijging van de graad van doctor
aan de Universiteit van Amsterdam
op gezag van de Rector Magnificus
prof. dr. ir. K. I. J. Maex
ten overstaan van een door het College voor Promoties ingestelde commissie,
in het openbaar te verdedigen in de Agnietenkapel
op donderdag 9 januari 2020, te 12:00 uur

door

Moritz Hieronymus Futscher

geboren te Wenen

**Promotiecommissie**

| | | |
|---|---|---|
| Promotor: | prof. dr. A. Polman | Universiteit van Amsterdam |
| Copromotor: | dr. B. Ehrler | AMOLF |
| Overige leden: | prof. dr. E. C. Garnett | Universiteit van Amsterdam |
| | dr. E. L. von Hauff | Vrije Universiteit Amsterdam |
| | prof. dr. L. J .A. Koster | Rijksuniversiteit Groningen |
| | prof. dr. P. Schall | Universiteit van Amsterdam |
| | dr. R. M. Williams | Universiteit van Amsterdam |
| | dr. S. D. Stranks | University of Cambridge |

Faculteit der Natuurwetenschappen, Wiskunde en Informatica.

To my wonderful wife.

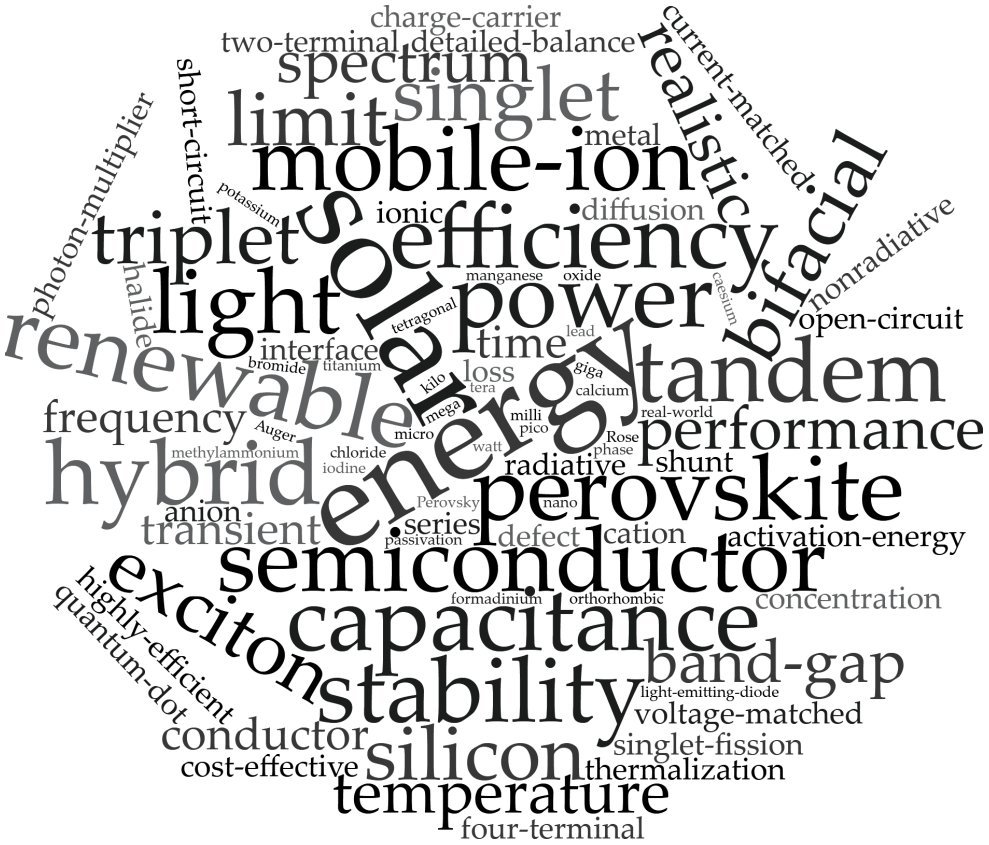


The thesis in a nutshell.

# Contents

*We have this handy fusion reactor in the sky called the sun. You don't have to do anything. It just works. It shows up every day and produces ridiculous amounts of power.*
*- Elon Musk*

# Introduction

The constant availability of power is crucial for the well-being of our societies. As an example, a typical European citizen today has a power requirement of 4.4 kilowatt (kW), averaged over the year, while a typical citizen of the United States needs 9.0 kW [1]. The current world average power demand per person is only 2.5 kW, mainly because large parts of the world are still living in poverty. However, as the world's population and economy continues to grow, the global demand for energy is rising rapidly, especially in developing countries [2, 3]. In 2018 the global energy demand increased by 2.3%, faster than ever before in this decade [1]. With an expected increase in the world population to about 11 billion people by the end of the century [4], we will soon have to supply more than 50 terawatt (TW), assuming an increase in average global power consumption to 5 kW per person. This is almost three times the 19 TW we currently produce worldwide.

Today's energy production consists of 80% fossil fuels (coal, gas, and oil), which leads to the emission of vast amounts of greenhouse gases – the fundamental driver of global climate change, with negative consequences for the environment and global human health caused by pollution [5]. For a sustainable energy future that meets our global climate targets while maintaining a high standard of living, we need a drastic change in the way we produce, supply, and consume energy.

Solar energy offers great potential to deliver a large part of the world's energy demand, and hence is expected to play a key role in the transition to clean energy worldwide [6]. In the last decade alone the levelised cost of electricity of solar power plants has dropped by more than 90%. Levelised costs are defined as the costs per kWh over the entire lifetime of a solar installation. Current levelised costs are as low as 0.05 €/kWh [7, 8], with record prizes of 0.02 €/kWh [9–11]. This developement makes solar energy the fastest-growing energy source in the world. In many regions of the world, the cost of solar energy is now below that of conventional sources such as coal, gas, oil, and nuclear. However, to ensure solar energy to be an integral part of our energy grid in the near future, levelised costs must be further reduced to 0.01 €/kWh [12].

Crystalline silicon solar cells dominate the current solar cell market with a share of more than 90%. However, the current generation of solar cells are unlikely to achieve the costs target of 0.01 €/kWh [13]. Since the costs of the solar panel itself

make up only about 50% of the total system costs of a solar installation [7], increasing the power conversion efficiency is key to further reducing the cost per kWh.

A promising way to increase the power conversion efficiency is to use solar cells in a tandem configuration. In a tandem solar cell configuration two solar cells are stacked on top of each other to achieve a higher power-conversion efficiency from incident solar irradiation to electricity, with great impact on cost reduction [14]. For this reason, both science and industry are urgently looking for a solar cell material which, together with silicon, is suitable for the realisation of a cost-efficient tandem solar cell. To achieve this goal, an efficient and stable solar cell material is needed that absorbs a different part of the solar spectrum than silicon. Metal halide perovskites are a promising material option to meet these requirements.

### METAL HALIDE PEROVSKITES

Perovskites are a class of materials with a crystal structure of $ABX_3$, where A-site cations are surrounded by a framework of octraheda with B-site cations at the centre and X-site anions at the corners (see Figure 1a) [15]. Due to their intriguing optoelectronic properties such as high charge-carrier mobilities, long diffusion lengths, strong absorption, low exciton binding energy, and a tunable band gap, perovskites have proven to be promising candidates for highly-efficient and cost-effective solar cells [16–20]. Perovskite solar cells thus have the potential to surpass today's technologies and pave the way for new applications including low-cost tandem solar cells. Unlike silicon solar cells, perovskites can be lightweight, flexible, and colourful and therefore open up new markets like building-integrated solar cells and solar windows. In addition, perovskites can be used in a variety of applications including light-emitting diodes, lasers, and X-ray detectors.

The first known perovskite was calcium titanium oxide ($CaTiO_3$), discovered by Gustav Rose in 1839 and named after the Russian mineralogist Lev Perovsky. Although perovskites have been known since the 19th century, their use for optoelectronic devices evolved only recently with the discovery of halide perovskites [21]. Metal halide perovskites date back to 1978, with the first synthesis and characterisation of methylammonium lead iodide [22]. However, it was not until 1995 that the potential of perovskites for optoelectronic devices was discovered [23].

In 2009, perovskites were introduced for the first time as an absorber material in a conventional dye-sensitised solar cell architecture achieving a power conversion efficiency of 4% [24]. However, the perovskite revolution started only in 2012 with the use of solid-state devices that achieved efficiencies above 10% [25, 26]. In the following years, their power conversion efficiency quickly climbed to more than 25% (see Figure 1b), almost as efficient as record silicon solar cells [27, 28]. In contrast,

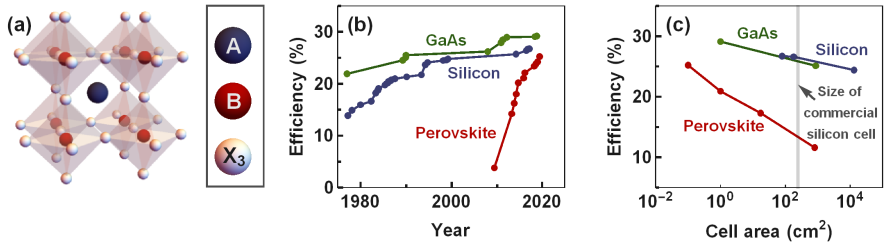


**Figure 1**: **(a)** Metal halide perovskite structure with the crystal structure of $ABX_3$. The A-site cation typically contains a mixture of organic cations such as methylammonium, formadinium, and inorganic caesium. The B-site cation typically represents lead and the X-site halide is bromide, iodide, or a combination of both. Record efficiencies for silicon, GaAs, and perovskite solar cells as a function of **(b)** time and **(c)** cell area [27, 28]. The standard size of a commercial silicon solar cell is 243 $cm^2$.

after more than 60 years of research, the efficiency of silicon and gallium arsenide (GaAs) solar cells are slowly approaching their theoretical efficiency limit.

Solar cells from GaAs yield the highest single-junction efficiencies with a record efficiency of 29% [27], close to their theoretical efficiency limit of 33%. Due to the high material and fabrication costs, however, their use is limited to space and concentrator applications. Perovskite solar cells have a theoretical efficiency of 32%, similar to that of GaAs solar cells. In contrast to GaAs, however, perovskites have low material and manufacturing costs and are not reliant on rare elements [29–31]. Hence, perovskite solar cells could have the same efficiency as GaAs solar cells but at much lower cost per kWh.

Although perovskite solar cells show very high efficiencies, so far, these are typically only for small devices with an area of only 0.1 $cm^2$. In order to build a perovskite/silicon tandem solar cell, the area of the perovskite must be scaled to the area of standard commercial silicon solar cells (243 $cm^2$). Increasing the solar cell area typically follows an inverse scaling law, with an efficiency reduction of about 1% absolute when the area is increased by an order of magnitude [32, 33]. For perovskite solar cells, however, this decrease is currently still much greater (see Figure 1.1c). To further increase the efficiency of large-area perovskite solar cells and to decrease the gap between laboratory cells and industrial modules, the dominant loss channels in perovskite solar cells must be understood to avoid them.

In the first part of this thesis we develop a model to simulate the performance of realistic solar cells. The model provides quantitative insight into the dominant

loss channels of perovskite solar cells and paves the way for further optimisations towards high perovskite/silicon tandem solar cell efficiencies. The performance of solar cells are typically evaluated under laboratory conditions that mimic a sunny summer day in the northern hemisphere, with an average temperature of 25 °C. The actual performance, however, is highly dependent on the location of deployment, especially for tandem solar cells. Our model allows to predict the expected energy yield of perovskite/silicon tandem solar cells under realistic outdoor illumination conditions.

To be able to use perovskites in commercial applications, they must meet the norms established by their inorganic counterparts. Silicon solar cells, for example, typically come with a 25-year warranty. Although great progress has been made in recent years in improving the stability of perovskites, they are far from being as stable. The main reason for the instability of perovskites is the migration of mobile ions through the device during operation, as perovskites are mixed ionic-electronic conductors [34, 35]. It has been shown that both A-site cations and X-site halides migrate in perovskite-based devices under typical operating conditions [36–40], resulting in an accelerated degradation of the devices. To produce long-lasting devices, key for the commercialisation of perovskite-based devices, this ion migration must be controlled. However, ion migration in perovskite-based devices is not well understood as the measured properties of mobile ions vary widely between measurements and theoretical predictions. The migration of mobile ions and their impact on the stability of perovskite-based devices is the subject of the second part of this thesis.

### Outline of this thesis

This section briefly addresses the outline of the thesis and the topics of the individual chapters. This thesis is divided into two main parts. The first part ranges from Chapter 1 to Chapter 5 and is based on simulations on the efficiency potential of next-generation solar cells. The second part ranges from Chapter 6 to Chapter 9 and is based on measurements of ion migration in perovskite-based devices.

**Part I: Efficiency potential under realistic conditions**

In **Chapter 1** we describe how tandem solar cells increase the efficiency of conventional solar cells and how realistic tandem solar cells are modelled by including material-specific parameters such as nonradiative recombination, optical losses, and parasitic resistances into the detailed-balance model.

In **Chapter 2** we analyse how measured solar spectra are influenced by different locations, times, and weather conditions. Subsequently, we investigate the influence

of changes in the solar spectrum and temperature on the limiting efficiency of different tandem solar cell configurations from *ideal* subcells based on measured outdoor illumination conditions.

In **Chapter 3** we continue by investigating the influence of outdoor illumination conditions on different perovskite/silicon tandem solar cell configurations from *realistic* subcells. Starting from a state-of-the-art perovskite solar cell with an area of 1 $cm^2$, we investigate how the improvement of the perovskite cell increases the efficiency of the different tandem solar cell configurations.

Bifacial silicon solar cells are promising for improving the efficiency of conventional silicon solar cells. In **Chapter 4** we investigate the efficiency potential of bifacial perovskite/silicon tandem solar cells under realistic operation conditions.

In **Chapter 5** we investigate the potential of singlet fission photon multipliers as an alternative to tandem solar cells. Singlet fission is an exciton multiplication process in organic semiconductors which converts one singlet exciton into two triplet excitons. This process can be used to modulate the incoming solar spectrum to reduce thermalization losses in conventional solar cells.

**Part II: Quantifying ion migration in metal halide perovskites**

In **Chapter 6** we review the difference in studying mobile ions by capacitance measurements in the frequency and in the time domain and show how activation energy, diffusion coefficient, sign of charge, concentration, and the length of the ionic double layer can be quantified.

In **Chapter 7** we quantify mobile ions using time-dependent capacitance measurements in the prototype metal halide perovskite $MAPbI_3$. To estimate the sample-to-sample and lab-to-lab variation, we measured solar cells manufactured in two different laboratories with a wide range of efficiencies.

Introduction of potassium into triple-cation mixed-halide perovskites reduces photo-induced ion segregation, which has been attributed to the mitigation of ion migration. However, the reason and mechanism for this suppression are not well understood. In **Chapter 8** we use capacitance measurements in the frequency and in the time domain to study ion migration in mixed perovskites with potassium passivation.

The partial substitution of lead by manganese increases the stability of perovskite light-emitting diodes, but the effects of manganese doping on ion migration are not well understood. In **Chapter 9** we use capacitance measurements in the frequency and in the time domain to study ion migration in these perovskite light-emitting diodes.

# Part I

# Efficiency potential under realistic conditions

# 1

# Detailed-balance calculations

Understanding performance limitations of solar cells helps to find and eliminate dominant loss channels and guides the way towards their limit. In the following we describe how the efficiency of solar cells is calculated based on the principle of the detailed balance. On the basis of the fundamental limits of single-junction solar cells, tandem solar cells are discussed as a possibility to exceed the single-junction limit by reducing thermalization losses. Finally, loss mechanisms present in real solar cells are included in the detailed-balance calculations to simulate realistic solar cells.

## 1.1 The Shockley-Queisser limit

In an ideal solar cell, the photocurrent density generated by a solar cell is defined by the incoming photon flux with an energy higher than the band gap $E_G$ as

$$J_G = q \int_{E_G}^{\infty} \Phi(E)\, dE, \tag{1.1}$$

where $q$ is the elementary charge and $\Phi(E)$ is the photon flux of the incident solar spectrum as a function of energy $E$, which corresponds to the number of photons per second per unit area and is defined as

$$\Phi(E) = \frac{\lambda E(\lambda)}{hc} \tag{1.2}$$

where $\lambda$ the wavelength, $h$ Plank's constant, $c$ the speed of light, and $E(\lambda)$ the energy of the incoming radiation as a function of wavelength. In the thermodynamic consideration of detailed balance, the rate of photon absorption must be balanced by the rate of photon emission. According to the generalised Planck's radiation law [41], the radiative recombination current density of an ideal solar cell can be described as

$$J_{Rad}(V) = f_w \frac{2\pi q n}{c^2 h^3} \int_{E_G}^{\infty} \frac{E^2}{\exp\left(\frac{E-qV}{k_B T}\right) - 1} dE \tag{1.3}$$

where $n$ is the refractive index of the surrounding medium, $k_B$ Boltzmann's constant, $T$ the temperature of the cell, $V$ the applied voltage, and $f_w$ a geometrical factor taking into account the angle upon which the photon flux is emitted from the cell. Assuming a flat plate that emits radiation only from the front and the rear side of the cell, the geometrical factor is $f_w = 2$. Often a perfect reflector is assumed on the back side of the solar cell reducing the geometrical factor to $f_w = 1$. This radiative recombination current density is an unavoidable loss for solar cells. For small voltages compared to the emitted photon energies, i.e. $E_G - qV \gg k_B T$, Equation 1.3 can be approximated to [23]

$$J_{Rad}(V) = J_R \left( \exp\left(\frac{qV}{k_B T}\right) - 1 \right). \tag{1.4}$$

The prefactor of $J_R$ accounts for the spontaneous generation of charge carriers. The overall current-voltage characteristic of an ideal solar cell can then be approximated as the sum of the light and the dark current densities as

$$J(V) = J_G - J_R \left( \exp\left(\frac{qV}{k_B T}\right) - 1 \right). \tag{1.5}$$

This is known as the superposition approximation. This relationship shows that a solar cell behaves like a diode in the dark with rectifying behaviour, i.e. providing a much larger current at forward bias (V $>$ 0) than at reverse bias (V $<$ 0). The resulting current-voltage characteristics of an ideal solar cell with a band gap of 1.34 eV is shown in Figure 1.1a, calculated at standard test conditions. Standard test

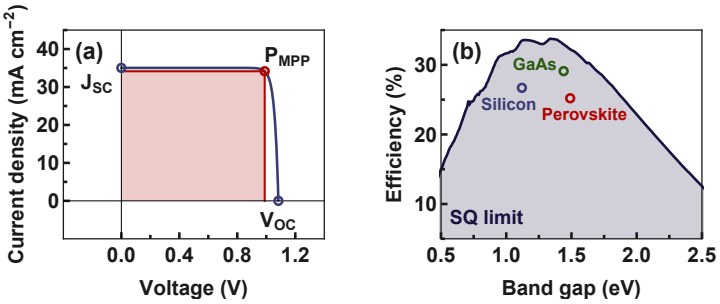


**Figure 1.1**: Shockley-Queisser limit. **(a)** Current-voltage characteristics of an ideal solar cell with a band gap of 1.34 eV. **(b)** Shockley-Queisser (SQ) limit of single-junction solar cells as a function of band gap. The inset shows the current record efficiency of a silicon (Si), a gallium arsenide (GaAs), and a perovskite solar cell. Calculated at standard test conditions (AM1.5G, 25 °C, 1000 W/m$^2$).

conditions are used so that results from different laboratories can easily be compared and assume an incident Air Mass 1.5 solar spectrum (AM1.5G) with a power density of 1000 W/m$^2$ and a temperature of 25 °C. Note that the sign convention used here is that the photocurrent is positive.

Some essential definitions can be described using the current-voltage characteristic shown in Figure 1.1a. The current density at zero voltage is called the short-circuit current density $J_{SC}$, corresponding to the largest photocurrent density that can be supplied by the cell. The maximum photovoltage that can be supplied by the cell is called the open-circuit voltage $V_{OC}$, and is defined as the voltage at zero current density. The solar cell produces its maximum power at the maximum power point $P_{MPP}$, where the product of current density and voltage reaches its maximum. The ratio of the maximum power to the product of short-circuit current density and the open-circuit voltage is called the fill factor, i.e. $FF = P_{MPP}/(J_{SC} \times V_{OC})$, which describes the 'squareness' of the current-voltage characteristic. The fill factor, the open-circuit voltage, and the short-circuit current are the key performance parameters used to characterise a solar cell. The maximum power-conversion efficiency $\eta$ is defined as the maximum output power $P_{max}$, divided by the power of the incident solar spectrum $P_{in}$ as

$$\eta = \frac{\text{Max}\,(P_{out})}{P_{in}} = \frac{J_{SC} V_{OC} FF}{P_{in}}. \tag{1.6}$$

From this relation, the maximum power-conversion efficiency is calculated as a function of the band gap (Figure 1.1b). The highest efficiency of 34% is achieved

with a band gap of 1.34 eV. This maximum results from an optimal balance between voltage and current density; at low band gaps, the efficiency is limited by the voltage of the cell because the open-circuit voltage decreases with decreasing band gap, while at large band gaps, the current-density reduces the efficiency because large band gap semiconductors absorb only a fraction of the incident light. This method of using detailed balance to calculate the maximum power-conversion efficiency of solar cells was first proposed by Shockley and Queisser in 1961 and is commonly referred to as the Shockley-Queisser limit [42].

## 1.2 BEYOND THE SINGLE-JUNCTION LIMIT

The Sun emits light with wavelengths from the ultraviolet to the infrared with a spectral distribution that resembles the spectrum of a black body with a temperature of 5760 K, as well as absorption dips caused by light passing through the Earth's atmosphere (see Section 2.3 for a detailed description of the solar spectrum). The broad nature of the solar spectrum causes the greatest losses in an ideal single-junction solar cell. Photons with an energy below the band gap are not absorbed by the solar cell, and photons with an energy above the band gap generate hot carriers that thermalize to the band-edge losing their excess energy to heat. In a silicon solar cell with a band gap of 1.12 eV, thermalization accounts for a 39% power loss using the AM1.5G standard solar spectrum, which is illustrated in Figure 1.2a. Reducing thermalization losses thus offers a great opportunity to achieve efficiencies exceeding the single-junction limit.

Tandem solar cells are one of the most promising strategies for reducing thermalization losses [43]. A tandem configuration consists of two or more cells that are optically coupled by absorbing different parts of the incident solar spectrum. This allows for more efficient conversion of the broad-band solar spectrum to output power by reducing the thermalization losses from 39% in a single-junction cell to 23% in a tandem configuration, as illustrated in Figure 1.2b. In a two cell configuration, the high-energy region is absorbed by the top cell, and the transmitted low-energy light is absorbed by the bottom cell. The current generated by the top cell and the bottom cell is thus determined by the solar spectrum reaching the cell and the light emitted by the second cell as

$$J_G^{top} = q\int_{E_G^{top}}^{\infty} \Phi\left(E\right) dE + f_w^{bottom} \frac{2\pi qn}{c^2 h^3} \int_{E_G^{bottom}}^{E_G^{top}} \frac{E^2}{\exp\left(\frac{E-qV_{bottom}}{k_B T} - 1\right)} dE \qquad (1.7)$$

and

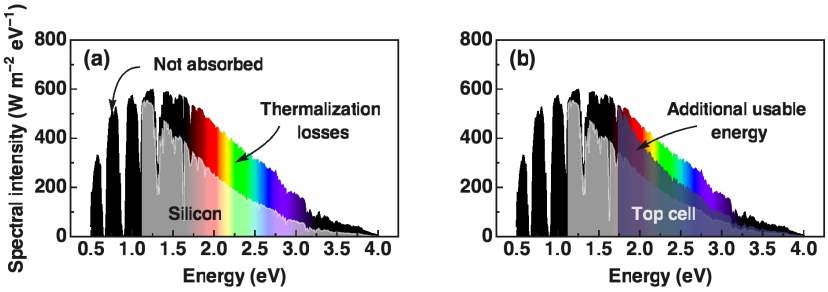


**Figure 1.2**: **(a)** A silicon solar cell absorbs all the light above its band gap of 1.12 eV. Photons with an energy below the band gap are not absorbed. Photons with an energy above the band gap lose their excess energy to heat. **(b)** By placing a high band gap solar cell on top of the silicon solar cell, thermalization losses can be reduced from 39% to 23%. The solar spectrum corresponds to the AM1.5G standard solar spectrum.

$$J_G^{bottom} = q\int_{E_G^{bottom}}^{E_G^{top}} \Phi\left(E\right) dE + f_w^{top}\frac{2\pi qn}{c^2h^3}\int_{E_G^{top}}^{\infty} \frac{E^2}{\exp\left(\frac{E-qV_{top}}{k_BT}-1\right)} dE \tag{1.8}$$

where $E_G^{top}$ is the band gap of the top cell and $E_G^{bottom}$ the band gap of the bottom cell. The top and the bottom cell can be connected in a monolithically-integrated two-terminal configuration where current matching is required, in a module configuration that requires voltage matching, or in an unconstrained four-terminal configuration where both subcells are electrically independent while still being optically coupled. The different tandem solar cell configurations are illustrated in Figure 1.3.

For a two-terminal configuration connected in series, current matching applies, i.e. $J = J_{top} = J_{bottom}$. The output power for a series tandem configuration is thus given by

$$P_{out}^{series} = \left(V_{top} + V_{bottom}\right) J\left(V\right). \tag{1.9}$$

In a two-terminal tandem configuration connected in parallel in a module level, $m$-series connected top cells are connected in parallel to $n$-series connected bottom cells. Since the top and the bottom cells are connected in parallel, voltage matching applies, i.e. $V = mV_{top} = nV_{bottom}$. The output power for a module tandem configuration is thus given by

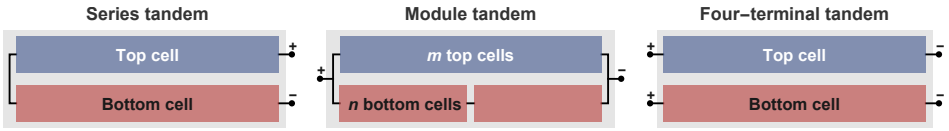


**Figure 1.3:** Schematic illustration of the different tandem solar cell configurations. **(Left)** Monolithically integrated two-terminal tandem in which the top cell and the bottom cell are electrically connected in series. **(Middle)** Mechanically stacked two-terminal module tandem in which the top cells and the bottom cells are electrically connected in parallel. **(Right)** Four-terminal tandem in which the top cell and the bottom cell are electrically independent.

$$P_{out}^{module} = \left( \frac{1}{m} J_{top}\left(V\right) + \frac{1}{n} J_{bottom}\left(V\right) \right) V. \tag{1.10}$$

Since a four-terminal tandem is not subject to either current or voltage matching, the output power for a four-terminal tandem is given by

$$P_{out}^{4T} = J_{top}\left(V\right) V_{top} + J_{bottom}\left(V\right) V_{bottom}. \tag{1.11}$$

The power conversion efficiency of the tandem solar cells is then defined as the maximum output power divided by the incoming power of the Sun. Under standard test conditions, the theoretical efficiency limit is increased from 34% in a single-junction solar cell to 45% for tandem solar cells from two subcells for all the different tandem configurations. However, the different combinations place different constraints on the choice of band gaps and the stability of the efficiency with changing solar spectra and temperatures, which is a key factor for the power conversion efficiency of tandem solar cells under real-world operation conditions. The effect of real-world climate conditions on the different tandem configurations will be subject of Chapter 2. As an alternative to tandem solar cells, thermalization losses in solar cells can be reduced by modulating the incoming solar spectrum, which is subject of Chapter 5.

## 1.3 Realistic solar cell model

In realistic solar cells, the efficiency is reduced due to nonradiative recombination via electronic defect states or Auger recombination, parasitic resistances, and optical losses. To model realistic solar cells, we incorporate nonradiative recombination into

the detailed-balance calculations by analytically solving the current-voltage characteristics for a p-n junction solar cell consisting of a quasi-neutral p-type region, a depletion region, and a quasi-neutral n-type region using the depletion and the superposition approximation following the work of Jenny Nelson [44]. The depletion approximation assumes that the electric field is zero in the quasi-neutral regions and varies linearly across the depletion region, the junction contains no free carriers, and the quasi-Fermi levels are constant across the depleted region. This allows to decouple solutions for the quasi-neutral regions and the depletion region. The superposition approximation furthermore allows to decouple the effect of bias from the effect of illumination by assuming that the recombination rates in the quasi-neutral regions are linear with the minority-carrier density. This is often referred to as the low injection regime, meaning that the photogenerated carrier density is smaller than the equilibrium majority-carrier density. In addition, we assume that the recombination rate is constant within the depleted regions and Shockley-Read-Hall recombination through electronic defect states is the dominant recombination process. This results in a nonradiative recombination current density $J_{NR}$ originating from the quasi-neutral and the depletion region of the p-n junction as

$$J_{NR}(V) = J_{NR,1}\left(\exp\left(\frac{qV}{k_BT}\right) - 1\right) + J_{NR,2}\left(\exp\left(\frac{qV}{2k_BT}\right) - 1\right) \tag{1.12}$$

with

$$J_{NR,1} = qn_i^2\left(\frac{D_n}{N_aL_n} + \frac{D_p}{N_dL_p}\right) \tag{1.13}$$

and

$$J_{NR,2} = \frac{qn_iw_D}{\sqrt{\tau_n\tau_p}}. \tag{1.14}$$

The first term ($J_{NR,1}$) is the recombination current density from the quasi-neutral regions due to minority-carrier diffusion and the second term ($J_{NR,2}$) the recombination current density from the depletion region. Here $n_i$ is the intrinsic charge carrier density, $D_n$ and $D_p$ the diffusion constants for electron and holes, $N_a$ and $N_d$ the doping densities of acceptor and donor, $L_n$ and $L_p$ the diffusion lengths for electron and holes, $w_D$ the width of the depletion region, and $\tau_n$ and $\tau_p$ the lifetimes of electrons and holes, respectively. The width of the depletion region is defined as

$$w_D = \sqrt{\frac{2\varepsilon_0\varepsilon}{q}\left(\frac{1}{N_a}+\frac{1}{N_d}\right)(V_{bi}-V)} \tag{1.15}$$

where $\varepsilon_0$ the vacuum permittivity, $\varepsilon$ the permittivity of the material, and $V_{bi}$ is the built-in bias. Equation 1.15 is only defined for $V_{bi}>V$, i.e. the width of the depletion region is zero for biases higher than the built-in bias.

In addition to nonradiative recombination, we take Auger recombination into account. Auger recombination involves three charge carriers, whereby the energy of an electron-hole pair is transferred to a third carrier. Auger recombination depends on the material used and is especially important at high carrier concentrations. It is defined as

$$J_{Auger}(V) = J_A\left(\exp\left(\frac{3qV}{2k_BT}\right)-1\right) \tag{1.16}$$

with

$$J_A = qLCn_i^3 \tag{1.17}$$

where $L$ is the thickness of the material and $C$ the material-specific Auger coefficient. To further account for additional optical losses such as parasitic absorption and reflection, the wavelength-dependent external quantum efficiency (EQE) is taken into account when calculating the photogenerated current density as

$$J_G = q\int_0^\infty \Phi(E)\,EQE(E)\,dE. \tag{1.18}$$

We furthermore include internal cell resistances due to parasitic series and shunt resistance, reducing the fill factor of the solar cell. The series resistance $R_S$ depends on the current density and results from current flow through the solar cell, typically due to contact resistance. This leads to a difference between the internal and the external voltage, which increases for increasing current density, i.e $\Delta V = JR_S$. The shunt resistance is caused by leakage currents through the cell, typically due to manufacturing defects. Finally, to model a realistic solar cell, we can add nonradiative recombination (Equation 1.12), Auger recombination (Equation 1.16), and parasitic resistances into the detailed-balance model (Equation 1.5). The equivalent circuit of

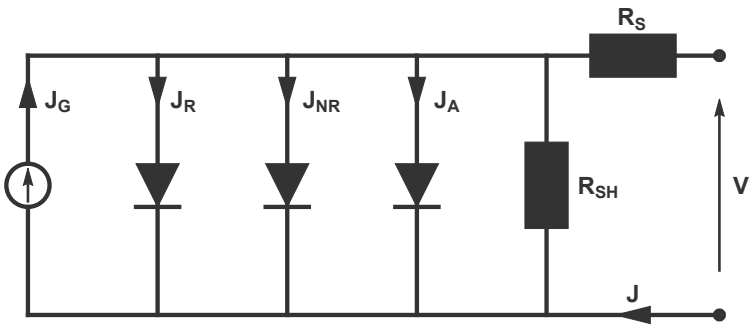


**Figure 1.4**: Equivalent circuit of the realistic solar cell model including photocurrent density ($J_G$), radiative recombination ($J_R$), nonradiative recombination ($J_{NR}$), Auger recombination ($J_A$), and parasitic series ($R_S$) and shunt ($R_{SH}$) resistances.

the realistic solar cell is shown in Figure 1.4. The current-voltage characteristic of a realistic solar cell is then given by

$$\begin{aligned} J(V) = {} & J_G(EQE) \\ & - J_R\left(\exp\left(\frac{q(V+JR_S)}{k_BT}\right)-1\right) \\ & - J_{NR,1}\left(\exp\left(\frac{q(V+JR_S)}{k_BT}\right)-1\right) \\ & - J_{NR,2}\left(\exp\left(\frac{q(V+JR_S)}{2k_BT}\right)-1\right) \\ & - J_A\left(\exp\left(\frac{3q(V+JR_S)}{2k_BT}\right)-1\right) \\ & - \frac{V+JR_S}{R_{SH}}. \end{aligned} \tag{1.19}$$

The last term is due to the shunt resistance. The current-voltage characteristics of a realistic solar cell can now be modelled by numerically solving Equation 1.19 for $J(V)$. The effects of the parasitic resistances, nonradiative recombination, and optical losses on the current-voltage characteristic are illustrated in Figure 1.5.

The ratio between radiative and nonradiative recombination can be described as the electroluminescent emission efficiency $\eta_{EL}$ [45], reducing Equation 1.19 to

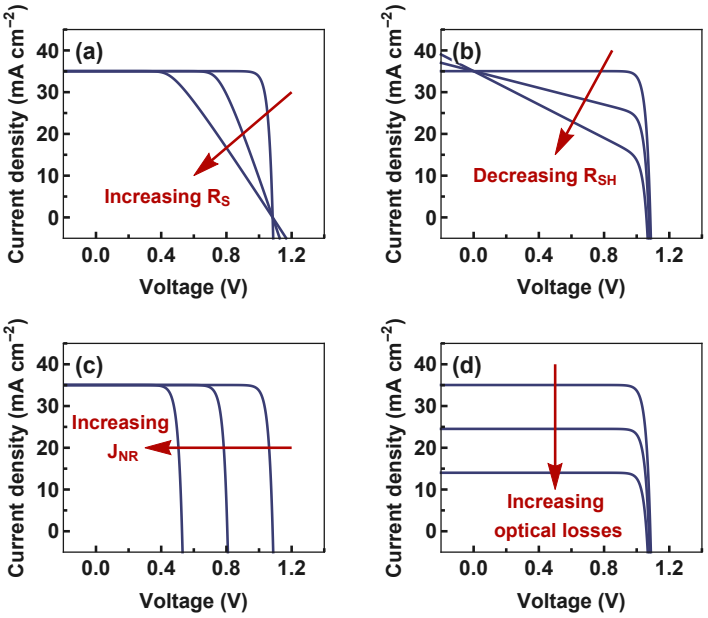


**Figure 1.5**: Realistic solar cell model. Effect of **(a)** parasitic series resistance ($R_S$), **(b)** shunt resistance ($R_{SH}$), **(c)** nonradiative recombination ($J_{NR}$), and **(c)** optical losses on the current-voltage characteristics of a solar cell with an band gap of 1.34 eV, calculated at standard test conditions (AM1.5G, 25 °C, 1000 W/m$^2$).

$$J\left(V\right)=J_G-\frac{J_R}{\eta_{EL}(V)}\left(\exp\left(\frac{q\left(V+JR_S\right)}{k_BT}\right)-1\right)-\frac{V+JR_S}{R_{SH}} \tag{1.20}$$

with

$$\eta_{EL}=\frac{J_R}{J_R+J_{NR,1}+J_{NR,2}\left(1+\left(\frac{q(V+JR_S)}{2k_BT}\right)\right)^{-1}+J_A\left(1+\left(\frac{3q(V+JR_S)}{2k_BT}\right)\right)^{-1}}. \tag{1.21}$$

Often, this is further approximated as

$$J(V)=J_G-J_0\left(\exp\left(\frac{q\left(V+JR_S\right)}{nk_BT}\right)-1\right)-\frac{V+JR_S}{R_{SH}} \tag{1.22}$$

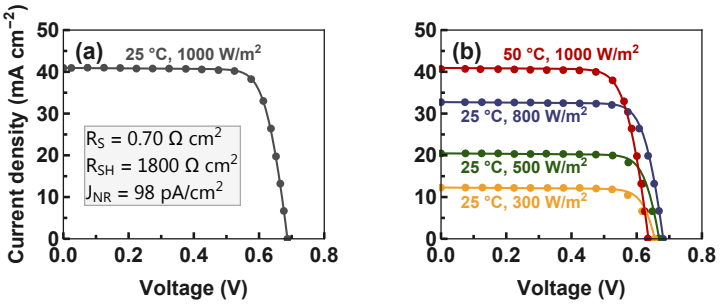


**Figure 1.6**: Modelled current-voltage characteristics of a commercially available SunPower C60 mono-crystalline silicon solar panel. The circles correspond to the measured values given in the data sheet. **(a)** The current-voltage characteristics at standard test conditions (AM1.5G, 25 °C, 1000 W/m$^2$) are used to obtain the amount of parasitic resistances and nonradiative recombination. **(b)** Current-voltage characteristics at different temperatures and irradiance. The fitting parameters remain as under standard test conditions. Measured data are represented with dots, fits with solid lines.

where $n$ is the ideality factor and $J_0$ the dark recombination current density. The ideality factor is often used to measure the quality of a solar cell. In an ideal solar cell with only radiative recombination the ideality factor is 1. However, an ideal factor of 1 does not mean that there is no nonradiative recombination. In reality, however, the ideality factor is often higher than 1 due to non-idealities within the solar cell, such as Shockley-Read-Hall recombination.

The model in Equation 1.19 can now be used to simulate temperature and irradiance effects of realistic solar cells by including materials specific parameters. The effect of parasitic resistances, nonradiative recombination, and optical losses on realistic perovskite/silicon tandem solar cells under real-world climate conditions is subject of Chapter 3.

To illustrate that the model accurately reflects trends in the current-voltage characteristics due to changes in temperature and irradiance, we fit the current-voltage characteristics of a commercially available SunPower C60 mono-crystalline silicon solar panel with an efficiency of 22.5% at standard test conditions (Figure 1.6a). Series resistance, shunt resistance, and the amount of nonradiative recombination are adjusted to obtain a good fit to the measurements. Figure 1.6b shows the measured and simulated current-voltage characteristics of the same cell at different temperatures and irradiance. In the model, only irradiance and temperature are adjusted, while the fitting parameters remain constant.

We note that that the model requires prior knowledge about the recombina-

tion channels in order to decide which nonradiative recombination of Equation 1.19 should be included to fit the current-voltage characteristics. Further, in reality, the ideality factor which corresponds to a specific recombination channel is not a constant [46] and can change with voltage [47], irradiance [48], temperature [49], or spectral shape, which might change the carrier distribution within the active layer and thereby the ratio of bulk- vs. surface recombination. Moreover, perovskites are mixed-ionic electronic conductors, and the migration of mobile ions through the device affects the potential within the device [50]. The current-voltage characteristics might hence change in a non-trivial way, leading to a different dependence on temperature and irradiance effects than what is reproduced by the model. The migration of mobile ions in perovskite-based devices is subject of Part II of this thesis.

*Published as:*

*M. H. Futscher and B. Ehrler, Efficiency limit of perovskite/Si tandem solar cells. ACS Energy Letters* ***1****, 863–868 (2016).*

# 2

# Ideal perovskite/silicon tandem solar cells

**Abstract**

Metal halide perovskite and silicon are the top material candidates for cost effective and >30% efficient tandem solar cells. We have analysed the influence of spectral and temperature changes on the limiting efficiency of perovskite/silicon tandem solar cells with different perovskite band gaps at two locations with distinctly different climate conditions: Utrecht, the Netherlands and Denver, Colorado, US. We compare voltage- or current-matched two-terminal and unconstrained four-terminal tandem assembly strategies using the detailed-balance model. Spectral and temperature variations measured over the course of an entire year lead to relative efficiency losses between 3.7 and 8.2% depending on the considered tandem configuration and location, suggesting that different locations may benefit from different tandem solar cell configurations. The monolithically integrated configuration is most affected by spectral variation since it is subject to current matching whereas the voltage-matched configuration is the least stable against temperature changes. Yet, spectral variations are far more important than temperature changes. Furthermore we show that the annual energy yield of realistic tandem solar cells strongly depends on the fill factor of the subcells.

## 2.1 Introduction

Metal halide perovskite/silicon tandem solar cells have been proposed as a promising candidate to surpass silicon efficiency records. Since the first report of a perovskite solar cell in 2009 [24], their power conversion efficiency has rapidly increased to more than 25% [27, 51]. In contrast, after 60 years of research, the power conversion efficiency of silicon solar cells is slowly approaching the Auger-recombination-constrained Shockley-Queisser limit close to 30% [18, 51]. To further increase the power conversion efficiency while simultaneously reducing the cost per kilowatt-hour (kWh), new strategies such as tandem configurations have to be applied. A tandem solar cell consists of two or more cells that are optically coupled by absorbing different parts of the incident spectrum (see Figure 1.2). This allows for more efficient conversion of the broad-band solar spectrum. In a two-cell configuration, the high-energy region of the spectrum is absorbed by the top cell, whereas the transmitted low-energy light is absorbed by the bottom cell. Metal halide perovskite-based cells are especially well-suited as a top cell for silicon-based tandem solar cells due to their high charge carrier mobility, high quantum yield, long diffusion length, sharp absorption edge, and a tunable band gap covering almost the entire solar spectrum [16, 18, 52–54]. Recently, it was shown that lead halide perovskites recycle light, meaning that power conversion efficiencies as high as those in GaAs-based solar cells might be feasible [55].

Several analyses on the limiting efficiency of tandem solar cells have been performed using detailed-balance calculations showing efficiencies up to 69.9% for an infinite number of subcells under 1-sun illumination [43, 56–61]. A key factor for the power conversion efficiency of tandem solar cells is the way that the subcells are connected. A perovskite/silicon tandem solar cell can be assembled in a two-terminal series connection where current matching is required, in a configuration that is voltage-matched at the module level, or as an unconstrained three- or four-terminal configuration where both subcells are electrically independent (see Figure 1.3). Monolithically integrated two-terminal [62–66], mechanically stacked four-terminal [67–72], and spectrally split four-terminal [73, 74] configurations have already been reported showing an increase of the overall efficiency compared to the silicon cell alone. The highest reported efficiency is 28.0% [27], exceeding the record silicon single-junction efficiency of 26.7% [75].

The three tandem configurations have an almost identical efficiency limit of about 45% under standard test conditions (AM1.5G, 1 kW/m$^2$, 25 °C). However, the tandem solar cell configurations place different constraints on the choice of band gap and the stability of the efficiency when the incident spectrum or cell temperature changes. The performance of the voltage-matched two-terminal and the four-terminal

configurations are most stable against varying spectral conditions [76, 77]. In contrast, the efficiency of the current-matched two-terminal configuration is the most stable against temperature changes [78, 79]. These dependencies suggest a nontrivial relation of the overall power-conversion efficiency with the environment [80, 81].

Here we analyse the theoretical efficiency limit of perovskite/silicon tandem solar cells, comparing all three assembly strategies with different perovskite band gaps under incident solar spectra measured in two different locations with distinctly different climate conditions. Spectral irradiance, ambient temperature, and relative humidity data were measured in Utrecht, the Netherlands and in Denver, Colorado, US in 2015 at an interval of 10 minutes during daylight hours. We use these spectra, irradiances, and the associated temperature to calculate the maximum efficiency of perovskite/silicon tandem solar cells via detailed-balance calculations for perovskite top cells of a 1.55 eV band gap and for the ideal perovskite band gap for the respective tandem configuration. Note that these calculations do not take any material specific parameters into account, which makes them valid for any material combination with the respective band gaps.

## 2.2 Limiting efficiency of tandem solar cells

In a thermodynamic consideration of detailed balance, the maximum power-conversion efficiency of silicon single-junction solar cells with a perfect reflector on the back side of the cell is limited to 33.5% for the AM1.5G spectrum at 25 °C, considering only radiative recombination as a loss mechanism and unity probability that photons with an energy above the band gap will produce one free charge carrier pair. This is commonly referred to as the Shockley-Queisser limit [42]. The two main losses arise due to the broad nature of the solar spectrum; photons with an energy below the band gap are transmitted, and photons with an energy above the band gap generate hot carriers that thermalize to the band edge (see Section 1.1 for details).

The most common tandem solar cell configuration is the monolithically integrated two-terminal in which the top cell and the bottom cell are optically stacked and electrically connected in series. In this configuration, the voltage of both cells adds and the photocurrent is limited by the cell producing the lower current. Consequently, when changes in the solar spectrum generate a mismatch between the current generated in the two subcells, the overall efficiency is reduced.

An alternative assembly for a tandem solar cell is the use of mechanically stacked cells in either a two- or four-terminal configuration. A mechanically stacked two-terminal module tandem consists of $n$ series-connected silicon bottom cells and $m$ series-connected perovskite top cells. Thereby, the perovskite cells can be voltage-

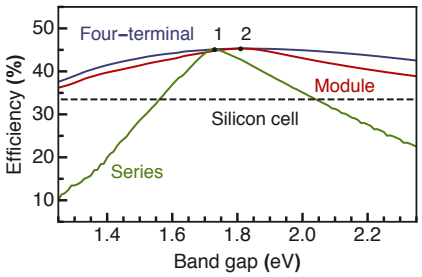


**Figure 2.1**: Efficiency limit of the three perovskite/silicon tandem solar cell configurations with different band gaps of the top cell obtained by detailed-balance calculations under standard test conditions (AM1.5G, 1 kW/m$^2$, 25 °C). The optimal band gap for the top cell is 1.73 eV (point 1) for the series tandem and 1.81 eV (point 2) for the module and the four-terminal tandem. The dashed line corresponds to the Shockley-Queisser limit of silicon.

matched with the silicon cells and electrically connected in parallel. In this configuration, the current of the perovskite cells and the silicon cells add and the maximum conversion efficiency is limited by the cell producing the lower voltage. A parallel connection has an advantage over a series connection because the open-circuit voltage ($V_{OC}$) changes only logarithmically with light intensity, whereas the short-circuit current density ($J_{SC}$) changes linearly. A module tandem is therefore more stable against spectral variations [76]. Conversely, temperature changes affect mostly the voltage of a solar cell; hence, we expect the two-terminal module tandem to be the least stable against temperature changes (see Section 2.6.3).

In an unconstrained four-terminal configuration, the top and bottom cells are electrically independent while still being optically coupled. A four-terminal tandem is not subject to either current or voltage matching, meaning that each subcell can maximise its power conversion efficiency independently. Consequently, a four-terminal tandem solar cell is expected to be the most stable against spectral and temperature changes.

To calculate the maximum efficiency for the different tandem solar cell configurations, detailed-balance calculations with modifications similar to work of De Vos [43] and Strandberg [79] are used (see Section 1.2 for details). For efficiency calculations of the module tandem, the ideal ratio of the number of perovskite top cells to the number of silicon bottom cells depends on the perovskite band gap. We set this ratio to 1/1.83 in order to match the efficiency-maximising band gap of the perovskite cell in the module configuration to the efficiency-maximising band gap of the perovskite cell in the four-terminal configuration. The limiting efficien-

cies for the two-terminal series tandem, the two-terminal module tandem, and the four-terminal tandem with a silicon bottom cell ($E_G$ = 1.12 eV) are shown in Figure 2.1. The limiting efficiency is 45.1% for the series tandem and 45.3% for the module and the four-terminal tandem under standard test conditions. Because the series tandem is subject to current matching, it features a narrow range of band gap combinations for the perovskite top cell from 1.57 to 2.04 eV where the efficiency limit exceeds the Shockley-Queisser limit of silicon. The module tandem requires matching of the photovoltage, which poses a weaker constraint on the band gap compared to matching of the photocurrent [76], while the electrically unconstrained four-terminal tandem allows for the broadest choice of band gap combinations. However, both the module and the four-terminal tandem configuration exceed the single-junction Shockley-Queisser limit of silicon for perovskite top cells with a band gap above 1.12 eV.

## 2.3 Spectral variations throughout the year

Climate conditions determine the amount of solar radiation that reaches the earth and affect the performance of tandem solar cell devices based on the spectral and temperature response of the considered tandem solar cell configuration. According to the Köppen–Geiger climate classification [82], the Netherlands has an oceanic climate with a narrow annual temperature range due to ocean currents, frequent precipitation, and variable weather, in many cases featuring an overcast sky. In contrast, Colorado has a steppe climate with lower precipitation and a broader annual temperature range, which on average is about 2 °C higher than that in the Netherlands.

The average photon energy (APE) is used to describe spectral irradiance distributions of measured spectra (see Section 2.6.4 for details). A high APE value corresponds to a blue-rich spectrum, whereas a low APE value corresponds to a red-rich spectrum. The APE was shown to be a suitable index to account for spectral irradiance variations [83–86]. The standard solar spectrum (AM1.5G) has an APE of 1.845 eV, calculated between 280 and 1107 nm, that is, for photons with an energy above the band gap of silicon. The APE values of the annual average spectrum at both locations (1.840 eV in the Netherlands and 1.850 eV in Colorado) are fairly similar to the APE of the standard spectrum (see Section 2.6.5 for the annual average spectra). However, the irradiance of the annual average spectrum at both locations (249 $W/m^2$ in the Netherlands and 432 $W/m^2$ in Colorado) is much lower than the irradiance of the standard spectrum (1000 $W/m^2$).

Figure 2.2 illustrates the wide distribution in measured spectral variations in the Netherlands and in Colorado. Inset (1) in Figure 2.2a shows a measured spectrum

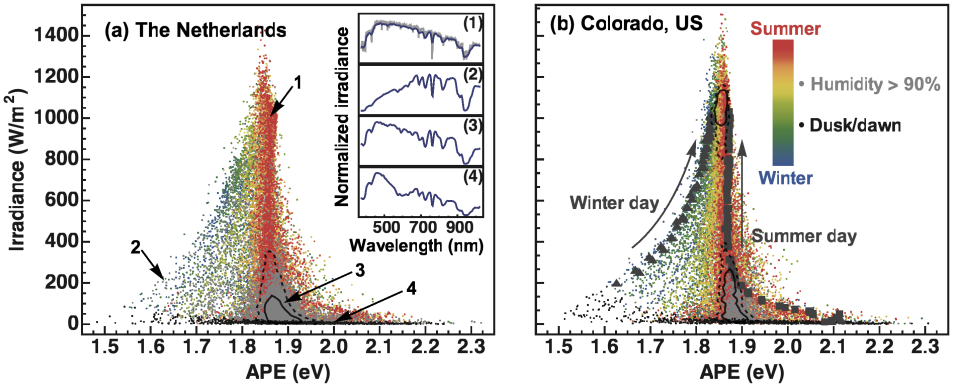


**Figure 2.2**: Spectral variations over the year 2015 in **(a)** the Netherlands [87] and in **(b)** Colorado [88]. The inset in (a) illustrates the wide variation in spectral distribution by means of exemplary solar spectra measured (1) at noon during the summer with the standard spectrum (AM1.5G) shaded in grey, (2) during a winter morning, (3) during a summer day with a high relative humidity, and (4) at dawn. The upright triangles and the squares in (b) correspond to the course of clear sky days measured in winter and in summer, respectively. The continuous and the dashed contour lines enclose 20 and 40% of the measured spectra, respectively.

during a sunny day at noon in summer, which closely follows the standard spectrum shaded in gray. Yet, only a small fraction of the measured spectra corresponds to the spectral distribution of the standard spectrum, indicating the importance of considering spectral variations governed by climate conditions for efficiency calculations of tandem solar cells.

During winter months, spectra are considerably red-shifted compared to the standard spectrum. An exemplary spectrum measured during a winter morning is shown in Figure 3a, inset (2). This seasonal effect on the spectral irradiance is due to the higher air mass in winter than in summer [89]. A higher air mass indicates that the solar radiation covers a longer path through the Earth's atmosphere, which results in an increase in wavelength-dependent Rayleigh scattering and selective absorption of the solar radiation by atmospheric molecules.

The humidity also has a strong effect on the spectral distribution. Spectral irradiance data with a humidity higher than 90% are indicated in grey in Figure 2.2, with an exemplary spectrum measured during a summer day with a high relative humidity close to 100% shown in inset (3). A high relative humidity (often coinci-

dent with high cloud coverage and rain) results in a lower irradiance with an APE slightly blue-shifted with respect to the standard spectrum. This is due to increased absorption by water vapour molecules at 724, 824, 938, and 1120 nm [90] and due to reduced Rayleigh scattering as more of the solar radiation is Mie-scattered by water vapour droplets, which only weakly depends on the wavelength [91].

Around dusk and dawn, spectra are blue-shifted with respect to the standard spectrum, as illustrated in Figure 2.2 by black dots for spectra measured up to 20 minutes before and after sunrise and sunset. The blue shift is due to absorption of solar radiation by the broad Chappuis band of ozone between 450 and 700 nm [92]. This appreciably affects the colour of the spectra only when the Sun is near the horizon, hence the path length of the solar radiation through the Earth's atmosphere is greatest [93]. An exemplary spectrum measured during dawn is shown in Figure 2.2a, inset (4).

Seasonal- and daytime-dependent variation of the spectrum is illustrated during the course of a clear sky winter (summer) day in Figure 2.2b by blue (red) triangles. In the winter, the spectrum is considerably red-shifted with respect to the standard spectrum. During the course of the day, the spectrum gradually blue shifts while the irradiance increases. When the day draws toward noon, the irradiance reaches its maximum and the APE is close to the standard spectrum. In the afternoon, the irradiance decreases and spectra undergo a red shift. Due to the lower air mass in summer months, the spectrum does not show the red-shifted APE values and remains much closer to the standard spectrum while mainly the irradiance changes during the course of a clear sky summer day.

## 2.4 Influence of spectral and temperature change

Calculated efficiency limits for perovskite/silicon tandem solar cells with the ideal band gap for the respective tandem configuration as a function of APE and irradiance are shown in Figure 2.3, taking spectral variations and temperature changes into account. Because the annually averaged APE of the two locations is similar to the one of the standard spectrum, the ideal band gap combinations for the Netherlands and Colorado are the same as those with the standard spectrum. Note that locations with an annually averaged APE dissimilar to the APE of the standard spectrum might have different ideal band gap combinations.

The limiting efficiency of a silicon cell is influenced little by spectral changes. The limiting efficiency of tandem solar cells on the other hand strongly depends on spectral and temperature changes. A shift in APE affects both the $J_{SC}$ and the $V_{OC}$ in the two subcells. Because the $J_{SC}$ has a stronger dependence on the photon flux than the $V_{OC}$, the current-matched series tandem is most affected by spectral changes. At

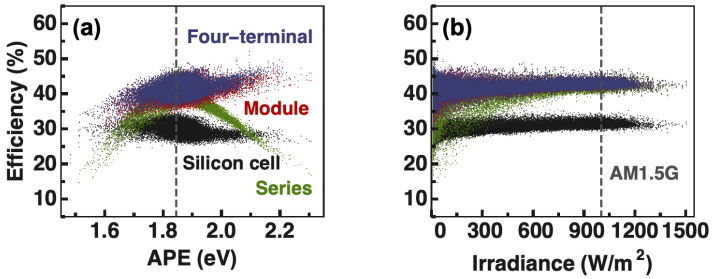


**Figure 2.3**: Efficiency limit of the three perovskite/silicon tandem configurations and a single-junction silicon cell under real illumination conditions as a function of **(a)** APE and **(b)** irradiance, obtained by detailed-balance calculations using data from both the Netherlands [87] and Colorado [88]. The dashed line indicates the APE and the irradiance of the standard solar spectrum (AM1.5G).

high APEs and low irradiances, the series tandem even features limiting efficiencies below the one of the single-junction silicon cell. Furthermore, module and four-terminal tandem solar cells show an increase in limiting efficiencies as the APE is increased because a larger part of the incident spectrum can be absorbed. The broad efficiency range for a given APE value is mostly due to different irradiance intensity because the efficiency logarithmically depends on the irradiance (see Section 2.6.6).

The intensity-weighted limiting power-conversion efficiencies in the Netherlands and Colorado of spectral irradiance to electricity averaged over the entire year are summarised in Table 2.1. The efficiency losses in realistic conditions compared to the standard test condition originating from spectral variations, temperature changes, and the use of a nonideal perovskite band gap are summarised in Figure 2.4a. Due to a higher average irradiance in Colorado than in the Netherlands, efficiency losses are generally higher in the Netherlands. The series tandem performs somewhat worse compared to the module and the four-terminal tandem due to its sensitivity to spectral changes. This effect is more pronounced in the Netherlands than that in Colorado due to stronger changes in the spectral shape. Limiting efficiencies of tandem solar cells furthermore decrease by up to 0.3% because of temperature changes. In total, the respective maximum annual energy yields for a perovskite/silicon tandem solar cell in the Netherlands and in Colorado are 531 and 893 kWh/m$^2$ for a series tandem, 543 and 910 kWh/m$^2$ for a module tandem, and 544 and 911 kWh/m$^2$ for a four-terminal tandem, respectively.

Up to now, we assumed the ideal band gap for the perovskite subcells. The limiting efficiency of perovskite/silicon tandem solar cells with the commonly used

**Table 2.1**: Power conversion efficiency limit over an entire year for the three perovskite/silicon tandem configurations and a single-junction silicon cell in Utrecht, the Netherlands (NL) [87] and in Colorado, US (CO) [88] and under standard test conditions (STC, AM1.5G, 1 kW/m$^2$, 25 °C) obtained by detailed-balance calculations.

| | Silicon cell (%) | Perovskite band gap (eV) | Series (%) | Module (%) | Four-terminal (%) |
|---|---|---|---|---|---|
| STC | 33.5 | ideal | 45.1 | 45.3 | 45.3 |
| | | 1.55 | 41.5 | 42.2 | 43.7 |
| NL | 31.1 | ideal | 41.5 | 42.4 | 42.5 |
| | | 1.55 | 38.3 | 39.6 | 40.9 |
| CO | 32.0 | ideal | 42.8 | 43.6 | 43.6 |
| | | 1.55 | 39.5 | 40.6 | 42.0 |

methalyammonium lead iodide ($MAPbI_3$) with a band gap of 1.55 eV is somewhat lower. A series tandem with a nonideal perovskite band gap strongly depends on the optical thickness of the perovskite top cell because an optically thick absorber does not achieve current matching (see Section 2.6.7). We therefore set the absorption of the top cell to 80% in order to maximise the efficiency of the series tandem with $MAPbI_3$ as a top cell. In this configuration, we observe similar trends as those for the ideal band gap (Figure 2.4b), with an additional penalty for the nonideal band gap between 3.5 (four-terminal) and 8.1% (series tandem). The limiting efficiency of a perovskite/silicon series tandem with optically thick $MAPbI_3$ is only 30.6% in the Netherlands and 31.3% in Colorado, taking only spectra changes into account. Consequently, perovskite/silicon tandem solar cells with optically thick $MAPbI_3$ should be built in either module or four-terminal configuration in order to surpass the single-junction Shockley-Queisser limit.

We note that in a realistic situation individual subcells might be affected by stability issues or changing outdoor illumination conditions such as partial shading, which has a direct influence on the performance of tandem solar cells. In particular, the series tandem strongly depends on the performance of individual subcells because the $J_{SC}$ is limited by the subcell generating the lowest current. In addition, perovskite solar cells are currently farther from their efficiency limit than the heavily optimised silicon cells [51], and calculations like the ones shown here should be performed whenever these tandem cells are to be employed on a large scale, for the particular location with realistic device parameters (see Chapter 3).

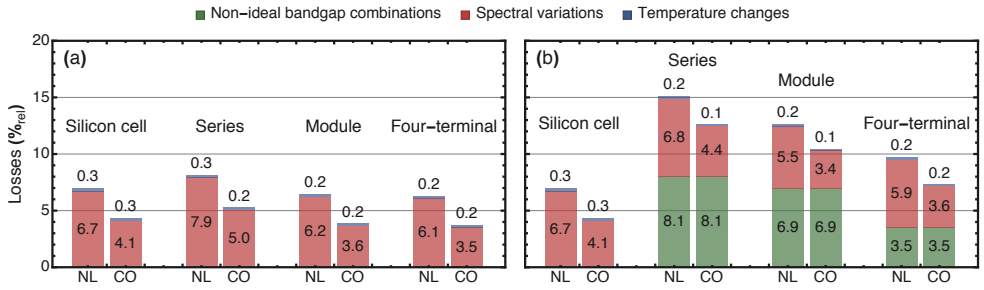


**Figure 2.4**: Effects of spectral variations, temperature changes, and the use of a non-ideal perovskite band gap on the maximum power-conversion efficiencies of the three perovskite/silicon tandem solar cells and a silicon single-junction cell in the Netherlands [87] and Colorado [88] obtained by detailed-balance calculations for **(a)** the ideal perovskite band gap for the respective tandem configuration and **(b)** a perovskite band gap of 1.55 eV.

## 2.5 Conclusion

In summary, we have analysed the influence of outdoor illumination conditions on the limiting efficiency of different perovskite/silicon tandem solar cell configurations. The efficiency of perovskite/silicon tandem solar cells is strongly affected by spectral and temperature changes. Consequently, weather conditions at the specific site of deployment should be taken into account when designing perovskite/silicon tandem solar cells. Among all of the perovskite/silicon tandem solar cell configurations, the current-matched series tandem is most affected by spectral variations and the use of a nonideal perovskite band gap. The impact of climate conditions on the limiting efficiency is primarily evident at low irradiances that comprise a significant amount of solar spectra measured throughout a year. These results indicate that perovskite/silicon tandem solar cells at different locations may require different tandem configuration and/or perovskite band gaps in order to minimize the cost per kWh. We show that by using a perovskite top cell with the ideal band gap for the respective tandem configuration, perovskite/silicon tandem solar cells with power conversion efficiency limits above 41% are possible for all three tandem configuration even at nonideal climate conditions.

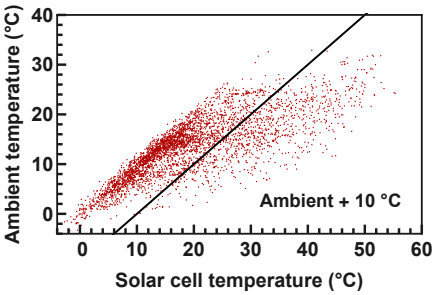


**Figure 2.5**: Ambient temperature as a function of a monocrystalline-silicon solar panel temperature measured in Utrecht, the Netherlands [87]. The continuous line indicates the assumption which was made in order account for temperature changes in Denver, Colorado, US.

## 2.6 Supporting information

### 2.6.1 Experimental

Measurements of solar spectra and temperatures were performed at the Utrecht Photovoltaic Outdoor Test facility (UPOT) [87] and at the NREL Outdoor Test Facility [88]. MS-700 (EKO Instruments) spectroradiometers operated at 25 $\pm$ 5 °C were used to measure the spectral irradiance between 350 and 1050 nm with an angular aperture of 180 °C and a spectral resolution of 3.3 nm at the two locations. The spectroradiometers were aligned with respect to the azimuth of the Sun with a 37 °C south tilt in Utrecht, the Netherlands and a 40 °C south tilt in Denver, Colorado, US. Light outside the spectral range of the spectroradiometers was included in the calculations by fitting measured spectra using a black-body spectrum with an effective temperature of 5777 K taking into account the molecular absorption in the Earth's atmosphere (see Section 2.6.2 for details). To measure the ambient dry bulb temperature and the relative humidity in Utrecht, the Netherlands and in Denver, Colorado, US WS600-UMB (G. Lufft Mess- und Regeltechnik) and HMP45C-L (Campbell Scientific) weather sensors were used, respectively. In Utrecht, the Netherlands the backside-temperature of a monocrystalline-silicon solar panel was used to account for temperature changes in detailed- balance calculations. Note that cell temperatures might differ from module temperatures. Figure 2.5 shows the ambient temperature as a function of the solar panel temperature. To account for temperature changes in Denver, Colorado, US, we assumed that the cells were a constant 10 °C above ambient temperature. Data from Denver, Colorado, US between July 8th and July 12th, 2015 are missing.

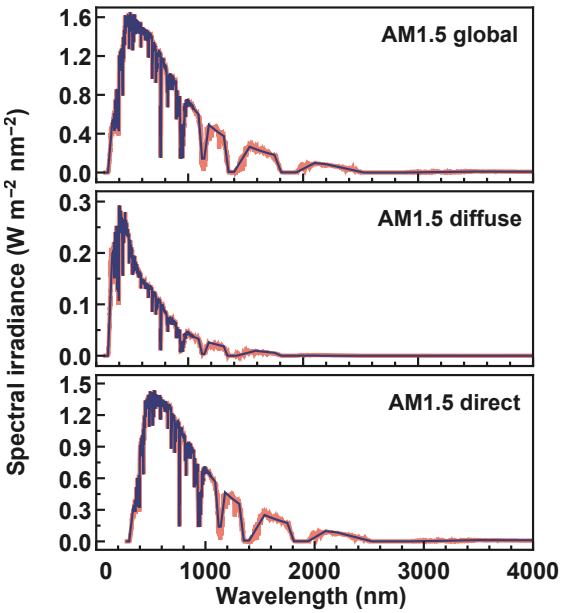


**Figure 2.6**: Fitted AM1.5 global, diffuse and direct solar spectra (blue) together with the unmodified AM1.5 solar spectra shaded in red.

**Table 2.2**: APE calculated in the range between 280 and 4000 nm, irradiance and efficiency limits for a single-junction (SJ) solar cell with a band gap of 1.12 eV and the three tandem solar cell configurations using a bottom cell with a band gap of 1.12 eV and the ideal band gap for the respective top cell of the fitted and the unmodified AM1.5 spectra obtained by detailed-balance calculations at 25 °C.

| | APE (eV) | Irradiance ($W/m^2$) | SJ (%) | Series (%) | Module (%) | Four-terminal (%) |
|---|---|---|---|---|---|---|
| Global | 1.46 | 1000.4 | 33.48 | 45.14 | 45.34 | 45.33 |
| Global fit | 1.46 | 1002.3 | 33.44 | 45.10 | 45.30 | 45.29 |
| Diffuse | 1.96 | 100.2 | 31.23 | 30.46 | 47.39 | 47.98 |
| Diffuse fit | 1.96 | 100.5 | 31.15 | 30.37 | 47.24 | 47.83 |
| Direct | 1.42 | 900.1 | 33.34 | 43.88 | 44.65 | 44.65 |
| Direct fit | 1.41 | 902.4 | 33.27 | 43.86 | 44.58 | 44.58 |

### 2.6.2 Fitting measured solar spectra

The used spectroradiometers measured the spectral irradiance between 350 and 1050 nm. In order to account for spectral regions which were not captured by the

**Table 2.3**: Mean APE calculated in the range between 280 and 1650 nm, mean irradiance and efficiency limits for a single-junction (SJ) solar cell with a band gap of 1.12 eV and the three tandem solar cell configurations using a bottom cell with a band gap of 1.12 eV and the ideal band gap for the respective top cell of fitted and measured spectra [88] obtained by detailed-balance calculations between 280 and 1650 nm at 300 K. The overall numbers are higher compared to the main text because the spectra here are only measured until 1650 nm, as oppose to the maximum wavelength of 4000 nm used in the main calculations.

| | APE (eV) | Irradiance ($W/m^2$) | SJ (%) | Series (%) | Module (%) | Four-terminal (%) |
|---|---|---|---|---|---|---|
| Measured | 1.68 | 294.6 | 34.70 | 46.13 | 47.97 | 48.04 |
| Fitted | 1.68 | 294.4 | 34.75 | 46.24 | 48.01 | 48.08 |

spectroradiometers, measured spectra were fitted using a black-body spectrum with an effective temperature of 5777 K to the shoulders of the solar spectrum in the spectral range between 860 and 890 nm and between 1000 and 1040 nm. The molecular absorption of the Earth's atmosphere was taken into account by subtracting irradiance in those regions. The cutoff and slope of the regions that were subtracted was optimised for optimum overlap with the AM1.5 global, diffuse, and direct solar spectrum simultaneously. To find the best fitting procedure, the AM 1.5 spectra were cut in order to have the same spectral range as the measured spectra (350 to 1050 nm) before fitting. The fitted AM1.5 spectra together with the unmodified AM1.5 spectra are shown in Figure 2.6. The irradiance and the efficiency limits for a single-junction Si solar cell and the three tandem solar cell configurations for the fitted and the unmodified AM1.5 spectra are summarised in Table 2.2.

In order to test the accuracy of the fitting procedure on real solar spectra, spectral irradiance measurements performed with EKO MS-710 and MS-712 spectroradiometers at the NREL Outdoor Test Facility [88] are used. Solar spectra were measured between 01.04.2015 and 01.04.2016 at an interval of 10 minutes during daylight hours. The MS-710 and the MS-712 spectroradiometers were operated at 25 °C $\pm$ 3 °C and at -5 °C $\pm$ 1 °C, respectively. The data were switched from the MS-710 to the MS-712 at 900 nm. Thereby, solar spectra in the range between 290 and 1650 nm are obtained. The measured spectra were cut in order to have the same spectral range as the spectra used in this work before fitting, i.e. between 350 and 1050 nm. The calculated irradiance of the fitted spectra against the irradiance the measured spectra is plotted in Figure 2.7. Together with the regression line that represents the linear relationship between the two values. The APE, the irradiance and the efficiency limits for a single-junction solar cell with a band gap of 1.12 eV and

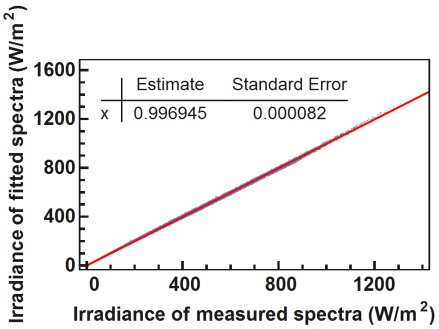


**Figure 2.7**: Linear regression of the calculated irradiance of the fitted solar spectra against the irradiance of the measured solar spectra.

the three tandem solar cell configurations for the measured and the fitted spectra are summarised in Table 2.3. The calculated values for the fitted spectra are in good agreement with the values for the measured spectra. Thus we assumed that the limiting power-conversion efficiency presented in this work has a confidence level of $\pm$ 0.1%abs.

### 2.6.3 Temperature dependent limiting efficiency

Figure 2.8a shows the open-circuit voltage ($V_{OC}$) and the short-circuit current ($J_{SC}$) as a function of temperature obtained by detailed-balance calculations of a single-junction solar cell with a band gap of 1.12 eV. Both $V_{OC}$ and $J_{SC}$ are normalised with respect to values obtained at 25 °C. The $V_{OC}$ is linearly depending on the temperature with a temperature coefficient of -1 mV/K, whereas the temperature dependence of $J_{SC}$ is insignificant. Note that detailed-balance calculations do not take any material dependent parameters into account such as the temperature dependence of semiconductor band gaps.

Figure 2.8b shows the temperature dependence for tandem solar cells with a bottom cell with a band gap of 1.12 eV and the ideal band gap for top cell for the respective tandem configuration. The relative change in efficiency per Kelvin is -0.15% for the single-junction cell with a band gap of 1.12 eV, - 0.13% for the module tandem, and - 0.12% for the series and the four-terminal tandem. Consequently, the voltage-matched module tandem is slightly more affected by temperature changes than series tandem configuration.

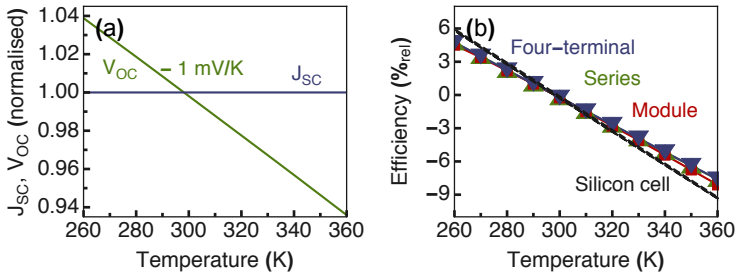


**Figure 2.8**: **(a)** Limit for the open-circuit voltage and the short-circuit current of a single-junction solar cell with a band gap of 1.12 eV with varied temperature. **(b)** Temperature dependence of the three tandem solar cell configurations and a single-junction solar cell with a band gap of 1.12 eV with varied temperature. Obtained by detailed-balance calculations using the AM1.5G standard solar spectrum.

### 2.6.4 Average photon energy

The average photon energy (APE) is defined as

$$APE = \frac{\int_{\lambda_{min}}^{\lambda_{max}} E\left(\lambda\right) d\lambda}{q \int_{\lambda_{min}}^{\lambda_{max}} \Phi\left(\lambda\right) d\lambda} \tag{2.1}$$

where $q$ is the elementary charge, $E$ is the spectral irradiance, $\lambda$ is the wavelength, and $\Phi$ is the photon flux as defined in Equation 1.2. Here $\lambda_{min}$ and $\lambda_{max}$ are chosen to be the minimum wavelength of the AM1.5 spectra and the wavelength corresponding to the band gap of silicon, i.e. 280 and 1107 nm, respectively. Note that different values for $\lambda_{min}$ and $\lambda_{max}$ can be found in literature resulting in small deviations from values obtained here. The photon flux is defined as in Equation 1.2.

### 2.6.5 Annual-averaged spectra

The annual-averaged spectra shown in Figure 2.9 are obtained by averaging all the measured solar spectra in the year 2015 in Utrecht, the Netherlands and in Denver, Colorado, US. The filled areas indicate regions in which APE values are obtained, i.e. 280 to 1107 nm.

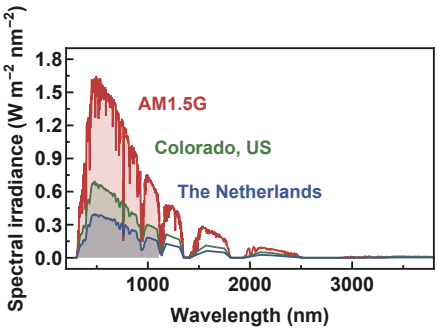


**Figure 2.9**: Annual-averaged spectra from 2015 in Utrecht, the Netherlands [87] and in Denver, Colorado, US [88] and the AM1.5G standard solar spectrum.

### 2.6.6 Irradiance dependent limiting efficiency

Figure 2.10 shows the limiting power-conversion efficiency as a function of irradiance for a single-junction solar cell with a band gap of 1.12 eV. The efficiency is logarithmically depending on the spectral irradiance.

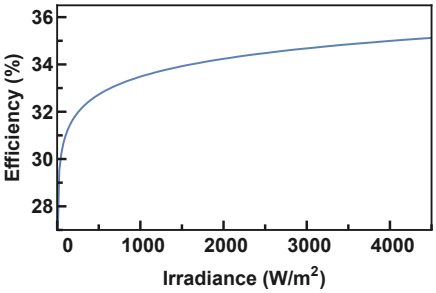


**Figure 2.10**: Efficiency limit of a single-junction solar cell with a band gap of 1.12 eV for the AM1.5G standard solar spectrum with varied spectral irradiance obtained by detailed-balance calculations at 25 °C.

### 2.6.7 Optically-thin series tandem

Figure 2.11 shows the maximum efficiency of a series connected tandem solar cell using bottom cell with a band gap of 1.12 eV calculated as described in Section 1.2 with modifications to account for the optical thickness of the top cell. The current density generated by the top cell and the bottom cell is determined by

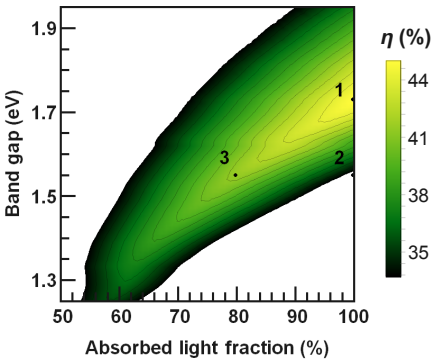


**Figure 2.11**: Limiting efficiency of a series connected tandem solar cell using a bottom cell with a band gap of 1.12 eV as a function of the band gap and absorbed light fraction of the top cell obtained by detailed-balance calculations under standard test conditions (AM1.5G, 1 kW/m$^2$, 25 °C). Only values exceeding the single-junction Shockley-Queisser limit with a band gap of 1.12 eV are shown. The efficiencies of points 1 to 3 are shown in the Table 2.4.

$$J_G^{top} = q \int_{E_G^{top}}^{\infty} \alpha \Phi \left( E \right) dE. \tag{2.2}$$

and

$$J_G^{bottom} = q \int_{E_G^{bottom}}^{E_G^{top}} \Phi \left( E \right) dE + q \int_{E_G^{top}}^{\infty} \left( 1 - \alpha \right) \Phi \left( E \right) dE. \tag{2.3}$$

where $q$ is the elementary charge, $\alpha$ is the absorbed light fraction of the top cell, and $\Phi$ the photon flux as defined in 1.2. Table 2.4 shows some calculated efficiencies for the ideal band gap for the top cell and for a top cell with a band gap of 1.55 eV, corresponding to the band gap of methalyammonium lead iodide ($MAPbI_3$).

**Table 2.4**: Limiting efficiency of a series connected tandem solar cell shown in Figure 2.11 obtained by detailed-balance calculations under standard test conditions (AM1.5G, 1 kW/m$^2$, 25 °C) using a bottom cell with a band gap of 1.12 eV.

| | Figure 2.11 | $E_G^{top}$ (eV) | $\alpha$ (%) | $\eta_{max}(\%)$ |
|---|---|---|---|---|
| Ideal band gap | Point 1 | 1.73 | 100 | 45.1 |
| $MAPbI_3$ | Point 2 | 1.55 | 100 | 32.4 |
| | Point 3 | 1.55 | 80 | 41.5 |

*Published as:*

*M. H. Futscher and B. Ehrler, Modeling the performance limitations and prospects of perovskite/Si tandem solar cells under realistic operating conditions. ACS Energy Letters* ***2****, 2089–2095 (2017).*

# 3

# Realistic perovskite/silicon tandem solar cells

**Abstract**

Perovskite/silicon tandem solar cells have the potential to considerably outperform conventional solar cells. Under standard test conditions, perovskite/silicon tandem solar cells already outperform the silicon single junction. Under realistic conditions, however, as we show, tandem solar cells made from state-of-the-art cells are hardly more efficient than the silicon cell alone. We model the performance of realistic perovskite/silicon tandem solar cells under real-world climate conditions, by incorporating parasitic cell resistances, nonradiative recombination, and optical losses into the detailed-balance calculations. We show quantitatively that when optimising these parameters in the perovskite top cell, perovskite/silicon tandem solar cells could reach efficiencies above 38% under realistic conditions, even while leaving the silicon cell untouched. Despite the rapid efficiency increase of perovskite solar cells, our results emphasise the need for further material development, careful device design, and light management strategies, all necessary for highly efficient perovskite/silicon tandem solar cells.

## 3.1 INTRODUCTION

Numerous perovskite/silicon tandem solar cells have been reported in series-connected, four-terminal, and module tandem configurations, increasing the efficiency of the silicon subcell alone [63–65, 67, 69, 71, 72, 94, 95]. With a record efficiency of 28.0% [27], perovskite/silicon tandem solar cells are already exceeding the record efficiency of silicon solar cells of 26.7% [96]. Yet, even the best perovskite/silicon tandem solar cells show much lower efficiencies than the detailed-balance efficiency limit. The efficiency is reduced due to parasitic absorption, nonradiative recombination ($J_{NR}$), undesirable series resistance ($R_S$) and shunt resistance ($R_{SH}$), and optical losses. Furthermore, as shown in Chapter 2, the power conversion efficiency of perovskite/silicon tandem solar cells is strongly affected by the considered tandem configuration, spectral variations, and temperature changes [97]. Using empirical models, it was shown that the energy yield potential of monolithically integrated perovskite/silicon tandem solar cells electrically connected in series are stronger effected by outdoor conditions than the four-terminal tandem configuration [98, 99]. These considerations show that the interplay of real-world climate conditions and realistic solar cell parameters has to be considered for an approximation of the performance of these cells.

Numerical optical simulations have shown that parasitic absorption losses in the perovskite top cell are one of the main limiting factors influencing the tandem efficiency and that perovskite/silicon tandem solar cells require careful photon management for optimum device performance [100–104]. Numerical models can provide deep insight into the working principles of perovskite/silicon solar cells [105], however, they require detailed knowledge about the specific device stack, rendering them unfavourable for fast characterisation of the energy yield of tandem devices. Analytical models have been developed for perovskite solar cells and perovskite/silicon tandem solar cells, showing the effect of device parameters such as nonradiative recombination, optical-thickness, and parasitic resistances and on the tandem efficiency [106, 107]. So far, however, a simple analytical model to understand the behaviour of realistic perovskite/silicon tandem solar cells under measured outdoor conditions is lacking.

Here we develop a simple, generic, and transferable model to simulate state-of-the-art perovskite solar cells by combining an optical model based on external quantum efficiency (EQE) measurements with an analytical electrical model based on current-voltage characteristics to predict the behaviour of realistic perovskite/silicon tandem solar cells under realistic conditions. This model provides clear guidelines to characterise and optimise perovskite/silicon tandem solar cells by quantitatively including physical parameters such as nonradiative recombination losses, parasitic

resistances, and optical losses into the detailed-balance model. Together with silicon bottom cells, we simulate realistic perovskite/silicon tandem solar cells under real-world climate conditions to predict the potential power yield. We show that the power conversion efficiency of perovskite/silicon tandem solar cells is hardly better than that of the single-junction silicon solar cell under realistic conditions, even when using one the best available perovskite and silicon solar cells to date (efficiency advantage <1.5% absolute). We also find that the three tandem connection schemes (connected electrically in series, on the module level, or as independent four-terminal devices) show almost identical efficiency values (<1.5% absolute difference). Only when reducing the parasitic absorption in the contacts do the tandem solar cells start to out-perform the single-junction silicon cell by 1.8-3.3% absolute. Finally, we show how a reduction in nonradiative recombination, optimised series and shunt resistance, and a reduction in optical losses for the perovskite cell could boost the efficiency advantage of the tandem cell up to 14.0% absolute (13.3% absolute for series tandem) compared to the single-junction cell. For these optimised cells, the connection scheme, as well as the climate conditions, become more important compared to nonoptimised cells.

## 3.2 Extended Shockley-Queisser limit

Including realistic solar-cell parameters such as nonradiative recombination and parasitic resistances into the detailed-balance limit calculations allows for simulating realistic solar cell performance under real-world climate conditions (temperature, irradiance, and spectrum). In the detailed-balance limit, all recombination is radiative, all light above the band gap is absorbed, and there are no optical losses (EQE = 1). Knowledge of the band gap, temperature, incoming spectrum, and intensity then allows calculating the limiting efficiency of a solar cell. We extend the detailed-balance calculations to include nonradiative recombination, series resistance, shunt resistance, and the fact that not all light above the band gap leads to photocurrent (optical losses, EQE > 1) (see Section 1.3 for details).
While efficiencies up to 25.2% have been reported for very small cells [27, 28], we model perovskite and silicon solar cells based on a devices $\geqslant$1 cm$^2$ to get more realistic values for the device resistances [75, 108]. The highest certified efficiencies for those large-area cell are around 20% [96]. We model a perovskite solar cell with an area of 1 cm$^2$ and an efficiency of 19.7% [109]. We note that due to the large sheet resistance in the transparent contacts, smaller area perovskite devices usually show higher efficiencies than larger area devices [109]. To simulate real-world climate conditions we use solar spectra, irradiance, and temperatures measured in Utrecht, the Netherlands [87] and in Denver, Colorado, US [88] in 2015 at an interval of 30

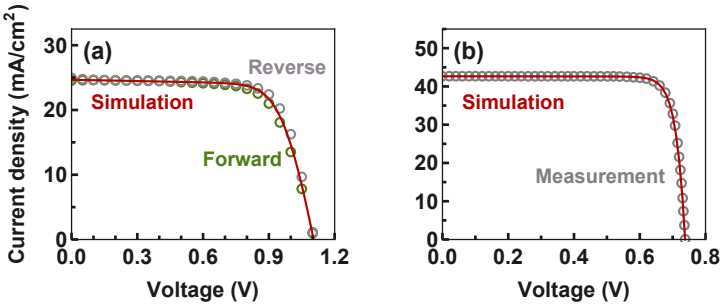


**Figure 3.1**: Modelled current–voltage characteristics of **(a)** a high-efficiency perovskite and **(b)** the record-efficiency silicon solar cell. The circles correspond to the measured data of (a) perovskite solar cell with a band gap of 1.49 eV [108] and (b) the silicon solar cell [75]. The fit parameters are summarised in Table 3.1.

**Table 3.1**: Modelled current–voltage characteristics of (a) a high-efficiency perovskite and (b) the record-efficiency silicon solar cells. The circles correspond to the measured data of the (a) perovskite solar cell with a band gap of 1.49 eV [108] and (b) silicon solar cell [75]. The fit parameters are summarised in Table 3.2

| | $R_S$ ($\Omega$ cm$^2$) | $R_{SH}$ ($\Omega$ cm$^2$) | $J_{NR}$ (pA/cm$^2$) | $J_{SC}$ (mA/cm$^2$) | $V_{OC}$ (V) | FF (%) | $\eta$ (%) |
|---|---|---|---|---|---|---|---|
| Perovskite | 3.10 | 1500 | 28.50 | 24.67 | 1.104 | 72.3 | 19.7 |
| Silicon | 0.08 | 10000 | 0.01 | 42.65 | 0.738 | 84.9 | 26.7 |

min during daylight hours.

We fit our model to the current-voltage characteristics of a high-efficiency perovskite and the record-efficiency silicon solar cells as shown in Figure 3.1. We include different mechanisms for nonradiative recombination for the silicon and perovskite subcells. To model the silicon cell, we take Auger recombination [52] and a nonradiative diffusion current of minority carriers into account. Since most of the perovskite layer is depleted [110–112], we assume the dominating recombination mechanism to be recombination from the depletion region. As a result, the dark current of the perovskite and the silicon solar cell have different dependencies on temperature, irradiance, and applied voltage (see Section 3.5.2 and Section 3.5.3 for details). The fitted parasitic resistances and dark current densities are summarised in Table 3.1. Optical losses such as reflection and parasitic absorption are included by fitting the EQE of the silicon and perovskite subcells. To account for the transparent contact of the perovskite top cell, we (optimistically) assume that it absorbs 10%

**Table 3.2**: Intensity-weighted power-conversion efficiency over an entire year for the three perovskite/silicon tandem configurations and the silicon solar cell under standard test conditions (STC, AM1.5G, 1 kW/m$^2$, 25 °C) and under real-world conditions at two locations with distinctively different climate conditions: Utrecht, the Netherlands (NL) [87] and Denver, Colorado (CO) [88].

| | Silicon cell (%) | Series (%) | Module (%) | Four-terminal (%) |
|---|---|---|---|---|
| STC | 26.7 | 27.6 | 28.5 | 28.5 |
| NL | 24.6 | 24.3 | 25.5 | 25.6 |
| CO | 25.0 | 25.3 | 26.4 | 26.4 |

of the incoming light prior to reaching the silicon subcell, with additional absorption in the blue-UV region of the spectrum (see Section 3.5.4) [95].

## 3.3 Performance under realistic operation conditions

Using these modelled perovskite and silicon subcells, we calculate the efficiency for current-matched series, voltage-matched module, and unconstrained four-terminal tandem assembly strategies as described in Section 3.5.4. The perovskite solar cell is based on a formamidinium lead iodide and methylammonium lead iodide mixture with a band gap of 1.49 eV [108]. The ideal band gap for a series-connected tandem solar cell with silicon as a bottom cell is 1.74 eV [66, 70], we therefore set the optical thickness of the perovskite top cell to 82% in order to current-match the perovskite top cell and the silicon bottom cell. An increase in the perovskite band gap would lead to an optically thicker perovskite layer (see Section 2.6.7). For the module tandem, the ratio between the number of perovskite top cells and silicon bottom cells was set to 1/1.39 in order to voltage-match one perovskite top cell with 1.39 silicon bottom cells. We calculate the efficiencies of single-junction cells and different tandem configurations under standard test conditions (AM1.5G, 1 kW/m$^2$, 25 °C) and under real-world climate conditions averaged over an entire year (see Table 3.2). The average efficiency is weighted with the incoming intensity, to allow for a calculation of the integrated power-conversion efficiency over the year.

Rather surprisingly, combining the high-efficiency perovskite and the record-efficiency silicon solar cells in a tandem configuration would increase the efficiency only marginally compared to the single-junction silicon solar cell alone. In fact, in the series tandem configuration, the efficiency is reduced by 0.3% absolute in the Netherlands, due to the stronger dependence on the incoming spectrum and irradiance. For this tandem configuration, the additional power generated in the per-

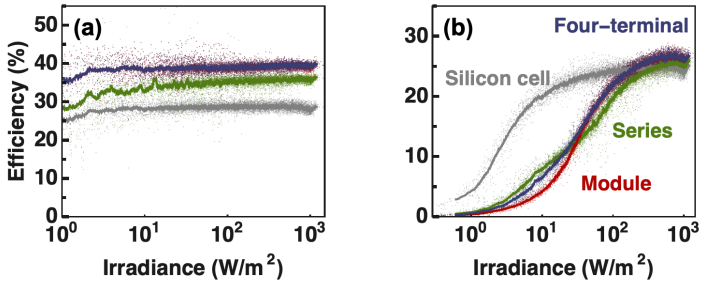


**Figure 3.2:** Efficiency of the three perovskite/silicon tandem configurations and the perovskite solar cell under real-world conditions as a function of irradiance calculated using solar spectra and temperatures measured in Utrecht, the Netherlands [87] for **(a)** ideal and **(b)** record efficiency silicon and perovskite subcells. The solid line represents a moving average of the data.

ovskite top cell does not outweigh the losses introduced by placing the perovskite cell on top of the silicon cell. We note that the difference between the different tandem configurations is less than 1.3% absolute, lower than expected from ideal cells. The losses compared to ideal cells are caused by shading part of the light from the silicon cell in the perovskite solar cell contacts, but also from electrical losses as the electrical characteristics of the perovskite cell are not as highly optimised as those of the silicon cell. These effects counteract some of the tandem specific losses due to spectrum and temperature changes, rendering the different tandem configurations similar in efficiency.

The efficiency of silicon solar cells and perovskite/silicon tandem solar cells as a function of solar irradiance, for ideal cells as discussed in Chapter 2 (Figure 3.2a), and with realistic solar cell parameters such as $J_{NR}$, $R_S$, and $R_{SH}$ (Figure 3.2b) shows that the difference in efficiency between ideal and realistic cells is most prominent in the low-intensity region. Crucially, electrical losses are particularly harmful at low light intensity and are hence typically underestimated when the solar cells are evaluated under standard test conditions. The strong decrease in efficiency at low irradiance is due to unfavourable $R_{SH}$, whereas the effects of $R_S$ and $J_{NR}$ are more prominent at high irradiance (see Section 3.5.5). In the following, we will examine how optimising the parameters of the perovskite cell, such as parasitic absorption in the contacts, improving the electrical characteristics, and eliminating all optical losses, can lead to a massive increase in efficiency compared to both the single-junction silicon cell, and the tandem cells made from state-of-the-art subcells.

Assuming no parasitic absorption in the transparent contact of the perovskite

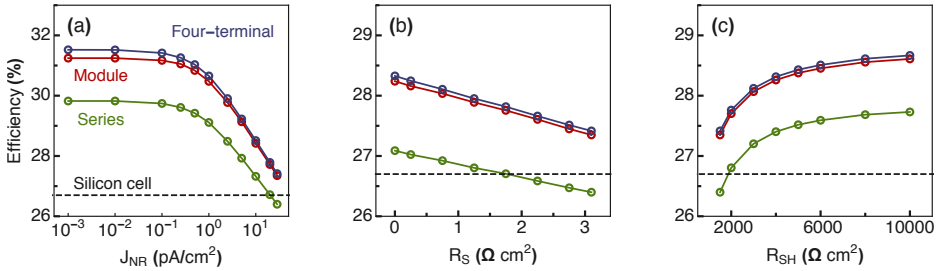


**Figure 3.3**: Effect of optimising **(a)** nonradiative recombination ($J_{NR}$), **(b)** series resistance ($R_S$), and **(c)** shunt resistance ($R_{SH}$), of the perovskite top cell on the intensity-weighted power-conversion efficiency over a year for the three perovskite/silicon tandem configuration calculated using solar spectra and temperatures measured in Utrecht, the Netherlands [87]. The dashed line indicates the performance of the silicon bottom cell at standard test conditions. The calculations assume no parasitic absorption in the perovskite cell contacts.

cell leads to an increase in the efficiency of tandem solar cells between 1.8 and 3.3% absolute compared to the silicon cell alone, depending on the considered tandem configuration and location. This increase stems from the increased current in the silicon subcell. While this scenario might be unrealistic for typical transparent contacts, novel contacting schemes as well as nanowire contacts have been proposed to reduce the overall optical losses in the transparent contact [113–118]. For simplicity, we assume no parasitic contact absorption in the perovskite top cell in the following discussion.

To understand the most practical ways to increase the efficiency of perovskite/silicon tandem solar cells, we systematically change the parameters $J_{NR}$, $R_S$, and $R_{SH}$ of the perovskite top cell in our model (Figure 3.3). For each calculation, the layer thickness of the perovskite top cell for the series tandem, and the ratio of silicon to perovskite cells for the module tandem were optimised for maximum efficiency. Reducing the nonradiative recombination to 1 fA/cm$^2$ of the perovskite subcell leads to a strong increase in power conversion efficiency of up to 4.4% absolute. Optimising parasitic resistances can further increase the efficiency by up to 1.3% absolute for $R_S$ = 0 Ω cm$^2$ and up to 2.0% absolute for $R_{SH}$ = 10000 Ω cm$^2$.

These changes in efficiency are different for the different tandem configurations. Due to the nonideal perovskite band gap of 1.49 eV for the modelled perovskite solar cell [108], the series tandem gains the least in efficiency by optimising the perovskite subcell compared to the module and the four-terminal tandem. This is especially

evident when optimising $J_{NR}$ and $R_S$ of the perovskite top cell, where the module and the four-terminal tandem gain about 0.5% absolute more in efficiency than the series tandem. The reduction of nonradiative recombination is slightly more beneficial for the four-terminal tandem than for the module tandem since the module tandem is subject to voltage-matching. However, the module tandem benefits notably more from a decrease in $R_S$ since a change in $R_S$ strongly changes the slope of the current-voltage characteristic close to the open-circuit voltage.

So far we used the EQE to account for optical losses due to reflection, parasitic absorption, and potential electrical losses. Assuming an ideal EQE of 1 for the perovskite subcell, the efficiency of the tandem cells can be further increased by about 0.4% for the series tandem and about 2.7% for the module and the four-terminal tandem. The series tandem is much less affected since the gain in current in the perovskite cell here is balanced by less light that it transmitted to the silicon cell. For the module and four-terminal tandem cell, the perovskite cell was optically thick to start with, so the additional EQE gain is almost exclusively a current gain for the overall tandem cell.

After optimising the perovskite subcell, there is a strong difference in efficiency between the series tandem, and the module and four-terminal tandem using a perovskite top cell with a nonideal band gap of 1.49 eV, due to the need for a semitransparent perovskite layer. This difference in efficiency between the tandem configurations almost vanishes by using a perovskite cell with an ideal band gap of 1.74 eV.

Taken together, optimising the perovskite cells can lead to an efficiency advantage of a tandem cells up to 13.3% absolute for the series tandem and 14.0% absolute for the four-terminal tandem, even when leaving the silicon cell untouched (Figure 3.4), reaching efficiencies up to 39.0%. When optimised, the perovskite solar cell alone has an efficiency of 32.1% for a nonideal band gap of 1.49 eV, and 28.4% for the ideal band gap of 1.74 eV under standard operating conditions (see Section 3.5.7 for details).

How much of this efficiency improvement is realistic for perovskite solar cells? While this question is difficult to answer in such a dynamic research field, it is sensible to consider the progress of other solar cell materials. The high series resistance of the perovskite solar cell can be reduced close to zero by optimised electrical contacts, e.g. including metal fingers. The shunt resistance has successfully been optimised to very high values for most established thin-film and silicon solar cells [119, 120]. Progress in optical performance, and in reducing the nonradiative recombination is more difficult to predict, but we note that silicon and GaAs cells have been optimised optically to achieve >95% EQE over a very broad spectral range [75, 121], and that the high radiative efficiency of some perovskite mixtures give reason to be optimistic about reducing the nonradiative recombination [122].

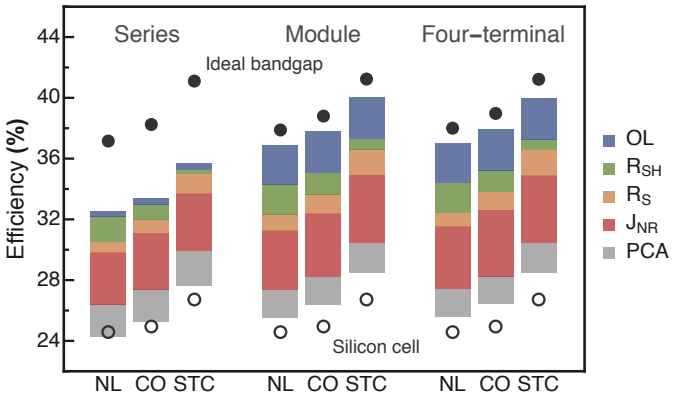


**Figure 3.4**: Effects of parasitic contact absorption losses (PCA), nonradiative recombination ($J_{NR}$), series resistance ($R_S$), shunt resistance ($R_{SH}$), and optical losses (OL) on the intensity-weighted power-conversion efficiency over a year for the three perovskite/silicon tandem configurations, calculated using standard test conditions (STC) and solar spectra and temperatures measured in Utrecht, the Netherlands (NL) [87] and in Denver, Colorado (CO) [88]. The empty circles indicate the efficiency of the silicon bottom cell alone. The filled circles indicate the tandem efficiency when using an optimised perovskite top cell with an ideal band gap of 1.74 eV.

In addition to the record efficiency silicon solar cell, we also simulate the performance of a tandem cell with a lower-efficiency silicon cell that is commercially available, a Sunpower solar cell with an efficiency of 22.5%. As above, we use the high-efficient perovskite solar cell with a band gap of 1.49 eV in a tandem configuration. The efficiency of the tandem cell is between 1.4 and 3.9% absolute higher compared to the Sunpower cell alone, less than expected for standard test conditions (2.7-4.4%). Optimising the perovskite top cell leads to an efficiency advantage of 16.1% (15.0% for the series tandem) absolute compared to the Sunpower cell alone, reaching efficiencies up to 37.0% (see Section 3.5.6 for details). These results show that a less efficient silicon cell is somewhat easier to improve when using it in a tandem cell.

The efficiencies for the tandem configurations are different for the different locations. the Netherlands comprises a larger fraction of low-irradiance solar spectra throughout the year compared to Colorado [97]. This difference in irradiance leads to a higher annual-averaged power conversion in Colorado than in the Netherlands (Figure 3.2). For the same reason, the reduction of $J_{NR}$ and the improvement of $R_S$ have a larger effect in Colorado, whereas the increase $R_{SH}$ has a larger effect in the Netherlands.

## 3.4 Conclusion

We simulated realistic perovskite/silicon tandem solar cells under real-world climate conditions. Our results show that, even with a high-efficiency perovskite and the record-efficiency silicon solar cells, a tandem cell would only marginally improve the efficiency of the silicon cell alone under realistic operating conditions. For the series tandem cell, the efficiency of the tandem configuration can even be lower than the single-junction silicon cell. When all parasitic absorption in the transparent contacts of the perovskite cell is reduced, the advantage in efficiency for the tandem cells amounts to 1.8-3.3% absolute compared to the silicon single-junction cell. This is far less than expected for ideal cells under ideal conditions, as the realistic cells are also more sensitive to the local climate conditions, in particular, the average irradiance. We show that further optimising parasitic cell resistances, nonradiative recombination, and optical losses of the perovskite top cell can boost the efficiency advantage of the tandem cells by up to 12.9% absolute when using the nonideal band gap of 1.49 eV, surpassing the single-junction Shockley-Queisser limit for all three tandem configurations under realistic operation conditions. This efficiency advantage can be further increased to 14.0% absolute when using the ideal perovskite band gap of 1.74 eV. We show that reducing the nonradiative recombination, optimising electrical nonidealities, and optical losses all have a large potential for efficiency gain. Optimising the perovskite cell also leads to an increased efficiency difference between the series-connected tandem cells and the four-terminal and module tandem cells.

Perovskite cells have shown breathtaking development in efficiency in recent years. Yet, our results highlight the need for a concerted effort in material development (reducing nonradiative recombination and tuning the band gap), device design (optimising cell resistances), and light management strategies (reducing optical losses and developing transparent contacts) to further increase the efficiency of perovskite cells, and develop highly efficient perovskite/silicon tandem solar cells.

## 3.5 Supporting information

### 3.5.1 Experimental

Measurements of the temperature, irradiance and solar spectrum were performed at the Utrecht Photovoltaic Outdoor Test facility (UPOT) in Utrecht, the Netherlands [87] and at the NREL Outdoor Test Facility in Denver, Colorado (US) [88] using identical MS-700 (EKO Instruments) spectroradiometers operated at $25 \pm 5$ °C. Light outside the spectral range of the spectroradiometers was included in the calculations by fitting measured spectra as described in Section 2.6.2. In Utrecht, the

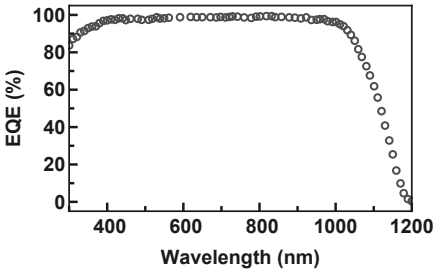


**Figure 3.5**: External quantum efficiency of a silicon solar cell [75] with an area of 79 $cm^2$ and an efficiency of 26.7% used to account for optical losses.

Netherlands the backside-temperature of a mono-crystalline silicon solar panel was used to account for temperature changes of the simulated tandem solar cells. To account for temperature changes in Denver, Colorado (US) we assume that the temperature of the solar cells $T_C$ depends on the ambient temperature $T_A$ and the solar irradiance $G$ as

$$T_C = T_A + kG \tag{3.1}$$

where $k$ is the Ross coefficient which is assumed to be 0.02 K $m^2$/W [123]. Data from Denver, Colorado, US between July 8th and July 12th, 2015 are missing.

### 3.5.2 Silicon solar cell model

To model the silicon solar cell, we fit the current-voltage characteristics of the current record silicon solar cell with an efficiency of 26.7% [75, 96]. The EQE of the record silicon solar cell is used to account for optical losses and parasitic absorption (see Figure 3.5). To account for spectral regions outside the published range we set the regions below 300 and above 1200 nm to 0% EQE.

Since silicon has an indirect band gap the diffusion length of electrons and holes are long compared to the width of the depletion region. Consequently, there is only very little recombination originating from the depletion region [44]. Nonradiative recombination current density of the silicon solar cell is thus calculated by approximating Equation 1.12 as

$$J_{NR}(V) = J_{NR,1}\left(\exp\left(\frac{qV}{k_B T}\right) - 1\right) \tag{3.2}$$

where $J_{NR,1}$ is calculated as

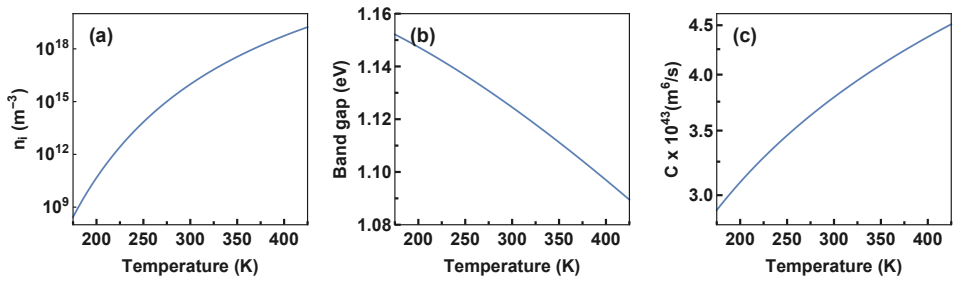


**Figure 3.6**: Temperature dependence of **(a)** the intrinsic charge carrier concentration, **(b)** the band gap, and **(c)** the Auger coefficient used to model the record silicon solar cell with an efficiency of 26.7%.

$$J_{NR,1} = \alpha n_i^2 \tag{3.3}$$

with the fitting parameter $\alpha$ to adjust the amount of nonradiative recombination due to diffusion limited current by minority carriers as well as surface and contact recombination [124]. The temperature dependence of the intrinsic charge carrier density is implemented in our model as [125]

$$n_i = 5.29 \times 10^{25} \frac{T}{300K}^{2.54} \exp\left(-\frac{6726K}{T}\right) \text{m}^{-3} \tag{3.4}$$

which is shown in Figure 3.6a. The temperature dependence of the band gap is calculated using Varshni's empirical Equation as [126]

$$E_G = E_{G,0K} - \frac{\xi T^2}{T + \chi} \tag{3.5}$$

with $E_{G,0K}$, $\xi$, and $\chi$ set to 1.17 eV, 4.73 $10^{-4}$, and 636 K, respectively [127]. The band gap of the simulated silicon solar cell as a function of temperature can be seen in Figure 3.6b. The thickness of the silicon wafer [75] is set to L = 165 µm and the temperature dependence of the Auger coefficient shown in Figure 3.6c is calculated as [128]

$$C = 3.79 \times 10^{-43} \sqrt{\left(\frac{T}{300K}\right)} \frac{\text{m}^6}{\text{s}}. \tag{3.6}$$

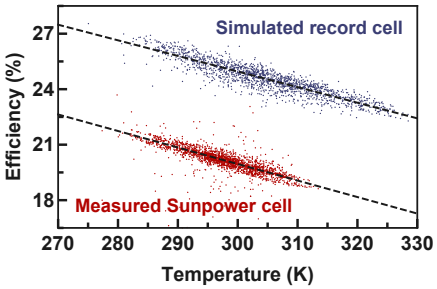


**Figure 3.7**: Performance of a Sunpower silicon cell measured at the AMOLF outdoor test facility together with the simulated performance of the record silicon single-junction solar cell at real-world climate conditions as a function of temperature. Only data with a solar irradiance higher than 500 W/m$^2$ are shown. The dotted lines correspond to linear regressions of the data used to quantify the temperature dependence.

The current-voltage characteristic of the modelled silicon solar cell can then be calculated by inserting Equation 3.2 in Equation 1.19, which then has only three fitting parameters: $\alpha$, $R_S$, and $R_{SH}$. The fitting parameters used to model the record silicon solar cell are shown in Table 3.1, which agree with values for high-efficient silicon solar cells [129].

In order to test the accuracy of the temperature dependence of our model we compare simulated record silicon solar cell efficiencies using spectral and temperature data measured in Utrecht, the Netherlands [87] in 2015 with measured efficiencies of an integrated-back contact Sunpower X-Series silicon solar panel with a nominal efficiency of 21.5% measured at AMOLF in Amsterdam, the Netherlands between January 1st and April 30th. The temperature-dependent efficiency of the simulated and the measured silicon solar cell is shown in Figure 3.7 for solar spectra with an irradiance higher than 500 W/m$^2$ showing that the simulation fits the temperature dependence of a measured silicon solar cell under real-world conditions reasonably well.

### 3.5.3 Perovskite solar cell model

To model the perovskite solar cell we fit the current-voltage characteristic of the a perovskite solar cell based on a formamidinium lead iodide and methylammonium lead iodide mixture with an area of 1 cm$^2$ and an efficiency of 19.7% [108]. Even though efficiencies above 25% have been published [28], these are typically on smaller cells. The EQE of the same perovskite solar cell is used to account for losses due to optical losses and parasitic absorption (see Figure 3.8). We distinguish between transmitted light (reabsorbed by the silicon cell in a tandem configuration)

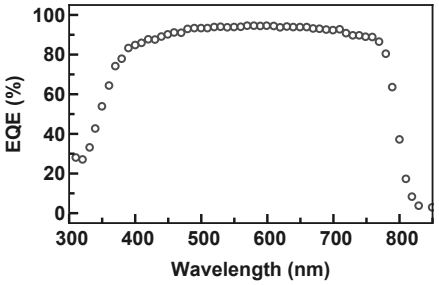


**Figure 3.8**: External quantum efficiency of the perovskite solar cell [96] with an area of 1 $cm^2$ and an efficiency of 19.7% used to account for optical losses.

and parasitic absorption and reflection as described in Section 3.5.4. To account for spectral regions outside the published range we set the regions below 300 and above 900 nm to 0% EQE.

Since perovskite strongly absorbs light, the perovskite film thickness in solar cells is typically on the order of a few hundred nanometer. Thus, most of the perovskite layer is depleted [110, 112]. Indeed it was found that the perovskite layer seems to be fully depleted at short-circuit conditions and at negative (reverse) bias [130]. The depletion layer was found to decrease when applying a positive (forward) bias [111]. As discussed in Section 1.3, recombination from the depletion region has an ideality factor of 2, which has often been observed for perovskite solar cells [131]. If the recombination would be limited by recombination of minority carriers outside the depletion region, surface recombination, or contact recombination, the ideality factor would be close to 1. We hence assume nonradiative recombination in the perovskite solar cell to be dominated by recombination from the depletion region [132]. By approximating Equation 1.12, nonradiative recombination current density of the perovskite solar cell is calculated as

$$J_{NR}(V) = J_{NR,2}\left(\exp\left(\frac{qV}{2k_BT}\right) - 1\right) \tag{3.7}$$

where $J_{NR,2}$ is calculated as

$$J_{NR,2} = \beta\frac{n_i}{\tau}\sqrt{V_{bi} - V}. \tag{3.8}$$

with the fitting parameter $\beta$ to adjust the amount of nonradiative recombination. Here, we assume that the lifetime for electrons and holes are the same. The built-in bias is proportional to the intrinsic charge carrier density and the temperature as

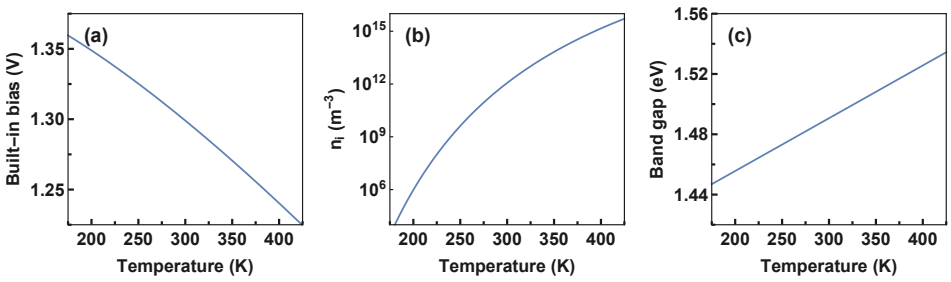


**Figure 3.9**: Temperature dependence of **(a)** the built-in bias, **(b)** the intrinsic charge-carrier concentration, and **(c)** the band gap used to model the perovskite solar cell.

$$V_{bi} \propto T \ln\left(\frac{1}{n_i^2}\right) \tag{3.9}$$

since the built-in bias is typically a bit higher than the open-circuit voltage we set it to 1.3 V at 25 °C, a bit higher than the open-circuit voltage of the Shockley-Queisser limit for a band gap of 1.49 eV (see Figure 3.9a). The density of states in the conduction band and in the valance band are assumed to be $N_C = N_V = 3.97 \times 10^{18}$ cm$^{-3}$ at 25 °C according to DFT calculations [105, 133]. The temperature-dependent intrinsic charge carrier density is thus calculated as

$$n_i = 7.36\ 10^{20}\ T^{3/2} \exp\left(-\frac{E_G}{2k_B T}\right) \text{ m}^{-3} \tag{3.10}$$

which is shown in Figure 3.9b. The band gap is assumed to increase by 0.35 meV per K and is calculated as [134]

$$E_G = 1.38565 \text{ eV} + 0.00035\ T\ \frac{\text{eV}}{\text{K}}. \tag{3.11}$$

We note that this temperature coefficient was derived for methylammonium lead iodide perovskite which might show different band gap changes compared to the formamidinium/methylammonium lead iodide mixture used in the modelled devices. The band gap of the simulated perovskite solar cell as a function of temperature can be seen in Figure 3.9c. Also different temperature coefficients have been reported for methylammonium lead iodide [135], which would lead to a slightly

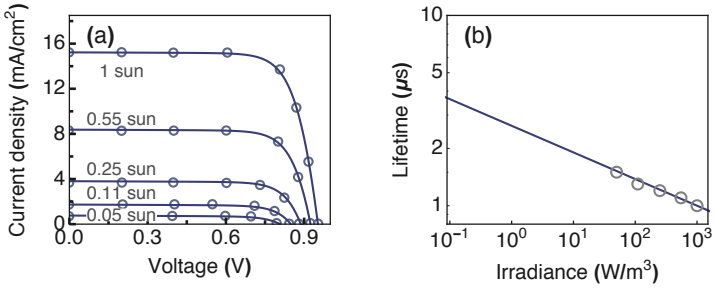


**Figure 3.10**: **(a)** Measured current-voltage characteristics [137] of a perovskite solar cell at different light intensities used to extrapolate irradiance-dependent charge-carrier lifetimes **(b)** used to model the perovskite solar cell.

reduced temperature effect in our model. Furthermore, methylammonium lead iodide perovskites undergo a phase transition from tetragonal to cubic close to 330 K [136], which is neglected in this study because it is not clear if it would be present in the modelled device.

The effect of irradiance on nonradiative recombination is included by using a charge carrier lifetime that depends on the solar irradiance $G$. The irradiance dependent charge carrier lifetime was included in the model by fitting current-voltage characteristics of methylammonium lead iodide perovskites measured at different light intensities [138]. The current-voltage characteristics were first fitted at 1-sun illumination to retrieve values for the parasitic absorption, resistance, and nonradiative recombination. At 1 sun, the charge carrier lifetime was set to 1 μs, in close agreement with many reports for this material [137, 139, 140]. These values were then used to fit current-voltage characteristics at different irradiances by changing only the irradiance and the charge carrier lifetime. The fitted current-voltage characteristics together with the obtained charge carrier lifetimes are shown in Figure 3.10. The irradiance dependent charge carrier lifetime to model the perovskite cell is then calculated as

$$\tau = 2.63 \left( \frac{G}{Wm^2} \right)^{-0.14} \mu s \tag{3.12}$$

where $G$ is the irradiance. A higher charge carrier lifetime at low irradiances would slightly decrease the effect of real-world climate conditions since it would reduce the nonradiative recombination. To test for the sensitivity of the fit on the lifetime dependence, we run our calculations for a much stronger irradiance dependence of

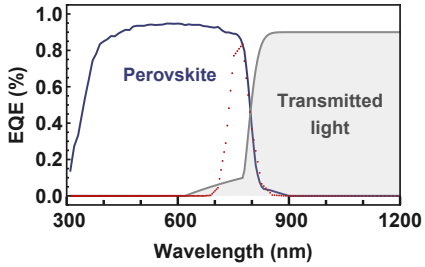


**Figure 3.11**: EQE model used to simulate realistic perovskite/silicon tandem cells. EQE of perovskite solar cell (blue) together with the fitted Gaussian distribution (red) used to model the below band gap transmission. Gray shaded areas represent the light which is transmitted to the silicon bottom cell.

the lifetime ($\tau$ = 100 $\left(\frac{G}{Wm^2}\right)^{-1/1.5}$). We find that the overall efficiency of the tandem cells increases only slightly, by 0.2% absolute. We note that the values for the charge carrier lifetime were extrapolated from measurements of a methylammonium lead iodide perovskite which might differ from charge carrier lifetimes of formamidinium lead iodide perovskites.
Since perovskite solar cells only show insignificant Auger recombination it is neglected in our model [17, 136]. The current-voltage characteristic of the modelled perovskite solar cell can then be calculated by inserting Equation 3.7 in Equation 1.19, which than has only three fitting parameters: $\beta$, $R_S$, and $R_{RS}$, including first- and second-order recombination where the first-order recombination is dominating, in agreement with many reports for perovskite-based solar cells [18]. The fitting parameters used to model the perovskite solar cell are shown in Table 3.1.

### 3.5.4 TANDEM SOLAR CELL MODEL

To calculate the efficiency of perovskite/silicon tandem solar cells, the current-voltage characteristic is modelled as described in Section 1.2. We assume a perfect reflector on the back side of the silicon bottom cell and no selective reflector between the perovskite top cell and the silicon bottom cell. For simplicity we neglect re-absorption of luminescence between the two subcells. Including the absorption of luminescence between the two subcells would increase the limiting efficiency of the tandem solar cells by less than 0.4% absolute. Optical losses are included by fitting a Gaussian distribution with a full width at half maximum (FWHM) of 53 meV to the onset of the EQE spectra of the perovskite cell. 10% of the light with an energy below the Gaussian distribution is assumed to be uniformly absorbed by parasitic absorption

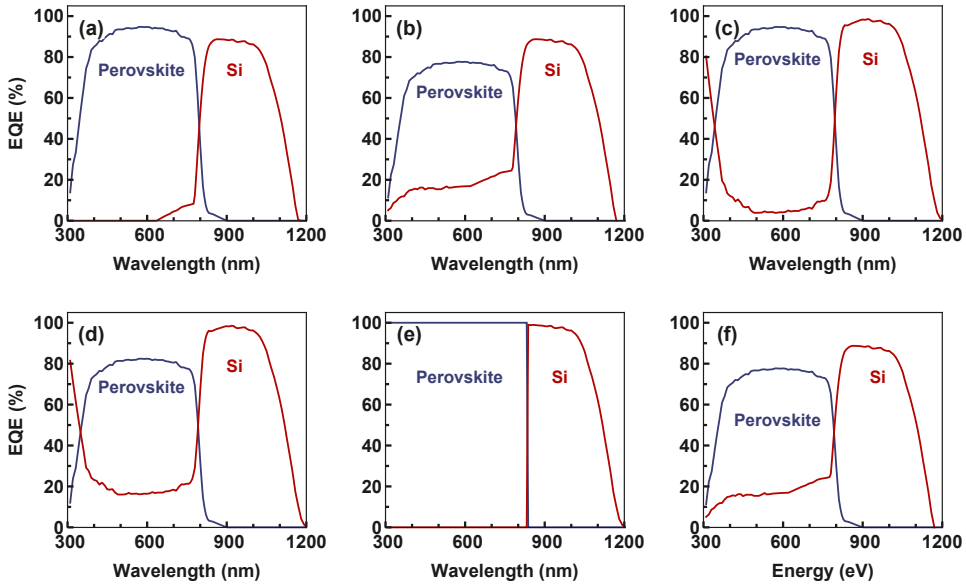


**Figure 3.12**: EQE of the modelled perovskite/silicon tandem solar cells for **(a), (b), (c)** the module and the four-terminal tandem and **(d), (e), (f)** the series tandem with an optical thin perovskite top cell to achieve current matching. (a), (d): State-of-the-art perovskite and record silicon subcells. (b), (e): State-of-the-art perovskite and record silicon subcells without contact losses. (c), (f): Record silicon subcell and perovskite subcell with an ideal EQE of 100% and no contact losses.

in the perovskite contacts. Light above the Gaussian distribution is almost completely absorbed in the perovskite. We include a small fraction of light between the band gap and 600 nm that is transmitted to follow published transmission curves [72]. The transmitted light by the perovskite top cell is shown in Figure 3.11 together with the fitted Gaussian distribution.

When neglecting transmission losses due to parasitic absorption and optical losses from the perovskite top cell the current density in the silicon bottom cell was calculated as

$$J_{G,Si} = q \int_0^\infty \Phi(E) \left[ EQE_{Si}(E) - EQE_{Perovskite}(E) \right] dE \tag{3.13}$$

where $q$ is the elementary charge, $EQE_{Si}$ the EQE of the silicon bottom cell,

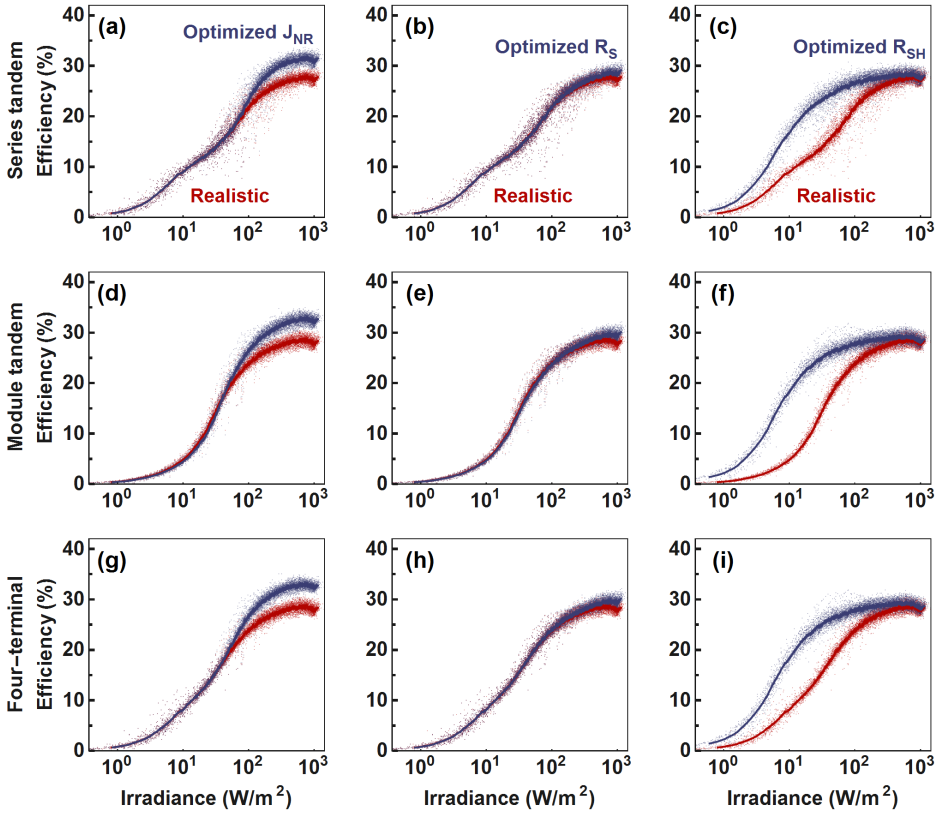


**Figure 3.13**: Impact of nonradiative recombination ($J_{NR}$), series resistance ($R_S$), and shunt resistance ($R_{SH}$) of **(a)**, **(b)**, **(c)** the series tandem, **(d)**, **(e)**, **(d)** the module tandem, and **(g)**, **(h)**, **(i)** the four-terminal tandem efficiency as a function of irradiance, respectively. The solid line represents a moving average of the data.

$EQE_{Perovskite}$ the EQE of the perovskite top cell, and $\Phi$ the photon flux as defined in Equation 1.2. For an optically thin perovskite top cell the current density was calculated as

$$J^{thin}_{G,Perovskite} = q \int_0^\infty \Phi\left(E\right)\ \gamma\ EQE_{Perovskite}\left(E\right) dE \tag{3.14}$$

and

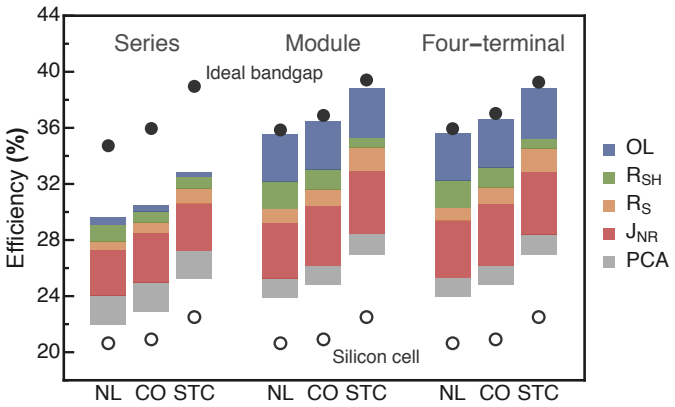


**Figure 3.14**: Effects of parasitic contact absorption losses (PCA), nonradiative recombination ($J_{NR}$), series resistance ($R_S$), shunt resistance ($R_{SH}$), and optical losses (OL) on the intensity-weighted power-conversion efficiency over a year for the three perovskite/silicon tandem configurations, calculated using standard test conditions (STC) and solar spectra and temperatures measured in Utrecht, the Netherlands (NL) [87] and in Denver, Colorado (CO) [88]. The empty circles indicate the efficiency of the silicon bottom cell alone. The filled circles indicate the tandem efficiency when using an optimised perovskite top cell with an ideal band gap of 1.75 eV.

$$J_{G,Si}^{thin} = q \int_0^\infty \Phi\left(E\right) \left[\gamma \, EQE_{Si}\left(E\right) - EQE_{Perovskite}\left(E\right)\right] dE \tag{3.15}$$

where $\gamma$ is the absorbed light fraction of the perovskite top cell. Note that this corresponds to an ideal case where all light not converted by the perovskite top cell is transmitted to the silicon bottom cell. The EQEs used to model the perovskite/silicon tandem solar cells are shown in Figure 3.12.

### 3.5.5 Impact of non-rad. recombination and parasitic resistances

Figure 3.13 show the effect of improving nonradiative recombination, series resistance, and shunt resistance of the perovskite top cell on the efficiency of perovskite/silicon tandem solar cells for the three different tandem configurations. Optimising nonradiative recombination and series resistance results in an overall increase in efficiency most prominent at high irradiance. Optimising shunt resistance on the other hand results in a strong increase in efficiency at low irradiance. In case of the series tandem, the effect of the stunt resistance of both the perovskite

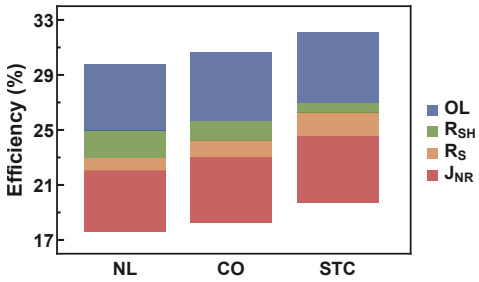


**Figure 3.15**: Effect of nonradiative recombination ($J_{NR}$), series resistance ($R_S$), shunt resistance ($R_{SH}$), and optical losses (OL) on the intensity-weighted power-conversion efficiency over a year for the modelled perovskite solar cell, calculated using standard test conditions (STC) and solar spectra and temperatures measured in Utrecht, the Netherlands (NL) [87] and in Denver, Colorado (CO) [88].

and the silicon cell is visible at low irradiance levels because it is subject to current matching.

### 3.5.6 Using a commercially available silicon solar cell

Figure 3.14 shows the effect of optimising the perovskite top cell on the efficiency of a perovskite/silicon tandem solar cell with the best performing, commercially available silicon solar cell as the bottom cell. The silicon cell was modelled after the SunPower C60 mono-crystalline silicon solar cell which has a short circuit current of 40.94 mA/cm$^2$, an open circuit voltage of 0.687 V, a fill factor of 80%, and an efficiency of 22.5%.

### 3.5.7 Optimising the perovskite solar cell

Figure 3.15 shows the efficiency of the perovskite cell alone with a band gap of 1.49 eV, when optimising nonradiative recombination, parasitic resistances and optical losses as described in the main text. The optimised perovskite cell with a band gap of 1.74 eV has a calculated efficiency of 28.4% using standard test conditions, 26.2% using solar spectra and temperatures measured in Utrecht, the Netherlands, and 27.1% using solar spectra and temperatures measured in Denver, Colorado.

# 4

# Bifacial perovskite/silicon tandem solar cells

**Abstract**

Bifacial solar modules can increase the energy yield over conventional solar modules by absorbing solar irradiation from both the front and rear side. We investigate the efficiency potential of using bifacial silicon solar cells in a tandem configuration with perovskites. We compare current-matched two-terminal and unconstrained four-terminal tandem solar cell configurations under real-world operation conditions. We find that the ideal perovskite band gap in a two-terminal bifacial perovskite/silicon tandem solar cell depends heavily on the albedo. By carefully designing the environment of the location of deployment, bifacial tandem solar cells allow record perovskite solar cells with a band gap of about 1.5 eV to be used in a tandem configuration with silicon. We show that using bifacial silicon solar cells increases the efficiency for the series tandem (6% absolute) even more than for the four-terminal tandem (5% absolute), as the current matching constraints of the series tandem are partially relaxed. As a result, both tandem configurations offer a similar efficiency potential under realistic operating conditions.

## 4.1 Introduction

As a result of global efforts towards cheap solar energy, levelised cost of electricity of solar power have fallen rapidly over the past years [7]. Increasing the power conversion efficiency now is one of the most important factors to further reduce levelised cost of solar energy [12, 14]. However, monofacial silicon solar cells, the most widely used solar cell technology, are approaching their theoretical efficiency limit [27, 51]. Using bifacial solar cells is a promising route to further reduce the cost per kilowatt-hour of silicon solar cells by absorbing ground-reflected and diffuse irradiation incident on the rear side of the cell in addition to the front irradiation [141–145]. Therefore, the International Technology Roadmap for Photovoltaics predicts bifacial silicon solar cells to have a market share of more than 35% by 2028 [146].

Tandem solar cells have the potential to further increase the efficiency of bifacial silicon solar cells by placing a solar cell with a higher band gap on top of the silicon solar cell [43]. Due to the excellent optoelectronic properties of metal halide perovskites, perovskite/silicon tandem solar cells have proven to be a promising candidate for reaching high power-conversion efficiencies beyond the single-junction Shockley-Queisser limit [147–149]. Tandem solar cells from monofacial silicon and perovskite already reach record efficiencies of 28%, higher than the efficiency of the record silicon solar cell alone [27].

A perovskite/silicon tandem solar cell consists of a silicon bottom cell and a perovskite top cell. The combination of two cells instead of one allows a more efficient use of the broadband solar spectrum (see Figure 1.2). The top and the bottom cell can be connected in different ways, most commonly either as a monolithically-integrated two-terminal series tandem or as a four-terminal tandem (see Figure 1.3 for a schematic illustration of the different tandem solar cell configurations). From an industrial point of view, the series tandem is of greatest interest as it requires only minor changes in the production compared to conventional silicon solar cells [150]. In addition, four-terminal tandem solar cells suffer from parasitic absorption and reflection losses from additional contact layers. On the other hand, the series tandem is subject to current matching, while in the four-terminal tandem the top and bottom cells are electrically independent. As a result, the different tandem configurations place different constraints on the choice of the band gap of the top cell, as we show in Chapter 2 and Chapter 3. Using a monofacial silicon solar cell, the four-terminal tandem configuration is rather insensitive to the choice of band gap of the top cell, where the series tandem reaches its maximum efficiency at 1.74 eV, with a significant reduction in efficiency when changing the band gap. We have furthermore shown that the series tandem is very sensitive to changes in the solar spectrum, since a change in the solar spectrum changes the absorbed light fraction

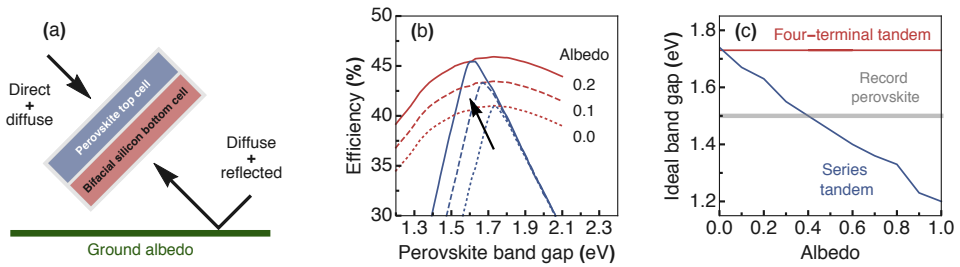


**Figure 4.1**: **(a)** Schematic illustration of a bifacial perovskite/silicon tandem solar cell that absorbs incident irradiation from both the front and rear. **(b)** Efficiency potential of the series and the four-terminal bifacial perovskite/silicon tandem solar cell with different band gaps of the perovskite top cell obtained by detailed-balance calculations under standard test conditions (AM1.5G, 1 kW/m$^2$, 25 °C) for different albedos. An albedo of 0 corresponds to monofacial silicon solar cells. **(c)** Optimal perovskite band gap for the top cell for the series and the four-terminal tandem as a function of albedo. The grey line corresponds to the band gap of the current record perovskite solar cell [27].

in the top and bottom cells and influences the current generated in each subcell.

Here we predict the efficiency potential of bifacial perovskite/silicon tandem solar cells (see Figure 4.1a for a schematic illustration of a bifacial perovskite/silicon tandem solar cell). We compare perovskite/silicon tandem solar cells in the series tandem configuration which requires current matching, and in the electrically unconstrained four-terminal configuration. In case of the series tandem, we find that the albedo strongly affects the ideal band gap of the perovskite top cell. We furthermore investigate the effect of realistic operation conditions on the efficiency of bifacial perovskite/silicon tandem solar cells and find that the current-matching constraints of the series tandem solar cell are partially relaxed, resulting in comparable efficiencies for series and four-terminal tandem solar cells under realistic operation conditions.

## 4.2 Efficiency potential of bifacial tandem solar cells

To calculate the potential efficiency of bifacial perovskite/silicon tandem solar cells, we adapt the model for calculating realistic tandem solar cells developed in Chapter 1 so that the silicon solar cell can absorb irradiation from both the front and the rear side. Assuming no parasitic absorption, photocurrent generated by the bifacial

silicon solar cell in a tandem configuration with perovskite is calculated as

$$\begin{aligned} J_G^{Si} = q \int_0^\infty [EQE_{Si}(E) - EQE_{Perovskite}(E)] \Phi^{front}(E)\, dE \\ + q \int_0^\infty \alpha\, \beta\, EQE_{Si}(E)\, \Phi^{rear}(E)\, dE \end{aligned} \tag{4.1}$$

where $q$ is the elementary charge, $EQE_{Si}$ and $EQE_{Perovskite}$ are the external quantum efficiencies of the silicon and the perovskite solar cell, and $\Phi^{front}$ and $\Phi^{rear}$ the photon flux of the incident solar spectrum on the front and the rear as defined in Equation 1.2. $\alpha$ is the albedo, i.e. how well the environment reflects the indecent irradiance onto the rear of the solar cell, which depends strongly on the surface. For example, the albedo is between 0.2 and 0.5 for grass, $\sim$ 0.3 for building concrete, $\sim$ 0.7 for sand, and $\sim$ 0.9 for snow [151]. We note that we assume a wavelength independent albedo, but in reality the albedo can have a strong wavelength dependence, affecting the efficiency of the device [151]. $\beta$ takes into account that the solar cell is not as efficient when illuminated from the rear as it is from the front. The bifaciality factor is then defined as the power upon illumination of the rear side divided by the power upon front side illumination with 1 sun. For state-of-the-art bifacial silicon solar cells, the bifaciality factor is typically between 0.7 and 0.95 [152].

Using the photocurrent for the bifacial silicon solar cell from Equation 4.1, we calculate the efficiency of bifacial perovskite/silicon tandem solar cells from Equation 1.19, assuming an almost ideal perovskite top cell, i.e $EQE$ = 1 above the band gap of the perovskite, a series resistance of 0.01 $\Omega$ cm$^2$, a shunt resistance of 10000 $\Omega$ cm$^2$, and only radiative recombination. To model the bifacial silicon solar cell we assume the $EQE$ and the electrical parameters of record silicon solar cell with an efficiency of 26.7%, i.e. a series resistance of 0.08 $\Omega$ cm$^2$, a shunt resistance of 10000 $\Omega$ cm$^2$, and a nonradiative recombination current density of 0.01 pA/cm$^2$ (see Section 3.5.2 for details), and a bifaciality factor of 0.9.

The efficiency potential of the series tandem and the four-terminal tandem solar cell are shown in Figure 4.1b as a function of perovskite band gap calculated at standard test conditions (AM1.5G, 1 kW/m$^2$, 25 °C). Note that we assume the same solar spectrum incident on the front and rear side of the tandem cell, scaled by the bifacial factor and albedo. A comparison of monofacial and bifacial solar cells in terms of efficiency is difficult because the bifacial cell has a higher input power than the monofacial cell due to the additional input power from the rear. To calculate the efficiency, we divide the output power in both cases by the input power of the front cell only (i.e. 1 kW/m$^2$ under standard test conditions). Similar to Figure 2.1, we find that the series tandem has a narrow range of band gaps where the efficiency is maximised because it is subject to current matching. The four-terminal tandem, on

the other hand, offers a wide range of band gap combinations in combination with silicon to achieve high efficiencies. At an albedo of 0.2, the efficiency gain for the series tandem is 4.5% and for the four-terminal tandem 4.9% absolute.

Increasing the albedo such that more irradiation is absorbed by the rear of the silicon solar cell shifts the ideal band gap of the top cell by -0.05 eV for every 0.1 for the series tandem (see Figure 4.1c). At an albedo of 0.4, the ideal band gap of the perovskite top cell corresponds to the band gap of the current record perovskite solar cell with a band gap of 1.5 eV [27]. Hence, a bifacial perovskite/silicon solar cell is not restricted to high band gap perovskites. The ability to use a perovskite with a band gap close to 1.5 eV may be critical for the production of stable perovskite/silicon solar cells, as high band gap perovskites are often affected by photo-induced phase separation due to halide migration [153–155]. However, since the ideal band gap and thus the efficiency is very sensitive to a change in irradiation from the rear, careful optimisation of the surroundings is necessary, as the irradiance of the rear side strongly depends on the surfaces, the orientation of the modules, the height of the module from the ground, and the arrangement of the modules [152].

## 4.3 Performance under realistic operation conditions

So far we have used standard test conditions to predict the efficiency potential of bifacial perovskite/silicon tandem solar cells. However, efficiencies of tandem solar cells are sensitive to spectral changes (see Chapter 2 and Chapter 3). We hence simulate the performance of the bifacial tandem solar cell under realistic operation conditions by taking variations in solar spectra and temperatures into account. We use solar spectra, irradiance, and temperatures measured in Utrecht, the Netherlands and in Denver, Colorado (US) in 2015 at an interval of 30 minutes during daylight hours (see Section 3.5.1 for details) [87]. Note that we assume the same solar spectrum for rear illumination as for front irradiation, scaled by the bifacial factor and albedo. In reality, however, the spectral shape and irradiance of the rear illumination may differ depending on the different contributions of diffuse and direct irradiation as well as the spectral dependence of the reflectivity of the surroundings.

Figure 4.2a shows the calculated efficiency as a function of average photon energy (APE) for a bifacial perovskite/silicon tandem solar cell with an albedo of 0.2. We use the ideal band gap for the perovskite top cell for both configurations, i.e. 1.63 eV for the series tandem and 1.73 eV for the four-terminal tandem solar cells. Note that we only show values with an irradiance greater than 50 $W/m^2$ in Figure 4.2a to highlight the effect of APE on the efficiency, which would otherwise be hidden under low irradiance data. A change in the shape of the solar spectrum changes the absorbed light fraction in the top and bottom cells. Therefore, the series

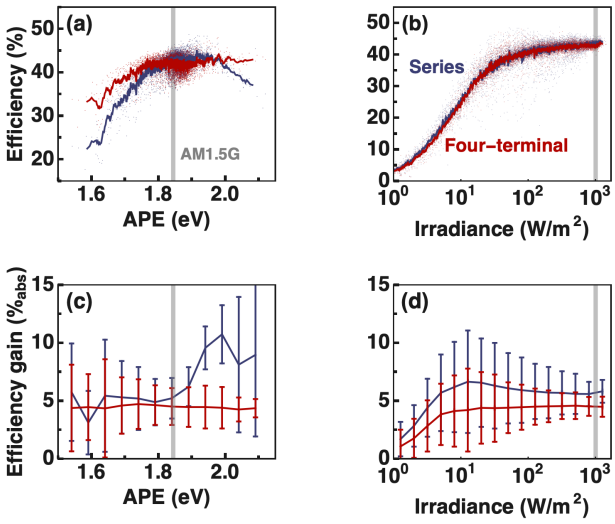


**Figure 4.2**: Efficiency potential of the two-terminal series and the four-terminal bifacial perovskite/silicon tandem solar cell under real-world conditions with an albedo of 0.2 as a function of **(a)** average photon energy (APE) and **(b)** irradiance calculated using solar spectra and temperatures measured in Utrecht, the Netherlands [87]. The solid line represents a moving average of the data. The gray line indicates the APE and the irradiance of the standard solar spectrum (AM1.5G). Absolute efficiency gain using a bifacial silicon solar cell instead of a monofacial silicon solar cell in a tandem configuration with perovskite as a function of **(c)** APE and **(d)** irradiance.

tandem is more affected by a change in the APE, as this leads to a current mismatch between the top and bottom cell, which reduces the efficiency of the series tandem. The changes in efficiency for varying irradiances are very similar for the series and the four-terminal tandem solar cell (Figure 4.2b). At low irradiances, the efficiency drops for both the series and the four-terminal tandem solar cell since parasitic resistors strongly influence the efficiency in low-light conditions. The observed efficiency changes as a function of irradiance differ from Figure 3.2 in Chapter 3 because here an almost ideal perovskite is used.

Next, we compare the efficiency of a bifacial perovskite/silicon tandem solar cell to a monofacial perovskite/silicon tandem solar cell. For the monofacial perovskite/silicon tandem solar cell we use the ideal band gap for the perovskite top cell for both configurations, i.e. 1.74 eV for the series tandem and 1.73 eV for the four-terminal tandem. The potential efficiencies for both the bifacial and the mono-

facial tandem solar cells under realistic operation conditions are summarised in Table 4.1. Using a bifacial silicon solar cell increases the efficiency of the series tandem by 6% and the four-terminal tandem by 5%. The efficiency improvement for the series tandem is higher than for the four-terminal tandem due to a partial relaxation of the current matching constraints. The additional photocurrent from the rear compensates for the current difference between the two subcells at high APEs (see Figure 4.2c). In reality, diffuse light on average could have an even higher APE, which may amplify this effect. Figure 4.2d shows that the efficiency increase for the series tandem is higher than for the four-terminal tandem for all irradiances occurring over the year, since even at high irradiances there is a broad distribution of APEs (see Figure 2.2).

**Table 4.1**: Efficiency potential of perovskite/silicon tandem solar cells with a monofacial and a bifacial silicon solar cell at realistic operation conditions.

| | Silicon cell (%) | Series tandem (%) | Four-terminal tandem (%) |
|---|---|---|---|
| Monofacial | 24.6 | 37.0 | 37.8 |
| Bifacial | 29.2 | 42.7 | 42.3 |

## 4.4 Conclusion

We simulated the efficiency potential of bifacial perovskite/silicon tandem solar cells under realistic operation conditions. We show that the ideal band gap for the two-terminal series tandem strongly depends on the albedo, allowing a wide range of band gaps for the perovskite top cell. The location, orientation, and environment of bifacial perovskite/silicon tandem solar cells must therefore be carefully designed for maximum energy yield. We find that the current-matched series tandem achieves comparable efficiencies under realistic operating conditions as the unconstrained four-terminal tandem, as current-matching constraints are partially lifted by the use of a bifacial silicon bottom cell. Using a bifacial silicon solar cell has the potential to increase the efficiency of perovskite/silicon tandem solar cells by 5 to 6% absolute for the four-terminal and the series tandem, respectively. Since both configurations have similar efficiency potentials, but the fabrication of series tandems requires fewer changes in the fabrication of conventional solar cells, our results suggest that the series tandem should be preferred over the four-terminal tandem solar cell configuration with bifacial bottom cells if the front and rear illumination are well known.

*Published as:*

*M. H. Futscher, A. Rao and B. Ehrler, The Potential of Singlet Fission Photon Multipliers as an Alternative to Silicon-Based Tandem Solar Cells. ACS Energy Letters* ***3****, 2587–2592 (2018).*

# 5

# The singlet fission photon multiplier

**Abstract**

Singlet fission, an exciton multiplication process in organic semiconductors that converts one singlet exciton into two triplet excitons, is a promising way to reduce thermalization losses in conventional solar cells. One way to harvest triplet excitons is to transfer their energy into quantum dots, which then emit photons into an underlying solar cell. We simulate the performance potential of such a singlet fission photon multiplier combined with a silicon base cell and compare it to a silicon-based tandem solar cell. We calculate the influence of various loss mechanisms on the performance potential under real-world operation conditions using a variety of silicon base cells with different efficiencies. We find that the photon multiplier is more stable against changes in the solar spectrum than two-terminal tandem solar cells. We furthermore find that, as the efficiency of the silicon base cell increases, the efficiency of the photon multiplier increases at a rate higher than that of the tandem solar cell. For current record silicon solar cells, the photon multiplier has the potential to increase the efficiency by up to 4.2% absolute.

## 5.1 INTRODUCTION

Criyalline silicon solar cells dominate the global solar cell market, and record efficiencies of 26.7% approach the Auger-recombination-constrained Shockley-Queisser limit [51, 52, 75]. For further improvement in the power conversion efficiency new solutions beyond the silicon single-junction cell are needed.

Conventional solar cells lose a major part of incident sunlight energy via thermalization of excited charge carriers [42]. For a silicon solar cell with a band gap of 1.12 eV, thermalization accounts for a 39% power loss using the AM1.5G solar spectrum (see Figure 1.2). The reduction of thermalization losses thus offers a great opportunity to achieve efficiencies above the Shockley-Queisser limit. Many strategies have been proposed to reduce thermalization losses of silicon solar cells, including tandem configurations and the modulation of the solar spectrum by down conversion.

In a tandem configuration with two subcells, a high-band-gap cell is placed on top of a low-band-gap cell [43]. Photons with a high energy are absorbed in the top cell, and the transmitted light is absorbed in the bottom cell, reaching record efficiencies of 32.8% with III-V semiconductors as the top cell and silicon as the bottom cell in a four-terminal configuration [156]. Perovskites are a class of materials that promise cost-effective and efficient tandem solar cells in combination with silicon [95, 97, 157]. However, tandem solar cells add extra costs and complexity to the fabrication process. They are furthermore sensitive to changes in solar spectrum and temperature during the course of a year, which reduces their efficiency under real-world conditions compared to laboratory conditions (see Chapter 2 and Chapter 3) [147, 148].

While tandem solar cells are studied extensively, partially because of the recent boom in perovskite research, alternatives such as spectral modulation have received considerably less attention. Modulating the solar spectrum by either up- or down-conversion of photons [77, 158–163], single-junction solar cells can operate at an efficiency comparable to that of tandem solar cells [159]. A down-conversion device absorbs high-energy photons with at least twice the band gap energy and emits twice as many photons with about half that energy. We call this device a "photon multiplier".

Singlet fission, a spin-allowed exciton multiplication process in organic semiconductors which converts one singlet exciton into two triplet excitons [164], is a suitable process for such a photon multiplier. Upon photoexcitation, organic semiconductors generate singlet excitons. If the energy of these singlet excitons $E(S_1)$ is close to twice the energy of the lowest-lying triplet exciton $E(T_1)$, i.e. $E(S_1) \approx 2E(T_1)$, singlet fission ($S_1 \rightarrow 2T_1$) can occur on sub-100 fs time scales [165]. Singlet

fission has been observed with very high efficiency [166–169], even for endothermic singlet fission, i.e. $E(S_1) < 2E(T_1)$. We note that there likely is an inevitable trade-off between entropic gain and triplet exciton yield. However, endothermic singlet fission with barriers as high as 200 meV was shown to be still highly efficient [170]. Triplet excitons can then transfer their energy to an inorganic semiconductor directly via a charge or an energy transfer or via a quantum-dot-mediated intermediate state [171]. While direct energy transfer into silicon would be desirable, as it avoids all other loss channels, it has not been shown to date [172] and would require changes to the silicon solar cell architecture. In contrast, the photon multiplier is a purely optical downconverter, which allows for easy integration into existing solar cell technologies without the need for changes to the underlying solar cell, even as an upgrade (see Figure 5.1a). To form the photon multiplier, the triplet excitons first transfer their energy into quantum dots. Within the quantum dots, the excitons recombine to emit photons [173, 174], whereby the exciton multiplication process becomes a photon multiplication process. Further details on singlet fission and the photon multiplier concept can be found in a recent review [175].

The efficiency limit of singlet fission solar cells essentially matches the efficiency limit for a two-junction tandem solar cell [176]. However, these efficiency limits are calculated for ideal cells under standard test conditions, and both cell types have very different potential loss mechanisms and a very different dependence on environmental conditions. Hence, here we simulate the potential performance of both types, but with realistic electrical and optical parameters, and simulate them under real-world environmental conditions using a variety of silicon base cells with different efficiencies. We simulate the performance of the current-matched series, the voltage-matched module, and the electrically independent four-terminal perovskite/silicon tandem solar cell. In the analysis, however, we focus on the series tandem, as the monolithic two-terminal configuration is the most attractive from an industrial point of view [149]. Our simulations provide clear guidelines to optimise photon multiplier devices by including physical parameters such as the energy of the singlet exciton, the energy and the full width at half-maximum (FWHM) of the quantum dot emission, losses due to absorption, transfer efficiency, and imperfect guiding of the emitted photons toward the bottom cell. We find that the photon multiplier is more stable against changing irradiation, spectral shape, and temperature than tandem solar cells, which are important factors in real-world performance. We furthermore find that, as the efficiency of the silicon base cell increases, the photon multiplier gains faster in efficiency than the tandem solar cell and that for current record silicon solar cells, the photon multiplier has the potential to increase the efficiency by up to 4.2% absolute.

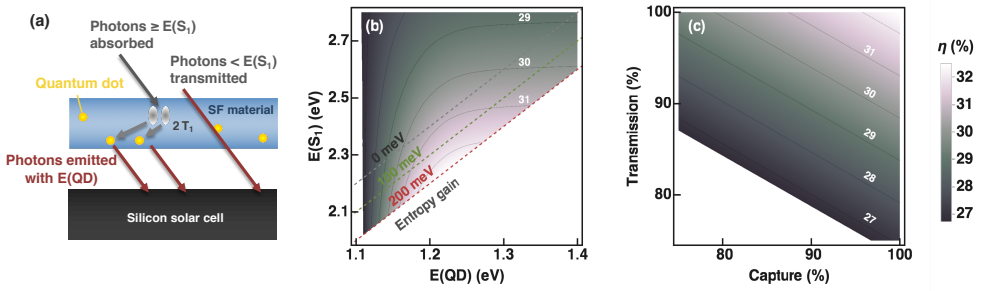


**Figure 5.1**: **(a)** Schematic illustration of the singlet fission photon multiplier device. **(b)** Efficiency of the singlet fission photon multiplier as a function of singlet exciton energy $E(S_1)$ and energy of quantum dot emission E(QD) assuming no transmission and capture losses. **(c)** Efficiency of the singlet fission photon multiplier as a function of capture and transmission losses below $E(S_1)$. The capture parameter is defined in the text as $\eta_{SF}/2 \times \eta_T \times \eta_{QD} \times \eta_C$. The calculations are performed at standard test conditions using a silicon base cell with an efficiency of 26.7%.

## 5.2 Photon multiplier model

To simulate the performance of the singlet fission photon multiplier in combination with a silicon solar cell, we model the modulation of the solar spectrum. The efficiency of the silicon solar cell is then calculated using the model developed in Chapter 1 and the modulated solar spectrum. The silicon solar cell is modelled by including realistic solar cell parameters such as Auger recombination, nonradiative recombination, and parasitic series and shunt resistance into detailed-balance calculations. To include parasitic absorption of the contacts, we include the external quantum efficiency (EQE) in the model. This allows for simulating the performance of both the silicon solar cell and the photon multiplier for changing solar spectra and temperatures (see Section 5.6.1 for details).

For a photon multiplier that absorbs all light above the energy of the singlet exciton $E(S_1)$ and where the quantum dots emit at the energy $E(QD) = 1/2\ E(S_1)$ with a FWHM of 30 meV, the optimum energetics are E(QD) = 1.21 eV and $E(S_1)$ = 2.42 eV. Including entropic gain, the optimal singlet exciton energy shifts to lower energies, while the energy for quantum dot emission remains almost constant. At 200 meV entropic gain, the optimum would be at E(QD) = 1.22 eV and $E(S_1)$ = 2.24 eV, where the efficiency of the record silicon solar cell would be enhanced from 26.7 to 32.5% (see Figure 5.1b).

In the following, we discuss the losses which for real devices will reduce this

**Table 5.1**: Parameters and efficiency ($\eta$) of the realistic and the optimistic singlet fission photomultiplier calculated at standard test conditions using a silicon base cell with an efficiency of 26.7%. The capture parameter is defined in the text as $\eta_{SF}/2 \times \eta_T \times \eta_{QD} \times \eta_C$.

| | Entropic gain (meV) | Transmission (%) | Capture (%) | FWHM (meV) | $\eta$ (%) |
|---|---|---|---|---|---|
| Realistic case | 100 | 95 | 85 | 30 | 29.0 |
| Optimistic case | 200 | 97 | 95 | 30 | 31.3 |

efficiency potential. To take transmission losses due to parasitic absorption and reflection by the photon multiplier into account, we assume that photons with an energy below $E(S_1)$ are homogeneously absorbed or reflected before reaching the silicon solar cell. Using transfer matrix simulations, we show that the reflection above the singlet fission band gap is less than 7% when placing a photon multiplier on top (see Section 5.6.2 for details). This value is likely to be improved by texturing and anti-reflection optimisation. In addition, we consider losses during the photon multiplication process, which are collectively referred to as capture losses. The efficiency of the singlet fission photon multiplier for different combinations of absorption and capture losses assuming a 30 meV FWHM for the quantum dot emission and 200 meV entropic gain is shown in Figure 5.1c. These capture losses include the triplet exciton yield from singlet fission ($\eta_{SF}$), the efficiency of triplet excitons diffusing to and transferring into the quantum dots ($\eta_T$), the photoluminescence quantum efficiency (PLQE) of the quantum dots ($\eta_{QD}$), and the fraction of photons emitted by the quantum dots toward the silicon solar cell ($\eta_C$). In the following we compare two cases of photon multipliers. A realistic case with an efficiency of 29.0% and an optimistic case with an efficiency of 31.3% using the record silicon base cell with an efficiency of 26.7% (for parameters, see Table 5.1). In the realistic and optimistic cases we assume a capture of 85% and 95%, respectively, which assumes high values for $\eta_{SF}$, $\eta_T$, $\eta_{QD}$, and $\eta_C$. In the following we provide evidence that these are, however, not unreasonable.

The triplet exciton yield from singlet fission ($\eta_{SF}$) was shown to reach values close to 200% for pentacene-based devices [166–169]. Because triplet transport occurs through a Dexter mechanism, triplets diffuse much slower than singlet excitons [177]. For endothermic singlet fission, however, triplet diffusion is enhanced by singlet-mediated pathway that allows for long diffusion lengths of triplet excitons [178, 179]. The energy transfer from the triplet exciton to the quantum dots via Dexter transfer ($\eta_T$) has been demonstrated with efficiencies >95% for lead chalcogenides-based quantum dots [173, 174]. We note that singlet excitons can also transfer their

energy to the quantum dots; this is, however, negligible for singlet fission materials with fast dynamics, because fission should kinetically out-compete energy transfer into the quantum dots. Because of the long triplet exciton diffusion length [178–180], only a small number of quantum dots need to be embedded in the singlet fission material. Ideally, the quantum dots are distributed evenly throughout the singlet fission material, spaced by the triplet diffusion length. We estimate that quantum dots distributed in a micrometer-thick singlet fission layer, spaced by 50 nm, would absorb less than 0.5% of the transmitted light and therefore do not consider any re-absorption losses in our model (see Section 5.6.2 for details). Although the highest reported PLQE for lead chalcogenides-based quantum dots ($\eta_{QD}$) with the desired energy of emission is only close to 50% [181, 182], we expect a PLQE of >95% to be realistic in the future, because quantum dots optimised for PLQE (e.g., metal chalcogenide and pnictide core-shell and lead halide perovskite quantum dots) [183] reach PLQE values close to unity. Part of the isotropic quantum dot emission falls within the escape cone determined by the critical angle and is lost. For a singlet fission material with a refractive index of 1.7, already less than 10% of light is within the escape cone (see Section 5.6.2). The other part is directly emitted into, or guided by total internal reflection toward the silicon bottom cell. The fraction of light guided to the silicon base cell ($\eta_C$) can further be increased by using a singlet fission material with a high dielectric constant or by asymmetric dielectric nanostructures close to the quantum dot emitters.

The current-voltage characteristics of the modelled realistic and optimistic photon multiplier together with the modulated photon flux reaching the silicon solar cell filtered by its EQE are shown in Figure 5.2a. The effect of FWHM on the efficiency is relatively small; however, a wider emission spectrum does shift the ideal quantum dot band gap to slightly higher energies (Figure 5.2b; see also Table 5.6 and Table 5.7).

## 5.3 TANDEM SOLAR CELL MODEL

To compare the potential of the photon multiplier to tandem solar cells, we simulate a monolithic two-terminal perovskite/silicon tandem solar cell with all parameters based on the high-efficient perovskite solar cell with an efficiency of 22.7% and an area of 0.09 $cm^2$ [108], except that we change the band gap to the ideal value of 1.68 eV in order to current-match the perovskite top cell with the silicon bottom cell. The perovskite cell features a shunt resistance of 5000 $\Omega$ $cm^2$, a series resistance of 0.32 $\Omega$ $cm^2$, and an electroluminescent emission efficiency of 0.15%. This leads to an efficiency of 20.9% for the perovskite solar cell and 32.7% for the tandem solar cell in combination with the record silicon solar cell with an efficiency of 26.7% (see

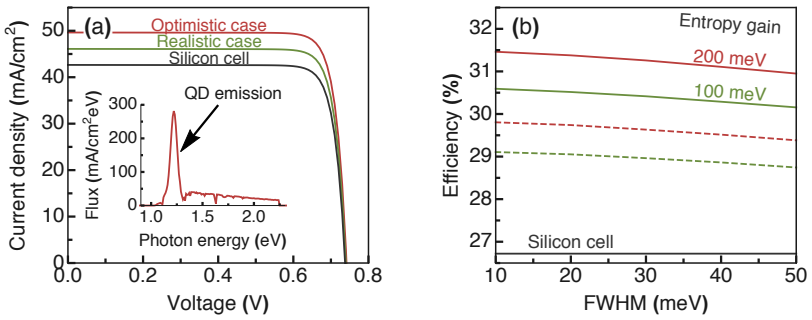


**Figure 5.2**: **(a)** Current–voltage characteristics of the modelled singlet fission photon multiplier on the silicon base cell with an efficiency of 26.7% for the optimistic case and the realistic case. The inset shows the modulated photon flux incident on the silicon base cell filtered by its external quantum efficiency. **(b)** Efficiency of the singlet fission photon multiplier as a function of full width at half-maximum (FWHM) for the quantum dot emission using a silicon base cell with an efficiency of 26.7%. The solid (dashed) lines assume 3% (5%) parasitic absorption losses below the singlet fission band gap and capture losses of 5% (15%). The black solid line indicates the efficiency of the silicon solar cell.

Section 5.6.3 for details). We note that we did not include any possible optical or electrical losses from the intermediate recombination layer required in practical tandem cells. The performance characteristics of the perovskite cell assumed here are hence optimistic and have not yet been achieved with this band gap.

## 5.4 Performance under realistic operation conditions

To simulate real-world conditions, we use solar spectra, irradiance, and temperatures measured in Utrecht, the Netherlands and in Denver, Colorado (US) in 2015 at an interval of 30 minutes during daylight hours [87, 88], as described in Section 3.5.1.

Figure 5.3a shows that the efficiency of the tandem solar cell and the photon multipliers over the course of the year. Because the photon multiplier acts as a passive optical film modulating the incident solar spectrum, no electrical contact with the silicon solar cell is required. The photon multiplier thus shifts the silicon solar cell to higher efficiencies without considerably changing its dependence on the irradiance. The difference to the tandem cell is most prominent in the low-intensity region. The decrease in efficiency for tandem cells at low irradiance is due to the shunt resistance from the perovskite top cell that adds to the shunt resistance from the silicon cell alone. At high irradiances, the tandem solar cell overtakes the silicon

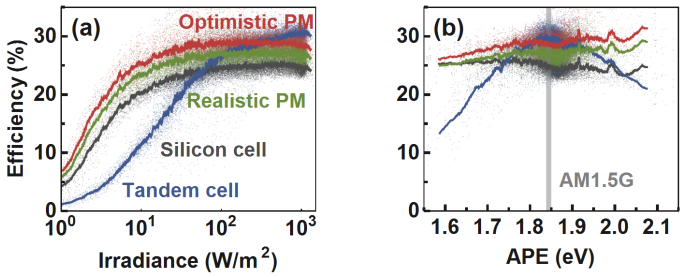


**Figure 5.3**: Efficiency of the two singlet fission photon multipliers (PM), the tandem solar cell, and the silicon solar cell as a function of **(a)** irradiance and **(b)** average photon energy (APE) using solar spectra and temperatures measured in the Netherlands and in Colorado with the record silicon base cell with an efficiency of 26.7% [87, 88]. The solid lines represent the moving average of the data. The APE is calculated for photons with an energy above the band gap of silicon. The gray line indicates the average photon energy of the AM1.5G standard solar spectrum.

solar cell and the two photon multipliers, as the increased shunt resistance at high current density is relatively less important.

Figure 5.3b shows that the efficiency of the silicon solar cell is only weakly affected by spectral changes, while the photon multiplier improves in efficiency with increasing average photon energy (APE). This is due to the modulation of the solar spectrum by the photon multiplier, which makes better use of the blue part of the incident solar spectrum. The tandem cell on the other hand is strongly affected by a shift of the APE away from standard test conditions because of the current-matching constraint of the monolithic two-terminal configuration. In a monolithic two-terminal configuration, the generated current is limited by the cell producing the lower current. A change in the spectral irradiance distribution therefore leads to a discrepancy between the current generated in the two subcells, which reduces the efficiency of the tandem solar cell. We note that we used values only with an irradiance greater than 50 $W/m^2$ in Figure 5.3b to highlight the effect of APE on the efficiency, which would otherwise be skewed by the reduction in efficiency of the various cells at low intensity.

In addition to the record silicon solar cell, we simulate the performance of the two photon multipliers and the tandem solar cell using a variety of silicon base cells with (certified) efficiencies varying from 17.8 to 26.7% under standard test conditions. We also include two silicon solar cells with no nonradiative recombination, with unity EQE, and with Auger recombination (29.9%) and without (30.6%). The

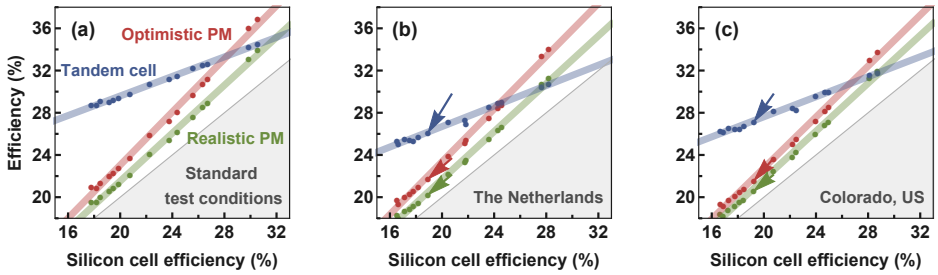


**Figure 5.4**: Efficiency of the two singlet fission photon multipliers (PM) and the tandem solar cell as a function of the silicon base cell efficiency under **(a)** standard test conditions and under real-world conditions averaged over the entire year and weighted with the incoming intensity, calculated using solar spectra and temperatures measured in **(b)** the Netherlands and **(c)** Colorado [87, 88]. The arrows indicate the change in efficiency from standard test conditions to real-world conditions.

band gap of the perovskite solar cell, E($S_1$), and E(QD) were optimised for each silicon solar cell (see Section 5.6.1 for details). Figure 5.4a shows the efficiencies of the tandem cell and the silicon cells with a photon multiplier, as a function of the silicon base cell efficiency under standard test conditions. The photon multiplier increases the current of the silicon solar cells by an almost constant percentage without changing the electrical properties. As a result, the absolute efficiency increase by the photon multiplier is almost constant for all silicon cells and even increases slightly for more efficient silicon cells (the slope is 1.1 in Figure 5.4a for the realistic case and 1.3 for the optimistic case). That increase is due to the (on average) higher EQE of the efficient silicon cells close to the band-edge which allows for more efficient use of the photons emitted from the photon multiplier. In addition, the quantum dot emission is slightly shifted toward the red for cells with a high EQE near the band edge, allowing for higher current gain.

In contrast, the tandem cell improves less upon the silicon cell efficiency for higher silicon efficiencies with a slope of 0.5 in Figure 5.4a. This arises because the perovskite front cell shades part of the spectrum reaching the cell underneath, which leads to a larger loss for an efficient silicon base cell. The difference in efficiency between the tandem cell and the photon multiplier thus becomes lower the more efficient the silicon base cell becomes, and the photon multiplier becomes as efficient as the tandem cell at a silicon base cell efficiency of 28.2% for the optimistic and 32.0% for the realistic case under standard test conditions.

Under realistic conditions, the slopes of the efficiency of the tandem cell and the

photon multipliers against the silicon base cells remain roughly constant (see Section 5.6.1 for linear fit parameters of Figure 5.4). However, the tandem cells show higher losses than the silicon cell alone compared to standard test conditions (offset of the fit in Figure 5.4), while the photon multiplier follows the efficiency drop of the silicon solar cell (see Figure 5.4b,c). This was already evident from Figure 5.3, because the dependence on irradiance and APE match the dependence of the silicon cell. The efficiency of the photon multiplier is therefore rather insensitive to the location of deployment, as is the efficiency of the silicon cell. In contrast, the efficiency of the tandem solar cell is strongly dependent on the location of deployment because of its sensitivity to changes in the solar spectrum. As a result, the efficiency of the tandem cell in the Netherlands is lower than that in Colorado. We note that the voltage-matched module tandem and the electrically independent four-terminal tandem are somewhat less sensitive to changes in the solar spectrum than the current-matched series tandem. However, the slope of the tandem efficiency against the efficiency of the silicon base cell is 0.5 for all three different tandem configurations (see Section 5.6.4 for details). The average intensity-weighted efficiency reduction due to real-world conditions is 2% for the two photon multipliers and the silicon solar cell in the Netherlands and in Colorado, while the efficiency of the series tandem cell is reduced by 3% in Colorado and by 4% in the Netherlands. The photon multiplier will then already be as efficient as the tandem solar cell at a silicon base-cell efficiency of 24.4% (26.6%) for the optimistic and 27.7% (28.9%) for the realistic case in the Netherlands (Colorado).

## 5.5 Conclusion

In conclusion, we simulate the performance potential of a singlet fission photon multiplier in comparison to a two-terminal tandem solar cell under real-world operation conditions. Compared to tandem solar cells, the photon multiplier has the advantage that it can be easily integrated into existing solar cell technologies, without the need for electrical contacts with the underlying solar cell. Unlike monolithic two-terminal tandem cells, the photon multiplier does not require current matching, making it more stable against changes in the solar spectrum.

To improve the efficiency of silicon solar cells by modulating the incident solar spectrum, however, some requirements must be met. The singlet fission material must have a high triplet exciton yield and a strong absorption. Furthermore, efficient energy transfer of the triplet excitons into the quantum dots is necessary, which must emit between 1.2 and 1.3 eV with a high PLQE. A large proportion of the emitted photons must then be directed toward the underlying silicon solar cell. If this is achieved, we find that a photon multiplier can increase the efficiency of

the record silicon solar cell by up to 4.2% absolute even at real-world environmental conditions, with little dependence on the location of deployment. The purely optical method of modulating the incident solar spectrum with a singlet fission photon multiplier thus offers a promising way to reduce thermalization losses.

## 5.6 Supporting information

### 5.6.1 Photon multiplier model

To model the modulation of the incident solar spectrum we assume that the singlet fission material absorbs everything above the energy of the singlet exciton E($S_1$) as

$$\Gamma = \int_{E(S_1)}^{\infty} \Phi\left(E\right) dE \tag{5.1}$$

where $\Phi$ is the photon flux of the incident solar spectrum as defined in Equation 1.2. Each absorbed photon generates one singlet exciton with an energy E($S_1$) which converts into two triplet excitons with an energy E($T_1$). The energy of the triplet excitons is then transferred into quantum dots which emit photons with an energy of E(QD) and a full width at half-maximum of $\sigma_{\mathrm{QD}}$ as

$$\Phi_{\mathrm{gain}}\left(E\right) = \frac{2\Gamma\gamma}{\sqrt{2\pi}\sigma_{\mathrm{QD}}} \exp\left(-\frac{\left(E - E\left(QD\right)\right)^2}{2\sigma_{QD}^2}\right) \tag{5.2}$$

where $\gamma$ is the capture parameter including the efficiency of triplet exciton yield from singlet fission ($\eta_{\mathrm{SF}}$), the efficiency of triplet excitons diffusion and transferring to quantum dots ($\eta_{\mathrm{T}}$), the photoluminescence quantum efficiency of the quantum dots ($\eta_{\mathrm{QD}}$), and the efficiency of photons emitted by the quantum dots reaching the silicon solar cell ($\eta_{\mathrm{C}}$), i.e. $\gamma = \eta_{\mathrm{SF}}/2\ \eta_T\ \eta_{\mathrm{QD}}\ \eta_{\mathrm{C}}$. In the ideal case, the capture parameter is unity. The generated photocurrent density in the bottom cell can then be calculated as

$$J_G = q\int_0^{E(S_1)} \left[\zeta\ \Phi\left(E\right) + \Phi_{\mathrm{gain}}\left(E\right)\right] EQE\left(E\right) dE \tag{5.3}$$

where $q$ is the elementary charge and $\zeta$ is the fraction of light transmitted through the photon multiplier and EQE is the external quantum efficiency of the bottom cell to take additional optical losses such as parasitic absorption in the bottom cell contacts into account. The current-voltage characteristic of a silicon solar cell below the

singlet fission photon multiplier is calculated with Equation 1.19, and the electroluminescent emission efficiency is calculated with Equation 1.21. The current-voltage characteristics of a singlet fission photon multiplier can then be modelled by including the EQE and the silicon thickness $L$, and adjusting $J_{NR}$, $R_S$, and $R_{SH}$.

To simulate the performance of a photon multiplier and a tandem solar cell as a function of the silicon solar cell efficiency, we fit our model to a variety of certified silicon solar cells. The parameters of the modelled silicon solar cells are shown in Table 5.2. Cell 1 to cell 13 are modelled after previous record silicon solar cells including monocrystalline and polycrystalline silicon solar cell, with cell 13 being the current record silicon solar cell. Cell 14 and 15 are hypothetical, idealised cells. Cell 14 and cell 15 both assume an ideal EQE of 100% above the silicon band gap, and cell 15 additionally assumes no Auger recombination. To optimise for maximum efficiency of the photon multiplier and the tandem solar cell, we optimise the band gap of the perovskite solar cell, the absorption edge of the singlet fission material E($S_1$), and E(QD) for each modelled silicon solar cell. The parameters for the optimistic and the realistic photon multiplier for each silicon solar cell are shown in Table 5.3 and Table 5.4, respectively. The parameters for the optimised perovskite solar cells for each silicon solar cell are shown in Table 5.5. The effect of FWHM on the efficiency is shown in Table 5.6 and Table 5.7. Table 5.8, Table 5.9, and Table 5.10 furthermore show the fitting parameters to Figure 5.4 in the main text.

### 5.6.2 Optical model

Placing a photon multiplier on a silicon solar cell influences the light that reaches the silicon solar cell. However, a photon multiplier has only a few interfaces more compared to a silicon solar cell with an antireflection coating. By optimising the cell design, most of the light can reach the silicon solar cell below the photon multiplier. Figure 5.5 shows transfer matrix simulations of a silicon solar cell with different anti-reflection coatings and a photon multiplier on a silicon solar cell [184]. Bare silicon has a high surface reflection of more than 30%. The reflection can be reduced by an anti-reflection coating, as shown for 70 nm SiN and 105 nm $SiO_2$ on 70 nm SiN. Similarly, the reflection is reduced by placing a photon multiplier consistent of a singlet fission material (in our case pentacene, 1000 nm) and quantum dots (PbS, 3 nm) on a silicon solar cell. By placing 110 nm of SiN between the silicon cell and the photon multiplier, the reflection is reduced to less than 7% above the singlet fission band gap. This value is likely to be improved by optimising the cell design. These simulations are furthermore based on flat surfaces. Texturing the surfaces would further reduce the reflection significantly.

To calculate the amount of light absorbed by the quantum dots, we estimate that the absorption of quantum dots distributed in a micron-thick singlet fission

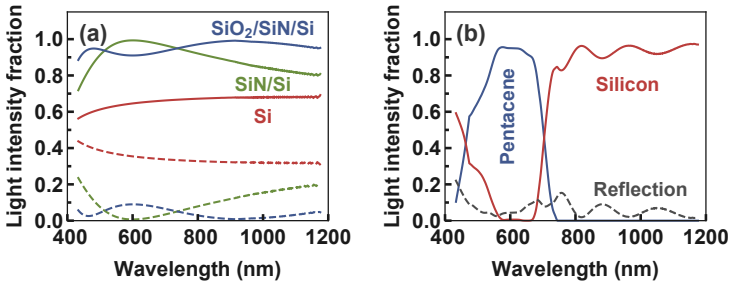


**Figure 5.5**: Transfer matrix simulations of **(a)** a silicon solar cell using different anti-reflection coatings and **(b)** a silicon solar cell with a photon multiplier on top. The continuous and the dashed lines in (a) correspond to the absorption and the reflection, respectively. The photon multiplier is assumed to consist of 1000 nm pentacene, 3 nm of PbS quantum dots, and 110 nm SiN. The n and k values for this simulation are taken from literature [185–188].

layer, spaced by 50 nm, is equal to the absorption of 3 nm thick PbS quantum dot layer. The absorption above the band gap of silicon can then be calculated using the Lambert–Beer law as

$$A = 1 - \int_{E_{G,Si}}^{\infty} \exp\left(-\frac{4\pi k\,(\lambda)}{3\text{ nm}}\right) d\lambda \tag{5.4}$$

resulting in an absorption of 0.44%.

Assuming that the quantum dots are isotropic emitters embedded in the singlet fission layer, part of the emission is lost due to out-coupling from the singlet fission layer to air, referred to as light within the escape cone. The fraction of light within the escape cone can be approximated as

$$\frac{\Omega}{4\pi} = \frac{1}{2}\,(1 - \cos\theta) \tag{5.5}$$

where $\omega$ is the solid angle of a cone and $\theta$ s the critical angle for total internal reflection. If the singlet fission material has a refractive index of 1.7 or higher, less than 10% of the light emitted by the quantum dots is within the escape cone.

### 5.6.3 Tandem solar cell model

To model a perovskite solar cell with an ideal band gap for a tandem solar cell in combination with silicon, we first fit the current-voltage characteristic of a perovskite solar cell with a band gap of 1.49 eV, an area of 0.09 $cm^2$, and an efficiency of

22.7% [108]. The current-voltage characteristic of the perovskite solar cell is calculated as described in Section 3.5.3. The electroluminescent emission efficiency ($\eta_{\mathrm{EL}}$) is calculated by approximating Equation 1.21 as

$$\eta_{\mathrm{EL}} = \frac{J_R}{J_R + J_{NR}\left(1 + \left(\frac{q(V+JR_S)}{2k_BT}\right)\right)^{-1}}. \tag{5.6}$$

The current-voltage characteristics of a perovskite solar cell can then be modelled by including the EQE and adjusting $J_{NR}$, $R_S$, and $R_{SH}$. The current-voltage characteristics of the modelled perovskite solar cell together with the fitting parameters and its EQE is shown in Figure 5.6.

To optimise for maximum perovskite/silicon tandem solar cell efficiency, we change the band gap of the perovskite solar cell artificially by scaling the EQE of the record perovskite solar cell in energy until current matching between the perovskite top cell and the silicon bottom cell is achieved while keeping the parasitic resistances and the electroluminescent emission efficiency constant. The modelled perovskite solar cell then has a band gap of 1.68 eV and an efficiency of 20.9%. The current-voltage characteristics of the modelled perovskite solar cell with an ideal band gap together with the fitting parameters and its EQE is shown in Figure 5.6.

The current-voltage characteristics of the perovskite/silicon tandem solar cell are then modelled as in Section 3.5.4. Optical losses are included by fitting a Gaussian distribution to the onset of the EQE spectra of the perovskite cell. 10% of the light with an energy below the Gaussian distribution is assumed to be uniformly absorbed by parasitic absorption in the perovskite contacts. The current-voltage characteristics of the modelled perovskite/silicon tandem solar cells together the EQE of the optimistic perovskite and the record silicon subcell is shown in Figure 5.7.

### 5.6.4 Different tandem solar cell configurations

To compare the efficiency potential of the current-matched series tandem, the voltage-matched module tandem, and the electrically-independent four-terminal tandem we calculate the efficiencies of the three tandem configurations for different silicon bottom cells as described in Section 3.5.4. To optimise for maximum perovskite/silicon tandem solar cell efficiency, we change the band gap of the perovskite solar cell artificially by scaling the EQE of the record perovskite solar cell in energy while keeping the parasitic resistances and the electroluminescent emission efficiency constant. For the module tandem, we furthermore change ratio between the number of perovskite top cells and silicon bottom cells to archive voltage-matching. Figure

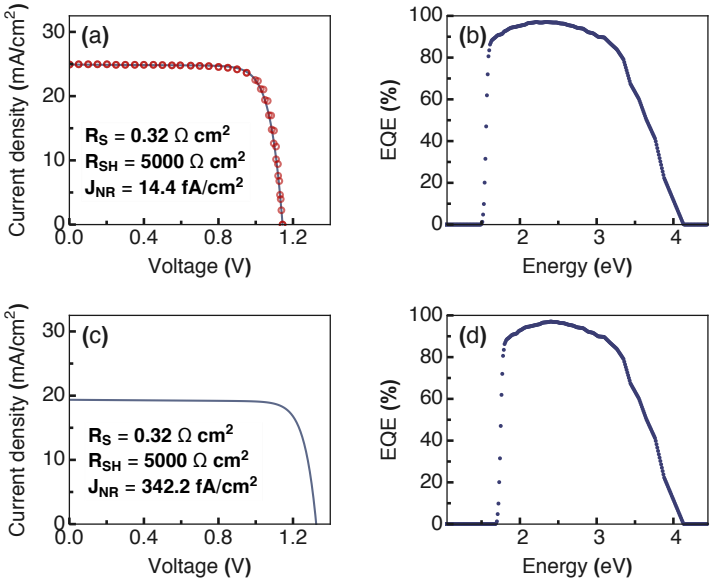


**Figure 5.6**: **(a)** Current-voltage characteristics and **(b)** external quantum efficiency of the high-efficiency perovskite solar cells with a band gap of 1.49 eV, an area of 0.09 $cm^2$, a $V_{OC}$ of 1.144 V, a $J_{SC}$ of 24.91 $mA/cm^2$, a fill factor of 79.6%, an $\eta_{EL}$ of 0.15% at maximum power point (MPP), and an efficiency of 22.7% [108]. The circles correspond to the measured data of the perovskite solar cell and the solid line corresponds to the modelled current-voltage characteristics. **(c)** Current-voltage characteristics and **(d)** external quantum efficiency of the modelled perovskite solar cells with a band gap of 1.68 eV, a $V_{OC}$ of 1.325 V, a $J_{SC}$ of 19.36 $mA/cm^2$, a fill factor of 81.5%, an $\eta_{EL}$ of 0.15% at MPP, and an efficiency of 20.9% used to model the perovskite/silicon tandem solar cell.

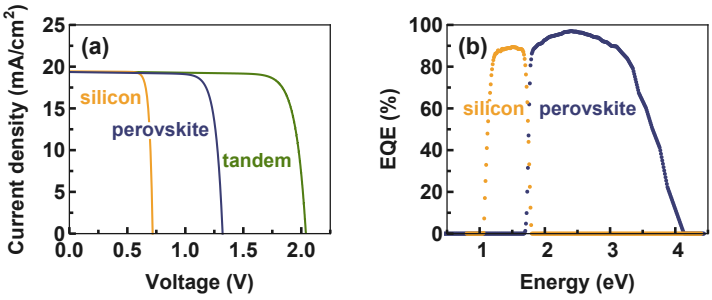


**Figure 5.7**: **(a)** Current-voltage characteristics and **(b)** external quantum efficiency of the modelled monolithic two-terminal perovskite/silicon tandem solar cell with an efficiency of 32.7% together with its subcells.

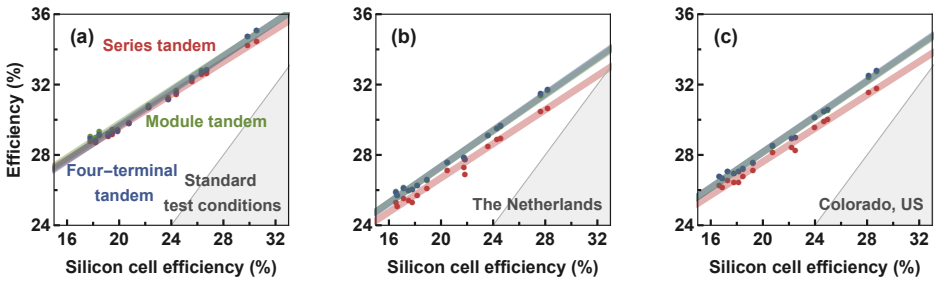


**Figure 5.8**: Efficiency of the tandem solar cells as a function of the silicon base cell efficiency under **(a)** standard test conditions and under real-world conditions averaged over the entire year and weighted with the incoming intensity, calculated using solar spectra and temperatures measured in **(b)** the Netherlands and **(c)** Colorado [87, 88].

5.8 shows the efficiencies of the different tandem cells as a function of the silicon-base-cell efficiency under standard test conditions and under real-world conditions. Both the module tandem and the four-terminal tandem are somewhat less sensitive to changes in the solar spectrum than the series tandem. The average intensity-weighted efficiency of the module tandem and the four-terminal tandem is reduced by 2% in Colorado and by 3% in the Netherlands due to real-world conditions, while the efficiency of the series tandem cell is reduced by 3% in Colorado and by 4% in the Netherlands. Table 5.11, Table 5.12, and Table 5.13 show the fitting parameters to Figure 5.8.

**Table 5.2**: Summary of modelled **silicon** solar cells calculated at standard test conditions (AM1.5G, 25 °C, 1 kWh/m$^2$). Thicknesses of active material L marked with an asterisk are estimates.

| Cell | Source | $V_{OC}$ (V) | $J_{SC}$ (mA/cm$^2$) | FF (%) | $\eta$ (%) | $R_S$ ($\Omega$ cm$^2$) | $R_{SH}$ ($\Omega$ cm$^2$) | $J_{NR}$ (fA/cm$^2$) | $\eta_{EL}$ (‰) | L ($\mu$ m) |
|---|---|---|---|---|---|---|---|---|---|---|
| 1 | [189] | 0.648 | 36.29 | 75.7 | 17.8 | 1.48 | 1800 | 400 | 0.13 | 170 |
| 2 | [190] | 0.638 | 37.19 | 76.7 | 18.2 | 1.15 | 1300 | 591 | 0.09 | 180* |
| 3 | [191] | 0.650 | 37.38 | 76.2 | 18.5 | 1.35 | 1800 | 386 | 0.13 | 180 |
| 4 | [192] | 0.649 | 37.50 | 78.9 | 19.2 | 0.82 | 1800 | 400 | 0.13 | 190 |
| 5 | [192] | 0.692 | 36.41 | 77.4 | 19.5 | 1.28 | 1200 | 72 | 0.71 | 180* |
| 6 | [193] | 0.657 | 38.10 | 79.5 | 19.9 | 0.73 | 2000 | 297 | 0.17 | 180* |
| 7 | [194] | 0.663 | 39.03 | 80.3 | 20.8 | 0.59 | 2000 | 241 | 0.21 | 190 |
| 8 | [195] | 0.674 | 41.07 | 80.5 | 22.3 | 0.60 | 3000 | 166 | 0.31 | 195 |
| 9 | [196] | 0.742 | 39.31 | 81.6 | 23.8 | 0.67 | 2000 | 10 | 4.98 | 150 |
| 10 | [193] | 0.736 | 41.39 | 80.1 | 24.4 | 0.75 | 800 | 13 | 3.84 | 200 |
| 11 | [197] | 0.740 | 41.81 | 82.7 | 25.6 | 0.47 | 4000 | 12 | 4.4 | 150 |
| 12 | [193] | 0.744 | 42.26 | 83.8 | 26.4 | 0.31 | 6000 | 10 | 5.3 | 200 |
| 13 | [96] | 0.738 | 42.65 | 84.9 | 26.7 | 0.08 | 10000 | 13 | 4.0 | 200 |
| 14 | - | 0.776 | 43.61 | 88.3 | 29.9 | 0.01 | 10000 | 1 | 69.9 | 200 |
| 15 | - | 0.814 | 43.61 | 86.1 | 30.6 | 0.01 | 10000 | 1 | 69.9 | 200 |

**Table 5.3**: Summary of parameters for the **optimistic** singlet fission photon multiplier and the resulting solar cell for each silicon bottom cell calculated at standard test conditions. The optimistic case assumes 200 meV entropy gain, 3% parasitic absorption losses below the singlet fission band gap, capture losses of 5%, and a FWHM for the quantum dot emission of 30 meV.

| Silicon cell | $E(S_1)$ (eV) | E(QD) (eV) | $V_{OC}$ (V) | $J_{SC}$ ($mA/cm^2$) | FF (%) | $\eta$ (%) |
|---|---|---|---|---|---|---|
| 1 | 2.20 | 1.20 | 0.652 | 43.15 | 74.5 | 21.0 |
| 2 | 2.26 | 1.23 | 0.642 | 43.91 | 75.3 | 20.9 |
| 3 | 2.28 | 1.24 | 0.654 | 43.51 | 75.3 | 21.4 |
| 4 | 2.32 | 1.26 | 0.652 | 43.14 | 78.4 | 22.1 |
| 5 | 2.30 | 1.25 | 0.695 | 41.90 | 76.8 | 22.4 |
| 6 | 2.32 | 1.26 | 0.660 | 43.60 | 79.1 | 22.8 |
| 7 | 2.32 | 1.26 | 0.666 | 44.50 | 80.0 | 23.7 |
| 8 | 2.26 | 1.23 | 0.678 | 47.76 | 80.1 | 25.9 |
| 9 | 2.30 | 1.25 | 0.754 | 45.05 | 81.3 | 27.3 |
| 10 | 2.26 | 1.23 | 0.740 | 47.68 | 79.8 | 28.1 |
| 11 | 2.28 | 1.24 | 0.744 | 48.48 | 82.5 | 29.7 |
| 12 | 2.26 | 1.23 | 0.748 | 49.22 | 83.7 | 30.8 |
| 13 | 2.24 | 1.22 | 0.742 | 49.63 | 85.0 | 31.3 |
| 14 | 2.18 | 1.19 | 0.780 | 52.29 | 88.4 | 36.0 |
| 15 | 2.18 | 1.19 | 0.819 | 52.29 | 86.2 | 36.9 |

**Table 5.4:** Summary of parameters for the **realistic** singlet fission photon multiplier and the resulting solar cell for each silicon bottom cell calculated at standard test conditions. The realistic case assumes 100 meV entropy gain, 5% parasitic absorption losses below the singlet fission band gap, capture losses of 15%, and a FWHM for the quantum dot emission of 30 meV.

| Silicon cell | $E(S_1)$ (eV) | E(QD) (eV) | $V_{OC}$ (V) | $J_{SC}$ ($mA/cm^2$) | FF (%) | $\eta$ (%) |
|---|---|---|---|---|---|---|
| 1 | 2.30 | 1.20 | 0.651 | 40.04 | 75.1 | 19.5 |
| 2 | 2.36 | 1.23 | 0.640 | 40.06 | 76.4 | 19.6 |
| 3 | 2.38 | 1.24 | 0.652 | 40.61 | 75.7 | 20.0 |
| 4 | 2.42 | 1.26 | 0.651 | 40.29 | 78.6 | 20.6 |
| 5 | 2.40 | 1.25 | 0.694 | 39.14 | 77.1 | 20.9 |
| 6 | 2.42 | 1.26 | 0.659 | 40.72 | 79.3 | 21.3 |
| 7 | 2.42 | 1.26 | 0.664 | 41.60 | 80.2 | 22.1 |
| 8 | 2.36 | 1.23 | 0.676 | 44.43 | 80.3 | 24.1 |
| 9 | 2.42 | 1.26 | 0.743 | 42.07 | 81.5 | 25.5 |
| 10 | 2.36 | 1.23 | 0.738 | 44.42 | 80.0 | 26.2 |
| 11 | 2.38 | 1.24 | 0.742 | 45.11 | 82.6 | 27.6 |
| 12 | 2.36 | 1.23 | 0.746 | 45.73 | 83.8 | 28.6 |
| 13 | 2.34 | 1.22 | 0.740 | 46.10 | 84.9 | 29.0 |
| 14 | 2.28 | 1.19 | 0.778 | 48.24 | 88.3 | 33.1 |
| 15 | 2.28 | 1.19 | 0.817 | 48.24 | 86.2 | 33.9 |

**Table 5.5**: Summary of the parameters for the modelled **perovskite** solar cell for each silicon bottom cell calculated at standard test conditions, together with the tandem solar cell efficiency. All modelled perovskite solar cells have a shunt resistance of 5000 $\Omega$ cm$^2$, a series resistance of 0.32 $\Omega$ cm$^2$, and an $\eta_{EL}$ of 0.15% at MPP.

| Cell | $E_G$ (eV) | $J_{NR}$ (fA/cm$^2$) | $V_{OC}$ (V) | $J_{SC}$ (mA/cm$^2$) | FF (%) | $\eta$ (%) | $\eta_{Tandem}$ (%) |
|---|---|---|---|---|---|---|---|
| 1 | 1.74 | 104 | 1.382 | 17.76 | 81.9 | 20.1 | 28.8 |
| 2 | 1.74 | 104 | 1.382 | 17.76 | 81.9 | 20.1 | 28.8 |
| 3 | 1.73 | 125 | 1.373 | 18.02 | 81.9 | 20.3 | 29.1 |
| 4 | 1.74 | 104 | 1.382 | 17.76 | 81.9 | 20.1 | 29.1 |
| 5 | 1.75 | 87 | 1.390 | 17.50 | 82.0 | 19.9 | 29.2 |
| 6 | 1.73 | 125 | 1.373 | 18.02 | 81.9 | 20.3 | 29.4 |
| 7 | 1.72 | 153 | 1.363 | 18.28 | 81.8 | 20.4 | 29.8 |
| 8 | 1.70 | 233 | 1.343 | 18.81 | 81.6 | 20.6 | 30.7 |
| 9 | 1.72 | 153 | 1.363 | 18.28 | 81.8 | 20.4 | 31.2 |
| 10 | 1.70 | 233 | 1.343 | 18.81 | 81.6 | 20.6 | 31.5 |
| 11 | 1.69 | 286 | 1.333 | 19.08 | 81.6 | 20.7 | 32.2 |
| 12 | 1.68 | 342 | 1.325 | 19.36 | 81.5 | 20.9 | 32.6 |
| 13 | 1.68 | 342 | 1.325 | 19.36 | 81.5 | 20.9 | 32.7 |
| 14 | 1.66 | 500 | 1.307 | 19.90 | 81.3 | 21.1 | 34.3 |
| 15 | 1.66 | 500 | 1.307 | 19.90 | 81.3 | 21.1 | 34.5 |

**Table 5.6**: Summary of parameters for the **optimistic** singlet fission photon multiplier and the resulting solar cell for different FWHM calculated at standard test conditions. The optimistic case assumes 200 meV entropy gain, 3% parasitic absorption losses below the singlet fission band gap, capture losses of 5%, and a FWHM for the quantum dot emission of 30 meV.

| FWHM (meV) | $E(S_1)$ (eV) | E(QD) (eV) | $V_{OC}$ (V) | $J_{SC}$ (mA/cm$^2$) | FF (%) | $\eta$ (%) |
|---|---|---|---|---|---|---|
| 10 | 2.22 | 1.21 | 0.742 | 49.94 | 85.0 | 31.5 |
| 22 | 2.24 | 1.22 | 0.742 | 49.81 | 85.0 | 31.4 |
| 30 | 2.24 | 1.22 | 0.742 | 49.63 | 85.0 | 31.3 |
| 40 | 2.26 | 1.23 | 0.742 | 49.40 | 85.0 | 31.1 |
| 50 | 2.26 | 1.23 | 0.741 | 49.16 | 85.0 | 30.9 |

**Table 5.7**: Summary of parameters for the **realistic** singlet fission photon multiplier and the resulting solar cell for different FWHM calculated at standard test conditions. The realistic case assumes 100 meV entropy gain, 5% parasitic absorption losses below the singlet fission band gap, capture losses of 15%, and a FWHM for the quantum dot emission of 30 meV.

| FWHM (meV) | $E(S_1)$ (eV) | E(QD) (eV) | $V_{OC}$ (V) | $J_{SC}$ ($mA/cm^2$) | FF (%) | $\eta$ (%) |
|---|---|---|---|---|---|---|
| 10 | 2.32 | 1.21 | 0.740 | 46.31 | 84.9 | 29.0 |
| 22 | 2.34 | 1.22 | 0.740 | 46.23 | 84.9 | 29.0 |
| 30 | 2.34 | 1.22 | 0.740 | 46.10 | 84.9 | 29.0 |
| 40 | 2.36 | 1.23 | 0.740 | 45.94 | 84.9 | 28.9 |
| 50 | 2.36 | 1.23 | 0.740 | 45.76 | 84.9 | 28.7 |

**Table 5.8**: Linear fitting parameters for the efficiency of the two singlet fission photon multipliers and the tandem solar cell as a function of the silicon solar cell efficiency under **standard test conditions**.

| | Offset | Slope |
|---|---|---|
| Realistic photon multiplier | -1.20 | 1.14 |
| Optimistic photon multiplier | -2.12 | 1.26 |
| Series tandem | 20.32 | 0.46 |

**Table 5.9**: Linear fitting parameters for the efficiency of the two singlet fission photon multipliers and the tandem solar cell as a function of the silicon solar cell efficiency under real-world conditions calculated using solar spectra and temperatures measured in **Utrecht, the Netherlands** [87].

| | Offset | Slope |
|---|---|---|
| Realistic photon multiplier | -0.96 | 1.13 |
| Optimistic photon multiplier | -1.62 | 1.25 |
| Series tandem | 17.00 | 0.48 |

**Table 5.10**: Linear fitting parameters for the efficiency of the two singlet fission photon multipliers and the tandem solar cell as a function of the silicon solar cell efficiency under real-world conditions calculated using solar spectra and temperatures measured in **Denver, Colorado (US)** [88].

| | Offset | Slope |
|---|---|---|
| Realistic photon multiplier | -1.02 | 1.14 |
| Optimistic photon multiplier | -1.38 | 1.21 |
| Series tandem | 18.13 | 0.47 |

**Table 5.11**: Linear fitting parameters for the efficiency of the three tandem solar cell configurations as a function of the silicon solar cell efficiency under **standard test conditions**.

| | Offset | Slope |
|---|---|---|
| Series tandem | 20.32 | 0.46 |
| Module tandem | 20.11 | 0.48 |
| Four-terminal tandem | 19.78 | 0.49 |

**Table 5.12**: Linear fitting parameters for the efficiency of the three tandem solar cell configurations as a function of the silicon solar cell efficiency under real-world conditions calculated using solar spectra and temperatures measured in **Utrecht, the Netherlands** [87].

| | Offset | Slope |
|---|---|---|
| Series tandem | 17.00 | 0.48 |
| Module tandem | 17.11 | 0.51 |
| Four-terminal tandem | 17.02 | 0.52 |

**Table 5.13**: Linear fitting parameters for the efficiency of the three tandem solar cell configurations as a function of the silicon solar cell efficiency under real-world conditions calculated using solar spectra and temperatures measured in **Denver, Colorado (US)** [88].

| | Offset | Slope |
|---|---|---|
| Series tandem | 18.13 | 0.47 |
| Module tandem | 18.16 | 0.50 |
| Four-terminal tandem | 18.09 | 0.51 |

# Part II

# Quantifying ion migration in metal halide perovskites

# 6

# Capacitance methods

**Abstract**

Perovskites have proven to be a promising candidate for highly-efficient solar cells, light-emitting diodes, and X-ray detectors, overcoming limitations of inorganic semiconductors. However, they are notoriously unstable. The main reason for this instability is the migration of mobile ions through the device during operation, as they are mixed ionic-electronic conductors. Here we show how measuring the capacitance in both the frequency and the time domain can be used to study ionic dynamics within perovskite devices, quantifying activation energy, diffusion coefficient, sign of charge, concentration, and the length of the ionic double layer in the vicinity of the interfaces. Measuring the transient of the capacitance furthermore allows for distinguishing between ionic and electronic effects.

## 6.1 Introduction

Measuring the temperature-dependent capacitance as a function of frequency or time is a well-established technique in experimental physics to quantify electronic defect states in semiconductors [198–201]. The most famous examples are deep-level transient spectroscopy (DLTS) [202] and thermal admittance spectroscopy (TAS) [203]. These techniques allow for quantifying activation energy, attempt-to-escape frequency, sign, and concentration of electronic defect states.

Due to the intriguing properties of perovskites such as high charge-carrier mobilities, long diffusion lengths, strong absorption, and low exciton binding energy, perovskites have been successfully used in many optoelectronic applications including light-emitting diodes, lasers, and X-ray detectors [204–207]. Both DLTS and TAS have been used to study perovskite-based devices [208–212]. To measure electronic defect states, these techniques rely on the depletion approximation, assuming that the depletion region is free of mobile carriers. In the case of perovskites, however, this assumption is not fulfilled because they are mixed ionic-electronic conductors, leaving slow charged carriers (mobile ions) within the depletion region [35]. Consequently, temperature-dependent capacitance measurements have led to numerous misleading results [213]. If used correctly, measuring the capacitance as a function of frequency or time can be used to quantify these mobile ions within the perovskite bulk [214–218].

## 6.2 Capacitance measurement

Most optoelectronic devices such as solar cells and light-emitting diodes can be approximated as a parallel-plate device with the active material sandwiched between the two contacts. The capacitance of such a parallel-plate device is given by

$$C = \frac{\varepsilon \varepsilon_0 A}{w_D} \tag{6.1}$$

where $\varepsilon_0$ is the vacuum permittivity, $A$ is the active area of the device, and $w_D$ is the depletion layer width, plus a possible additional dielectric contribution of the contact layers. In case of full depletion, $w_D$ corresponds to the thickness of the active layer, i.e the thickness of the perovskite layer. The dielectric permittivity of the material $\varepsilon = \varepsilon' + i\varepsilon''$ is a complex frequency-dependent tensor. To obtain the complex capacitance of the device we measure the impedance response by applying a time-varying electric field with amplitude $V_0$ at frequency $\omega$ and measuring the current response $I_0 \sin(\omega t + \Phi)$, as indicated in Figure 6.1. The impedance $Z$ is defined as

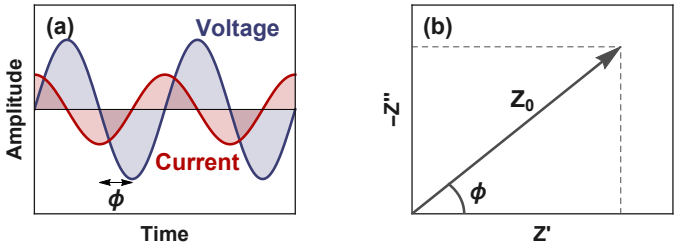


**Figure 6.1**: **(a)** Impedance measurements are based applying a sinusoidal voltage with a certain frequency and measuring the current response. **(b)** Impedance expressed as the modulus $Z_0$ and the phase angle $\Phi$.

$$Z(t) = \frac{V_0 \sin(\omega t)}{I_0 \sin(\omega t + \Phi)} = Z_0 e^{-i\Phi} = Z' - iZ'' \tag{6.2}$$

where $\Phi$ is the phase delay between the voltage input and the current response, and the modulus $Z_0 = V_0/I_0$ is the ratio between the amplitude of the voltage and the current signal. The complex capacitance is given by

$$C^*(\omega) = (i\omega Z)^{-1} = C'(\omega) - iC''(\omega) \tag{6.3}$$

where $C'$ and $C''$ are coupled by the Kramers-Kroning relations [219]. In semiconductor devices, the measurement of the capacitance thus measures the complex dielectric permittivity of the device.

## 6.3 Frequency versus time domain

In a dielectric material with a Debye relaxation, i.e. a physical process exhibiting an exponential relaxation with a single time constant $\tau$, the complex dielectric response function is

$$\varepsilon(\omega) = \varepsilon'(\omega) - i\varepsilon''(\omega) = \varepsilon_\infty + \frac{\varepsilon_s - \varepsilon_\infty}{1 + i\omega\tau} \tag{6.4}$$

where $\varepsilon_s$ and $\varepsilon_\infty$ are the static and asymptotic high frequency values of the dielectric constant, respectively [220]. The real part ($\varepsilon'$) is a measure of the ability to store

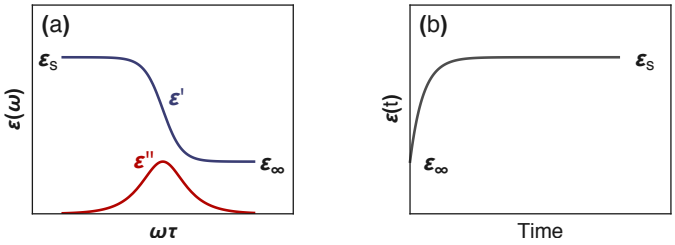


**Figure 6.2**: Debye dielectric material represented in **(a)** the frequency domain and **(b)** the time domain after a step function of applied electric field. Both the frequency and the time domain contain identical information.

energy in the dielectric material and the imaginary part ($\varepsilon''$) is a measure of the dielectric loss (see Figure 6.2a). In the imaginary part one can see a distinctive peak at a frequency of $\omega_0 = 1/\tau$, corresponding to the maximum dielectric loss in the material, i.e. the irreversible transfer of energy from the external stimulus to the dielectric material. At lower frequencies, the electrical displacement can follow the applied electric field, whereas at higher frequencies, the material has no time to respond.

Alternatively, one can instead measure the transient response of the system following an abrupt change in driving field. Using Laplace transformation to convert Equation 6.4 from the frequency domain into the time domain then yields

$$\varepsilon(t) = \varepsilon_\infty + (\varepsilon_s - \varepsilon_\infty)\left(1 - \exp\left(-\frac{t}{\tau}\right)\right) \tag{6.5}$$

which is illustrated in Figure 6.2b. Both the frequency and the time domain contain identical information.

The physical origin of a Debye process leading to the dielectric permittivity shown in Figure 6.2 can, for example, be the thermal emission of trapped charge carriers or the migration of mobile ions within the perovskite bulk. The magnitude of $\varepsilon_s - \varepsilon_\infty$ is then directly related to the number of trapped charge-carriers or mobile ions.

In the case of electronic defect states within the band gap, the kinetics of charge-carrier capture and emission can be described in the context of the Shockley-Read-Hall model [221, 222]. In this model, the time constant measured is due to thermal emission of trapped charge-carriers (see Section 6.7.2 for details). However,

the model assumes that the measured time constant results solely from the occupation/emission of electronic defect states. If a significant density of mobile ions is present within the studied material, this analysis may yield misleading results as the migration of mobile ions typically dominates the slow capacitance signal, and it hence cannot be assigned to be solely from electronic defect states [213].

In the following we show how this dominating signal can be used to study ion migration, both in the frequency domain with impedance spectroscopy, and in the time domain with transient ion drift. Finally, we suggest that the time domain can be used to also measure electronic defect states by suppressing the signal from mobile ions.

## 6.4 Impedance spectroscopy

Impedance spectroscopy measures the capacitance as a function of frequency to observe dielectric relaxation in a material as shown in Figure 6.2a. To illustrate the difference between impedance spectroscopy and transient ion drift, we measure a perovskite-based device illustrated in Figure 6.3a (details of the device are found in Section 6.7.1). We measure the modulus and the phase angle at short circuit in the dark (Figure 6.3b) to obtain the complex capacitance from Equation 6.3. Figure 6.3c shows the real part and Figure 6.3d the imaginary part of the complex capacitance. At low frequencies, the phase angle is close to -90°, showing that the device operates in a capacitor-like manner. At high frequencies, the contact resistance is dominating the measured impedance response resulting in a decrease in phase angle. The real part of the capacitance shows a plateau at medium frequencies (Figure 6.3c). Assuming that the perovskite layer is mostly depleted at short circuit, we obtain a dielectric constant of 7.3 $\pm$ 0.1 based on the mean of three measurements, which is in good agreement with the dielectric constant obtained for $CsPbBr_3$ [223]. We observe a small increase in the real part of the capacitance $C'$ at low frequencies which is accompanied with a peak in the imaginary part $C''$, similar to the dielectric relaxation shown in Figure 6.2. The peak in the imaginary part shifts to lower frequencies with decreasing temperatures, which corresponds to the presence of a thermally-activated process. In perovskite-based devices such a behaviour typically arises from the migration of mobile ions within the perovskite layer [224]. We hence assume in the following that the loss signal arises from ion migration. Later we validate this assumption with transient ion drift.

Due to the different work functions of the contacts, the perovskite layer is subject to an internal electric field. This leads to an accumulation of mobile ions at the contact interfaces [225]. Mobile ions that accumulated at the contact interfaces form a diffuse ionic double layer that strongly influences the current injection rates of

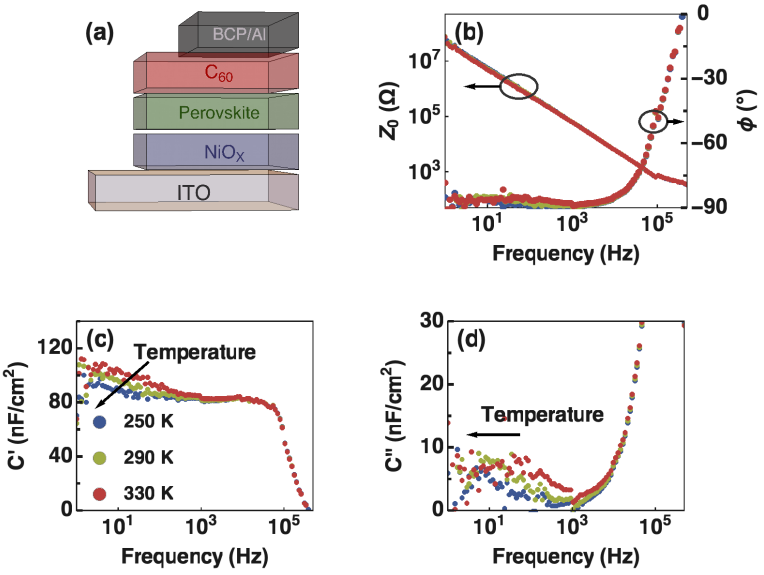


**Figure 6.3**: **(a)** Schematic representation of the device structure. **(b)** Modulus (Z) and phase angle ($\Phi$) of the perovskite-based device measured at short circuit in the dark together with the corresponding **(c)** real and **(d)** imaginary part of the complex capacitance. The peak in the imaginary part corresponds to the temperature-dependent diffusion of mobile ions within the ionic double layer. The temperature dependence reveals the activation energy and the pre-factor.

perovskites-based devices under operation [214]. The application of an oscillating voltage with a frequency $\omega$ then leads to the migration of mobile ions with a peak in the imaginary part of the complex capacitance with a maximum at the frequency

$$\omega_0 = 2\pi f_0 = \frac{1}{\tau} = \frac{D}{l^2} \tag{6.6}$$

where $f$ is the measured angular frequency and $l$ the diffusion length. Often, the ion diffusion length is assumed to correspond to the Debye length $l_D$ given by [226]

$$l_D = \sqrt{\frac{\varepsilon\varepsilon_0 k_B T}{q^2 N}} \tag{6.7}$$

where $k_B$ is Boltzmann's constant, $T$ the temperature, and $N$ is the doping density. The diffusion coefficient can be expressed as [227, 228]

$$D = \frac{\nu_a d^2}{6} \exp\left(-\frac{\Delta G}{k_B T}\right) = \frac{\nu_a d^2}{6} \exp\left(\frac{\Delta S}{k_B}\right) \exp\left(-\frac{\Delta H}{k_B T}\right) \tag{6.8}$$

where $\nu_a$ is the attempt frequency of an ionic jump and $d$ the jump distance. $\Delta G$, $\Delta S$, and $\Delta H$ are the change in Gibbs free energy, entropy, and enthalpy during the jump of a mobile ion. The activation enthalpy is often referred to as the activation energy $E_A$. The attempt frequency is the frequency of an attempt to break or loosen a bond, related to the molecular vibration frequency and often assumed to be in the order of $10^{12}$ $s^{-1}$ [229]. Assuming that the attempt frequency is temperature independent, Equation 6.8 can be simplified to

$$D = D_0 \exp\left(-\frac{E_A}{k_B T}\right) \tag{6.9}$$

where $D_0$ is a temperature-independent pre-factor. Thus, assuming that the diffusion of mobile ions is primarily within the Debye layer in the vicinity to the interfaces, Equation 6.6 can be written as

$$\tau = \frac{\varepsilon_0 \varepsilon k_B T}{q^2 N D_0} \exp\left(\frac{E_A}{k_B T}\right). \tag{6.10}$$

By plotting the measured frequency as function of temperature in an Arrhenius plot, the activation energy for ion migration can be obtained (see Figure 6.6a). We obtain an activation energy of 0.13 $\pm$ 0.01 eV, based on the mean of three measurements.

Note that also in the presence of electronic defect states, an increase in capacitance at low frequencies is expected [203], which cannot be distinguished from the effect of mobile ions. In addition, the diffusion coefficient can only be obtained if the diffusion length within the perovskite is known. Here, we assumed that the diffusion length is equal to the length of the Debye layer. However, it has also been suggested that the migration of mobile ions extends throughout the perovskite bulk [230, 231]. Furthermore, it was shown that the interfaces play an important role as charge accumulation at interfaces leads to an additional increase in capacitance at low frequencies [232–234]. Capacitance measurements in the time domain offer the complementary information needed to assign the observed feature to the migration of mobile ions. Only when measuring the transient of the capacitance can the diffusion coefficient be obtained without prior knowledge of the diffusion length. Transient capacitance measurements furthermore allow to distinguish between effects caused by electronic defect states and mobile ions.

## 6.5 TRANSIENT ION DRIFT

Transient ion-drift measurements are based on measuring the capacitance transient after applying a voltage bias [235]. The voltage is chosen such that it collapses the depletion layer within the perovskite. The depletion layer width $w_D$ is approximated as [127]

$$w_D = \sqrt{\frac{2\varepsilon_0\varepsilon}{qN}\left(V_{bi} - V\right)} \tag{6.11}$$

where $V_{bi}$ is the built-in potential. The depletion capacitance is directly related to the depletion width as

$$C_{dl} = \varepsilon_0\varepsilon\frac{A}{w_D} = A\sqrt{\frac{q\varepsilon_0\varepsilon N}{2\left(V_{bi} - V\right)}}. \tag{6.12}$$

Applying a bias thus decreases the depletion layer width, increasing the measured capacitance (see Figure 6.4a). The capacitance of the device is obtained by an equivalent circuit model (see Section 6.7.3 for details). At higher voltages, the diffusion capacitance $C_d$ starts to dominate the measured capacitance, due to the accumulation of minority carriers near the depletion region. The diffusion capacitance is given as

$$C_d = \frac{q^2 l N_e A}{k_B T}\exp\left(\frac{qV}{nk_B T}\right) \tag{6.13}$$

where $N_e$ is the total equilibrium charge density at a given voltage $V$ and $n$ is the diode ideality factor [217, 236]. In the case the depletion capacitance can clearly be distinguished from the diffusion capacitance, plotting $C^{-2}(V)$ allows to extract the doping density and the built-in potential of the device using Equation 6.12 (see Figure 6.4b) [237, 238]. This is commonly referred to as the Mott-Schottky analysis. We obtain a built-in potential of $0.95 \pm 0.05$ V and a doping density of $(7 \pm 1)\ 10^{17}$ cm$^{-3}$, based on the mean of three measurements.

To measure the transient of the capacitance we apply a bias of 1.25 V, which completely collapses the depletion layer. We note that we are already in the diffusion capacitance regime when applying a 1.25 V bias voltage. However, the initial capacitance change caused by the discharge due to the accumulation of minority carriers is much faster than the time resolution of our instrument. The measured capacitance rise and decay are shown in Figure 6.5, measured at 10 kHz where the

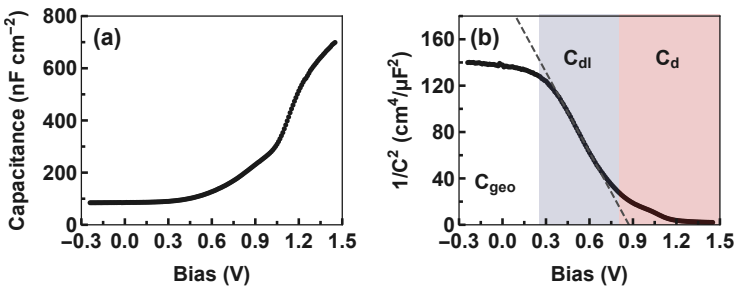


**Figure 6.4**: **(a)** Capacitance-voltage measurement and **(b)** Mott-Schottky plot of a perovskite-based device measured at 300 K in the dark at 10 kHz, illustrating different capacitance regimes. Only at a certain voltage regime can the depletion capacitance $C_{dl}$ clearly be identified. At high voltages, the diffusion capacitance $C_d$ starts to dominate the measured capacitance. The linear fit reveals the built-in bias and the doping density. The capacitance is calculated assuming a capacitor in series with a resistor (see Section 6.7.3).

phase angle is close to -90°, such that the measured capacitance is not affected by the series resistance of the device.

Applying a forward bias decreases the depletion width of the device. Mobile ions are now able to diffuse within the perovskite bulk which eventually leads to a uniform ion distribution within the previously depleted region. After removing the bias, the depletion width increases quickly by the movement of electric charge, depleting most of the perovskite bulk according to Equation 6.11. Mobile ions within the depleted regions will drift towards the interfaces following the internal electric field, changing the depletion width as

$$w_D\left(t\right) = \sqrt{\frac{2\varepsilon_0\varepsilon}{q\left(N \pm N_{Ion}\left(t\right)\right)}\left(V_{bi} - V\right)} \tag{6.14}$$

where $N_{Ion}(t)$ is the density of mobile ions within the depletion region. For ions with the same charge as minority carriers, the sign of the capacitance change is positive and for ions with the same charge as majority carriers, the sign is negative. The capacitance as a function of time can thus be written as

$$C\left(t\right) = C(\infty)\left(1 \pm \frac{N_{Ion}(t)}{N}\right)^{\frac{1}{2}} \approx C(\infty)\left(1 \pm \frac{N_{Ion}(t)}{2N}\right) \tag{6.15}$$

where $C(\infty)$ is the junction capacitance at steady state. The approximation is valid as long as the density of the mobile ions is much lower than the doping density.

To find $N_{Ion}(t)$ we assume that the thermal diffusion is negligible against drift and solve the drift equation following the work of Heiser *et al.* [216, 235]. The temporal evolution of the mobile ions drifting towards the interface can then be described with

$$\frac{\delta N_{Ion}\left(t\right)}{\delta t} = -\frac{\delta}{\delta x} N_{Ion}\left(t\right) \mu E \tag{6.16}$$

where $\mu$ is the mobility of mobile ions and $E$ is the electric field in the depletion region. Assuming that the electric field is static and varies linearly within the depletion region as

$$E\left(x\right) = E_0 \left(1 - \frac{x}{w_D}\right), \tag{6.17}$$

and that the drift of mobile ions is not affecting the electric field, we can solve Equation 6.16 for $N_{Ion}(t)$. Equation 6.8 can then be written as

$$C\left(t\right) = C\left(\infty\right) \pm \Delta C \exp\left(-\frac{t}{\tau}\right) \tag{6.18}$$

with the time constant $\tau$ given by

$$\tau = \frac{w_D}{\mu E}. \tag{6.19}$$

$\Delta C$ is the capacitance change due to the drift of mobile ions towards the interface, directly related to the mobile ion density as

$$\Delta C = C\left(\infty\right) - C\left(0\right) = C\left(\infty\right) \frac{N_{Ion}}{2N}. \tag{6.20}$$

By expressing the electric field as a function of the doping density as

$$E = \frac{q w_D N}{\varepsilon_0 \varepsilon}, \tag{6.21}$$

together with the Einstein relation, the time constant can be written as

$$\tau = \frac{k_B T \varepsilon_0 \varepsilon}{q^2 D N} \tag{6.22}$$

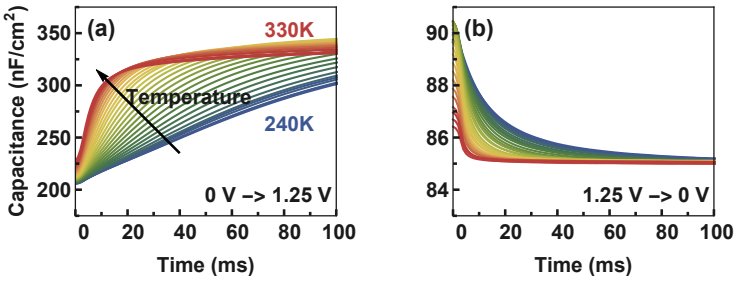


**Figure 6.5**: **(a)** Capacitance rise and **(b)** decay of the perovskite-based device measured at 10 kHz where the measured capacitance corresponds to the change in depletion capacitance of the device. The capacitance is calculated assuming a capacitor in parallel with a resistor.

This equation can now be used to extract the diffusion coefficient and activation energy from the measured capacitance transients. Note that this equation is the same as Equation 6.10, which describes the time constant for ion migration in the frequency domain.

Note that we have assumed a linear electric field within the depletion region and that the electric field is unaffected by the drift of mobile ions, which is only true if the density of mobile ions is small compared to the background doping density. In the case of a mobile ion density close to the background doping density, the transient would have a non-exponential behaviour making the analysis more complex [216]. We have furthermore assumed that the total ion concentration is conserved, i.e. mobile ions are not diffusing into the contact layers.

To distinguish mobile ions from traps we use the difference in rise and decay time of the capacitance. In the case of mobile ions, the rise time (Figure 6.5a) due to diffusion of mobile ions is expected to be longer than the decay time due to drift of mobile ions (Figure 6.5b). In contrast, the capture-rate for electronic defect states is much higher than the emission rate, resulting in a faster rise time compared to the decay time. Measuring the rise and the decay of the capacitance thus allows to distinguish between capacitance changes due to electronic defect states and mobile ions (see Section 6.7.4 for details).

Another unique feature of transient ion-drift measurements is that one can differentiate between mobile cations and mobile anions. Here, the negative capacitance change in Figure 6.5b measures an increase in depletion width due to ions migrating towards the contact interfaces. The Mott-Schottky plot shows a p-type behaviour of the perovskite (Figure 6.4), corresponding to the migration of an anion. We hence can attribute the measured changes in capacitance due to bromide migration, pre-

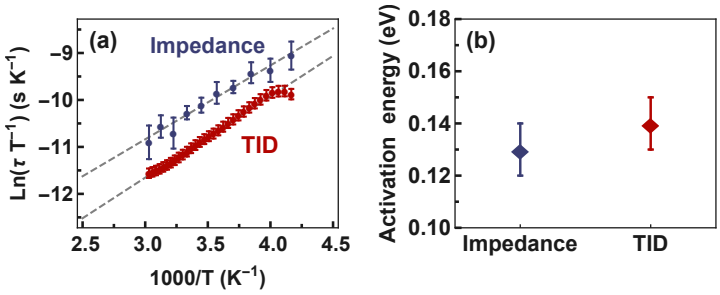


**Figure 6.6**: Arrhenius plot of the measured thermal emission rates by **(a)** impedance spectroscopy and **(b)** transient ion drift (TID). **(c)** Activation energies obtained from the two measurement techniques based on the mean of three measurements each.

sumably due to vacancy-mediated migration [37, 239].

The Arrhenius plots along with the obtained activation energies for both impedance spectroscopy and transient ion-drift measurements are shown in Figure 6.6. Similar to impedance spectroscopy measurements, we obtain an activation energy of $0.14 \pm 0.01$ eV, based on the mean of three measurements. The obtained activation energy is consistent with theoretical predictions and experimental observations for the migration of bromide in $MAPbBr_3$ and $CsPbBr_3$(0.09 to 0.25 eV) [240–242].

From the capacitance transients we obtain a concentration of $(5.1 \pm 2.5) \times 10^{16}$ $cm^{-3}$ and a diffusion coefficient of $(3.1 \pm 0.4) \times 10^{-11}$ $cm^2/s$ for the mobile anions. We can now use this coefficient together with the frequency of the dielectric loss peak (Figure 6.3d) to obtain a diffusion length for ion migration of $6.2 \pm 0.4$ nm from Equation 6.6. The calculated diffusion length is larger than the Debye length of $3.9 \pm 0.3$ nm calculated from Equation 6.7. Hence, the assumption that the diffusion of mobile ions during frequency-dependent capacitance measurements is limited to the Debye layer is not fulfilled. This underestimation of the diffusion length explains the difference between the time constants extracted from impedance spectroscopy and transient ion-drift measurements in Figure 6.6a.

## 6.6 Conclusion

Capacitance techniques must be applied with caution to mixed ionic-electronic conductors, because the measured capacitance features can be caused by mobile ions rather or electronic defect states. We have shown that transient ion-drift measurements have the virtue that a distinction between electronic defect states and mobile ions can be made. In addition, transient ion drift allows fast and non-destructive

quantification of activation energy, diffusion coefficient, sign of charge, and concentration of mobile ions in perovskite-based devices. Using the diffusion coefficient obtained by transient ion drift, the length of the ionic double layer can be determined from impedance spectroscopy measurements.

Since the migration of mobile ions is a key degradation mechanism in perovskite-based devices, reducing ion migration is crucial for the fabrication of stable devices. Capacitance techniques provide a tool to systematically investigate the effects of different passivation agents, fabrication methods, and perovskite compositions on ion migration in full perovskite-based devices guiding the way to long-lasting devices, critical for commercialisation.

## 6.7 Supporting information

### 6.7.1 Experimental

**Device fabrication.** ITO substrates were cleaned by sonicating sequentially in detergent (Micron - 90), water (twice) and Acetone (twice) for 10 minutes in each and they were soaked in boiling isopropanol for 20 minutes to remove the leftover organic contamination. The substrates were then treated with $O_2$ plasma for 5 minutes using 0.5 Torr $O_2$ gas at 500 W. On top of these cleaned substrates, 30 µL precursor solution of $NiO_X$ was spin coated at 2500 rpm with an acceleration of 2500 rpm/s. The films were immediately transferred to a hot plate, which was kept at 100 °C and annealed at 300 °C for 3 hours. After cooling the $NiO_X$ films, a thin layer of perovskite was made by spin coating perovskite precursor solution at 1000 rpm for 10 seconds and ramped up to 3000 rpm for 45 seconds. After 20 seconds, 90 µL of chloroform (anti-solvent) was dripped on the spinning perovskite layer. The precursor solutions were prepared by dissolving 0.3 M of each MABr (Sigma, $>$ 98%), $PbBr_2$ (Sigma, $>$ 99.99%), PEABr (Dyesol $>$ 98%), $PbI_2$ (Sigma, $>$ 99,99%), MAI (Sigma, $>$ 98%), and $CsPbI_3$ in DMF, and $CsPbBr_3$ in DMSO. The perovskite precursor solution was prepared by mixing appropriate ratios of the precursor solutions to get $PEABr_{0.2}Cs_{0.4}MA_{0.6}PbBr_3$ perovskite in DMF/DMSO. The precursor solution was filtered through a 0.2 µm PTFE membrane before use. The thickness of the perovskite is about 80 nm. The detailed preparation of precursor solutions is reported in previous work [243]. After coating the perovskite layer, the films were taken into an evaporation chamber where 50 nm $C_{60}$, 5 nm BCP, and 60 nm Ag were sequentially deposited at $10^{-6}$ mbar.

**Electrical measurements.** All measurements are performed in a Janis VPF-100 liquid nitrogen cryostat at a pressure below 2 x $10^{-6}$ mbar in the dark. Samples are loaded into the cryostat inside a nitrogen-filled glovebox to avoid air exposure. Capacitance-voltage characteristics are measured at 10 kHz with an AC frequency

of 50 mV from 1.45 to -0.25 V with a step size of 0.01 V. Impedance spectroscopy measurements are performed with an AC voltage of 50 mV at short circuit between 240 and 330 K in steps of 10 K. Transient ion-drift measurements are measured at 10 kHz with an AC voltage of 20 mV between 240 and 330 K in steps of 2 K. The temperature accuracy is 0.2 K.

### 6.7.2 SHOCKLEY-READ-HALL-MODEL

In the Shockley-Read-Hall model, the thermal emission rate of trapped electrons is given by

$$\frac{1}{\tau} = e_n = \sigma_n \nu_{th} N_C \exp\left(-\frac{E_T}{k_B T}\right) \tag{6.23}$$

where $\sigma_n$ is the capture cross section for capturing electrons, $\nu_{th}$ the thermal velocity, $N_C$ the density of states in the conduction band, $E_T$ the depth of the trap from the conduction band, $k_B$ Boltzmann's constant, and $T$ the temperature [221, 222]. Taking the temperature dependence of the pre-factors into account, this can be simplified to

$$e_n = A(T) \exp\left(-\frac{E_T}{k_B T}\right) \tag{6.24}$$

where $A = A_0 T^2$ is the attempt-to-escape frequency. An analogous expression holds for the thermal emission rate of trapped holes. By measuring the time constant as a function of temperature, the depth of the trap and the attempt-to-escape frequency can be obtained. When the time constant is measured from the transient of the capacitance, this technique is called deep-level transient spectroscopy (DLTS) originally developed by Lang *et al.* [203], and when the time constant is measured from the frequency-dependence of the capacitance, this technique is called thermal admittance spectroscopy (TAS) originally developed by Walter *et al.* [202].

### 6.7.3 EQUIVALENT CIRCUIT MODEL

The complex impedance of a parallel-plate device can be modelled with a resistor in parallel and a resistor in series to a capacitor, as shown in Figure 6.7.

If the capacitance is measured at one frequency, however, the complex impedance must be obtained with a model consisting only of two free parameters, i.e. one resistor and one capacitor. Time-dependent and voltage-dependent capacitance measurements can thus be modelled with a resistor either in parallel or in series to the

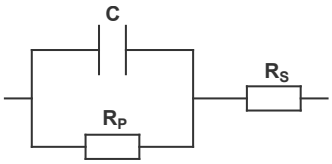


**Figure 6.7**: Circuit model of a resistor in parallel ($R_P$) and a resistor in series ($R_S$) with a capacitor (C).

**Table 6.1**: Comparison of capacitance calculated with a capacitor either in series or in parallel with a resistor.

| | Series | Parallel |
|---|---|---|
| Impedance | $R + \frac{1}{i\omega C}$ | $\left(R + \frac{1}{i\omega C}\right)^{-1}$ |
| Capacitance | $-\frac{1}{\omega \mathrm{Im}(Z)}$ | $\frac{1}{\omega}\mathrm{Im}\left(\frac{1}{Z}\right)$ |

capacitor as shown in Figure 6.8 and Table 6.1. At high impedance the series resistance can be neglected, at low impedance the shunt resistance can be neglected. As long as the device does not suffer from resistive losses, however, the capacitance is identical for both models.

To measure the transient of the capacitance, we neglect the series resistance assuming a resistor in parallel with a capacitor. We thus choose the measuring frequency such that the impedance is not limited by the series resistance of the device, i.e. the phase angle has to be close to -90°.

Due to carrier injection at large biases, the series resistance can often no longer be neglected. In this case, the capacitance can be calculated as a function of voltage assuming a capacitor in series with a resistor. Figure 6.8c shows the difference in capacitance as a function of voltage assuming a capacitor in series or in parallel with a resistor. At low biases, the difference between the two models is negligible. At high biases, there is a growing difference in capacitance obtained from the two models. In our case, however, the differences between the two models in the values obtained with the Mott-Schottky analysis are small, i.e. 0.89 and 0.87 V for the built-in bias and 8.0 x $10^{17}$ and 8.1 x $10^{17}$ $cm^{-3}$ for the doping density, for a capacitor in parallel and in series with a resistor, respectively.

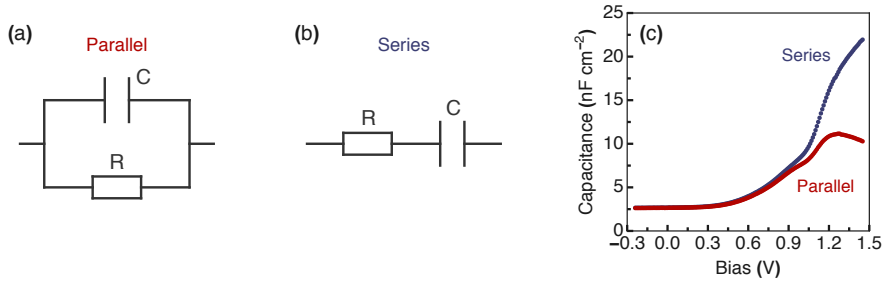


**Figure 6.8**: Circuit model of a capacitor (C) **(a)** in parallel and **(b)** in series with a resistor (R). **(c)** Capacitance as a function voltage of a perovskite-based device calculated assuming a capacitor in series or in parallel with a resistor as a function of voltage measured at 300 K in the dark at 10 kHz.

**Table 6.2**: Comparison of rise and decay times of electronic defect states and mobile ions at room temperature assuming a defect state with a trap energy between 0.2 and 0.6 eV. $D$ the diffusion coefficient of mobile ions, $q$ the elementary charge, and $V_{bi}$ the built-in potential.

| | Electronic defect states | Mobile ions |
|---|---|---|
| Rise time (s) | $\frac{1}{\sigma \nu_{th} N} \approx 10^{-13} - 10^{-10}$ | $\frac{w_D^2}{D} \approx 10^{-1} - 10^{1}$ |
| Decay time (s) | $\frac{1}{\sigma \nu_{th} N} \exp\left(\frac{E_T}{k_B T}\right) \approx 10^{-10} - 10^{0}$ | $\frac{w_D^2 k_B T}{D q V_{bi}} \approx 10^{-3} - 10^{0}$ |

### 6.7.4 Rise and decay time

The characteristic rise and decay times for both mobile ions and electronic defect states are shown in Table 6.2. For mobile ions, the rise time is assumed to be due to diffusion from the interfaces into the perovskite bulk. The decay time is assumed to be due to drift of mobile ions from the bulk towards the interfaces, i.e. $T = w_D/\mu E$, where $w_D$ is the depletion width and $\mu$ is the mobility of mobile ions. The electric field is approximated as $E = V_{bi}/w_D$. The rise and decay time follow from the Shockley-Read-Hall model. Consequently, electronic defect states and mobile ions show different ratios between rise and decay time, so that a distinction can be made between them.

Figure 6.9 shows measured capacitance transients after a filling voltage of 1.25 V for different periods of time. Applying a voltage pulse for 2 seconds allows mobile

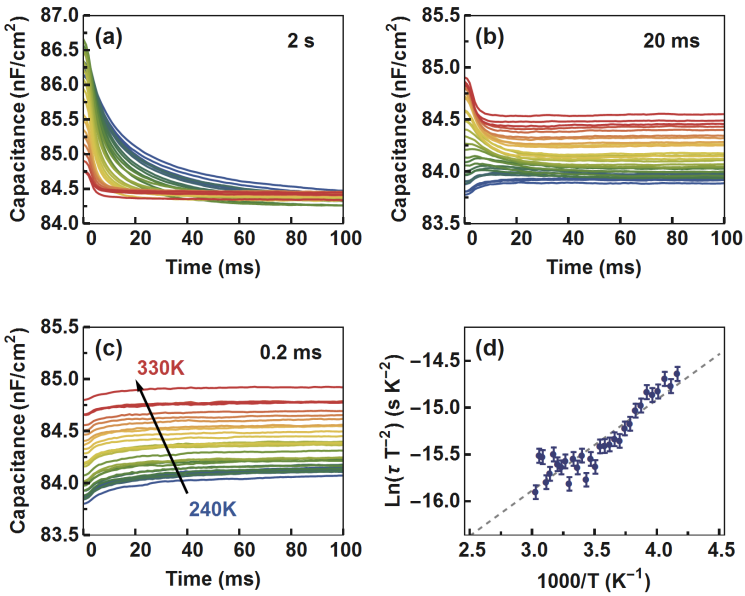


**Figure 6.9**: Capacitance transient measurements between 240 and 330 K in steps of 3 K measured at 0 V at 10 kHz. Capacitance transients are measured after applying a bias of 1.25 V for **(a)** 2 seconds **(b)** 20 milliseconds **(c)** 0.2 milliseconds. **(d)** Arrhenius plot of the thermal emission rates obtained from (c) The linear fit reveals the activation energy and the attempt-to-escape frequency of electronic defect states.

ions to be measured, since mobile ions have sufficient time to diffuse from the interfaces into the perovskite bulk (Figure 6.9a). On the other hand, applying a voltage bias of 0.2 milliseconds only fills electronic defect states present in the material, as ions do not have enough time to react (Figure 6.9c). When applying a bias of 20 milliseconds, both ions and electronic defects states are measured (Figure 6.9b). The Arrhenius plot of the measured thermal emission rates for electronic defect states is shown in Figure 6.9d. We obtain an activation energy of 84 $\pm$ 7 meV, a concentration of 3 x $10^{15}$ $cm^{-3}$ and an attempt-to-escape frequency of (1.3 $\pm$ 0.4) $10^{13}$ $s^{-1}$. The obtained concentration of electronic defect states is much lower than the concentration of mobile ions. We therefore assume that the presence of electronic defect states is not influencing our measurements of mobile ions.

*Published as:*

*M. H. Futscher, J. Lee, L. McGovern, L. A. Muscarella, T. Wang, M. I. Haider, Azhar Fakharuddin, L. Schmidt-Mende and B. Ehrler, Quantification of ion migration in $CH_3NH_3PbI_3$ perovskite solar cells by transient capacitance measurements. Materials Horizons* ***6****, 1497-1603 (2019).*

# 7

# $MAPbI_3$ perovskite solar cells

**Abstract**

Ion migration in metal halide perovskite films leads to device degradation and impedes large-scale commercial applications. We use transient ion-drift measurements to quantify activation energy, diffusion coefficient, and concentration of mobile ions in methylammonium lead triiodide ($MAPbI_3$) perovskite solar cells, and find that their properties change close to the tetragonal-to-orthorhombic phase transition temperature. We identify three migrating ion species which we attribute to the migration of iodide ($I^-$) and methylammonium ($MA^+$). We find that the concentration of mobile $MA^+$ ions is one order of magnitude higher than the one of mobile $I^-$ ions, and that the diffusion coefficient of mobile $MA^+$ ions is three orders of magnitude lower than the one for mobile $I^-$ ions. This quantification of mobile ions in $MAPbI_3$ will lead to a better understanding of ion migration and its role in operation and degradation of perovskite solar cells.

## 7.1 Introduction

Unlike conventional inorganic solar cell materials, metal halide perovskites are ionic solids that exhibit ion migration, complicating the efficiency measurements and the definition of a steady-state condition in these cells [244]. This ion migration has also been shown to be a pathway for the degradation of perovskite solar cells [245, 246]. The understanding of ion migration within perovskite solar cells is therefore crucial for the fabrication of stable perovskite devices.

In methylammonium lead triiodide ($MAPbI_3$), both anions ($I^-$) and cations (methylammonium $MA^+$, $Pb^{2+}$) can migrate due to the presence of vacancies, interstitials, or antisite substitutions. A large variety of activation energies for ion migration have been published, both measured experimentally and predicted theoretically. Theoretical calculations predict activation energies between 0.08 and 0.58 eV, 0.46 and 1.12 eV, and 0.80 and 2.31 eV for the migration of $I^-$, $MA^+$, and $Pb^{2+}$, respectively [34, 240, 247–249]. Attempts to experimentally determine the activation energy have given a similar variety of results [39, 40, 108, 218, 250–253]. Most experimental techniques further fail to distinguish between the charge of the ions (anions and cations), which can lead to mis-assignment of the ion species.

Here we quantify the activation energy, diffusion coefficient, sign of charge, and concentration of mobile ions in $MAPbI_3$ using transient ion drift, one of the most powerful methods to quantify ion migration [216, 235]. We show that probing the capacitance change associated with ion migration requires to measure the capacitance transients on the timescale of seconds. Using transient ion drift we identify footprints of distinct mobile ion species which we attribute to the migration of $I^-$ (activation energy 0.29 eV) and $MA^+$ (0.39 – 0.90 eV). We find that the concentration of mobile $MA^+$ ions is one order of magnitude higher than the one of mobile $I^-$ ions, and that the diffusion coefficient of mobile $MA^+$ ions is three orders of magnitude lower than the one for mobile $I^-$ ions. As a result, the migration of $MA^+$ ions leads to a capacitance transient with a time scale of seconds, where the migration of $I^-$ ions results in a transient with a time scale of less than a millisecond at 300 K. This quantification leads to a better understanding of ion migration, which is a crucial step towards stable perovskite solar cells.

## 7.2 Transient ion drift

Transient ion-drift measurements rely on the external application of an electric field as shown in Section 6.5. We use a diode configuration to study ion migration. Our diode consists of an inverted planar perovskite solar cell architecture with a solution-processed $NiO_X$ film as a hole-transporting layer and $C_{60}$ as an electron-

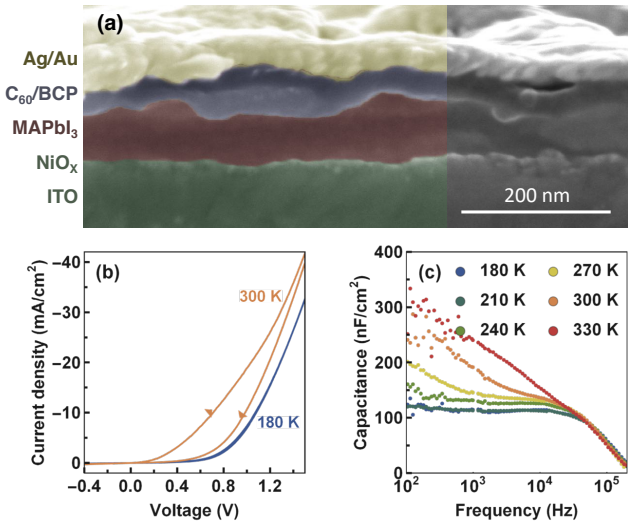


**Figure 7.1**: Inverted $MAPbI_3$ device characteristics. **(a)** Cross-section scanning electron microscopy, **(b)** current–voltage characteristics measured in the dark, and **(c)** impedance spectroscopy measured in the dark at 0 V with an AC perturbation of 20 mV. The high capacitance at low frequencies is attributed to the migration of mobile ions in the vicinity of the contact interfaces. The capacitance corresponds to the real part of the complex capacitance.

transport layer [254], as shown in Figure 7.1a. We chose the inverted solar cell structure over the standard one due to the strong tendency of the latter to accumulate charges, both electronic and ionic, at the $TiO_2$/perovskite interface resulting in a capacitive hysteresis and additional dielectric contributions, which is reduced in the inverted structure (see Section 7.5.2) [255]. In the inverted solar cell architecture, PEDOT:PSS (poly(3,4-ethylenedioxythiophene)–poly(styrenesulfonate)) is the most widely used hole-transport material, however, its high acidity and tendency to absorb water might lead to unwanted device degradation [256]. We furthermore avoid using spiro-MeOTAD (2,20,7, 70-tetrakis[N,N-di(4-methoxy-phenyl)amino]-9,90-spiro-bifluorene) since typical dopants such as lithium salts lead to instabilities due to their high sensitivity to moisture, and can show misleading features in the transient ion-drift measurements due to the additional dopant ion migration [257, 258]. The current–voltage characteristics of a perovskite solar cell in the dark in forward and reverse voltage scans are shown in Figure 7.1b (see Figure 7.7 for current–voltage characteristics measured at 1 sun). We observe a significant difference between the forward and reverse scanning direction at 300 K. When cooling the perovskite solar cell, this current– voltage hysteresis is strongly reduced and almost

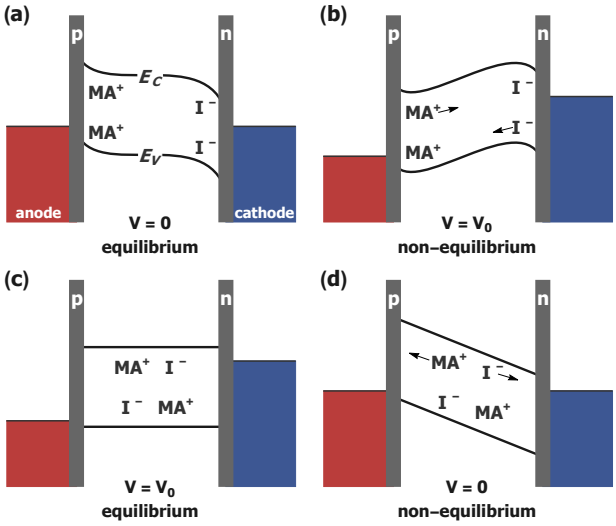


**Figure 7.2**: Influence of ion migration on the band energies. **(a)** At short circuit, mobile $MA^+$ and $I^-$ ions accumulate at the interface partially screening the built-in electric field. **(b)** When applying a forward bias ($V_0$), mobile ions will drift towards the bulk, **(c)** resulting in a uniform ion distribution within the perovskite layer. **(d)** After removing the forward bias, the built-in electric towards the interfaces results in a capacitance transient used to quantify ion migration. $E_C$ is the conduction band energy and $E_V$ the valance band energy.

vanishes at 180 K (see inset Figure 7.1b, and Figure 7.8 for current–voltage curves measured between 180 and 330 K). This has previously been attributed to the inhibition of the ion migration at low temperatures [259, 260].

The transient ion-drift technique relies on probing the ion migration in the perovskite layer using capacitance transients at different temperatures. To find the suitable AC frequency regime for measuring capacitance transients, we study the frequency-dependence of the capacitance of the perovskite diode in the dark (see Figure 7.1c). At low frequencies, the capacitance is dominated by mobile ions which accumulate near the contact interfaces [237]. When reducing the temperature, both the current–voltage hysteresis and the ionic capacitance contribution are strongly reduced until they disappear close to 180 K. At high frequencies, the capacitance is reduced due to the series resistance of the conductive contact layers reducing the cut-off frequency of the device. Between the two limits lies a relatively constant plateau, related to the geometric capacitance of the device, which is related to the perovskite permittivity (see Section 7.5.4 for details).

We chose to measure the capacitance at 10 kHz, at the plateau of the capacitance. Transient ion drift uses the transient capacitance response following a voltage

pulse at different temperatures (see schematic Figure 7.2). We apply a forward bias of 0.4 V for 1 second, which reduces the width of depletion region and leads to a new equilibrium distribution within the previously depleted region (Figure 7.2a–c), changing the capacitance of the device. This change in capacitance did not increase further with longer pulse widths, indicating that a uniform distribution of ions was reached after the 1 second voltage pulse duration (see Figure 7.10) [216]. We avoid using higher external voltages since Yuan *et al.* found that external electrical fields as low as 3 V $\mu m^{-1}$ at 330 K can lead to the formation of $PbI_2$ in $MAPbI_3$ [261]. After turning off the voltage pulse, the built-in electric field will drive both the mobile ions and electric charges back to the contact interfaces (Figure 7.2d). Mobile anions will follow the electrons and mobile cations will follow the holes, resulting in a capacitance transient. We measure this capacitance transient at temperatures between 180 and 350 K (see Figure 7.3a), above the first-order phase transition from tetragonal to orthorhombic near 165 K [262, 263]. We see no capacitance transient at low temperatures ($<$ 190 K), while a negative capacitance change grows in between 190 and 280 K until the capacitance decay it is too fast to measure. At higher temperatures, we observe a positive change in capacitance. Assuming the total ion concentration is conserved, the electric field varies linearly across the depletion region, and thermal diffusion of ions is negligible compared to ion drift, the change in capacitance depends only on the temperature, activation energy, diffusion coefficient, and concentration of mobile ions as [264]

$$C(t) = C(\infty) \pm \Delta C \exp\left(-\frac{t}{\tau}\right) \tag{7.1}$$

where $\Delta C$ is the change in capacitance due to the drift of mobile ions towards the interfaces, $C(\infty)$ the steady-state capacitance, and $\tau$ is the time constant for ion migration (see Section 6.5 for details). The assumption that the electric field varies linearly across the depletion region is supported by recent studies showing that the electric field varies approximately linearly within the perovskite layer when the perovskite layer is subjected to an external or internal electric field [50, 265]. We can describe the measured capacitance transients using exponential functions, which further corroborates that the assumption of a linear field is valid in our devices (see Section 7.5.6) [216]. We note that Weber *et al.* found an additional interface dipole at the perovskite/$SnO_2$ interface [50]. This interface dipole is deliberately omitted in our structure by using $NiO_X$ and $C_{60}$ as extraction layers (see Section 7.5.2). As metals are prone to reacting with $I^-$ and mobile ions and can diffuse into the transport layers [266, 267], we have ensured to perform our measurements shortly after the fabrication of the diodes. In addition, we have carefully chosen the AC frequency to ensure that the measured capacitance is not affected by potential ion diffusion

through the transport layers (see Section 7.5.7).

## 7.3 Mobile ions in $MAPbI_3$

To identify processes associated to the capacitance changes we use the rate window analysis, originally introduced by Lang to analyse deep-level transient spectroscopy (DLTS) measurements [202]. The capacitance change extracted by this method is given by $\Delta C = C(t_1) - C(t_2)$, where $t_1$ and $t_2$ depend on the typical decay times of the capacitance at a certain temperature to extract a peak associated with each activation energy. When choosing $t_1 = 2t_2$ from milliseconds to seconds we find three peaks corresponding to three separate processes, which we label A1, C1, and C2 (see Figure 7.3b). The capacitance change associated with C1 and C2 both are positive and describe the migration of a cation. A1 is negative and describes the migration of an anion. We hence assign A1 to the migration of $I^-$ ions and C1 and C2 to the migration of $MA^+$ ions. We exclude the migration of $Pb^{2+}$ ions since theoretical studies suggest that they are unlikely to migrate [34]. Note that we cannot rule out the migration of $H^+$ ions, which was calculated to have an activation energy of 0.29 eV [268]. However, the predicted concentration of $H^+$ ions in $MAPbI_3$ is in the order of $10^{11}$ $cm^{-3}$ [35], orders of magnitude lower than what we have measured.

The temperature dependence of the peaks in the rate window analysis together with their time scales can be used to obtain activation energy and diffusion coefficient of ion migration. This method, however, uses only two points of each transient to extract the time scales. To quantify ion migration using all data points, we fit the measured capacitance changes to exponential decays to obtain the time constants $\tau$ at different temperatures (Equation 7.1). By means of an Arrhenius plot we can extract both the activation energy and diffusion coefficient (see Figure 7.3). We again identify the three species, C1, C2, and A1, where A1 occurs at much faster timescales and lower temperatures.

To estimate the sample-to-sample, and lab-to-lab variation we measured solar cells fabricated at AMOLF and at the University of Konstanz, with power conversion efficiencies ranging from 1 to 12% (see Section 7.5.9 for details). The obtained characteristics of mobile ions for all the devices are shown in Figure 7.4 and the mean values are summarised in Table 7.1. We find that the activation energy for the migration of $I^-$ ions is very reproducible across all devices, while the activation energy for the migration of $MA^+$ ions depends strongly on the fabrication conditions, which is consistent with the wide distribution of activation energies for the migration of $MA^+$ ions in the literature. The wide distribution of activation energies for the migration of $I^-$ ions in the literature could be explained by the misinterpretation of mobile ion species, since most techniques cannot distinguish between the migration

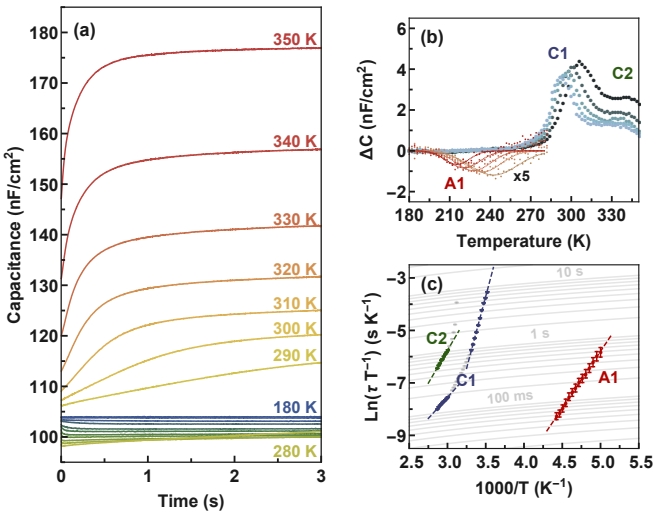


**Figure 7.3**: Ion migration in $MAPbI_3$. **(a)** Capacitance transient measurements between 180 and 350 K with steps of 10 K measured at 0 V with an AC voltage of 10 mV at 10 kHz after a pulse of 0.4 V for 1 second. **(a)** Rate-window plot of measured capacitance transients with different time constants ranging from milliseconds (red) to seconds (blue) reveal three ion species with different thermal emission rates. We attribute A1 to the migration of $I^-$ ions and C1 and C2 to the migration of $MA^+$ ions. **(a)** Arrhenius plot of the observed thermal emission rates as a function of temperature. The linear fit reveals the activation energy and the diffusion coefficient of the mobile ion species. The capacitance is calculated assuming a capacitor in parallel with a resistor.

of anions and cations. The transient ion-drift measurements are able to simultaneously distinguish between mobile cations and anion, and detect low concentrations of mobile impurities ($\sim 0.01\%$ of the doping density). Our measurements thus show that many theoretical calculations cannot be experimentally verified within the margin of error.

Interestingly, we obtain a diffusion coefficient of $10^{-9}$ $cm^2$ $s^{-1}$ for $I^-$ ions which is three orders of magnitude higher than the diffusion coefficient for $MA^+$ ions of $10^{-12}$ $cm^2$ $s^{-1}$ (see Table 7.1). The diffusion coefficients measured here are very close to the diffusion coefficients measured with NMR ($10^{-9}$ $cm^2$ $s^{-1}$ for $I^-$ and $10^{-15}$ to $10^{-12}$ $cm^2$ $s^{-1}$ for $MA^+$) [36, 37], and to those obtained by Yuan *et al.* ($4 \times 10^{-11}$ $cm^2$ $s^{-1}$ for $MA^+$) [39], Li *et al.* ($5 \times 10^{-8}$ to $6 \times 10^{-9}$ $cm^2$ $s^{-1}$ for $I^-$) [38], and Bertoluzzi *et al.* ($8 \times 10^{-9}$ $cm^2$ $s^{-1}$ for $I^-$) [269], which supports our assignment of A1 to the migration

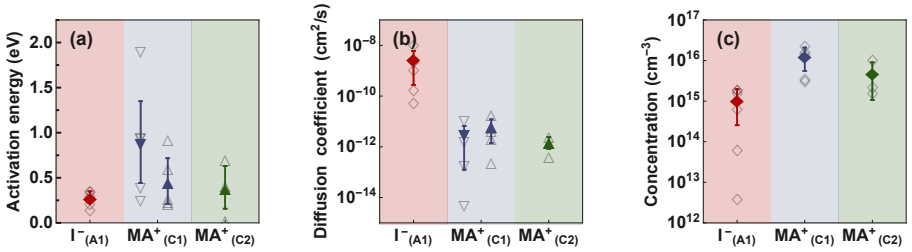


**Figure 7.4**: Characteristics of mobile ions in MAPbI$_3$. **(a)** Activation energy, **(b)** diffusion coefficient at 300 K, **(c)** and concentration of mobile ions in MAPbI$_3$ perovskites obtained by transient ion drift. The downward and the upward triangle represents measurements below and above the tetragonal-to-cubic phase-transition temperature. The values are summarised in Table 7.1.

of $I^-$ ions and C1 and C2 to the migration of $MA^+$ ions. These values also suggest that the measured capacitance change is due to the migration of ions and not to the migration of vacancies. Solute-dopant pairing can significantly slow down the ionic diffusion [216], which could be the reason for the slow diffusion of $MA^+$ ions. Only the $MA^+$ ions have a transient decay time in the order of seconds at typical operation temperatures ($<$ ms for $I^-$). Thus, our results suggest that mobile $MA^+$ ions are the origin of the observed current–voltage hysteresis in MAPbI$_3$ perovskite solar cells. Previously, also $I^-$ has been assigned responsible for the current–voltage hysteresis in MAPbI$_3$ solar cells [34], however, the sensitivity of transient ion-drift to the sign of the ion excludes this possibility.

Close to the tetragonal-cubic phase-transition temperature (327 K) [35] we observe a decrease in activation energy and an increase in diffusion coefficient for one of the migrating $MA^+$ ions (C1) (with the exception for the device with a power conversion efficiency of 1%). A similar behaviour has previously been observed and attributed to the volume change in the unit cell at temperatures close to the tetragonal-cubic phase transition [231, 270]. Note that C2 might show a similar behaviour at lower temperatures, however, the activation energy of C2 in the tetragonal phase could not be resolved in our measurements due to its long time constant. The obtained activation energies of the two migration pathways for $MA^+$ (C1 and C2) in the cubic phase are comparable, yet the diffusion coefficient of C1 is somewhat higher than the diffusion coefficient of C2. Using Kelvin probe force microscopy, Yun *et al.* found that ion migration near grain boundaries is much faster than inside the grains due to higher ionic diffusivity at grain boundaries [271]. We thus speculate

**Table 7.1**: Characteristics of mobile ions in $MAPbI_3$. The diffusion coefficient is calculated for 300 K.

| | A1 | C1 | | C2 |
|---|---|---|---|---|
| Migrating ion species | $I^-$ | $MA^+$ | | $MA^+$ |
| Charge | negative | positive | | positive |
| Concentration ($cm^{-3}$) | $(1.1 \pm 0.9) \times 10^{15}$ | $(1.3 \pm 0.8) \times 10^{16}$ | | $(5.0 \pm 4.0) \times 10^{15}$ |
| Phase structure | tetragonal | tetragonal | cubic | cubic |
| Activation energy (eV) | $0.29 \pm 0.06$ | $0.90 \pm 0.45$ | $0.46 \pm 0.25$ | $0.39 \pm 0.24$ |
| Diffusion coeff. ($cm^2\ s^{-1}$) | $(3.1 \pm 2.8) \times 10^{-9}$ | $(3.4 \pm 3.3) \times 10^{-12}$ | $(6.8 \pm 5.3) \times 10^{-12}$ | $(1.6 \pm 0.8) \times 10^{-12}$ |

that these are both mobile $MA^+$ species where C1 has a higher diffusion coefficient, which could be due to ion movement in vicinity of grain boundaries.

The concentration of mobile ions is obtained from the height of the measured capacitance transients, as described in Section 6.5. The obtained concentrations for mobile $I^-$ and $MA^+$ ions are summarised in Figure 7.4c. We note that we assume a typical doping density of $1 \times 10^{17}$ $cm^{-3}$ for all the measured perovskite films and temperatures (see Section 7.5.4) [224]. Although the density of mobile ions depends on the fabrication, we find that the concentration of the mobile $MA^+$ ions is systematically about one order of magnitude higher than that of the mobile $I^-$ ions. The measured mobile ion concentration is rather low compared to other studies, which report values of around $10^{18}$ $cm^{-3}$ [269]. However, several recent studies measure a mobile ion concentration comparable to what we measure, on the order of $10^{15}$ $cm^{-3}$ [50, 265], suggesting that less than 10% of the screening of the electric field within the perovskite layer is produced by the presence of mobile ions. We note that electrical neutrality is still given, as the concentration obtained is the concentration of mobile ions within the perovskite film, not all ions present in the perovskite film.

Capacitance transients such as the ones observed here could also originate from electronic defect states. A powerful method to measure charge-carrier traps is DLTS [202], a method which is very similar to transient ion drift. DLTS has been used to study fast (milliseconds) charge trapping in perovskite solar cells [210], in contrast, ion migration in perovskites typically proceeds on long timescales of milliseconds to seconds [272, 273]. Furthermore, the ratio of rise and decay times of the capacitance in DLTS and transient ion drift is different, so that we can distinguish ion migration from trapping and de-trapping of charge carriers (see Section 7.5.8 and Section 6.7.4 for details) [235]. We can therefore attribute the observed transients as the result of ion migration rather than electronic defect states. Atomistic simulations furthermore suggest that deep-level defects require high formation energies between 2 and 6 eV, such that their formation is unlikely [274].

## 7.4 Conclusion

To conclude, we have shown that transient ion drift is a fast and accurate method to quantify, with high precision, the activation energy, diffusion coefficient, sign of charge, and concentration of mobile ions in perovskite solar cells. In $MAPbI_3$ perovskites we observe that both $MA^+$ and $I^-$ are migrating. We find that the concentration of mobile $MA^+$ ions is significantly higher than the concentration of mobile $I^-$ and that the diffusion coefficient of $I^-$ ions is three orders of magnitude higher than the diffusion coefficient of $MA^+$ ions. On timescales associated with current–voltage measurements, only the migration of $MA^+$ ions is slow enough to cause a current–voltage hysteresis in $MAPbI_3$ solar cells. The migration of $I^-$ ions is still relevant for the device operation, and the degradation of perovskite solar cells. The migration of mobile $I^-$ ions is very reproducible across devices fabricated in different laboratories, while the migration of mobile $MA^+$ ions strongly depends on the fabrication, which explains the wide distribution of activation energies for the migration of $MA^+$ ions in literature. Our measurements guide the future theoretical investigation into ion migration in halide perovskites and offer quantitative insight into the parameters of the mobile ion species, and hence the degradation pathways of perovskite solar cells.

## 7.5 Supporting information

### 7.5.1 Experimental

**Device fabrication.** Device 1, 2, and 3 were fabricated as described hereafter, with the exception of device 2 which was fabricated using a $NiO_X$ precursor solution of 0.3 M that was spun on the cleaned ITO glass at 4000 rpm for 15 seconds: Laser patterned indium tin oxide (ITO) glass substrates were cleaned by ultra-sonication for 20 minutes subsequently in detergent in deionized water, deionized water, acetone, and isopropanol, followed by oxygen plasma for 20 minutes at 100 W. Nickel oxide ($NiO_X$) precursor solution (0.1 M nickel(II) nitrate hexahydrate (Aldrich) in ethanol) filtered with a 0.45 μm PTFE membrane was spun on the cleaned ITO glass at 4000 rpm for 30 seconds. This step was then repeated two times [254]. Annealing at 350 °C for 1 hour with a ramping speed of 3 °C/min induced $NiO_X$ film formation. The $MAPbI_3$ perovskite precursor solution was prepared by mixing of total 1.35 M of methylammonium iodide (MAI, solaronix) and lead(II) iodide ($PbI_2$, Aldrich) with 1:1 molar ratio dissolved in N,N-dimethylformamide (anhydrous, Aldrich) at 60 °C. The $MAPbI_3$ precursor solution was filtered through a 0.45 μm PTFE membrane spun onto $NiO_X$ coated substrates at 5000 rpm for 25 seconds in a nitrogen filled glove box. 5 seconds after the beginning of the rotation, 180 μL of chlorobenzene

anti-solvent (anhydrous, Aldrich) was quickly dropped onto the substrate. After the $MAPbI_3$ spinning process, the substrates were annealed at 100 °C for 15 minutes. 30 nm of $C_{60}$ (0.5 Å/s rate, 99.9%, Aldrich), 8 nm of bathocuproine (0.2 Å/s, 99.99%, Aldrich), 50 nm of silver (1 Å/s, 99.99%, Kurt J. Lesker) and 150 nm of gold electrode (1 Å/s, 99.999%, Kurt J. Lesker) were sequentially deposited on top of $MAPbI_3$ layer by thermal sublimation/evaporation at pressures below 2 x $10^{-7}$ mbar. Device 1 is used in the main text.

Device 4, 5, and 6 were fabricated as described hereafter: The $MAPbI_3$ perovskite precursor solution was prepared by mixing of total 1.5 M of methylammonium iodide (MAI, Solaronix) and lead(II) iodide ($PbI_2$, TCI) with 1:1 molar ratio dissolved in N,N-dimethylformamide (anhydrous, Aldrich) and DMSO for 3 hours at 60 °C. 50 µL of the $MAPbI_3$ precursor solution filtered through a 0.45 µm sized PTFE membrane was spun onto $NiO_X$ coated substrates at 4000 rpm for 50 seconds in a nitrogen-filled glove box. 10 seconds after the beginning of the rotation, 300 µL of diethyl ether anti-solvent (anhydrous, Aldrich) was quickly dropped onto the substrate. After the $MAPbI_3$ spinning process, the substrates were annealed at 100 °C for 3 minutes. 45 nm of $C_{60}$ (0.2 Å/s) was deposited on top of the $MAPbI_3$ layer by thermal sublimation at pressures below 8 x $10^{-6}$ mbar. A thin layer of bathocuproine (99.99%, Aldrich) dissolved in ethanol (0.5 mg/ml) was then spun on top of the $C_{60}$ layer with 6000 rpm for 15 seconds. Finally, 100 nm of silver (1 Å/s) was deposited by thermal evaporation at pressures below 8 x $10^{-6}$ mbar.

**Electrical measurements.** To avoid air exposure, the sample was loaded into a Janis VPF-100 liquid nitrogen cryostat inside a nitrogen-filled glovebox. Current-voltage, impedance spectroscopy, capacitance-voltage, and transient ion-drift measurements were performed at a pressure below 2 x $10^{-6}$ mbar in the dark using a commercially available DLTS system from Semetrol. To ensure thermal equilibrium the temperature of the sample was held constant for at least 30 minutes before current-voltage, impedance spectroscopy, and capacitance-voltage measurements. Capacitance transient measurements were performed from 180 to 350 K in steps of 2 K with a heating rate of about 2 K per minute. The sample was held at 180 K for one hour before starting the transient ion-drift measurement.

**Imaging of device cross-section.** To obtain a clean cross-section of the device, it was immersed in liquid nitrogen for 60 seconds and cleaved in the centre. The cross-sectional image was taken with a FEI Verios 460 scanning electron microscope in the secondary electron mode. An acceleration voltage of 5 kV and a working distance of 4 mm were used and field immersion mode was applied for an optimised resolution.

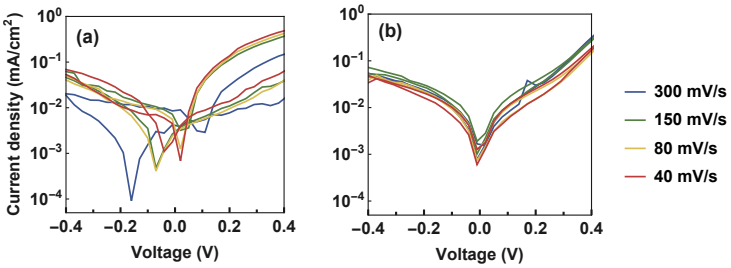


**Figure 7.5**: Dark current-voltage characteristics of diodes based on **(a)** $TiO_2$/$MAPbI_3$/spiro-OMeTAD and **(b)** $NiO_X$/$MAPbI_3$/$C_{60}$ illustrating different hysteretic effects as a function of the scan rate.

### 7.5.2 Effect of contact layers

By measuring the current-voltage characteristic at different scan rates, a distinction can be made between capacitive and non-capacitive hysteresis [255]. Figure 7.5 illustrates the effect of capacitive hysteresis in perovskite solar cells using $TiO_2$ as an electron transport material. This effect is attributed to the accumulation of both ionic and electronic charges at the $TiO_2$/perovskite interface in a highly reversible manner resulting in a double-layer structure [255]. This effect is not observed in the inverted structure using $NiO_X$.

Figure 7.6 shows the capacitance versus frequency at different temperatures for the inverted and the regular perovskite solar cell structure. At the temperature range between 180 and 300 K no phase transition of the $MAPbI_3$ layer is to be expected. However, the regular devices structure shows a strong change in the high-frequency region at these temperatures, indicating dielectric contributions of contact layers play an important role.

### 7.5.3 Dark and light current-voltage characteristics

Inverted perovskite solar cells have been shown to have only little hysteresis when illuminated [232, 275–277], but hysteresis may still be present in the dark. Figure 7.7 shows the current- voltage characteristic of an inverted perovskite solar cell measured with a scan rate of 300 mV/second under 1 sun from a solar simulator (Oriel 92250A) using a Keithley 2636A source-measure unit after 15 minute light soaking. During this measurement, the sample was masked and placed in nitrogen inside an air-tight sample holder. Figure 7.8 shows current-voltage characteristics of an inverted perovskite solar cell in the dark, measured between 180 and 330 K. We note that there is a significant difference between the current-voltage hystere-

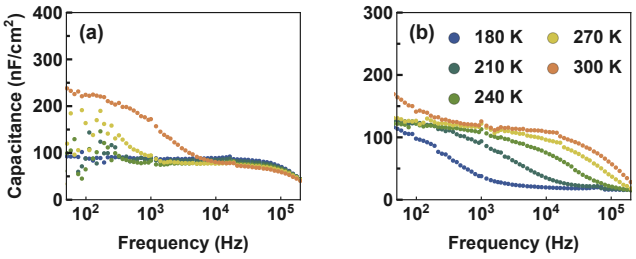


**Figure 7.6**: Impedance spectroscopy measured at different temperatures in the dark at 0V with an AC perturbation of 20 mV of **(a)** an inverted ($NiO_X/MAPbI_3/C_{60}$) and **(b)** a regular ($TiO_2/C_{60}/MAPbI_3$/spiro-OMeTAD) and perovskite solar cell. The capacitance corresponds to the real part of the complex capacitance.

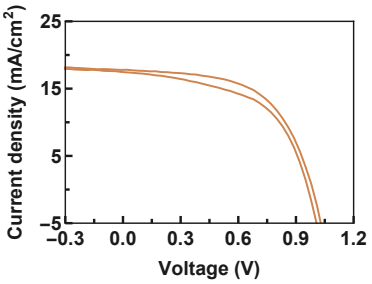


**Figure 7.7**: Current-voltage characteristics of an inverted perovskite solar cell ($NiO_X/MAPbI_3/C_{60}$) measured at 1 sun at room temperature.

sis measured in the dark and under illumination. This difference may be caused by photo-induced ion migration, which shifts the hysteretic response to different time scales. In fact, it has been shown that the activation energy for ion migration is reduced by illumination [253, 278]. When the perovskite solar cell is cooled, the current-voltage hysteresis is reduced and almost vanishes at 180 K.

### 7.5.4 Mott-Schottky characteristics

Figure 7.9 shows the capacitance as a function of voltage measured at 10 kHz, where the measured capacitance corresponds to the geometric capacitance and the series resistance can be neglected (see Figure 1c). We observe a plateau at low voltage, which indicates full depletion under short-circuit conditions. In such a case of full depletion, the geometrical capacitance is related to the perovskite permittivity (Equation 6.1). Assuming a parallel plate capacitor with the thickness of the perovskite layer, we obtain a permittivity of 15.3 for the perovskite layer, averaged

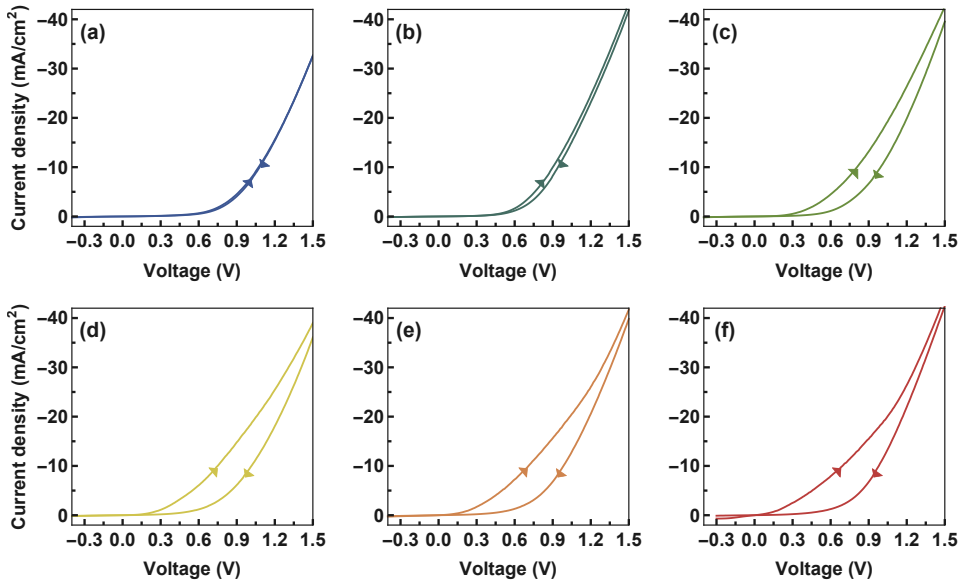


**Figure 7.8**: Temperature dependent current-voltage hysteresis measured in the dark at **(a)** 180, **(b)** 210, **(c)** 240, **(d)** 270, **(e)** 300, and **(f)** 330 K.

over the measured temperatures, somewhat lower than the calculated value of 24.1 from electronic structure calculation in the absence of molecular reorientations [279].

When a voltage $V$ is applied in forward direction, the depletion capacitance $C_{dl}$ increased. This increase in capacitance is correlated to a decrease in depletion-layer width. The depletion capacitance as a function of applied voltage can be approximated by the Mott-Schottky relation as [127]

$$C_{dl} = A\sqrt{\frac{q\varepsilon_0\varepsilon N}{2(V_{bi} - V)}} \tag{7.2}$$

where $A$ is the area of the device, $q$ the elementary charge, $\varepsilon_0$ the vacuum permittivity, $\varepsilon$ the perovskite permittivity, $N$ the doping density, and $V_{bi}$ the built-in potential. From the $C^{-2}(V)$ pot we obtain a built-in potential of 0.92 V and a doping density of 7.0 x $10^{16}$ cm$^{-3}$. The slope of the Mott-Schottky plot furthermore suggests a p-type MAPbI$_3$ layer. Theoretical calculations predict that the p-type doping of MAPbI$_3$ originates from negatively charged $Pb^{2+}$ and $MA^+$ vacancies, where positively charged $I^-$ vacancies might result in n-type doping [280]. Note that the

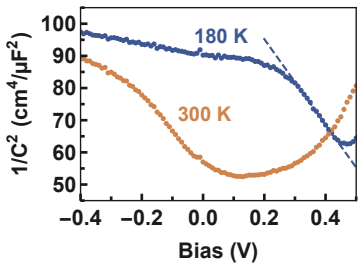


**Figure 7.9**: Mott-Schottky characteristics of an inverted perovskite solar cell ($NiO_X/MAPbI_3/C_{60}$) measured at 300 and 180 K in the dark with an AC perturbation of 10 mV at 10 kHz. The capacitance is calculated assuming a capacitor in parallel with a resistor.

Mott-Schottky analysis is only meaningful when the depletion capacitance can be clearly identified [237]. Since the ionic capacitance contribution dominates the depletion capacitance at high temperatures, we performed the Mott-Schottky analysis at 180 K.

For the calculation of the concentration of mobile ions, a constant doping density of 1 x $10^{17}$ $cm^{-3}$ is assumed for all devices. Since our obtained doping concentration at 180 K is close to typical vales at room temperature (1 x $10^{17}$ $cm^{-3}$) [237], we believe that the measured temperature window lies within the extrinsic region in which the doping density is reasonably constant.

### 7.5.5 Ion redistribution

Figure 7.10 shows the amplitude of the capacitance transient as a function of filling pulse duration. Since the amplitude has reached its maximum at 1 second filling pulse duration, we assume that a uniform ion distribution is reached after applying a filling pule of 1 second.

### 7.5.6 Fitting capacitance transients

Figure 7.11 shows measured capacitance transients from 180 to 350 K with steps of 10 K measured at 0 V after applying a voltage pulse of 0.4 V for 1 second (identical to Figure 7.3a). The grey dotted lines in Figure 7.11a indicate the modelled capacitance decay due to ionic drift according to the values in Table 7.2. For the Arrhenius plot we limited the data analysis to temperatures where the number of exponentials to use was evident from the scan and the fit quality was good (as indicated by the colours in Figure 7.3c). Figure 7.11b to 7.11e exemplary show fits to capacitance decays at 200, 240, 290, and 340 K.

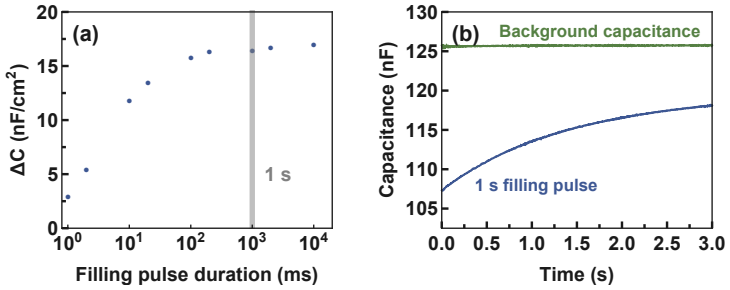


**Figure 7.10**: **(a)** Amplitude of the capacitance transient when applying a voltage of 0.4 V as a function of filling pulse duration. The grey line indicates the filling pulse duration used for the transient ion-drift measurements. **(b)** Background capacitance and capacitance transient after applying a filling pulse of 0.4 V for 1 second at 300 K. The capacitance transient was measured after the background capacitance had reached a steady state. The capacitance is calculated assuming a capacitor in parallel with a resistor.

### 7.5.7 Impedance spectroscopy

In a perovskite solar cell, mobile ions can migrate through the transport layer towards the electrodes [254]. As metals are prone to reacting with $I^-$ ion, this ion migration can induce an additional series resistance related to contact degradation [130]. It is thus important to carefully choose an AC measuring frequency for which the impedance response corresponds to the capacitive character of the device, as oppose to the resistances.

Figure 7.12 shows the impedance response of the perovskite solar cells at different temperatures. A phase angle close to 90° indicates that the impedance corresponds to the capacitance of the device. At frequencies above 10 kHz, the phase angle increases while the modulus approaches the series resistance of the device, indicating that the capacitance response is governed by the series resistance. We therefore measure the capacitance as a function of voltage and time with an AC frequency of 10 kHz, where the impedance response is dominated by the capacitance of the device over the whole temperature range of interest.

### 7.5.8 Mobile ions versus electronic defect states

To distinguish between ion diffusion and electronic effects such as trapping and detrapping, we compare the rise and decay time of capacitance following the forward bias and returning to short circuit conditions [235]. For mobile ions, it is expected that the time required to lead to a uniform ion distribution after applying a forward bias is longer than the time required for ions to drift back to the interfaces after

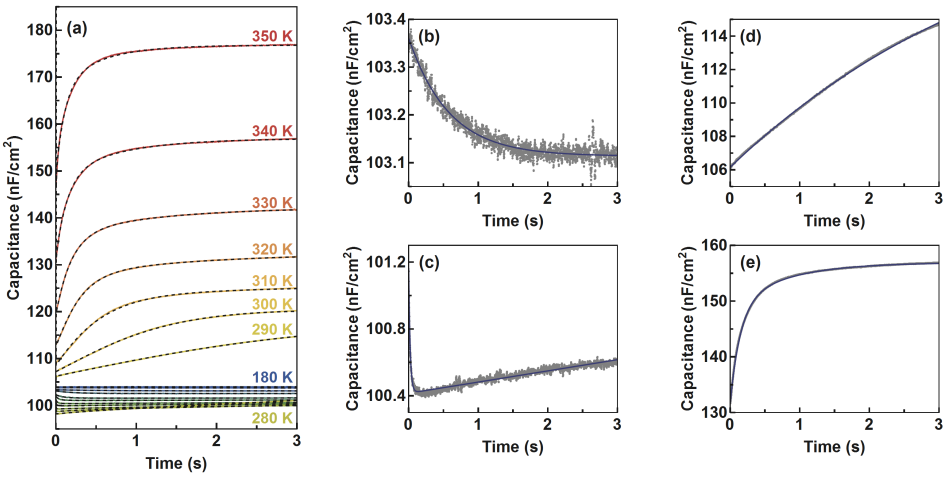


**Figure 7.11**: **(a)** Measured capacitance transients together with the modelled capacitance decay due to ionic drift of A1, C1, and C2 shown as black dotted lines. Exemplary fits of measured capacitance decay at **(b)** 200, **(c)** 240, **(d)** 290, and **(d)** 340 K. One exponential decay function is used to fit (b) and (d) and two exponential decay functions to fit (c) and (e). Grey points are experimentally measured data and blue lines are obtained fits. The capacitance is calculated assuming a capacitor in parallel with a resistor.

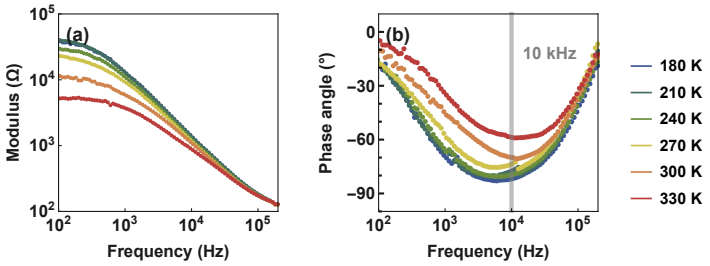


**Figure 7.12**: Impedance spectroscopy of an inverted perovskite solar cell ($NiO_X/MAPbI_3/C_{60}$) measured at 0 V with an AC perturbation of 20 mV in the dark, separated in **(a)** modulus and **(b)** phase angle.

removal of the forward bias. In contrast, for electronic defect states the capture rate is much higher than the emission rate (see Section 6.7.4 for details). Figure 7.13 shows the measured capacitance transient of an inverted perovskite solar cell

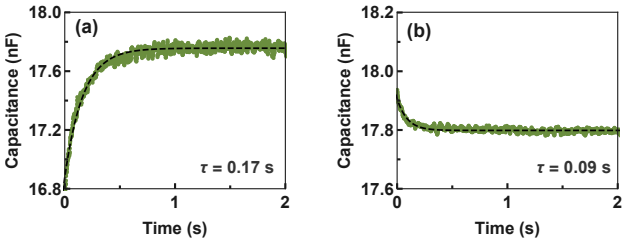


**Figure 7.13**: Capacitance transient of an inverted perovskite solar cell ($NiO_X/MAPbI_3/C_{60}$) measured in the dark **(a)** while applying a voltage pule of 0.4 V and **(b)** at short circuit, after removing the voltage bias. The dashed lines are fits obtained using an exponential decay function with the timescale indicated in the inset. The capacitance is calculated assuming a capacitor in parallel with a resistor.

measured at 210 K, showing that the measured capacitive transient is due to the diffusion of mobile ions.

### 7.5.9 Statistics and reproducibility across laboratories

Many examples in the literature show that the performance of perovskite solar cells depend heavily on the fabrication, even in the same laboratory. Also, ions are presumably affected by, and affecting degradation. To study this, we measure seven different devices and compare the transient ion-drift response.

Device 1 corresponds to the device shown in Figure 7.1 and Figure 7.3. Device 2 corresponds to a device fabricated in the same way as device 1. Device 3 represent a poor performing device. Devices 4, 5, and 6 are devices fabricated in the laboratory of the University of Konstanz. All devices have the same device structure ($NiO_X/MAPbI_3/C_{60}$), but the $MAPbI_3$ layer has an average thickness of 105 nm in devices 1, 2, and 3 and 275 nm in devices 4, 5, and 6. The values obtained for activation energy, diffusion coefficient, and concentration for mobile ions for the measured samples are summarised in Table 7.2 to Table 7.7. Note that we could not resolve the slow $MA^+$ species in the devices manufactured at the University of Konstanz.

A typical current-voltage characteristic curve together with an external quantum efficiency spectrum of an inverted perovskite solar cell fabricated in Konstanz is shown in Figure 7.14. We furthermore note that in devices with an average $MAPbI_3$ thickness of 275 nm, we observed an initial capacitance decay at high temperatures which we relate to the redistribution of ions inside the depletion layer (see Figure 7.15) [216]. For DLTS, such an initial decay in capacitance is not expected, as the drift of free charge carriers out of the depletion layer is much faster than the emission

**Table 7.2**: Characteristics of mobile ions in **device 1** with a short-circuit current density of 17.7 mA/cm$^2$, an open-circuit voltage of 0.98 V, a fill factor of 56%, and a power conversion efficiency of 9.6%. The diffusion coefficient is calculated for 300 K.

| | A1 | C1 | | C2 |
|---|---|---|---|---|
| Migrating ion species | $I^-$ | $MA^+$ | | $MA^+$ |
| Charge | negative | positive | | positive |
| Concentration (cm$^{-3}$) | $(1.7 \pm 0.1) \times 10^{15}$ | $(2.5 \pm 0.1) \times 10^{16}$ | | $(1.1 \pm 0.1) \times 10^{16}$ |
| Phase structure | tetragonal | tetragonal | cubic | cubic |
| Activation energy (eV) | $0.37 \pm 0.01$ | $0.95 \pm 0.02$ | $0.28 \pm 0.01$ | $0.43 \pm 0.01$ |
| Diffusion coeff. (cm$^2$ s$^{-1}$) | $(3.2 \pm 1.4) \times 10^{-9}$ | $(1.8 \pm 2.4) \times 10^{-12}$ | $(4.7 \pm 2.7) \times 10^{-12}$ | $(4.4 \pm 3.7) \times 10^{-13}$ |

**Table 7.3**: Characteristics of mobile ions in **device 2** with a short-circuit current density of 13.4 mA/cm$^2$, an open-circuit voltage of 0.88 V, a fill factor of 48%, and a power conversion efficiency of 5.7%. The diffusion coefficient is calculated for 300 K.

| | A1 | C1 | | C2 |
|---|---|---|---|---|
| Migrating ion species | $I^-$ | $MA^+$ | | $MA^+$ |
| Charge | negative | positive | | positive |
| Concentration (cm$^{-3}$) | $(2.1 \pm 0.1) \times 10^{15}$ | $(3.9 \pm 0.1) \times 10^{15}$ | | $(2.4 \pm 0.1) \times 10^{15}$ |
| Phase structure | tetragonal | tetragonal | cubic | cubic |
| Activation energy (eV) | $0.39 \pm 0.01$ | $0.40 \pm 0.01$ | $0.23 \pm 0.02$ | $0.04 \pm 0.03$ |
| Diffusion coeff. (cm$^2$ s$^{-1}$) | $(11.6 \pm 2.5) \times 10^{-9}$ | $(3.4 \pm 2.1) \times 10^{-12}$ | $(6.4 \pm 11.1) \times 10^{-12}$ | $(1.6 \pm 3.7) \times 10^{-12}$ |

rate. The capacitance change due to transient ion drift, however, can be due to a combination of both the redistribution inside the depletion layer and the drift of mobile ions towards the contacts.

**Table 7.4**: Characteristics of mobile ions in **device 3** with a short-circuit current density of 3.6 mA/cm$^2$, an open-circuit voltage of 0.74 V, a fill factor of 37%, and a power conversion efficiency of 1.0%. The diffusion coefficient is calculated for 300 K.

| | A1 | C1 | | C2 |
|---|---|---|---|---|
| Migrating ion species | $I^-$ | $MA^+$ | | $MA^+$ |
| Charge | negative | positive | | positive |
| Concentration (cm$^{-3}$) | $(2.1 \pm 0.1) \times 10^{15}$ | $(3.4 \pm 0.1) \times 10^{15}$ | | $(1.7 \pm 0.1) \times 10^{15}$ |
| Phase structure | tetragonal | tetragonal | cubic | cubic |
| Activation energy (eV) | $0.23 \pm 0.01$ | $0.26 \pm 0.01$ | $0.62 \pm 0.01$ | $0.71 \pm 0.01$ |
| Diffusion coeff. (cm$^2$ s$^{-1}$) | $(2.2 \pm 0.8) \times 10^{-9}$ | $(11.5 \pm 2.1) \times 10^{-12}$ | $(20.1 \pm 16.6) \times 10^{-12}$ | $(2.8 \pm 2.7) \times 10^{-12}$ |

**Table 7.5**: Characteristics of mobile ions in **device 4** with a short-circuit current density of 14.9 mA/cm$^2$, an open-circuit voltage of 0.96 V, a fill factor of 62%, and a power conversion efficiency of 8.8%. The diffusion coefficient is calculated for 300 K.

| | A1 | C1 | |
|---|---|---|---|
| Migrating ion species | $I^-$ | $MA^+$ | |
| Charge | negative | positive | |
| Concentration (cm$^{-3}$) | $(4.3 \pm 0.3) \times 10^{12}$ | $(1.6 \pm 0.1) \times 10^{16}$ | |
| Phase structure | tetragonal | tetragonal | cubic |
| Activation energy (eV) | $0.28 \pm 0.09$ | $1.91 \pm 0.06$ | $0.94 \pm 0.06$ |
| Diffusion coeff. (cm$^2$ s$^{-1}$) | $(0.2 \pm 1.8) \times 10^{-9}$ | $(5.3 \pm 23.2) \times 10^{-15}$ | $(1.7 \pm 7.1) \times 10^{-13}$ |

**Table 7.6**: Characteristics of mobile ions in **device 5** with a short-circuit current density of 16.1 mA/cm$^2$, an open-circuit voltage of 0.97 V, a fill factor of 66%, and a power conversion efficiency of 10.2%. The diffusion coefficient is calculated for 300 K.

| | A1 | C1 | |
|---|---|---|---|
| Migrating ion species | $I^-$ | $MA^+$ | |
| Charge | negative | positive | |
| Concentration (cm$^{-3}$) | $(7.0 \pm 1.4) \times 10^{13}$ | $(1.8 \pm 0.2) \times 10^{16}$ | |
| Phase structure | tetragonal | tetragonal | cubic |
| Activation energy (eV) | $0.16 \pm 0.05$ | $0.96 \pm 0.07$ | $0.25 \pm 0.03$ |
| Diffusion coeff. (cm$^2$ s$^{-1}$) | $(0.1 \pm 0.3) \times 10^{-9}$ | $(2.0 \pm 11.3) \times 10^{-13}$ | $(2.5 \pm 5.9) \times 10^{-12}$ |

**Table 7.7**: Characteristics of mobile ions in **device 6** with a short-circuit current density of 17.2 mA/cm$^2$, an open-circuit voltage of 1.02 V, a fill factor of 70%, and a power conversion efficiency of 12.1%. The diffusion coefficient is calculated for 300 K.

| | A1 |
|---|---|
| Migrating ion species | $I^-$ |
| Charge | negative |
| Concentration (cm$^{-3}$) | $(6.9 \pm 0.8) \times 10^{14}$ |
| Phase structure | tetragonal |
| Activation energy (eV) | $0.32 \pm 0.05$ |
| Diffusion coeff. (cm$^2$ s$^{-1}$) | $(1.2 \pm 5.7) \times 10^{-9}$ |

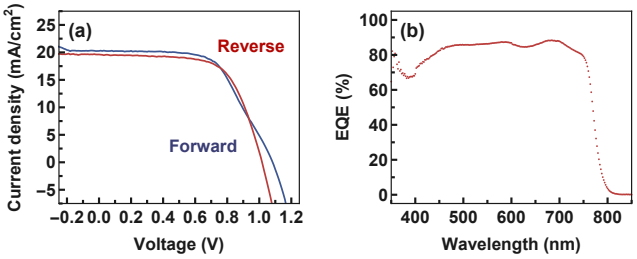


**Figure 7.14**: **(a)** Current-voltage characteristic curve and **(b)** external quantum efficiency (EQE) spectrum of an inverted perovskite solar cell fabricated in Konstanz, made in the same way as the devices 4 to 6, with a short-circuit current density of 19.9 mA/cm$^2$, an open-circuit voltage of 1.04 V, a fill factor of 63%, and a power conversion efficiency of 13.0%. The integrated current density of the EQE spectrum with the AM1.5G solar spectrum is 21.1 mA/cm$^2$, very close to the value obtained from the current-voltage measurements.

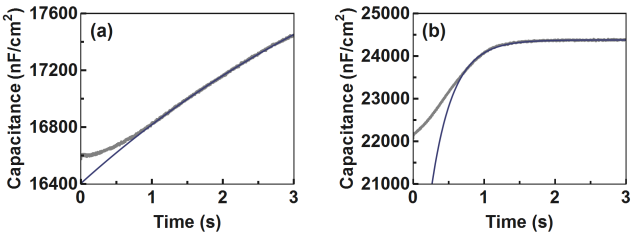


**Figure 7.15**: Ion-drift-induced capacitance transient measured at **(a)** 320 and at **(b)** 340 K in addition to an initial capacitance decrease is attributed to the redistribution of ions inside the depletion layer [216]. Grey points are experimentally measured data and blue lines are single exponential fits. The capacitance is calculated assuming a capacitor in parallel with a resistor.

# 8

# Perovskite solar cells with potassium passivation

**Abstract**

Record-efficiency perovskite solar cells are made from a mixture of halides including bromide and iodine. However, photo-induced ion migration in these mixed-halide perovskites leads to an undesirable phase separation into a bromide-rich and an iodide-rich domain. Recently it has been shown that the introduction of potassium into triple-cation mixed-halide perovskites reduces this ion segregation, which has been attributed to the mitigation of ion migration. Using transient ion drift, we study ion migration in these triple-cation mixed-halide perovskites and compare them to the prototypical halide perovskite, $MAPbI_3$. We find that activation energy and concentration of mobile halide ions are similar in triple-cation mixed-halide and $MAPbI_3$ perovskites, but that the diffusion coefficient is one to two orders of magnitude lower in the triple-cation mixed-halide perovskites. We furthermore find that the activation energy of mobile halide ions in these triple-cation mixed-halide perovskites is not influenced by potassium passivation, but that the concentration decreases by one order of magnitude. The suppression of ion migration, presumably mobile bromides, explains the reduced photo-induced phase separation in mixed-cation mixed-halide perovskites with potassium passivation.

## 8.1 Introduction

Metal halide are a class of materials sharing the same crystal structure $ABX_3$. In high-efficiency perovskite solar cells, A typically represents a mixture of methylammonium ($MA^+$), formamidinium ($FA^+$), and caesium ($Cs^+$), B represents lead ($Pb^{2+}$), and X is a mixture of iodide ($I^-$) and bromide ($Br^-$), depending on the desired band gap [70, 281].

Due to ion migration in perovskites, they are mixed ionic-electronic conductors [34, 35]. Both cations and anions were shown to migrate in perovskites [36–40, 215, 269], however, the migration of halide ions is most detrimental regarding device stability as they can migrate to the electrodes degrading the device [266, 267]. In mixed-halide perovskites containing both bromide and iodine, the migration of mobile halides furthermore results in photo-induced ion segregation into a bromide-rich and iodine-rich domain [153–155]. This segregation is undesirable as it locally changes the band gap of the perovskite and thus its optoelectronic properties. Recently, it was shown that introducing potassium ($K^+$) into mixed-cation mixed-halide perovskites inhibits this phase segregation which was attributed to the mitigation of ion migration [282, 283]. However, the reason and mechanism of this suppression is not understood.

We quantify the migration of mobile ions in mixed-cation mixed-halide perovskite solar cells using capacitance transient measurements. To exclude interfacial effects, we test different device architectures. We find that activation energy and concentration of mobile halides are comparable across different device architectures, but that the diffusion coefficient differs by one order of magnitude presumably because the growth of the perovskite is influenced by the extraction layers. The activation energy and concentration of mobile halides in mixed-cation mixed-halide perovskites are similar to those typically found in $MAPbI_3$, but the diffusion coefficient is one to two orders of magnitude lower. We furthermore find that the addition of potassium into the perovskite significantly decreases the concentration of mobile ions, explaining the inhabitation of the ion segregation in mixed-halide perovskite solar cells containing potassium.

## 8.2 Ion migration in mixed-halide perovskites

To study ion migration in mixed-cation mixed-halide perovskite solar cells, we fabricate solar cells in an inverted (FTO/PTAA/$Cs_{0.05}FA_{0.79}MA_{0.16}Pb(I_{0.84}Br_{0.16})_3$/$C_{60}$/BCP/Au) and a regular (FTO/$TiO_2$/$Cs_{0.05}FA_{0.79}MA_{0.16}Pb(I_{0.84}Br_{0.16})_3$/spiro-MeOTAD/Au) perovskite solar cell structure (see Figure 8.1a and b for an illustration of the device structures). Both solar cells were prepared from the same perovskite solution

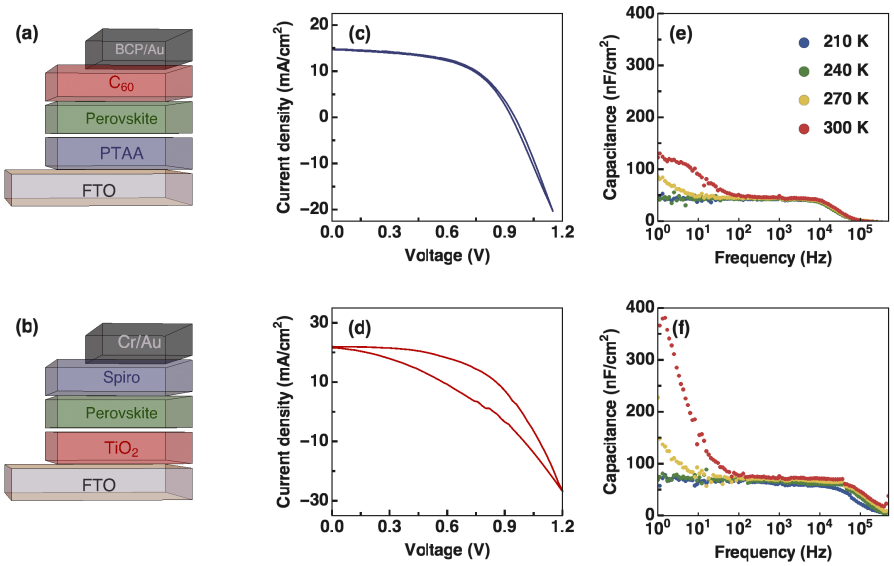


**Figure 8.1**: Schematic representation of **(a)** the inverted and **(b)** the regular device structure. Current-voltage measurements at 1 sun of the **(c)** inverted and **(d)** the regular solar cell structure measured at room temperature and frequency-dependent capacitance measurements of **(e)** the inverted and **(f)** the regular solar cell structure measured at different temperatures at short circuit in the dark. The capacitance corresponds to the real part of the complex capacitance.

at identical fabrication conditions. Figure 8.1c and Figure 8.1d shows the measured current-voltage characteristics at 1 sun of the inverted and the regular perovskite solar cell structure. In contrast to the inverted structure, the regular structure features a large difference in current-voltage characteristics when measured in forward and reverse scanning direction. This current-voltage hysteresis has often been attributed to the migration of mobile ions within the perovskites [284, 285].

We characterise the ion migration using transient ion drift, a capacitance-based technique [216, 235]. To investigate the difference between the capacitance response of the inverted and the regular device architecture, we measure the frequency-dependent capacitance at different temperatures at short circuit in the dark (Figure 8.1e and Figure 8.1f). For the inverted structure (Figure 8.1e) we observe an increase in capacitance at low frequencies due to mobile ions accumulating at the contact interfaces forming a diffuse ionic double layer [214, 217, 224]. Decreasing the temperature decreases the capacitance at low frequencies as mobile ions can

no longer migrate. The decrease in capacitance at high frequencies is due to series resistance of the contact layers. At frequencies between 100 Hz and 10 kHz the capacitance corresponds to the geometrical capacitance of the device plus a possible additional dielectric contribution of the contact layers [286].

Similarly, the frequency-dependent capacitance response of the regular structure (Figure 8.1f) shows a temperature-dependent capacitance increase at low frequencies. However, the capacitance increase is much higher for the regular structure than for the inverted one. Consequently, this additional capacitance arises due to the presence of the selective contacts ($TiO_2$ and/or spiro-MeOTAD) rather than the perovskite layer itself [232]. The large capacitance at low frequency in the regular structure hints towards the formation of a Helmholtz layer at the contact interfaces, i.e. a thin layer of ions adsorbed at the contact interfaces, forming an interface dipole in addition to the diffuse ionic double layer [217]. Using Kelvin probe measurements, such an interface dipole has recently been observed at the interface between $SnO_2$ and $MAPbI_3$ [50]. The capacitance between 100 Hz and 10 kHz for the regular structure is also higher than for the inverted one, indicating additional dielectric contributions in the regular device structure from $TiO_2$ and/or spiro-MeOTAD.

To quantify ion migration within the bulk of the perovskite we measure the transient of the capacitance at short circuit after applying a voltage bias (see Section 6.5 for details) [216, 235]. Applying a forward bias to the perovskite device decreases the depletion-layer width (Equation 6.11). Mobile ions diffuse from the interfaces to the previously depleted region. After removing the bias, the depletion-layer width increases. Mobile ions within the depleted region drift towards the interface changing the capacitance of the device as

$$C\left(t\right) = C\left(\infty\right) \pm C\left(\infty\right) \frac{N_{Ion}}{2N} \exp\left(-\frac{t}{\tau}\right) \tag{8.1}$$

where $C\left(\infty\right)$ is the steady-state capacitance, $N_{Ion}$ the concentration of mobile ions, and $\tau$ a time constant given by

$$\tau = \frac{k_B T \varepsilon_0 \varepsilon}{q^2 D N} \tag{8.2}$$

where $k_B$ is Boltzmann's constant, $T$ the temperature, $\varepsilon_0$ the vacuum permittivity, $\varepsilon$ the permittivity of the perovskite layer, $N$ the doping density, and $q$ the elementary charge. We assume a static dielectric constant of 20 and a doping density of 1 x $10^{17}$ $cm^{-3}$, often observed for these perovskite solar cells [237]. The diffusion coefficient is given by

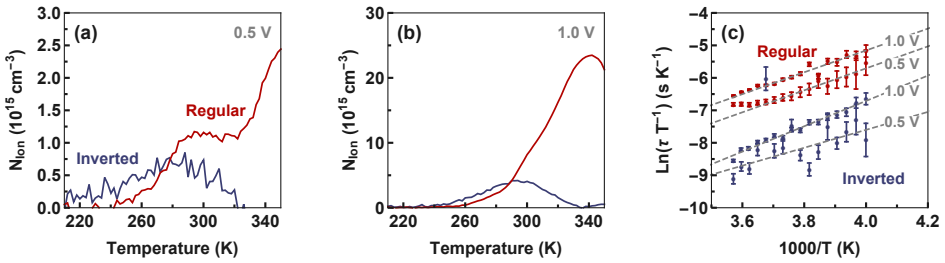


**Figure 8.2**: Measured mobile halide concentration in the inverted and in the regular solar cell structure after applying a bias of **(a)** 0.5 and **(b)** 1.0 V for 2 seconds at short circuit. At temperatures above 300 K, an additional capacitance contribution due to dielectric contributions of the contact layers is visible for the regular solar cell structure. **(c)** Arrhenius plot revealing the activation energy and the diffusion coefficient of mobile halides.

$$D = \frac{\nu_a d^2}{6} \exp\left(-\frac{E_A}{k_B T}\right) \tag{8.3}$$

where $E_A$ is the activation energy, $\nu_a$ the attempt frequency of an ionic jump, and $d$ the jump distance.[33]

We measure the capacitance transient of both the regular and inverted device for different temperatures for a bias voltage of 0.5 and 1.0 V (see Section 8.5.1). Using Equation 8.1 we can extract the density of ions mobile at each temperature. At low temperatures the ionic movement is frozen out, while at high temperatures the capacitance decay is too fast for us to observe. We hence see a peak in concentration which corresponds to the concentration of mobile ions of a species with migration on a characteristic timescale (see below).

We find a negative capacitance change, which corresponds to the migration of an anion under the assumption of a p-type perovskite [216]. We hence assume that the measured capacitance transient is due to the migration of mobile halides. Figure 8.2a shows the concentration of mobile ions in the inverted and the regular structure measured after applying a moderate bias of 0.5 V. In the inverted structure we observe one peak due to migration of halides (see Section 8.5.1 for details). The maximum height of the peak corresponds to the concentration of mobile ions within the probed perovskite region. Since the bias we used only partly collapses the depletion region, higher voltages are needed to obtain the maximum concentration of mobile ions within the perovskite bulk. In the inverted structure, we observe

**Table 8.1**: Summary of results obtained by transient ion-drift measurements. The values are based on two measurements for each filling voltage. The diffusion coefficient is calculated for 300 K. See Section 8.5.1 for individual measurements.

| | Activation energy (eV) | Diffusion coefficient ($cm^2/s$) | Concentration ($cm^{-3}$) |
|---|---|---|---|
| Inverted | $0.29 \pm 0.07$ | $(1.2 \pm 7.1)\ 10^{-10}$ | $5 \times 10^{15}$ |
| Regular | $0.29 \pm 0.04$ | $(2.2 \pm 6.7)\ 10^{-11}$ | $4 \times 10^{15}$ |

a clear plateau with a mobile ion density of $5 \times 10^{15}$ $cm^{-3}$. In the regular structure, we find an additional contribution arising at temperatures above $\sim$ 280 K which is absent in the inverted structure. This additional capacitance contribution is especially prominent when measuring the capacitance transient after applying a higher bias of 1.0 V (Figure 8.2b). We suspect that this additional capacitance contribution is due to the formation of an interface dipole at the perovskite/$TiO_2$ interface, as observed in impedance spectroscopy measurements (Figure 8.1f). Note that the migration of lithium from spiro-MeOTAD into the perovskite layer might also be the reason for this change in capacitance.

By fitting the capacitance decay at temperatures between 250 and 280 K, for which additional capacitance components due to the contact interfaces are small, the activation energy, the diffusion coefficient, and the concentration of mobile halide ions can be obtained by means of an Arrhenius plot (see Figure 8.2c). The obtained characteristics for mobile ions in the inverted and the regular device structure for a bias of 0.5 and 1.0 V are summarised in Table 8.1.

We find that the activation energy and concentration of mobile halides are comparable for both device architectures, and are furthermore very similar to previous results obtained for the migration of halides in $MAPbI_3$ (see Chapter 7). The diffusion coefficient in the inverted structure is almost one order of magnitude higher than in the regular structure. This difference might be due to a different morphology or a different doping density of the perovskite films as the perovskite precursor solutions were spin-coated on different transport layers. The diffusion coefficient in the regular device structure is closer to the diffusion coefficient of $10^{-12}$ $cm^2/s$ calculated from observed current-voltage hysteresis [284, 285]. The higher diffusion coefficient of mobile halides in the inverted solar cell structure would hence explain the difference in current-voltage hysteresis. However, we cannot exclude that the difference in the current-voltage characteristics may also originate from the interface polarisation in the regular solar cell structure [232].

In $MAPbI_3$ the diffusion coefficient of mobile halides is in the order of $10^9$ $cm^2/s$,

too fast to explain observed current-voltage characteristics [38, 215]. However, $MA^+$ ions have a diffusion coefficient in the order of $10^{-12}$ $cm^2/s$ in $MAPbI_3$ [37, 215]. In mixed-cation mixed-halide perovskites, we find no evidence of mobile cations, suggesting that cation migration is impeded in these perovskites. However, halide ions have a much lower diffusion coefficient compared to $MAPbI_3$. We speculate that the difference in diffusion coefficient is due to the migration of $Br^-$ in mixed-halide perovskites rather than the diffusion of $I^-$, as $Br^-$ has a lower diffusion coefficient in the order of $10^{-11}$ $cm^2/s$ in $MAPbBr_3$ single crystals [239]. Consequently, we suspect that in $MAPbI_3$ the current-voltage hysteresis is due to the migration of mobile cations, whereas in mixed-cation mixed-halide perovskites the hysteresis is due to the migration of mobile halides.

## 8.3 Effect of potassium passivation

Next we investigate the effect of potassium passivation on mobile halides in mixed-cation mixed-halide perovskite solar cells with the configuration ITO/$SnO_2$/perovskite/spiro-MeOTAD/Au. This device structure is very similar to the regular structure above and allows for the comparison of the doped and undoped perovskites. Potassium content of up to 10% $K^+$ ions out of all the monovalent cations in the precursor solution have shown to be beneficial for the photoluminescence efficiency, photoconductivity, and the phase stability [282]. Figure 8.3 shows frequency-dependent capacitance measurements with 0%, 10%, and 20% KI, measured at different temperatures at short circuit in the dark. Similar to frequency-dependent capacitance shown in Figure 8.1f, we observe an increase in the capacitance at low frequency due to the migration of mobile ions in vicinity to the contact interfaces. When adding 10% KI into the perovskite precursor solution, the inflection point at which the increase in capacitance begins to rise shifts to higher frequencies, before decreasing again at 20% KI. This indicates either a change in diffusion length $l$ or diffusion coefficient $D$ of mobile ions since the time constant of the diffusion of mobile ions is given by

$$\frac{1}{\tau} = 2\pi f_0 = \frac{D}{l^2} \tag{8.4}$$

where $f_0$ corresponds to the frequency of ion migration [230]. In addition, we observe a distinctive, temperature-dependent decrease in capacitance with decreasing temperature at frequencies above 1 kHz. This effect could relate to a change in dielectric contribution of the contact layer $SnO_2$. At a concentration of 20% KI the dielectric contribution from the contact layers changes significantly. At high potassium concentration, a thin potassium layer was found to form at the interface

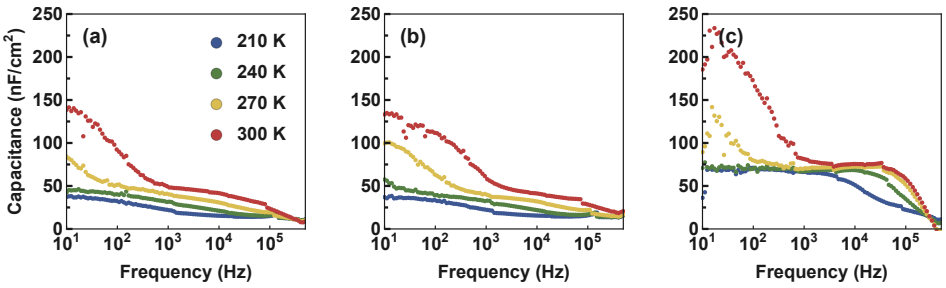


**Figure 8.3**: Frequency-dependent capacitance measurements of perovskite solar cells with **(a)** 0%, **(b)** 10%, and **(c)** 20% KI measured at different temperatures at short circuit in the dark. The solar cell structure consist of ITO/$SnO_2$/$Cs_{0.05}FA_{0.79}MA_{0.16}Pb(I_{0.83}Br_{0.17})_3$ + KI/spiro-MeOTAD/Au. The capacitance corresponds to the real part of the complex capacitance.

and grain boundaries [282], possible changing the dielectric contribution from the contact layers. We note that although the overall capacitance is strongly interface-dependent, the capacitance transients from mobile ion migration should be interface independent, as shown above.

To investigate if the change in inflection point is due to a change in diffusion coefficient, we perform transient ion-drift measurements using a small voltage bias of 0.5 V to avoid interfacial effects (see Section 8.5.2 for details). The results of the transient ion-drift measurements are summarised in Figure 8.4. Similar to mixed-cation mixed-halide perovskites in the inverted and in the regular solar cell structure, we observe an activation energy of (0.28 $\pm$ 0.01) eV, a diffusion coefficient of (2.5 $\pm$ 0.9) $10^{-10}$ $cm^2/s$, and a concentration in the order of $10^{15}$ $cm^{-3}$ in the case without KI. Upon adding KI into the perovskite precursor solution, we find that the activation energy of mobile halides remains constant, indicating that the ion migration mechanism is not affected by potassium passivation. The diffusion coefficient increases when adding 10% KI into the perovskite precursor solution, and slightly decreases again at higher concentrations, in agreement with frequency-dependent capacitance measurements (Figure 8.3). A similar behaviour has recently been observed in mixed-cation mixed-halide perovskites with KI using time-resolved photoluminescence imaging [287]. We furthermore find a strong reduction in the concentration of mobile halides by one order of magnitude when adding KI into the perovskite precursor solution. The reduction of mobile halides is in agreement with recent findings that show that potassium is not incorporated into the perovskite bulk but selectively binds to bromide, thereby removing excess bromide from the per-

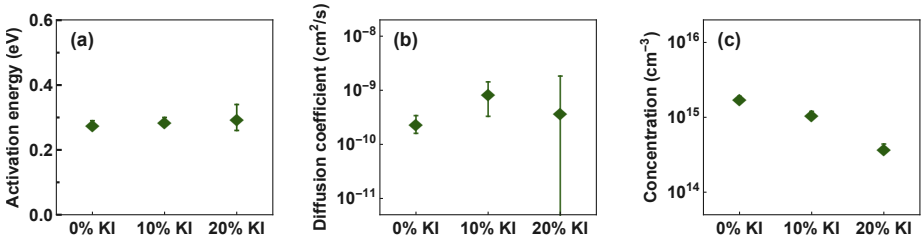


**Figure 8.4:** Characteristics of mobile halide ions in mixed-cation mixed-halide perovskite solar cells without and with 10% and 20% potassium passivation. **(a)** Activation energy, **(c)** diffusion coefficient, and **(c)** concentration obtained by transient ion-drift measurements.

ovskite bulk [283, 288]. This further supports our assignment of the mobile halide species to bromides. Thus, we suspect that the potassium addition reduces the density of bromide interstitials, hence reducing the mobile ion concentration. We assume that potassium passivation reduces the halide vacancies, which increases the jump distance $d$ of mobile ions and thus increasing the diffusion coefficient. The subsequent reduction of diffusion coefficient at higher KI concentrations might be related to the formation of potassium rich domains within the perovskite, or due to the decreasing grain sizes of the perovskite at high KI concentrations.

Using the diffusion coefficients from transient ion-drift measurements, we can estimate the diffusion length of mobile ions from impedance spectroscopy measurements (see Section 8.5.2 for details). We find that the diffusion length decreases slightly from 7 to 5 nm when 10% KI is added into the perovskite precursor solution. At concentrations of 20% KI, it increases again to 7 nm. Assuming that the diffusion of mobile ions is limited to the ionic double layer near the interfaces, this indicates a change in the width of the ionic double layer. We suspect that this ionic double layer leads to the trapping of charge carriers during operation, which causes device degradation [289, 290]. A decrease in ionic double layer might thus be advantageous for the stability of the device.

## 8.4 Conclusion

In conclusion, we quantified ion migration in mixed-cation mixed-halide perovskites with different device architectures. We find that bromides migrate, and that the activation energy and concentration between different device architectures are very similar, while the diffusion coefficient varies by one order of magnitude between

the different architectures. We suspect that this difference in diffusion coefficient is due to the different film growth of the perovskite layer on different substrates. We find no evidence of mobile cations, suggesting that cation migration is impeded in mixed-cation mixed-halide perovskites. We furthermore find that the activation energy of mobile halides in triple-cation mixed-halide perovskites is not influenced by potassium passivation, but that the concentration of mobile halides decreases by one order of magnitude. The reduction of ion migration in potassium-passivated perovskite solar cells explains the suppression of photo-induced ion segregation. This quantification of mobile ions in triple-cation mixed-halide perovskites will lead to a better understanding of ion migration and the influence of passivating agents on that migration, crucial for the fabrication of stable perovskite solar cells.

## 8.5 Supporting information

**Device fabrication.** Devices in the inverted (FTO/PTAA/perovskite/BCP/Au) solar cell structure were fabricated as described hereafter: Laser patterned fluorine tin oxide (FTO) substrates were cleaned by ultra-sonication for 15 minutes subsequently in detergent in deionized water, deionized water, acetone, and isopropanol, followed by oxygen plasma etching for 15 minutes at 100 W. PTAA was spun at 6000 rpm for 30 seconds using 3 mg/mL in toluene. The film was then annealed for 10 minutes at 100 °C. After the films had cooled down, the perovskite precursor solution was spun at 4000 rpm for 30 seconds with 2000 rpm/s acceleration and deceleration. After 12 seconds, ethyl acetate (anti-solvent) was dripped onto the substrate. $Cs_{0.05}MA_{0.16}FA_{0.79}Pb(I_{0.84}Br_{0.16})_3$ was prepared by dissolving 1.5 M of $PbI_2$ and $PbBr_2$ in DMF/DMSO (4:1 v/v). The solutions were annealed at 180 °C for 10 minutes. After the solution had cooled down to room temperature, MABr and FAI were added to $PbBr_2$ and $PbI_2$ to reach a concentration of 1.24 M each. The solutions were mixed to achieve $(FAPbI_3)_{83}(MAPbBr_3)_{17}$. Finally, 5 vol% 1.5 M CsI was added to the perovskite solution. The perovskite films were annealed at 100 °C for 30 minutes. 30 nm of $C_{60}$, 8 nm of BCP, and 100 Au were sequentially deposited on top of the perovskite layer by thermal sublimation/evaporation at pressures below $2 \times 10^{-6}$ mbar.

Devices in the regular (FTO/$TiO_2$/perovskite/spiro-MeOTAD/Au) solar cell structure were fabricated as described hereafter: FTO substrates were cleaned in the same way as described above. $TiO_2$ compact layers were deposited onto the FTO by spray pyrolysis at 450 °C from a precursor solution of titanium diisopropoxide bis(acetylacetonate) in anhydrous ethanol and acetyl acetone. The substrates were annealed at 450 °C for 5 minutes before cooling down. The substrates were then transferred into the glovebox to deposit the perovskite layer. The

perovskite layer was prepared in the same way as described above. After the perovskite has cooled down, spiro-OMeTAD was spun at 4000 rpm for 20 seconds with an acceleration of 2000 rpm/s. Spiro-OMeTAD was doped with with Li-TFSI, tris(2-(1H-pyrazol-1-yl)-4-tert-butylpyridine)cobalt(III) tri[hexafluorophosphate] (FK209), and 4-tert-butylpyridine (TBP) at molar ratios of 0.5, 0.03, and 3.3 respectively. Finally, 100 nm Au was evaporated at pressures below 2 x $10^{-6}$ mbar (0.3 Å/s).

Devices in the regular solar cell structure (ITO/$SnO_2$/perovskite/spiro-MeOTAD/Au) with potassium passivation were fabricated as described hereafter: Indium tin oxide (ITO) substrates were sonicated in detergent (Decon 90) in deionized water, deionized water, and isopropanol, followed by oxygen plasma etching for 5 minute. The $SnO_2$ precursor (15% in $H_2O$ colloidal dispersion) diluted in deionized water was spin-coated on substrates at 3000 rpm for 30 seconds. The substrates were annealed at 180 °C for 30 minutes. The substrates were immediately transferred into a nitrogen-filled glovebox after cooling to room temperature before perovskite deposition. $Cs_{0.05}MA_{0.16}FA_{0.79}Pb(I_{0.84}Br_{0.16})_3$ was prepared by dissolving 1.1 M $PbI_2$, 0.22 M $PbBr_2$, 1 M FAI and 0.2 M MABr in a vial containing 1 mL anhydrous DMF:DMSO (4:1 v/v) mixed solution. 5 vol% 1.5 M CsI stock solution was added to the perovskite solution, and then the vial was stirred at 100 °C for 30 minutes. Perovskite solution was spin-coated on substrates using a two-step program with 1000 rpm for 10 seconds and then 6000 rpm for 35 seconds. Chlorobenzene was dropped on top of the substrates 10 seconds before the program ended. The perovskite films were annealed at 100 °C for 40 minutes. Spiro-MeOTAD as a hole transport layer (HTL) was prepared by dissolving 72 mg spiro-MeOTAD in 1 mL chlorobenzene, doped with 28.8 µL 4-tert-Butylpyridine (tBP), 17.5 µL Li-TFSI (520 mg/mL in acetonitrile) and 28.8 µL FK 209 Co(III) TFSI (300 mg/ml in acetonitrile). When the perovskite films had cooled to room temperature, spiro solution was spin-coated on top of perovskite films at 4000 rpm for 20 seconds. Finally, 80 nm gold was evaporated on top of the samples at 5 x $10^{-6}$ mbar vacuum level with evaporation rate of 0.3 Å/s.

**Device characterisation.** Current-voltage characteristics were measured under 1 sun illumination from a solar simulator (Oriel 92250A) using a Keithley 2636A source-measure unit. The scan rate was about 100 mV/second. During the measurement, the samples were masked and placed in nitrogen in an air-tight sample holder.

**Capacitance measurements.** To perform capacitance measurements, the samples were loaded into a Janis VPF-100 liquid nitrogen cryostat inside a nitrogen-filled glovebox. Capacitance measurements were performed at pressures below 2 x $10^{-6}$ mbar in the dark. The capacitance transient measurements were performed between 210 and 350 K in steps of 2 K. Before each capacitance transient measurement, the temperature was maintained for at least 1 minute with an accuracy of

**Table 8.2**: Summary of results obtained by transient ion-drift measurements for mixed-cation mixed-halide perovskites in the inverted and the regular solar cell structure. The diffusion coefficient is calculated for 300 K.

| | Filling voltage (V) | Activation energy (eV) | Diffusion coefficient ($cm^2/s$) | Concentration ($cm^{-3}$) |
|---|---|---|---|---|
| Inverted | 0.5 | $0.24 \pm 0.07$ | $(1.2 \pm 7.0)\ 10^{-10}$ | $6 \times 10^{14}$ |
| Inverted | 1.0 | $0.34 \pm 0.02$ | $(1.1 \pm 1.4)\ 10^{-10}$ | $4 \times 10^{15}$ |
| Regular | 0.5 | $0.29 \pm 0.02$ | $(2.7 \pm 5.0)\ 10^{-11}$ | $1 \times 10^{15}$ |
| Regular | 1.0 | $0.29 \pm 0.03$ | $(1.6 \pm 4.5)\ 10^{-11}$ | $5 \times 10^{15}$ |

0.2 K. At each temperature, capacitance transients were averaged over 20 scans. Frequency-dependent capacitance measurements were performed between 210 and 300 K in steps of 30 K. Before each impedance spectroscopy measurement, the temperature was maintained for at least 15 minutes with an accuracy of 0.2 K.

### 8.5.1 Regular versus inverted structure

Figure 8.5 shows the measured capacitance transients of the inverted and the regular solar cell structure between 250 and 280 K after applying a bias of 0.5 and 1.0 V. The capacitance change is negative and hence describes the migration of an anion under the assumption of a p-type perovskite layer. The transients are measured at 2 and 10 kHz for the inverted and the regular structure, respectively, where the series resistance of the device is negligible. The values obtained for activation energy, diffusion coefficient, and concentration are summarised in Table 8.2. The height of the transient is related to the concentration of mobile ions (see Figure 8.2a and Figure 8.2b in the main text). The Arrhenius plot is shown in Figure 8.2c in the main text. Note that in the regular device structure we limit the linear fit to temperatures below 270 K to ensure that additional capacitance components from to the interfaces do not affect the analysis. To calculate the diffusion coefficient, we assume a dielectric constant of 20 and a doping density of $1 \times 10^{17}$ $cm^{-3}$.

Figure 8.6 show the measured capacitance transients of the inverted and the regular solar cell structure between 310 and 330 K after a bias of 1.0 V. In this temperature range, we see an additional capacitance component in the regular device structure with $TiO_2$ and spiro-MeOTAD as contact layers which is absent in the inverted one. We suspect that this additional capacitance feature is linked to the formation of an interface dipole at the $TiO_2$/perovskite interface with an activation energy of 0.14 eV (Figure 8.6c).

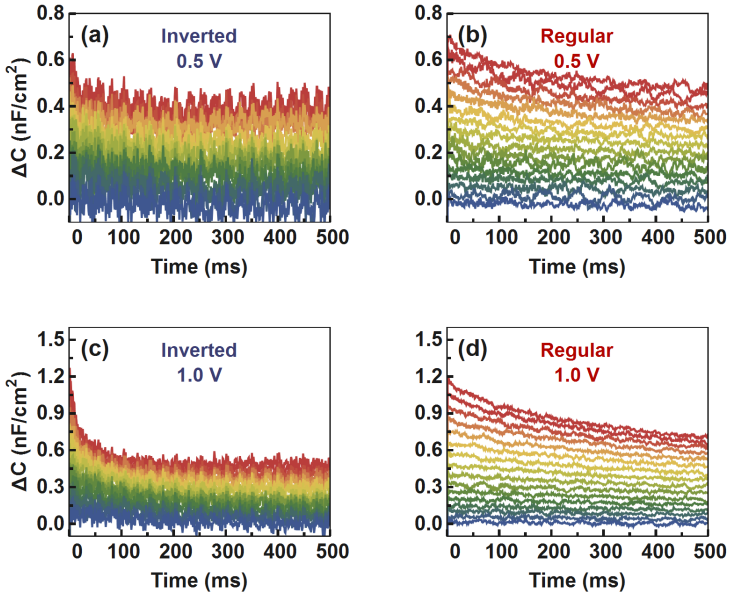


**Figure 8.5**: Capacitance transients of mixed-cation mixed-halide perovskites in the inverted solar cell structure measured at 2 kHz after applying a bias of **(a)** 0.5 and **(c)** 1.0 V and in the regular structure measured at 10 kHz after applying a bias of **(b)** 0.5 and **(d)** 1.0 V. Measurements are performed in the dark at short circuit. The capacitance is calculated assuming a capacitor in parallel with a resistor.

### 8.5.2 Potassium passivation

Figure 8.7 show the capacitance transients of the mixed-cation mixed-halide perovskite with 0, 10, and 20% KI mixed into the perovskite precursor solution measured between 220 and 260 K after applying a bias of 0.5 V. The values obtained for activation energy, diffusion coefficient, and concentration are summarised in Table 8.3. The height of the transient is related to the concentration of mobile ions (see Figure 8.8a). The Arrhenius plot is shown in Figure 8.8b. To calculate the diffusion coefficient, we assume a dielectric constant of 20 and a doping density of $1 \times 10^{17}$ $cm^{-3}$.

Figure 8.9 show the imaginary part of the complex capacitance of the mixed-cation mixed-halide perovskite solar cell with the structure FTO/$SnO_2$/perovskite/spiro-MeOTAD/Au measured at 300 K. The peak in the imaginary part corresponds to the diffusion of mobile ions (Equation 8.4). Knowing the diffusion coefficient $D$ from transient ion-drift measurements, we can calculate the diffusion length $l$. The

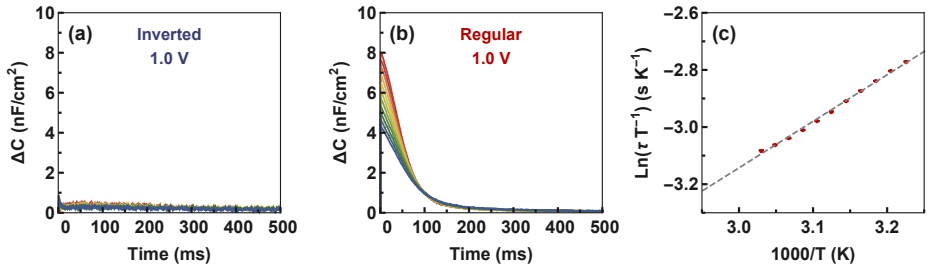


**Figure 8.6**: Capacitance transients of mixed-cation mixed-halide perovskites in **(a)** the inverted and **(b)** the regular solar cell structure between 310 and 330 K after applying a bias of 1.0 V measured at 2 kHz and 10 kHz, respectively. Measurements are performed in the dark at short circuit. **(c)** Arrhenius plot revealing the activation energy of the observed capacitance feature in the regular solar cell structure. The capacitance is calculated assuming a capacitor in parallel with a resistor.

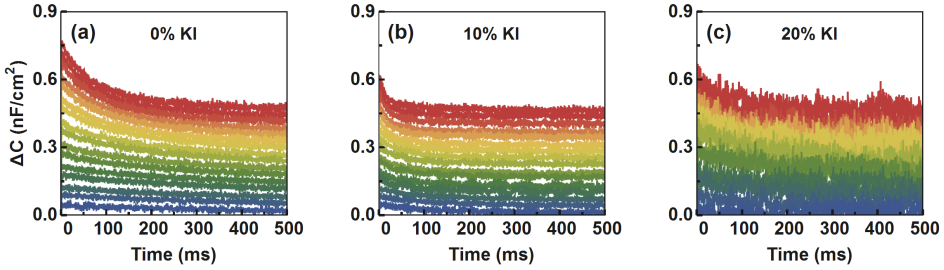


**Figure 8.7**: Capacitance transients of mixed-cation mixed-halide perovskites with **(a)** 0%, **(b)** 10%, and **(c)** 20% KI measured at 10 kHz after applying a bias of 0.5 V. Measurements are performed in the dark at short circuit. The capacitance is calculated assuming a capacitor in parallel with a resistor.

obtained diffusion lengths are shown as an inset in Figure 8.9.

**Table 8.3**: Summary of results obtained by transient ion-drift measurements for mixed-cation mixed-halide perovskites with potassium passivation. The diffusion coefficient is calculated for 300 K.

| | Filling voltage (V) | Activation energy (eV) | Diffusion coefficient ($cm^2/s$) | Concentration ($cm^{-3}$) |
|---|---|---|---|---|
| 0% KI | 0.5 | $0.28 \pm 0.01$ | $(2.5 \pm 0.9)\ 10^{-10}$ | $2 \times 10^{15}$ |
| 10% KI | 0.5 | $0.29 \pm 0.01$ | $(8.8 \pm 5.5)\ 10^{-10}$ | $1 \times 10^{15}$ |
| 20% KI | 0.5 | $0.30 \pm 0.04$ | $(3.9 \pm 14.4)\ 10^{-10}$ | $4 \times 10^{14}$ |

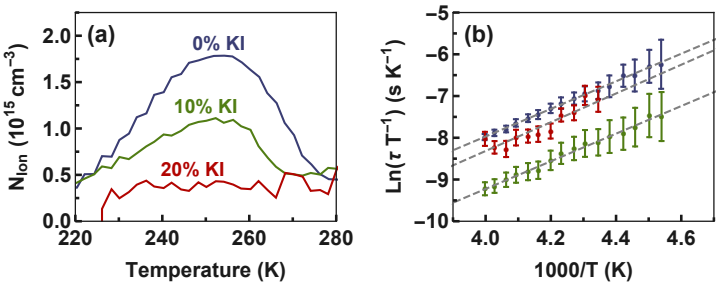


**Figure 8.8**: Capacitance transients of mixed-cation mixed-halide perovskites with **(a)** 0%, **(b)** 10%, and **(c)** 20% KI measured at 10 kHz after applying a bias of 0.5 V. Measurements are performed in the dark at short circuit.

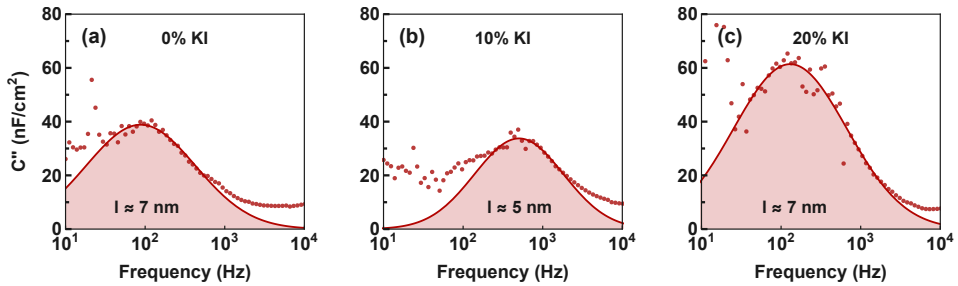


**Figure 8.9**: Imaginary part of the complex capacitance for mixed-cation mixed-halide perovskites with **(a)** 0, **(b)** 10, and **(c)** 20% KI measured at 300 K in the dark at short circuit.

# 9

# Perovskite light-emitting diodes with manganese substitution

**Abstract**

Metal halide perovskite light-emitting diodes have recently emerged as high-performance devices. However, they degrade rapidly. This degradation has been attributed to the migration of mobile ions within the perovskite. Manganese doping increases the stability of perovskite light-emitting diodes, but the effects of manganese doping on ion migration are not well understood. We use impedance spectroscopy and transient ion-drift measurements to show that manganese doping in perovskite-based devices enhances the activation energy and reduces the width of the ionic double layer and the diffusion coefficient of mobile ions. These changes in the behaviour of mobile ions help to understand the improved stability in perovskite light-emitting diodes upon manganese doping and lead to a better understanding of the influence of passivating agents on ion migration and thus on stability of the devices.

## 9.1 INTRODUCTION

Perovskites show great promise for light-emitting applications. Since the first report of a perovskite light-emitting diode (LED) in 2014 with an external quantum efficiency (EQE) of electroluminescence of 1% [291], the EQE has increased to >20% using quasi-2D/3D perovskite structures [292–295]. While perovskite LEDs show high efficiency, their progress has so far been hampered by fast device degradation [296]. Perovskites are mixed electronic-iconic conductors containing mobile ions, and these ions have been linked to the poor stability of perovskite LEDs [296, 297].

Lead halide perovskite have a crystal structure of $ABX_3$, where the A-site cation typically contains methylammonium, formamidinium, or caesium, with the best-performing devices containing a mixture of these cations [70, 298, 299]. The B-site cation represents lead and the X-site halide is typically a combination of chloride, bromide, or iodide, depending on the desired band gap [53].

Many strategies have been developed to increase the stability of perovskite-based optoelectronic devices, often focusing on A-site dopants such as azetidinium and guanidinium [300–303]. This increase in stability upon partial cation substitution was recently shown to be due to a suppression of ion transport [304].

In addition to A-site doping, B-site doping has also shown positive effects on both performance and the stability of perovskite-based optoelectronic devices [305–309]. Specifically, by introducing manganese ($Mn^{2+}$) into the perovskite, an increase in efficiency, brightness, and stability of perovskite LEDs was observed. Enhanced efficiency and brightness has been attributed to reduced nonradiative recombination and evidenced by improved photoluminescence quantum yiels after doping [225, 310]. However, the origin of the increase in operational stability is still unclear. Using first-principle calculations, Zou *et al.* found that doping $CsPbBr_3$ quantum dots with $Mn^{2+}$ increases the formation energy of a nanocrystal from its isolated atoms and thus significantly improves the thermal stability [305]. Presumably, this change also affects the behaviour of mobile ions, which is one of the main causes of the instability of perovskite LEDs [296]. The effect on $Mn^{2+}$ doping on ion migration, however, has not yet been investigated.

Here, to study the effect of $Mn^{2+}$ doping on mobile ions we employ impedance spectroscopy and transient ion-drift measurements on perovskite LEDs. We use $PEABr_{0.2}Cs_{0.4}MA_{0.6}PbBr_3$ quasi-bulk 2D/3D perovskites, both $Mn^{2+}$ doped and undoped, to fabricate the LEDs. The capacitance measurements follow the migration of ions after a voltage perturbation at different temperatures. We find that $Mn^{2+}$ doping increases the activation energy for ion migration and reduces the diffusion coefficient, enhancing the stability of perovskite LEDs. This quantification leads to

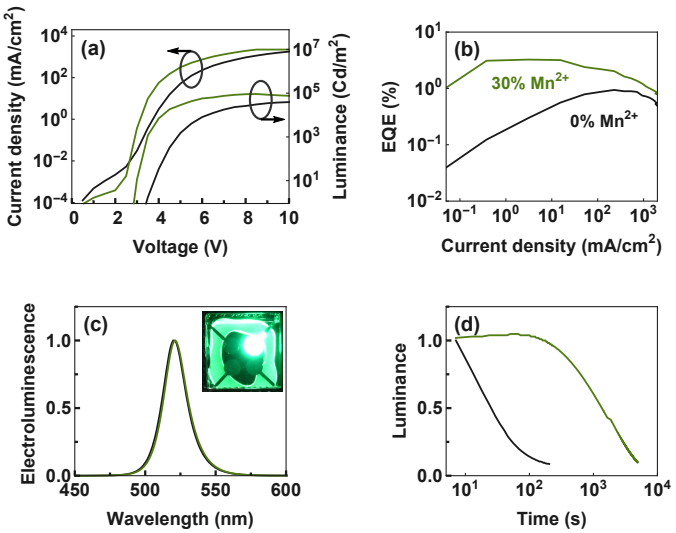


**Figure 9.1**: Characteristics of perovskite light-emitting diodes (LEDs). **(a)** Current density-voltage-luminance curves, **(b)** external quantum efficiency (EQE), **(c)** electroluminescence spectra showing peak at 520 nm, and **(d)** operational stability of LEDs operated at a current density of 3 mA/cm$^2$ for both doped and undoped perovskites. The inset in (c) shows an image of the LED.

a better understanding of the influence of passivation agents on ion migration in perovskite-based optoelectronic devices.

## 9.2 Device characteristics and stability improvement

The architecture of the LEDs used in this study consists of ITO/PEDOT/PFI/perovskite/TpBi/LiF/Al. Here, PFI is an ionomer that acts as a buffer layer and prevents any charge leakages out of the device. On top of this, an $\sim$ 80 nm thick perovskite layer is deposited by spin-coating the perovskite precursors. To make the doped perovskite layers, we replaced 30% $PbBr_2$ with $MnBr_2$ in the precursor solution. The detailed fabrication process can be found in Section 6.7.1.

After doping with $Mn^{2+}$, we observe a striking change in the device performance, similar to previous work [309]. From the current density-voltage-luminance curves, a significant reduction in the current leakage is observed (Figure 9.1a). The device brightness is increased from 26,000 to 89,800 Cd/m$^2$ after $Mn^{2+}$ doping. Further, control devices showed a maximum EQE of 0.9% which is increased to 3.3%

after doping (Figure 9.1b). Both the devices showed an emission peak at 520 nm as shown in Figure 9.1c. Most importantly, the operational stability increased significantly compared to the control devices. The initial luminance for the $Mn^{2+}$ doped device is 148 $Cd/m^2$ and it took 22 minutes to reach the 50% of initial value. The control device, however, showed lower luminance at t = 0 and decreased to 50% of the initial value in less than 1 minute. Both the devices were operated under constant current density of 3 $mA/cm^2$. This striking increase in operational stability after doping is not limited to green (bromide perovskites) LEDs, but also observed in sky blue (chloride bromide) and red perovskite LEDs.[21] To understand the impact $Mn^{2+}$ doping, we turned to impedance spectroscopy and transient ion-drift measurements.

## 9.3 Impedance spectroscopy

Impedance spectroscopy is a powerful and nondestructive electrical characterisation method to study optoelectronic devices [201, 214, 225, 311]. It is based on applying a small AC voltage with varying frequency ($f$) to the device and recording the current response. The measurement can then be used to obtain the frequency-dependent real (C′) and imaginary part (C″) of the complex capacitance of the device (see Section 6.4 for details). Figure 9.2a and Figure 9.2b shows the measured real and imaginary part of the complex capacitance of the perovskite LED at different temperatures. At low frequencies, an increase in real part of the capacitance is observed (Figure 9.2a) which is accompanied by a peak in the imaginary part of the capacitance that shifts from 26 to 3 Hz when decreasing temperature from 330 to 240K (Figure 9.2b). At high frequencies, the capacitance decreases due to the increase in series resistance of the contact layers. At an intermediate frequency, where the imaginary part of the complex capacitance is small, the capacitance is related to the geometric capacitance of the device (Equation 6.1).

The low-frequency peak in Figure 9.2b indicates a relaxation process with a time constant $\tau = 1/(2\pi f)$ [312]. To obtain the time constant of the relaxation process, we fit a Gaussian distribution to the low-frequency region. Assuming that the relaxation process is due to the diffusion of mobile ions within the Debye layer $l_D$, the time can be written as [229]

$$\tau = \frac{l_D^2}{D} \tag{9.1}$$

where $D$ is the diffusion coefficient given by

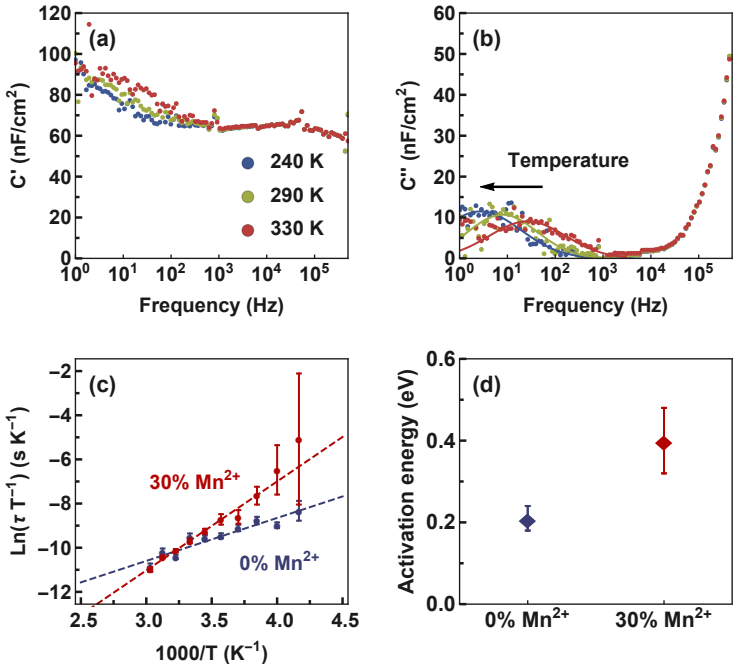


**Figure 9.2**: Impedance spectroscopy measurements. **(a)** Real (C′) and **(b)** imaginary part (C″) of the complex capacitance measured in the dark at 0 V with an AC voltage of 50 mV. **(c)** Arrhenius plot of the observed thermal emission rates as a function of temperature. The linear fit reveals the activation energy. **(d)** The effect of $Mn^{2+}$ doping on the activation energy measured by impedance spectroscopy. The values are based on the mean of three measurements each. See Section 9.6.2 for individual measurements.

$$D = D_0 \exp\left(-\frac{E_A}{k_B T}\right) \tag{9.2}$$

where $E_A$ is the activation energy and $D_0 = \frac{\nu_a d^2}{6} \exp\left(\Delta S / k_B\right)$ a pre-factor. See Equation 6.7 for the definition of the Debye length. $\nu_a$ is the attempt frequency of an ionic jump, $d$ the jump distance, $\Delta S$ the change in entropy during the jump. By plotting the time constant as a function of temperature $T$ in an Arrhenius plot, the activation energy can be determined via

$$\tau = \frac{\varepsilon_0 \varepsilon k_B T}{q^2 N D_0} \exp\left(\frac{E_A}{k_B T}\right) \tag{9.3}$$

where $\varepsilon_0$ is the vacuum permittivity, $\varepsilon$ the permittivity of the perovskite layer, $k_B$ Boltzmann's constant, $N$ the doping density, and $q$ the elementary charge. For the undoped perovskite LEDs we obtain an activation energy of 0.21 $\pm$ 0.03 eV. Upon doping with $Mn^{2+}$, we find an increase in the activation energy to 0.40 $\pm$ 0.08 eV (see Figure 9.2c). This increase is a first indication that the improved device stability may stem from suppressed ion migration.

We extract the activation energy from the low-frequency capacitance, which is commonly assigned to ion migration [214]. However, such an increase in capacitance at low frequencies can have many reasons. Most prevalent explanations include charge accumulation at the contact interfaces [232–234], diffusion of ions though the bulk perovskite [230, 231], diffusion of ions accumulated at the interfaces [218, 313], and electronic defect states [208, 209]. For this reason, additional measurements are needed to attribute the increase in activation energy to a change in ion migration.

The capacitance due to the accumulation of both charge carriers and mobile ions at the interfaces is highly dependent on the contact materials [234]. In addition to the LED structure, we therefore measure an inverted structure consisting of $NiO_X$/perovskite/$C_{60}$/BCP, which is often used for perovskite solar cells. In this structure the contacts have only a small influence on the impedance measurement, since a change in temperature mainly changes the low-frequency capacitance [215, 304]. For this inverted solar cells structure we find a similar increase in activation energy from 0.13 $\pm$ 0.01 to 0.28 $\pm$ 0.06 eV after $Mn^{2+}$ doping (see Section 9.6.2), suggesting that the increase in activation energy is not determined by the interfaces. Therefore, we tentatively assign the increase in activation energy upon $Mn^{2+}$ doping to bulk ion migration. We emphasise that the observed capacitance changes in frequency-dependent capacitance measurements can be due to both mobile ions and electronic defect states. To distinguish between these two, we measure the time-dependent capacitance.

## 9.4 Transient ion drift

To determine whether the increase in activation energy measured by impedance spectroscopy is due to electronic defect states or mobile ions, we use transient ion-drift measurements. This technique relies on measuring the transient capacitance after applying a bias. The voltage is chosen in such a way that the depletion region collapses within the perovskite layer (see Section 9.6.3). In the case of electronic defect states, the application of a bias would lead to the charge-carrier traps being filled [202]. After removing the bias, the release of charge carriers from defect states would result in a capacitance transient. On the other hand, in the case of mobile

ions, the application of a voltage bias would lead to a redistribution of mobile ions within the perovskite layer, as ions diffuse into the previously depleted region [216]. After removing the voltage bias, mobile ions would drift towards the interfaces due to the presence of the internal electric field within the device, resulting in a capacitance transient caused by a change in depletion-layer width [215]. The difference between electronic defect states and mobile ions is: for mobile ions, the capacitance rise due to the diffusion of mobile ions away from the interfaces is expected to be slower than the decay time caused by the drift of mobile ions towards the interfaces [235]. In contrast, for electronic defect states the capture rate of charge carriers is much higher than the emission rate, resulting in faster rise time compared to the decay time (see Section 6.7.4 for details on the difference between the rise and decay times of mobile ions and electronic defect states). With the inverted solar cell structure, we observe a ratio between rise and decay time characteristic for mobile ions (see Section 9.6.4). For the LED structures, the ratio between rise and decay time points towards a measurement of electronic defect states instead. We speculate that mobile ions are not visible in the LED structure due to the high voltage biases required to collapse the depletion region, which leads to a considerable charge injection and hence a large diffusion capacitance. In some cases, this can even result in decomposition of the perovskite into its precursors [261]. We therefore use the solar cell structure to quantify mobile ions using transient ion-drift measurements.

Under the assumption of a linear electric field across the depletion region, that thermal diffusion is negligible compared to ion drift, and that the total ion concentration is conserved, the capacitance transient can be described with [264]

$$C\left(t\right) = C\left(\infty\right) \pm C\left(\infty\right) \frac{N_{Ion}}{2N} \exp\left(-\frac{t}{\tau}\right) \tag{9.4}$$

where $C\left(\infty\right)$ is the steady-state capacitance, $N_{Ion}$ the density of mobile ions and $\tau$ a time constant given by (see Section 6.5)

$$\tau = \frac{k_B T \varepsilon_0 \varepsilon}{q^2 D N}. \tag{9.5}$$

Perovskite permittivity and the doping density are obtained by impedance spectroscopy measurements and voltage dependent capacitance measurements respectively (see Section 9.6.2 and Section 9.6.3).

Figure 9.3a and Figure 9.3b show capacitance transients following a voltage bias of 1.25 V applied for 2 seconds on undoped and the $Mn^{2+}$-doped perovskite, and measured with a 20 mV AC perturbation at 10 kHz. The capacitance change is negative and hence describes the migration of an anion under the assumption of a

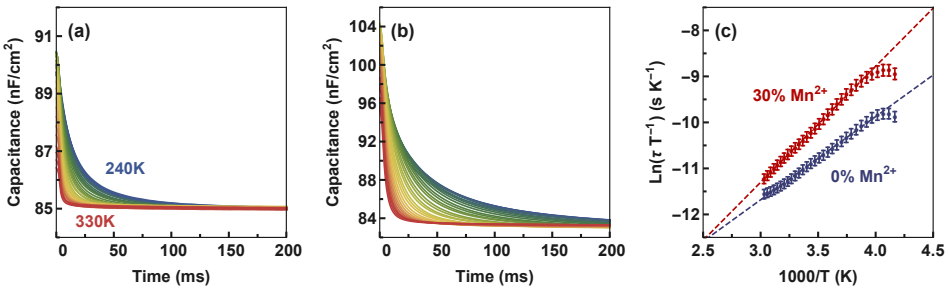


**Figure 9.3**: Transient ion-drift measurements between 240 and 330 K in steps of 3 K measured at 0 V for **(a)** the undoped and **(b)** $Mn^{2+}$-doped perovskite. **(c)** Arrhenius plot of the observed thermal emission rates as a function of temperature. The linear fit reveals the activation energy and the diffusion coefficient for ion migration. The capacitance is calculated assuming a capacitor in parallel with a resistor.

p-type perovskite layer, as indicated in the Mott-Schottky plot (see Section 9.6.3). We therefore assign the measured signal to the migration of bromide ions. To quantify ion migration, we fit the capacitance transient using exponential decay functions. By means of an Arrhenius plot both the activation energy and the diffusion coefficient can be obtained (see Figure 9.3c). The obtained activation energies and diffusion coefficients for ion migration based on the mean value of three measurements each are shown in Figure 9.4a and Figure 9.4b and summarised Table 9.1.

As in impedance spectroscopy, we find that $Mn^{2+}$ doping increases the activation energy from $0.14 \pm 0.01$ to $0.30 \pm 0.07$ eV, which we can now assign to migration of bromide within the perovskite bulk. The activation energy of 0.14 eV for the migration of bromide in undoped $PEABr_{0.2}Cs_{0.4}MA_{0.6}PbBr_3$ is very close to theoretically predicted activation energies for bromide in $MAPbBr_3$ (0.09 eV) [240] and consistent with measured activation energies in $CsPbBr_3$ (0.09 to 0.25 eV) [241, 242].

In addition to the increase in activation energy we find a strong increase of the pre-factor of the diffusion coefficient $D_0$ of three orders of magnitude from $10^{-6}$ to $10^{-3}$ $cm^2/s$ (see Section 9.6.5). We assume that this increase is due to the a change in the migration entropy $\Delta S$ upon $Mn^{2+}$ doping that depends on the change in lattice vibrations during migration [314]. This indicates that vacancy formation in the undoped perovskite lead to larger change in lattice vibrations than in the $Mn^{2+}$-doped case, possibly due to the stronger bond between lead and bromide than between lead and manganese. The reduced ionic radius would also decrease the distance an ion covers per jump, thereby also reducing the pre-factor.

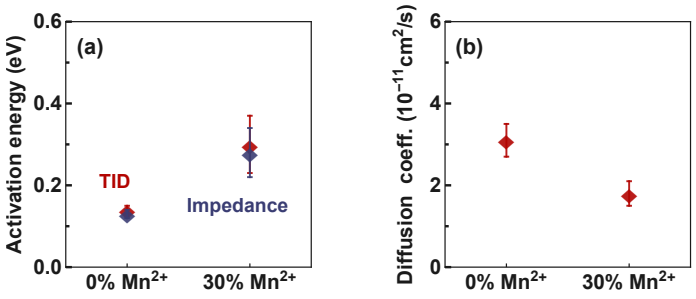


**Figure 9.4**: The effect of $Mn^{2+}$ doping on mobile ions. **(a)** Activation energy, and **(b)** diffusion coefficient at 300 K obtained by transient ion-drift (TID, red) and impedance spectroscopy (blue) measurements. The values of the transient ion-drift measurements are summarised in Table 9.1.

We find a reduction in diffusion coefficient from (3.1 $\pm$ 0.4) x $10^{-11}$ to (1.8 $\pm$ 0.3) x $10^{-11}$ $cm^2/s$ upon $Mn^{2+}$ doping and a concentration of mobile ions in the order of $10^{16}$ $cm^{-3}$. The diffusion coefficient for bromide ions is two orders of magnitude lower than typical diffusion coefficients of $10^{-9}$ $cm^2/s$ obtained for iodide ions in $MAPbI_3$ perovskites (see Chapter 7), and two orders of magnitude higher than the diffusion coefficient for bromide in $MAPbBr_3$ ($10^{-11}$ $cm^2/s$),[239] which shows that the diffusion coefficient depends strongly on the perovskite composition. We find that the diffusion coefficient and the activation energy are highly reproducible in our devices, while the ion concentration varies from sample-to-sample (see Section 9.6.5). This trend indicates that the fabrication conditions determine the density of halide vacancies responsible for ion migration [37, 239], but that the bulk properties such as activation energy and diffusion coefficient are largely independent of the ion density.

We note that only transient ion-drift measurements allow to distinguish between mobile anions and mobile cations and can be used to directly extract the diffusion coefficient of mobile ions. To extract the diffusion coefficient with impedance spectroscopy measurements, the diffusion length of the ions must be known.

At short-circuit conditions, mobile ions accumulate in close vicinity to the contacts forming a diffuse double layer [214]. Knowing the diffusion coefficient from transient ion-drift measurements we can now calculate the width of ionic double layer from our impedance spectroscopy measurements using Equation 9.1. The decrease in diffusion coefficient indicates a reduction in the ionic double layer width upon $Mn^{2+}$ doping from 6.2 $\pm$ 0.4 to 5.1 $\pm$ 0.2 nm in the solar cell structure and from

**Table 9.1**: Summary of results obtained using transient ion-drift measurements. The values are based on the mean of three measurements each. The diffusion coefficient is calculated for 300 K. See Section 9.6.5 for results from individual measurements.

| | Activation energy (eV) | Diffusion coefficient ($cm^2/s$) |
|---|---|---|
| Undoped | $0.14 \pm 0.01$ | $(3.1 \pm 0.4)\ 10^{-11}$ |
| Doped | $0.30 \pm 0.07$ | $(1.8 \pm 0.3)\ 10^{-11}$ |

$8.0 \pm 1.0$ to $6.7 \pm 0.5$ nm in the LED structure. As this ionic double layer may cause significant electrical stress to the perovskite layer under operation [287, 289, 290], we suspect that a reduction in the ionic double layer width reduces the degradation of perovskite LEDs under operation.

Both impedance spectroscopy and transient ion drift show an increase in activation energy for the migration of bromide upon $Mn^{2+}$ doping. We assume that this increase in activation energy is due to the smaller ionic radius of $Mn^{2+}$ ($\sim 0.97$ Å) compared to $Pb^{2+}$ ($\sim 1.33$ Å) [315], which stabilises the perovskite lattice and reduces the migration of mobile ions in perovskite.

Since the degradation of perovskite LEDs is mainly related to ion migration from the perovskite layer to the interfaces and into contact layer [296], we suspect that the suppression of ion migration is the reason for the increased stability of the $Mn^{2+}$-doped devices. We furthermore suspect that the increased activation energy due to the contracted perovskite lattice suggests a reduced migration of other ions from the electrodes, i.e. Au, In, or Sn [316, 317], into the perovskite bulk, which is another significant degradation pathway of perovskite LEDs.

## 9.5 Conclusion

We have investigated the effect of manganese doping on mobile ions in $PEABr_{0.2}Cs_{0.4}MA_{0.6}PbBr_3$ perovskites. Manganese improves both efficiency and long-term stability in light-emitting diodes made from these materials. Using temperature-dependent impedance spectroscopy and transient ion-drift measurements, we found that manganese doping increases the activation energy of mobile bromide ions twofold and decreases the diffusion coefficient within the bulk of the perovskite. As a result, we assume that the amount of mobile bromide ions migrating into the contact layers is reduced, which increases the stability of the device. We suspect that this increased activation energy for ion migration within the perovskite bulk reduces migration of ions from the contact layers into the perovskite bulk. We furthermore find a reduction in the width of the ionic double layer near the contact interfaces. These results

help to explain the improved stability of manganese doped light-emitting diodes and lead to a better understanding of ion migration and the influence of passivating agents on managing migration.

## 9.6 Supporting information

### 9.6.1 Experimental

**Device fabrication.** ITO substrates were cleaned by sonicating in detergent (Micron - 90), water, and acetone, before submersion in boiling IPA. The dryed films were treated with $O_2$ plasma for 5 minutes at 500 W using 0.5 Torr $O_2$ gas. A thin layer of PEDOT:PSS (Clevios PVP Al 4083, filtered through a 0.4 μm PVDF filter) was spun at 4000 rpm for 40 seconds with a ramp of 2500 rpm/s on the cleaned ITO glass. The films were then annealed at 145 °C for 30 minutes. After cooling, a thin layer of perfluoro ionomer (Nafion, PFI) was spun at 3000 rpm for 45 seconds using 10 μL/mL PFI in isopropanol. After drying at 145 °C for 10 minutes, the perovskite layer was spun from 0.3 M precursors in appropriate ratio to make $PEA_{0.2}Br_{0.2}Cs_{0.4}MA_{0.6}Pb_{(1-y)}Mn_yBr_3$, where y = 0 and 0.3. See Section 6.7.1 and [309] for details on the precursor solutions. $MnBr_2$ (Sigma, > 98%) was prepared by dissolving 0.3 M in DMF. The spin coating conditions were 1000 rpm for 10 seconds and 3000 rpm for 45 seconds, and after 20 seconds 90 μL chloroform (anti-solvent) was dripped to control the crystallisation. The films were then taken into an evaporation chamber, where 40 nm TpBi, 1.1 nm LiF, and 60 nm Al were deposited consecutively. The fabrication of devices with $NiO_X$ and $C_{60}$ as selective-contact layers is described in Section 6.7.1.

**Device characterisation.** The devices were packed using epoxy and glass before performing any measurements outside the glove box. Current density-voltage-luminance curves were measured using an HP4145A and a calibrated half-inch ThorLabs photodiode. Electroluminescence spectra were taken with an Ocean Optics QE Pro at 0.5 mA supplied by a Keithley 2400 source-measure unit. Stability curves were determined by measuring the electroluminescence over time at constant current.

**Capacitance measurements.** The capacitance measurements were performed in a Janis VPF-100 liquid nitrogen cryostat at a pressure below $2 \times 10^{-6}$ mbar in the dark using a commercially available DLTS system from Semetrol. To avoid air exposure, the samples were loaded into the cryostat inside a nitrogen-filled glovebox. The capacitance transient measurements were performed between 240 and 340 K in steps of 2 to 3 K. Before each capacitance transient measurement, the temperature was maintained for at least 1 minute with an accuracy of 0.2 K. In order to obtain a good signal-to-noise ratio, the capacitance transients were averaged over 20 scans.

**Table 9.2**: Summary of activation energies ($E_A$) and perovskite permittivities ($\varepsilon$) for the **LED** structure using impedance spectroscopy measurements.

| | Sample 1 | | Sample 2 | | Sample 3 | |
|---|---|---|---|---|---|---|
| | $\varepsilon$ | $E_A$ (eV) | $\varepsilon$ | $E_A$ (eV) | $\varepsilon$ | $E_A$ (eV) |
| Undoped | $5.9 \pm 0.1$ | $0.22 \pm 0.02$ | $5.9 \pm 0.1$ | $0.23 \pm 0.02$ | $5.9 \pm 0.1$ | $0.17 \pm 0.02$ |
| Doped | $5.2 \pm 0.1$ | $0.35 \pm 0.02$ | $5.2 \pm 0.1$ | $0.35 \pm 0.04$ | $5.3 \pm 0.1$ | $0.50 \pm 0.04$ |

**Table 9.3**: Summary of activation energies ($E_A$) and perovskite permittivities ($\varepsilon$) for the **solar cell** structure using impedance spectroscopy measurements.

| | Sample 1 | | Sample 2 | | Sample 3 | |
|---|---|---|---|---|---|---|
| | $\varepsilon$ | $E_A$ (eV) | $\varepsilon$ | $E_A$ (eV) | $\varepsilon$ | $E_A$ (eV) |
| Undoped | $7.4 \pm 0.1$ | $0.14 \pm 0.01$ | $7.4 \pm 0.1$ | $0.13 \pm 0.01$ | $7.2 \pm 0.1$ | $0.13 \pm 0.01$ |
| Doped | $6.3 \pm 0.1$ | $0.24 \pm 0.02$ | $7.2 \pm 0.1$ | $0.22 \pm 0.03$ | $6.2 \pm 0.1$ | $0.39 \pm 0.05$ |

Impedance spectroscopy measurements were performed between 240 and 340 K in steps of 10 K. Before each impedance spectroscopy measurement, the temperature was maintained for at least 5 minutes with an accuracy of 0.2 K.

### 9.6.2 Impedance spectroscopy measurements

Figure 9.5 shows the real and the imaginary part of the complex capacitance of the inverted perovskite solar cells structure at different temperatures. Assuming the capacitance at 10 kHz corresponds to the geometric capacitance of the device, the perovskite permittivity $\varepsilon$ is related to the geometric capacitance ($C_{geo}$) as

$$C_{geo} = \frac{\varepsilon \varepsilon_0 A}{d} \tag{9.6}$$

where $\varepsilon_0$ is the vacuum permittivity, $A$ the area of the device, and $d$ is the thickness of the perovskite layer. The activation energies and perovskite permittivities obtained are summarised in Table 9.2 and Table 9.3. For the perovskite permittivity, the value is calculated from the mean of the permittivity at all recorded temperatures.

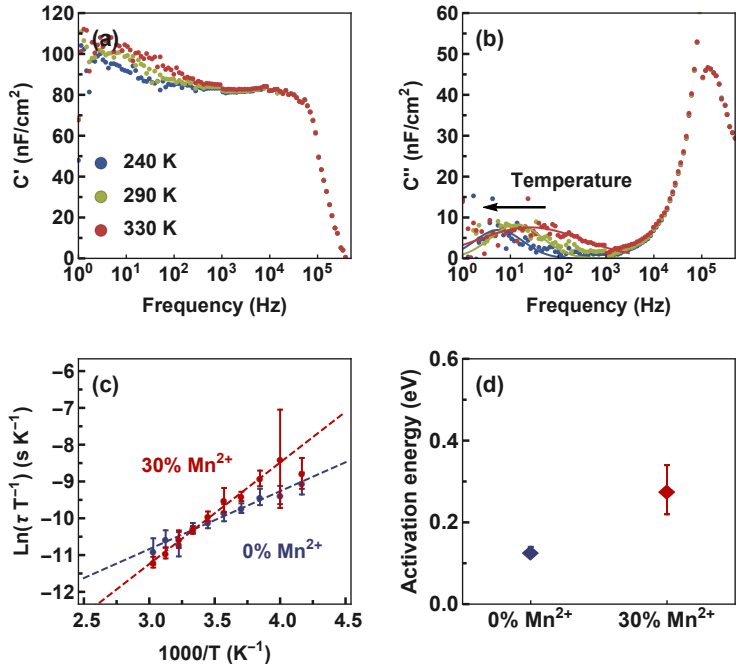


**Figure 9.5**: Impedance spectroscopy measurements of the solar cell structure. **(a)** Real and **(b)** imaginary part of the complex capacitance measured in the dark at 0 V with an AC voltage of 50 mV. **(c)** Arrhenius plot of the thermal emission rates as a function of temperature. The linear fit reveals the activation energy. **(d)** The effect of $Mn^{2+}$ doping on the activation energy measured by impedance spectroscopy. The values are based on the mean of three measurements each.

### 9.6.3 Mott-Schottky characteristics

Figure 9.6 shows the capacitance as a function of voltage for one of the LED and one of the solar cell structures measured at 10 kHz, where the measured capacitance corresponds to the geometric capacitance and the series resistance can be neglected (see Figure 9.5 and Figure 9.1).

When a voltage $V$ is applied in forward direction, the depletion capacitance $C_{dl}$ is increased. This increase in capacitance is correlated to a decrease in depletion-layer width. The depletion capacitance as a function of applied voltage can be approximated by the Mott-Schottky relation as

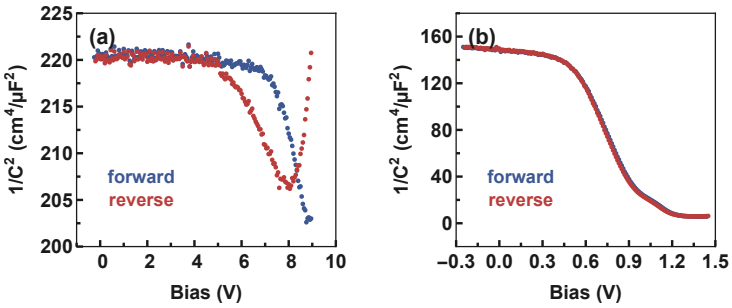


**Figure 9.6**: Mott-Schottky characteristics of **(a)** the LED and **(b)** the inverted solar cell structure measured at 300 K in the dark with an AC perturbation of 20 mV at 10 kHz.

**Table 9.4**: Summary of obtained doping densities ($N$) and built-in biases ($V_{bi}$) for the solar cell structure.

| | Sample 1 | | Sample 2 | | Sample 3 | |
|---|---|---|---|---|---|---|
| | $V_{bi}$ (V) | $N$ (cm$^{-3}$) | $V_{bi}$ (V) | $N$ (cm$^{-3}$) | $V_{bi}$ (V) | $N$ (cm$^{-3}$) |
| Undoped | 0.88 | 8 x $10^{17}$ | 0.96 | 7 x $10^{17}$ | 1.02 | 7 x $10^{17}$ |
| Doped | 1.08 | 4 x $10^{17}$ | 1.09 | 8 x $10^{17}$ | 1.06 | 6 x $10^{17}$ |

$$C_{dl} = A\sqrt{\frac{q\varepsilon_0\varepsilon N}{2\left(V_{bi}-V\right)}} \tag{9.7}$$

where $A$ is the area of the device, $q$ the elementary charge, $N$ the doping density, and $V_{bi}$ the built-in potential. From the $C^{-2}\left(V\right)$ plot the built-in potential and the doping density can be obtained. The slope of the Mott-Schottky plot furthermore suggests that the perovskite layer is p-type. The results from the Mott-Schottky analysis are summarised in Table 9.4.

Only in the case of the solar cell structure we can distinguish the depletion capacitance from the chemical capacitance from the different slopes in the Mott-Schottky plot. We therefore apply the Mott-Schottky analysis only to the solar cell structure.

### 9.6.4 Ions versus charges

To distinguish between ion diffusion and electronic effects such as trapping and detrapping, we compare the rise and decay time of capacitance following the forward bias and returning to short circuit conditions. The voltage bias is chosen such that

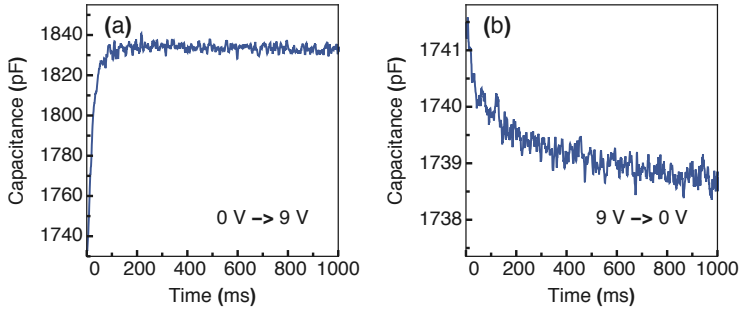


**Figure 9.7**: Capacitance transient of the LED structure measured in the dark **(a)** while applying a voltage pulse of 9.0 V (rise time) and **(b)** at short-circuit after applying a voltage pule of 9.0 V (decay time).

the depletion region within the perovskite collapses. For this condition, we chose a voltage of 9 V for the LED structure and 1.25 V for the solar cell structure (see Figure 9.6). For mobile ions, the rise time due to diffusion is expected to be longer than the decay time due to drift. In contrast, for traps the capture rate is much higher than the emission rate, resulting in a longer decay time compared to the rise time. Figure 9.7 and Figure 9.8 show the measured capacitance transient of the LED and the solar cell structure measured at 300 K. In the LED structure, the rise time is shorter than the decay time, indicating electronic defect states. In the solar cells structure, the rise time is longer than the decay time, showing that the measured capacitance transient is due to the diffusion of mobile ions. See Section 6.7.4 for a more detailed description of the differences between ions and electronic defect states.

### 9.6.5 Transient ion-drift measurements

The activation energies, diffusion coefficients, and concentrations for the solar cell structure are summarised in Table 9.5 and Table 9.6.

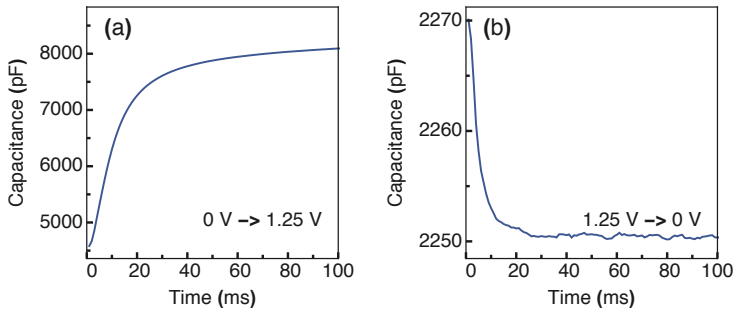


**Figure 9.8**: Capacitance transient of the solar cell structure measured in the dark **(a)** while applying a voltage pulse of 1.25 V (rise time) and **(b)** at short-circuit after applying a voltage pule of 1.25 V (decay time).

**Table 9.5**: Characteristics of mobile ions in the **undoped** perovskite obtained by transient ion-drift measurements. The diffusion coefficient is calculated for 300 K.

| | Sample 1 | Sample 2 | Sample 3 |
|---|---|---|---|
| Activation energy (eV) | $0.16 \pm 0.01$ | $0.14 \pm 0.01$ | $0.14 \pm 0.01$ |
| Diffusion coeff. ($cm^2/s$) | $(2.8 \pm 0.4) \times 10^{-11}$ | $(3.5 \pm 0.6) \times 10^{-11}$ | $(3.1 \pm 0.6) \times 10^{-11}$ |
| Concentration ($cm^{-3}$) | $8.8 \times 10^{16}$ | $3.2 \times 10^{16}$ | $3.2 \times 10^{16}$ |
| Pre-factor $D_0$ ($cm^2/s$) | $(3.5 \pm 6.7) \times 10^{-6}$ | $(2.0 \pm 3.4) \times 10^{-6}$ | $(1.9 \pm 3.2) \times 10^{-6}$ |

**Table 9.6**: Characteristics of mobile ions in the perovskites **doped** with 30% $Mn^{2+}$ obtained by transient ion-drift measurements. The diffusion coefficient is calculated for 300 K.

| | Sample 1 | Sample 2 | Sample 3 |
|---|---|---|---|
| Activation energy (eV) | $0.32 \pm 0.01$ | $0.22 \pm 0.01$ | $0.35 \pm 0.01$ |
| Diffusion coeff. ($cm^2/s$) | $(2.0 \pm 0.7) \times 10^{-11}$ | $(1.5 \pm 0.1) \times 10^{-11}$ | $(1.9 \pm 1.7) \times 10^{-11}$ |
| Concentration ($cm^{-3}$) | $4.3 \times 10^{15}$ | $3.6 \times 10^{17}$ | $7.7 \times 10^{15}$ |
| Pre-factor $D_0$ ($cm^2/s$) | $(1.5 \pm 6.0) \times 10^{-3}$ | $(2.0 \pm 5.3) \times 10^{-5}$ | $(4.6 \pm 19.8) \times 10^{-3}$ |

# References


1. International Energy Agency -IEA-. *Global energy and CO2 status report 2018* tech. rep. March (International Energy Agency, 2019), 15.
2. Kharas, H. *The unprecedented expansion of the global middle class an update* tech. rep. February (2017), 1–2.
3. Asafu-Adjaye, J. The relationship between energy consumption, energy prices and economic growth: Time series evidence from Asian developing countries. *Energy Economics* **22,** 615–625 (2000).
4. Anderson, M. G. & Katz, P. B. Strategic sourcing. *The International Journal of Logistics Management* **9,** 1–13 (1998).
5. Oreskes, N. Beyond the ivory tower: The scientific consensus on climatic change. *Science* **306,** 1686 (2004).
6. Creutzig, F. *et al.* The underestimated potential of solar energy to mitigate climate change. *Nature Energy* **2,** 17140 (2017).
7. Kost, C. *et al. Levelized cost of electricity - renewable energy technologies* tech. rep. (Fraunhofer ISE, 2018).
8. Green, M. A. How did solar cells get so cheap? *Joule* **3,** 631–633 (2019).
9. Willuhn, M. Brazil A-4 auction signs 211 MW of solar for record-low price of $0.0175 kWh. *PV-Magazine* (2019).
10. Weaver, J. Los Angeles seeks record setting solar power price under 2 ¢/kWh. *PV-Magazine* (2019).
11. Weaver, J. New record low solar power price? 2.175 ¢/kWh in Idaho. *PV-Magazine* (2019).
12. Sivaram, V. & Kann, S. Solar power needs a more ambitious cost target. *Nature Energy* **1,** 16036 (2016).
13. Sivaram, V., Dabiri, J. O. & Hart, D. M. The need for continued innovation in solar, wind, and energy storage. *Joule* **2,** 1639–1642 (2018).
14. Egan, R. J. & Chang, N. L. When every cent counts. *Nature Energy* **3,** 361–362 (2018).

15. Goldschmidt, V. M. Die Gesetze der Krystallochemie. *Die Naturwissenschaften* **14,** 477–485 (1926).

16. De Wolf, S *et al.* Organometallic halide perovskites: sharp optical absorption edge and its relation to photovoltaic performance. *Journal of Physical Chemistry Letters* **5,** 1035–1039 (2014).

17. Wehrenfennig, C., Eperon, G. E., Johnston, M. B., Snaith, H. J. & Herz, L. M. High charge carrier mobilities and lifetimes in organolead trihalide perovskites. *Advanced Materials* **26,** 1584–1589 (2014).

18. Johnston, M. B. & Herz, L. M. Hybrid perovskites for photovoltaics: charge-carrier recombination, diffusion, and radiative efficiencies. *Accounts of Chemical Research* **49,** 146–154 (2016).

19. Green, M. A. & Ho-Baillie, A. Perovskite solar cells: The birth of a new era in photovoltaics. *ACS Energy Letters* **2,** 822–830 (2017).

20. Snaith, H. J. Present status and future prospects of perovskite photovoltaics. *Nature Materials* **17,** 372–376 (2018).

21. Moller, C. K. Crystal structure and photoconductivity of caesium plumbohalides. *Nature* **182,** 1436 (1958).

22. Weber, D. $CH_3NH_3Pb_3X_3$, ein Pb(II)-System mit kubischer Perowskitstruktur. *Zeitschrift fur Naturforschung - Section B Journal of Chemical Sciences* **33,** 1443–1445 (1978).

23. Baruch, P., De Vos, A., Landsberg, P. T. & Parrott, J. E. On some thermodynamic aspects of photovoltaic solar energy conversion. *Solar Energy Materials and Solar Cells* **36,** 201–222 (1995).

24. Kojima, A, Teshima, K, Shirai, Y & Miyasaka, T. Organometal halide perovskites as visible-light sensitizers for photovoltaic cells. *Journal of the American Chemical Society* **131,** 6050–6051 (2009).

25. Lee, M. M., Teuscher, J., Miyasaka, T., Murakami, T. N. & Snaith, H. J. Efficient hybrid solar cells based on meso-superstructured organometal halide perovskites. *Science* **338,** 643–647 (2012).

26. Kim, H. S. *et al.* Lead iodide perovskite sensitized all-solid-state submicron thin film mesoscopic solar cell with efficiency exceeding 9%. *Scientific Reports* **2** (2012).

27. Green, M. A. *et al.* Solar cell efficiency tables (version 54). *Progress in Photovoltaics: Research and Applications* **27,** 565–575 (2019).

28. NREL. *Best research-cell efficiency chart — photovoltaic research — NREL* tech. rep. (2019).

29. Rong, Y. *et al.* Challenges for commercializing perovskite solar cells. *Science* **361,** eaat8235 (2018).

30. Ávila, J., Momblona, C., Boix, P. P., Sessolo, M. & Bolink, H. J. Vapor-deposited perovskites: The route to high-performance solar cell production? *Joule* **1,** 431–442 (2017).

31. Deng, Y. *et al.* Surfactant-controlled ink drying enables high-speed deposition of perovskite films for efficient photovoltaic modules. *Nature Energy* **3,** 560–566 (2018).

32. Galagan, Y. Perovskite solar cells: Toward industrial-scale methods. *Journal of Physical Chemistry Letters* **9,** 4326–4335 (2018).

33. Li, Z. *et al.* Scalable fabrication of perovskite solar cells. *Nature Reviews Materials* **3,** 18017 (2018).

34. Eames, C. *et al.* Ionic transport in hybrid lead iodide perovskite solar cells. *Nature Communications* **6,** 7497 (2015).

35. Frost, J. M. & Walsh, A. What is moving in hybrid halide perovskite solar cells? *Accounts of Chemical Research* **49,** 528–535 (2016).

36. Senocrate, A. *et al.* Slow $CH_3NH_3^+$ diffusion in $CH_3NH_3PbI_3$ under light measured by solid-state NMR and tracer diffusion. *Journal of Physical Chemistry C* **122,** 21803–21806 (2018).

37. Senocrate, A. *et al.* The nature of ion conduction in methylammonium lead iodide: A multimethod approach. *Angewandte Chemie International Edition* **56,** 7755–7759 (2017).

38. Li, C., Guerrero, A., Huettner, S. & Bisquert, J. Unravelling the role of vacancies in lead halide perovskite through electrical switching of photoluminescence. *Nature Communications* **9,** 5113 (2018).

39. Yuan, Y. *et al.* Photovoltaic switching mechanism in lateral structure hybrid perovskite solar cells. *Advanced Energy Materials* **5,** 1500615 (2015).

40. Li, C., Guerrero, A., Zhong, Y. & Huettner, S. Origins and mechanisms of hysteresis in organometal halide perovskites. *Journal of Physics: Condensed Matter* **29,** 193001 (2017).

41. Würfel, P. The chemical potential of radiation. *Journal of Physics C: Solid State Physics* **15,** 3967–3985 (1982).

42. Shockley, W. & Queisser, H. J. Detailed balance limit of efficiency of p-n junction solar cells. *Journal of Applied Physics* **32,** 510–519 (1961).

43. Vos, A. D. Detailed balance limit of the efficiency of tandem solar cells. *Journal of Physics D: Applied Physics* **13,** 839–849 (1980).

44. Nelson, J. *The Physics of Solar Cells* (Imperial College Press, 2003).
45. Rau, U. Reciprocity relation between photovoltaic quantum efficiency and electroluminescent emission of solar cells. *Physical Review B - Condensed Matter and Materials Physics* **76,** 1–8 (2007).
46. Wheeler, S. *et al.* Transient optoelectronic analysis of the impact of material energetics and recombination kinetics on the open-circuit voltage of hybrid perovskite solar cells. *The Journal of Physical Chemistry C* **121,** 13496–13506 (2017).
47. Stellwag, T. *et al. Effects of perimeter recombination on GaAs-based solar cells* in *IEEE Conference on Photovoltaic Specialists* (IEEE, 1990), 442–447.
48. Chegaar, M. *et al.* Effect of illumination intensity on solar cells parameters. *Energy Procedia* **36,** 722–729 (2013).
49. Verschraegen, J., Burgelman, M. & Penndorf, J. Temperature dependence of the diode ideality factor in $CuInS_2$-on-Cu-tape solar cells. *Thin Solid Films* **480-481,** 307–311 (2005).
50. Weber, S. A. L. *et al.* How the formation of interfacial charge causes hysteresis in perovskite solar cells. *Energy & Environmental Science* **11,** 2404–2413 (2018).
51. Polman, A., Knight, M., Garnett, E. C., Ehrler, B. & Sinke, W. C. Photovoltaic materials – present efficiencies and future challenges. *Science* **352,** 307 (2016).
52. Tiedje, T., Yablonovitch, E., Cody, G. D. & Brooks, B. G. Limiting efficiency of silicon solar cells. *IEEE Transactions on Electron Devices* **31,** 711–716 (1984).
53. Noh, J. H., Im, S. H., Heo, J. H., Mandal, T. N. & Seok, S. I. Chemical management for colorful, efficient, and stable inorganic - organic hybrid nanostructured solar cells. *Nano Letters* **13,** 1764–1769 (2013).
54. Noel, N. K. *et al.* Lead-free organic-inorganic tin halide perovskites for photovoltaic applications. *Energy and Environmental Science* **7,** 3061–3068 (2014).
55. Pazos-Outón, L. M. *et al.* Photon recycling in lead iodide perovskite solar cells. *Science* **351,** 1430–1433 (2016).
56. Martí, A. & Araújo, G. L. Limiting efficiencies for photovoltaic energy conversion in multigap systems. *Solar Energy Materials and Solar Cells* **43,** 203–222 (1996).
57. Brown, A. S. & Green, M. A. Detailed balance limit for the series constrained two terminal tandem solar cell. *Physica E: Low-dimensional Systems and Nanostructures* **14,** 96–100 (2002).
58. Brown, A. S. & Green, M. A. Limiting efficiency for current-constrained two-terminal tandem cell stacks. *Progress in Photovoltaics: Research and Applications* **10,** 299–307 (2002).

59. White, T. P., Lal, N. N. & Catchpole, K. R. Tandem solar cells based on high-efficiency c-Si bottom cells: Top cell requirements for >30% efficiency. *IEEE Journal of Photovoltaics* **4,** 208–214 (2014).

60. Almansouri, I., Ho-Baillie, A. & Green, M. A. Ultimate efficiency limit of single-junction perovskite and dual-junction perovskite/silicon two-terminal devices. *Japanese Journal of Applied Physics* **54,** 08KD04 (2015).

61. Strandberg, R. *Spectral and temperature sensitivity of area de-coupled tandem modules* in *2015 IEEE 42nd Photovoltaic Specialist Conference, PVSC 2015* (IEEE, 2015), 1–6.

62. Mailoa, J. P. *et al.* A 2-terminal perovskite/silicon multijunction solar cell enabled by a silicon tunnel junction. *Applied Physics Letters* **106,** 121105 (2015).

63. Bailie, C. D. *et al.* Semi-transparent perovskite solar cells for tandems with silicon and CIGS. *Energy and Environmental Science* **8,** 956–963 (2015).

64. Werner, J. *et al.* Efficient near-infrared-transparent perovskite solar cells enabling direct comparison of 4-terminal and monolithic perovskite/silicon tandem cells. *ACS Energy Letters* **1,** 474–480 (2016).

65. Albrecht, S. *et al.* Monolithic perovskite/silicon-heterojunction tandem solar cells processed atlow temperature. *Energy and Environmental Science* **9,** 81–88 (2016).

66. Albrecht, S. *et al.* Towards optical optimization of planar monolithic perovskite/silicon-heterojunction tandem solar cells. *Journal of Optics* **18,** 1–10 (2016).

67. Löper, P. *et al.* Organic–inorganic halide perovskite/crystalline silicon four-terminal tandem solar cells. *Physical Chemistry Chemical Physics* **17,** 1619–1629 (2015).

68. Lang, F. *et al.* Perovskite solar cells with large-area CVD-graphene for tandem solar cells. *Journal of Physical Chemistry Letters* **6,** 2745–2750 (2015).

69. Duong, T. *et al.* Semitransparent perovskite solar cell with sputtered front and rear electrodes for a four-terminal tandem. *IEEE Journal of Photovoltaics* **6,** 679–687 (2016).

70. McMeekin, D. P. *et al.* A mixed-cation lead mixed-halide perovskite absorber for tandem solar cells. *Science* **351,** 151–155 (2016).

71. Werner, J. *et al.* Efficient monolithic perovskite/silicon tandem solar cell with cell area >1 $cm^2$. *Journal of Physical Chemistry Letters* **7,** 161–166 (2016).

72. Chen, B. *et al.* Efficient semitransparent perovskite solar cells for 23.0%-efficiency perovskite/silicon four-terminal tandem cells. *Advanced Energy Materials* **6,** 1601128 (2016).

73. Sheng, R. *et al.* Four-terminal tandem solar cells using $CH_3NH_3PbBr_3$ by spectrum splitting. *Journal of Physical Chemistry Letters* **6,** 3931–3934 (2015).

74. Uzu, H. *et al.* High efficiency solar cells combining a perovskite and a silicon heterojunction solar cells via an optical splitting system. *Applied Physics Letters* **106,** 013506 (2015).

75. Yoshikawa, K. *et al.* Silicon heterojunction solar cell with interdigitated back contacts for a photoconversion efficiency over 26%. *Nature Energy* **2,** 17032 (2017).

76. Liu, H. *et al.* The realistic energy yield potential of GaAs-on-Si tandem solar cells: a theoretical case study. *Optics Express* **23,** A382–90 (2015).

77. Pazos-Outón, L. M. *et al.* A silicon-singlet fission tandem solar cell exceeding 100% external quantum efficiency with high spectral stability. *ACS Energy Letters* **2,** 476–480 (2017).

78. Lentine, A. L., Nielson, G. N., Okandan, M., Cruz-Campa, J. L. & Tauke-Pedretti, A. Voltage matching and optimal cell compositions for microsystem-enabled photovoltaic modules. *IEEE Journal of Photovoltaics* **4,** 1593–1602 (2014).

79. Strandberg, R. Detailed balance analysis of area de-coupled double tandem photovoltaic modules. *Applied Physics Letters* **106,** 33902 (2015).

80. Krishnan, P *et al.* Response to simulated typical daily outdoor irradiation conditions of thin-film silicon-based triple-band-gap, triple-junction solar cells. *Solar Energy Materials and Solar Cells* **93,** 691–697 (2009).

81. Louwen, A., de Waal, A. C., Schropp, R. E. I., Faaij, A. P. C. & van Sark, W. G.J.H. M. Comprehensive characterisation and analysis of PV module performance under real operating conditions. *Progress in Photovoltaics: Research and Applications* **25,** 218–232 (2017).

82. Kottek, M., Grieser, J., Beck, C., Rudolf, B. & Rubel, F. World map of the Köppen-Geiger climate classification updated. *Meteorologische Zeitschrift* **15,** 259–263 (2006).

83. Betts, T. R., Jardine, C. N., Gottschalg, R., Infield, D. G. & Lane, K. *Impact of spectral effects on the electrical parameters of multijunction amorphous silicon cells* in *Proceedings of the 3rd World Conference on Photovoltaic Energy Conversion* (2003).

84. Minemoto, T., Nakada, Y., Takahashi, H. & Takakura, H. Uniqueness verification of solar spectrum index of average photon energy for evaluating outdoor performance of photovoltaic modules. *Solar Energy* **83,** 1294–1299 (2009).

85. Liu, H., Aberle, A. G., Buonassisi, T. & Peters, I. M. On the methodology of energy yield assessment for one-Sun tandem solar cells. *Solar Energy* **135,** 598–604 (2016).

86. Louwen, A., De Waal, A. C. & Van Sark, W. G. *Evaluation of different indicators for representing solar spectral variation* in *2017 IEEE 44th Photovoltaic Specialist Conference, PVSC 2017* (IEEE, 2017), 1–5.

87. Van Sark, W. G., Louwen, A., de Waal, A. C., Elsinga, B. & Schropp, R. E. I. *UPOT: the Utrecht photovoltaic outdoor test facility* in *27th European Photovoltaic Solar Energy Conference and Exhibition* (WIP, 2012), 3247–3249.

88. Stoffel, T. & Andreas, A. *NREL solar radiation research laboratory (SRRL): Baseline measurement system (BMS); Golden, Colorado (Data)* tech. rep. (1981).

89. Kasten, F. & Young, A. T. Revised optical air mass tables and approximation formula. *Applied Optics* **28,** 4735 (1989).

90. Nann, S. & Riordan, C. Solar spectral irradiance under clear and cloudy skies: Measurements and a semiempirical model. *Journal of Applied Meteorology* **30,** 447–462 (2002).

91. Bohren, C. F. in *The optics encyclopedia* (Wiley-VCH, Weinheim, Germany, 2007).

92. Hulburt, E. O. Explanation of the brightness and color of the sky, particularly the twilight sky. *Journal of the Optical Society of America* **43,** 113 (1953).

93. Dave, J. V. & Sekera, Z. Effect of ozone on the total sky and global radiation recieived on a horizontal surface. *Journal of Meteorology* **16,** 211–212 (2002).

94. Jaysankar, M. *et al.* Four-terminal perovskite/silicon multijunction solar modules. *Advanced Energy Materials* **7,** 1602807 (2017).

95. Bush, K. A. *et al.* 23.6%-efficient monolithic perovskite/silicon tandem solar cells with improved stability. *Nature Energy* **2,** 17009 (2017).

96. Green, M. A. *et al.* Solar cell efficiency tables (version 50). *Progress in Photovoltaics: Research and Applications* **25,** 668–676 (2017).

97. Futscher, M. H. & Ehrler, B. Efficiency limit of perovskite/Si tandem solar cells. *ACS Energy Letters* **1,** 863–868 (2016).

98. Duck, B. C. *et al. Energy yield potential of perovskite-silicon tandem devices* in *2016 IEEE 43rd Photovoltaic Specialists Conference (PVSC)* (IEEE, 2016), 1624–1629.

99. Paetzold, U. W. *et al.* Optical loss analyses and energy yield modelling of perovskite/silicon multijunction solar cells. *Light, Energy and the Environment,* SoW2C.4 (2016).

100. Grant, D., Weber, K., Stocks, M. & White, T. P. *Optical optimization of perovskite-silicon reflective tandem solar cell* in *Light, Energy and the Environement 2015* (OSA, Washington, D.C., 2015), PTh3B.3.

101. Grant, D. T., Catchpole, K. R., Weber, K. J. & White, T. P. Design guidelines for perovskite/silicon 2-terminal tandem solar cells: an optical study. *Optics Express* **24,** A1454 (2016).

102. Jäger, K., Korte, L., Rech, B. & Albrecht, S. Numerical optical optimization of monolithic planar perovskite-silicon tandem solar cells with regular and inverted device architectures. *Optics Express* **25,** A473 (2017).

103. Santbergen, R. *et al.* Minimizing optical losses in monolithic perovskite/c-Si tandem solar cells with a flat top cell. *Optics Express* **24,** A1288 (2016).

104. Martins, A., Borges, B.-H. V., Li, J., Krauss, T. F. & Martins, E. R. Photonic intermediate structures for perovskite/c-silicon four terminal tandem solar cells. *IEEE Journal of Photovoltaics* **7,** 1190 –1196 (2017).

105. Zhou, Y. & Gray-Weale, A. A numerical model for charge transport and energy convention of perovskite solar cells. *Physical Chemistry Chemical Physics* **18,** 4476–4486 (2015).

106. Islam, M., Wahid, S. & Alam, M. K. Physics-based modeling and performance analysis of dual junction perovskite/silicon tandem solar cells. *Physica Status Solidi (a)* **13,** 1–13 (2016).

107. Sun, X., Asadpour, R., Nie, W., Mohite, A. D. & Alam, M. A. A physics-based analytical model for perovskite solar cells. *IEEE Journal of Photovoltaics* **5,** 1389–1394 (2015).

108. Yang, W. S. *et al.* High-performance photovoltaic perovskite layers fabricated through intramolecular exchange. *Science* **348,** 235–1237 (2015).

109. Yang, W. S. *et al.* Iodide management in formamidinium-lead-halide–based perovskite layers for efficient solar cells. *Science* **356,** 1376 –1379 (2017).

110. Laban, W. A. & Etgar, L. Depleted hole conductor-free lead halide iodide heterojunction solar cells. *Energy & Environmental Science* **6,** 3249 (2013).

111. Guerrero, A., Juarez-Perez, E. J., Bisquert, J., Mora-Sero, I. & Garcia-Belmonte, G. Electrical field profile and doping in planar lead halide perovskite solar cells. *Applied Physics Letters* **105,** 133902 (2014).

112. Aharon, S., Gamliel, S., Cohen, B. E. & Etgar, L. Depletion region effect of highly efficient hole conductor free $CH_3NH_3PbI_3$ perovskite solar cells. *Physical Chemistry Chemical Physics* **16,** 10512–10518 (2014).

113. Bryant, D. *et al.* A transparent conductive adhesive laminate electrode for high-efficiency organic-inorganic lead halide perovskite solar cells. *Advanced Materials* **26,** 7499–7504 (2014).

114. Sciacca, B., van de Groep, J., Polman, A. & Garnett, E. C. Solution-grown silver nanowire ordered arrays as transparent electrodes. *Advanced Materials* **28,** 905–909 (2016).

115. Ago, H., Petritsch, K., Shaffer, M. S. P., Windle, A. H. & Friend, R. H. Composites of carbon nanotubes and conjugated polymers for photovoltaic devices. *Advanced Materials* **11,** 1281–1285 (1999).

116. You, P., Liu, Z., Tai, Q., Liu, S. & Yan, F. Efficient semitransparent perovskite solar cells with graphene electrodes. *Advanced Materials* **27,** 3632–3638 (2015).

117. Lee, J. M., Futscher, M. H., Pazos-Outon, L. M. & Ehrler, B. Highly transparent singlet fission solar cell with multi-stacked thin metal contacts for tandem applications. *Progress in Photovoltaics: Research and Applications* **25,** 936–941 (2017).

118. Adhyaksa, G. W., Johlin, E. & Garnett, E. C. Nanoscale back contact perovskite solar cell design for improved tandem efficiency. *Nano Letters* **17,** 5206–5212 (2017).

119. Feurer, T. *et al.* Progress in thin film CIGS photovoltaics – research and development, manufacturing, and applications. *Progress in Photovoltaics: Research and Applications* **25,** 645–667 (2017).

120. Sites, J., Munshi, A., Kephart, J., Swanson, D. & Sampath, W. S. *Progress and challenges with CdTe cell efficiency* in *Conference record of the IEEE photovoltaic specialists conference* (IEEE, 2016), 3632–3635.

121. Kayes, B. M. *et al. 27.6% conversion efficiency, a new record for single-junction solar sells under 1 sun illumination* in *2011 37th IEEE Photovoltaic Specialists Conference* (IEEE, 2011), 4–8.

122. Deschler, F. *et al.* High photoluminescence efficiency and optically-pumped lasing in solution-processed mixed halide perovskite semiconductors. *The Journal of Physical Chemistry Letters* **5,** 1421–1426 (2014).

123. Liu, H. *et al.* Predicting the outdoor performance of flat-plate III-V/Si tandem solar cells. *Solar Energy* **149,** 77–84 (2017).

124. Green, M. A. Limiting efficiency of bulk and thin-film silicon solar cells in the presence of surface recombination. *Progress in Photovoltaics: Research and Applications* **7,** 327–330 (1999).

125. Misiakos, K. & Tsamakis, D. Accurate measurements of the silicon intrinsic carrier density from 78 to 340 K. *Journal of Applied Physics* **74,** 3293–3297 (1993).

126. Varshni, Y. Temperature dependence of the energy gap in semiconductors. *Physica* **34,** 149–154 (1967).

127. S. M. Sze, K. N. *Physics of semiconductor devices* 739–751 (John Wiley & Sons Inc, 2014).

128. Dziewior, J., Schmid, W. & Dziewior, J. Auger coefficients for highly doped and highly excited silicon. *Applied Physics Letters* **346,** 11–14 (1977).

129. Smith, D. D. *et al.* Toward the practical limits of silicon solar cells. *IEEE Journal of Photovoltaics* **4,** 1465–1469 (2014).

130. Guerrero, A. *et al.* Interfacial degradation of planar lead halide perovskite solar cells. *ACS Nano* **10,** 218–224 (2016).

131. Agarwal, S. *et al.* On the uniqueness of ideality factor and voltage exponent of perovskite-based solar cells. *Journal of Physical Chemistry Letters* **5,** 4115–4121 (2014).

132. Leong, W. L. *et al.* Identifying fundamental limitations in halide perovskite solar cells. *Advanced Materials* **28,** 2439–2445 (2016).

133. Zhou, Y. *et al.* Photovoltaic performance and the energy landscape of $CH_3NH_3PbI_3$. *Physical Chemistry Chemical Physics* **17,** 22604–22615 (2015).

134. Saidi, W. A., Ponce, S. & Monserrat, B. Temperature dependence of the energy levels of methylammonium lead iodide perovskite from first principles. *The Journal of Physical Chemistry Letters* **7,** 5247–5252 (2016).

135. Dittrich, T., Awino, C., Prajongtat, P., Rech, B. & Lux-Steiner, M. C. Temperature dependence of the band gap of $CH_3NH_3PbI_3$ stabilized with PMMA: A modulated surface photovoltage study. *Journal of Physical Chemistry C* **119,** 23968–23972 (2015).

136. Milot, R. L., Eperon, G. E., Snaith, H. J., Johnston, M. B. & Herz, L. M. Temperature-dependent charge-carrier dynamics in $CH_3NH_3PbI_3$ perovskite thin films. *Advanced Functional Materials* **25,** 6218–6227 (2015).

137. DeQuilettes, D. W. *et al.* Impact of microstructure on local carrier lifetime in perovskite solar cells. *Science* **348,** 683–686 (2015).

138. Marinova, N. *et al.* Light harvesting and charge recombination in $CH_3NH_3PbI_3$ perovskite solar cells studied by hole transport layer thickness variation. *ACS Nano* **9,** 4200–4209 (2015).

139. Kiermasch, D. *et al.* Improved charge carrier lifetime in planar perovskite solar cells by bromine doping. *Scientific Reports* **6,** 1234–1237 (2016).

140. Herz, L. M. Charge-carrier dynamics in organic-inorganic metal halide perovskites. *Annual Review of Physical Chemistry* **67,** 65–89 (2016).

141. Kopecek, R. & Libal, J. Towards large-scale deployment of bifacial photovoltaics. *Nature Energy* **3,** 443–446 (2018).

142. Geerligs, L., Zhang, D., Janssen, G. & Luxembourg, S. *4-terminal and 2-terminal tandem modules in bifacial operation: Model analysis and comparison* in *35th European Photovoltaic Solar Energy Conference and Exhibition* (WIP, 2018), 676–680.

143. Imran, H. *et al.* High-performance bifacial perovskite/silicon double-tandem solar cell. *IEEE Journal of Photovoltaics* **8,** 1222–1229 (2018).

144. Khan, M. R. & Alam, M. A. Thermodynamic limit of bifacial double-junction tandem solar cells. *Applied Physics Letters* **107,** 223502 (2015).

145. Asadpour, R., Chavali, R. V., Ryyan Khan, M. & Alam, M. A. Bifacial Si heterojunction-perovskite organic-inorganic tandem to produce highly efficient solar cell. *Applied Physics Letters* **106,** 243902 (2015).

146. ITRPV. International technology roadmap for photovoltaic (ITRPV), ninth edition, 2018 results. *ITRPV* (2018).

147. Futscher, M. H. & Ehrler, B. Modeling the performance limitations and prospects of perovskite/Si tandem solar cells under realistic operating conditions. *ACS Energy Letters* **2,** 2089–2095 (2017).

148. Hörantner, M. T. & Snaith, H. J. Predicting and optimising the energy yield of perovskite-on-silicon tandem solar cells under real world conditions. *Energy and Environmental Science* **10,** 1983–1993 (2017).

149. Werner, J., Niesen, B. & Ballif, C. Perovskite/silicon tandem solar cells: Marriage of convenience or true love story? – an overview. *Advanced Materials Interfaces* **5,** 1700731 (2018).

150. Leijtens, T., Bush, K. A., Prasanna, R. & McGehee, M. D. Opportunities and challenges for tandem solar cells using metal halide perovskite semiconductors. *Nature Energy* **3,** 828–838 (2018).

151. Russell, T. C., Saive, R., Augusto, A., Bowden, S. G. & Atwater, H. A. The influence of spectral albedo on bifacial solar cells: A theoretical and experimental study. *IEEE Journal of Photovoltaics* **7,** 1611–1618 (2017).

152. Liang, T. S. *et al.* A review of crystalline silicon bifacial photovoltaic performance characterisation and simulation. *Energy and Environmental Science* **12,** 116–148 (2019).

153. Slotcavage, D. J., Karunadasa, H. I. & McGehee, M. D. Light-induced phase segregation in halide-perovskite absorbers. *ACS Energy Letters* **1,** 1199–1205 (2016).

154. Yoon, S. J., Kuno, M. & Kamat, P. V. Shift happens. how halide ion defects influence photoinduced segregation in mixed halide perovskites. *ACS Energy Letters* **2,** 1507–1514 (2017).

155. Zhang, H. *et al.* Phase segregation due to ion migration in all-inorganic mixed-halide perovskite nanocrystals. *Nature Communications* **10,** 1088 (2019).

156. Essig, S. *et al.* Raising the one-sun conversion efficiency of III-V/Si solar cells to 32.8% for two junctions and 35.9% for three junctions. *Nature Energy* **2,** 17144 (2017).

157. Hörantner, M. T. *et al.* The potential of multijunction perovskite solar cells. *ACS Energy Letters* **2,** 2506–2513 (2017).

158. Trupke, T., Green, M. A. & Würfel, P. Improving solar cell efficiencies by up-conversion of sub-band-gap light. *Journal of Applied Physics* **92,** 4117–4122 (2002).

159. Tayebjee, M., Rao, A. & Schmidt, T. All-optical augmentation of solar cells using a combination of up- and downconversion. *Journal of Photonics for Energy* **8,** 1 (2018).

160. Trupke, T., Green, M. A. & Würfel, P. Improving solar cell efficiencies by down-conversion of high-energy photons. *Journal of Applied Physics* **92,** 1668–1674 (2002).

161. Shpaisman, H., Niitsoo, O., Lubomirsky, I. & Cahen, D. Can up- and down-conversion and multi-exciton generation improve photovoltaics? *Solar Energy Materials and Solar Cells* **92,** 1541–1546 (2008).

162. Timmerman, D., Izeddin, I., Stallinga, P., Yassievich, I. N. & Gregorkiewicz, T. Space-separated quantum cutting with silicon nanocrystals for photovoltaic applications. *Nature Photonics* **2,** 105–109 (2008).

163. Davis, N. J. *et al.* Singlet gission and triplet transfer to PbS quantum dots in TIPS-tetracene carboxylic acid ligands. *Journal of Physical Chemistry Letters* **9,** 1454–1460 (2018).

164. Smith, M. B. & Michl, J. Singlet fission. *Chemical Reviews* **110,** 6891–6936 (2010).

165. Wilson, M. W. B. *et al.* Ultrafast dynamics of exciton fission in polycrystalline pentacene. *Journal of the American Chemical Society* **133,** 11830–11833 (2011).

166. Congreve, D. N. *et al.* External quantum efficiency above 100% in a singlet-exciton-fission–based organic photovoltaic cell. *Science* **340** (2013).

167. Yoo, S., Domercq, B. & Kippelen, B. Efficient thin-film organic solar cells based on pentacene/$C_{60}$ heterojunctions. *Applied Physics Letters* **85,** 5427 (2004).

168. Ramanan, C., Smeigh, A. L., Anthony, J. E., Marks, T. J. & Wasielewski, M. R. Competition between singlet fission and charge separation in solution- processed blend films of 6,13-bis(triisopropylsilylethynyl)pentacene with sterically-encumbered perylene-3,4:9,10-bis(dicarboximide)s. *Journal of the American Chemical Society* **134,** 386–397 (2011).

169. Rao, A. *et al.* Exciton fission and charge generation via triplet excitons in pentacene/$C_{60}$ bilayers. *Journal of the American Chemical Society* **132,** 12698–12703 (2010).

170. Burdett, J. J. & Bardeen, C. J. The dynamics of singlet fission in crystalline tetracene and covalent analogs. *Accounts of chemical research* **46,** 1312–1320 (2013).

171. Tabernig, S. W., Daiber, B., Wang, T. & Ehrler, B. Enhancing silicon solar cells with singlet fission: The case for Förster resonant energy transfer using a quantum dot intermediate. *Journal of Photonics for Energy* **8,** 1 (2018).

172. MacQueen, R. *et al.* Crystalline silicon solar cells with tetracene interlayers: The path to silicon-singlet fission heterojunction devices. *Materials Horizons* **5,** 1065–1075 (2018).

173. Tabachnyk, M. *et al.* Resonant energy transfer of triplet excitons from pentacene to PbSe nanocrystals. *Nature Materials* **13,** 1033–1038 (2014).

174. Thompson, N. J. *et al.* Energy harvesting of non-emissive triplet excitons in tetracene by emissive PbS nanocrystals. *Nature Materials* **13,** 1039–1043 (2014).

175. Rao, A. & Friend, R. H. Harnessing singlet exciton fission to break the Shockley-Queisser limit. *Nature Reviews Materials* **2,** 17063 (2017).

176. Hanna, M. C. & Nozik, A. J. Solar conversion efficiency of photovoltaic and photoelectrolysis cells with carrier multiplication absorbers. *Journal of Applied Physics* **100,** 74510 (2006).

177. Yost, S. R., Hontz, E., Yeganeh, S. & Van Voorhis, T. Triplet vs singlet energy transfer in organic semiconductors: The tortoise and the hare. *The Journal of Physical Chemistry C* **116,** 17369–17377 (2012).

178. Wan, Y. *et al.* Cooperative singlet and triplet exciton transport in tetracene crystals visualized by ultrafast microscopy. *Nature Chemistry* **7,** 785–792 (2015).

179. Zhu, T., Wan, Y., Guo, Z., Johnson, J. & Huang, L. Two birds with one stone: Tailoring singlet fission for both triplet yield and exciton diffusion length. *Advanced Materials* **28,** 7539–7547 (2016).

180. Köhler, A & Bässler, H. Triplet states in organic semiconductors. *Materials Science and Engineering: R: Reports* **66,** 71–109 (2009).

181. Hinds, S. *et al.* NIR-emitting colloidal quantum dots having 26% luminescence quantum yield in buffer solution. *Journal of the American Chemical Society* **129,** 7218–7219 (2007).

182. Greben, M., Fucikova, A. & Valenta, J. Photoluminescence quantum yield of PbS nanocrystals in colloidal suspensions. *Journal of Applied Physics* **117,** 144306 (2015).

183. Akkerman, Q. A., Rainò, G., Kovalenko, M. V. & Manna, L. Genesis, challenges and opportunities for colloidal lead halide perovskite nanocrystals. *Nature Materials* **17,** 394–405 (2018).

184. Burkhard, G. F., Hoke, E. T. & McGehee, M. D. Accounting for interference, scattering, and electrode absorption to make accurate internal quantum efficiency measurements in organic and other thin solar cells. *Advanced Materials* **22,** 3293–3297 (2010).

185. Yang, L. *et al.* Solution-processable singlet fission photovoltaic devices. *Nano letters* **15,** 354–358 (2014).

186. Ehrler, B., Wilson, M. W. B., Rao, A., Friend, R. H. & Greenham, N. C. Singlet exciton fission-sensitized infrared quantum dot solar cells. *Nano Letters* **12,** 1053–1057 (2012).

187. Green, M. A. & Keevers, M. J. Optical properties of intrinsic silicon at 300 K. *Progress in Photovoltaics: Research and Applications* **3,** 189–192 (1995).

188. Gao, L., Lemarchand, F. & Lequime, M. Exploitation of multiple incidences spectrometric measurements for thin film reverse engineering. *Optics Express* **20,** 15734–15751 (2012).

189. Green, M. A., Emery, K., Hishikawa, Y., Warta, W. & Dunlop, E. D. Solar cell efficiency tables (version 38). *Progress in Photovoltaics: Research and Applications* **19,** 565–572 (2011).

190. Green, M. A., Emery, K., Hishikawa, Y., Warta, W. & Dunlop, E. D. Solar cell efficiency tables (version 39). *Progress in Photovoltaics: Research and Applications* **20,** 12–20 (2012).

191. Green, M. A., Emery, K., Hishikawa, Y., Warta, W. & Dunlop, E. D. Solar cell efficiency tables (version 40). *Progress in Photovoltaics: Research and Applications* **20,** 606–614 (2012).

192. Green, M. A., Emery, K., Hishikawa, Y., Warta, W. & Dunlop, E. D. Solar cell efficiency tables (version 47). *Progress in Photovoltaics: Research and Applications* **24,** 3–11 (2016).

193. Green, M. A. *et al.* Solar cell efficiency tables (version 49). *Progress in Photovoltaics: Research and Applications* **25,** 3–13 (2017).

194. Green, M. A., Emery, K., Hishikawa, Y., Warta, W. & Dunlop, E. D. Solar cell efficiency tables (version 45). *Progress in Photovoltaics: Research and Applications* **23,** 1–9 (2015).

195. Green, M. A., Emery, K., Hishikawa, Y., Warta, W. & Dunlop, E. D. Solar cell efficiency tables (version 51). *Progress in Photovoltaic Research and applications* **26,** 12–20 (2012).

196. Green, M. A., Emery, K., Hishikawa, Y., Warta, W. & Dunlop, E. D. Solar cell efficiency tables (version 48). *Progress in Photovoltaics: Research and Applications* **24,** 905–913 (2016).

197. Green, M. A., Emery, K., Hishikawa, Y., Warta, W. & Dunlop, E. D. Solar cell efficiency tables (version 44). *Progress in Photovoltaics: Research and Applications* **22,** 701–710 (2014).

198. Miller, G. L., Lang, D. V. & Kimerling, L. C. Capacitance transient spectroscopy. *Annual Review of Materials Science* **7,** 377–448 (2003).

199. Heath, J. & Zabierowski, P. in *Advanced characterization techniques for thin film solar cells* 93–119 (Wiley-VCH, Weinheim, Germany, 2016).

200. Li, J. V. & Ferrari, G. *Capacitance spectroscopy of semiconductors* (Jenny Stanford Publishing, 2018).

201. Von Hauff, E. Impedance spectroscopy for emerging photovoltaics. *Journal of Physical Chemistry C* **123,** 11329–11346 (2019).

202. Lang, D. V. Deep-level transient spectroscopy: A new method to characterize traps in semiconductors. *Journal of Applied Physics* **45,** 3023–3032 (1974).

203. Walter, T., Herberholz, R., Müller, C. & Schock, H. W. Determination of defect distributions from admittance measurements and application to Cu(In,Ga)$Se_2$ based heterojunctions. *Journal of Applied Physics* **80,** 4411–4420 (1996).

204. Miyata, A. *et al.* Direct measurement of the exciton binding energy and effective masses for charge carriers in organic-inorganic tri-halide perovskites. *Nature Physics* **11,** 582–587 (2015).

205. Shi, D. *et al.* Low trap-state density and long carrier diffusion in organolead trihalide perovskite single crystals. *Science* **347,** 519–522 (2015).

206. Yakunin, S. *et al.* Detection of X-ray photons by solution-processed lead halide perovskites. *Nature Photonics* **9,** 444–449 (2015).

207. Stranks, S. D. & Snaith, H. J. Metal-halide perovskites for photovoltaic and light-emitting devices. *Nature Nanotechnology* **10,** 391–402 (2015).

208. Zhao, Y. *et al.* Perovskite seeding growth of formamidinium-lead-iodide-based perovskites for efficient and stable solar cells. *Nature Communications* **9,** 1607 (2018).

209. Chen, Y. *et al.* Impacts of alkaline on the defects property and crystallization kinetics in perovskite solar cells. *Nature communications* **10,** 1112 (2019).

210. Heo, S. *et al.* Deep level trapped defect analysis in $CH_3NH_3PbI_3$ perovskite solar cells by deep level transient spectroscopy. *Energy and Environmental Science* **10,** 1128–1133 (2017).

211. Rosenberg, J. W., Legodi, M. J., Rakita, Y., Cahen, D. & Diale, M. Laplace current deep level transient spectroscopy measurements of defect states in methylammonium lead bromide single crystals. *Journal of Applied Physics* **122,** 145701 (2017).

212. Polyakov, A. Y. *et al.* Trap states in multication mesoscopic perovskite solar cells: A deep levels transient spectroscopy investigation. *Applied Physics Letters* **113,** 263501 (2018).

213. Almora, O., García-Batlle, M. & Garcia-Belmonte, G. Utilization of temperature-sweeping capacitive techniques to evaluate band gap defect densities in photovoltaic perovskites. *The Journal of Physical Chemistry Letters* **10,** 3661–3669 (2019).

214. Wang, H., Guerrero, A., Bou, A., Al-Mayouf, A. M. & Bisquert, J. Kinetic and material properties of interfaces governing slow response and long timescale phenomena in perovskite solar cells. *Energy & Environmental Science* **12,** 2054–2079 (2019).

215. Futscher, M. H. *et al.* Quantification of ion migration in $CH_3NH_3PbI_3$ perovskite solar cells by transient capacitance measurements. *Materials Horizons* **6,** 1497–1503 (2019).

216. Heiser, T. & Weber, E. Transient ion-drift-induced capacitance signals in semiconductors. *Physical Review B* **58,** 3893–3903 (1998).

217. Lopez-Varo, P. *et al.* Device physics of hybrid perovskite solar cells: Theory and experiment. *Advanced Energy Materials* **8,** 1702772 (2018).

218. Pockett, A. *et al.* Microseconds, milliseconds and seconds: deconvoluting the dynamic behaviour of planar perovskite solar cells. *Physical Chemistry Chemical Physics* **19,** 5959–5970 (2017).

219. de L. Kronig, R. On the theory of dispersion of X-rays. *Journal of the Optical Society of America* **12,** 547 (1926).

220. Debye, P. Part I. Dielectric constant. Energy absorption in dielectrics with polar molecules. *Transactions of the Faraday Society* **30,** 679–684 (1934).

221. Shockley, W. & Read, W. T. Statistics of the recombinations of holes and electrons. *Physical Review* **87,** 835–842 (1952).

222. Hall, R. N. Electron-hole recombination in germanium. *Physical Review* **87,** 387 (1952).

223. Yang, Z. *et al.* Impact of the halide cage on the electronic properties of fully inorganic cesium lead halide perovskites. *ACS Energy Letters* **2,** 1621–1627 (2017).

224. Almora, O. *et al.* Capacitive dark currents, hysteresis, and electrode polarization in lead halide perovskite solar cells. *Journal of Physical Chemistry Letters* **6,** 1645–1652 (2015).

225. Bisquert, J., Garcia-Belmonte, G. & Guerrero, A. in *Organic-inorganic halide perovskite photovoltaics: from fundamentals to device architectures* 163–199 (Springer, 2016).

226. Hückel, E. in *Ergebnisse der exakten Naturwissenschaften* 199–276 (Springer, 1924).

227. Vineyard, G. H. Frequency factors and isotope effects in solid state rate processes. *Journal of Physics and Chemistry of Solids* **3,** 121–127 (1957).

228. Meggiolaro, D., Mosconi, E. & De Angelis, F. Formation of surface defects dominates ion migration in lead-halide perovskites. *ACS Energy Letters* **4,** 779–785 (2019).

229. Koettgen, J., Zacherle, T., Grieshammer, S. & Martin, M. Ab initio calculation of the attempt frequency of oxygen diffusion in pure and samarium doped ceria. *Physical Chemistry Chemical Physics* **19,** 9957–9973 (2017).

230. Peng, W. *et al.* Quantification of ionic diffusion in lead halide perovskite single crystals. *ACS Energy Letters* **3,** 1477–1481 (2018).

231. Bag, M. *et al.* Kinetics of ion transport in perovskite active layers and its implications for active layer stability. *Journal of the American Chemical Society* **137,** 13130–13137 (2015).

232. Kim, H.-S. *et al.* Control of I-V hysteresis in $CH_3NH_3PbI_3$ perovskite solar cell. *The Journal of Physical Chemistry Letters* **6,** 4633–4639 (2015).

233. Zarazua, I. *et al.* Surface recombination and collection efficiency in perovskite solar cells from impedance analysis. *The Journal of Physical Chemistry Letters* **7,** 5105–5113 (2016).

234. Guerrero, A. *et al.* Properties of contact and bulk impedances in hybrid lead halide perovskite solar cells including inductive loop elements. *The Journal of Physical Chemistry C* **120,** 8023–8032 (2016).

235. Heiser, T. & Mesli, A. Determination of the copper diffusion coefficient in silicon from transient ion-drift. *Applied Physics A Solids and Surfaces* **57,** 325–328 (1993).

236. Bisquert, J. Chemical capacitance of nanostructured semiconductors: Its origin and significance for nanocomposite solar cells. *Physical Chemistry Chemical Physics* **5,** 5360–5364 (2003).

237. Almora, O., Aranda, C., Mas-Marzá, E. & Garcia-Belmonte, G. On Mott-Schottky analysis interpretation of capacitance measurements in organometal perovskite solar cells. *Applied Physics Letters* **109,** 173903 (2016).

238. Fischer, M., Tvingstedt, K., Baumann, A. & Dyakonov, V. Doping profile in planar hybrid perovskite solar cells identifying mobile ions. *ACS Applied Energy Materials* **1,** acsaem.8b01119 (2018).

239. Luo, Y. *et al.* Direct observation of halide migration and its effect on the photoluminescence of methylammonium lead bromide perovskite single crystals. *Advanced Materials* **29,** 1703451 (2017).

240. Azpiroz, J. M., Mosconi, E., Bisquert, J. & De Angelis, F. Defect migration in methylammonium lead iodide and its role in perovskite solar cell operation. *Energy and Environmental Science* **8,** 2118–2127 (2015).

241. Mizusaki, J., Arai, K. & Fueki, K. Ionic conduction of the perovskite-type halides. *Solid State Ionics* **11,** 203–211 (1983).

242. Cho, H. *et al.* High-efficiency solution-processed inorganic metal halide perovskite light-emitting diodes. *Advanced Materials* **29,** 1700579 (2017).

243. Gangishetty, M. K., Hou, S., Quan, Q. & Congreve, D. N. Reducing architecture limitations for efficient blue perovskite light-emitting diodes. *Advanced Materials* **30,** 1706226 (2018).

244. Snaith, H. J. *et al.* Anomalous hysteresis in perovskite solar cells. *The Journal of Physical Chemistry Letters* **5,** 1511–1515 (2014).

245. Nandal, V. & Nair, P. R. Predictive modeling of ion migration induced degradation in perovskite solar cells. *ACS Nano* **11,** 11505–11512 (2017).

246. Bowring, A. R., Bertoluzzi, L., O'Regan, B. C. & McGehee, M. D. Reverse bias behavior of halide perovskite solar cells. *Advanced Energy Materials* **8,** 1702365 (2018).

247. Haruyama, J., Sodeyama, K., Han, L. & Tateyama, Y. First-principles study of ion diffusion in perovskite solar cell sensitizers. *Journal of the American Chemical Society* **137,** 10048–10051 (2015).

248. Meloni, S. *et al.* Ionic polarization-induced current-voltage hysteresis in $CH_3NH_3PbX_3$ perovskite solar cells. *Nature Communications* **7,** 10334 (2016).

249. Delugas, P., Caddeo, C., Filippetti, A. & Mattoni, A. Thermally activated point defect diffusion in methylammonium lead trihalide: Anisotropic and ultrahigh mobility of iodine. *Journal of Physical Chemistry Letters* **7,** 2356–2361 (2016).

250. Game, O. S., Buchsbaum, G. J., Zhou, Y., Padture, N. P. & Kingon, A. I. Ions matter: description of the anomalous electronic behavior in methylammonium lead halide perovskite devices. *Advanced Functional Materials* **27,** 1606584 (2017).

251. Xing, J. *et al.* Ultrafast ion migration in hybrid perovskite polycrystalline thin films under light and suppression in single crystals. *Physical Chemistry Chemical Physics* **18,** 30484–30490 (2016).

252. Yu, H., Lu, H., Xie, F., Zhou, S. & Zhao, N. Native defect-induced hysteresis behavior in organolead iodide perovskite solar cells. *Advanced Functional Materials* **26,** 1411–1419 (2016).

253. DeQuilettes, D. W. *et al.* Photo-induced halide redistribution in organic-inorganic perovskite films. *Nature Communications* **7,** 11683 (2016).

254. Yin, X. *et al.* High efficiency inverted planar perovskite solar cells with solution-processed $NiO_X$ hole contact. *ACS Applied Materials & Interfaces* **9,** 2439–2448 (2017).

255. Garcia-Belmonte, G. & Bisquert, J. Distinction between capacitive and noncapacitive hysteretic currents in operation and degradation of perovskite solar cells. *ACS Energy Letters* **1,** 683–688 (2016).

256. Manders, J. R. *et al.* Solution-processed nickel oxide hole transport layers in high efficiency polymer photovoltaic cells. *Advanced Functional Materials* **23,** 2993–3001 (2013).

257. Zhang, Y. *et al.* Charge selective contacts, mobile ions and anomalous hysteresis in organic–inorganic perovskite solar cells. *Materials Horizons* **2,** 315–322 (2015).

258. Luo, Q. *et al.* Iodide-reduced graphene oxide with dopant-free spiro-OMeTAD for ambient stable and high-efficiency perovskite solar cells. *Journal of Materials Chemistry A* **3,** 15996–16004 (2015).

259. Ginting, R. T. *et al.* Low-temperature operation of perovskite solar cells: With efficiency improvement and hysteresis-less. *Nano Energy* **27,** 569–576 (2016).

260. Bruno, A. *et al.* Temperature and electrical poling effects on ionic motion in MAPbI3 photovoltaic cells. *Advanced Energy Materials* **7,** 1700265 (2017).

261. Yuan, Y. *et al.* Electric-field-driven reversible conversion between methylammonium lead triiodide perovskites and lead iodide at elevated temperatures. *Advanced Energy Materials* **6,** 1501803 (2016).

262. Weller, M. T. *et al.* Complete structure and cation orientation in the perovskite photovoltaic methylammonium lead iodide between 100 and 352 K. *Chem. Commun.* **51,** 4180–4183 (2015).

263. Onoda-Yamamuro, N., Yamamuro, O., Matsuo, T. & Suga, H. p-T phase relations of $CH_3NH_3PbX_3$ (X = Cl, Br, I) crystals. *Journal of Physics and Chemistry of Solids* **53,** 277–281 (1992).

264. Zamouche, A., Heiser, T. & Mesli, A. Investigation of fast diffusing impurities in silicon by a transient ion drift method. *Applied Physics Letters* **66,** 631 (1995).

265. Birkhold, S. T. *et al.* Interplay of mobile ions and injected carriers creates recombination centers in metal halide perovskites under bias. *ACS Energy Letters* **3,** 1279–1286 (2018).

266. Bi, E. *et al.* Diffusion engineering of ions and charge carriers for stable efficient perovskite solar cells. *Nature Communications* **8,** 15330 (2017).

267. Wang, S. *et al.* Silver iodide formation in methyl ammonium lead iodide perovskite solar cells with silver top electrodes. *Advanced Materials Interfaces* **2,** 1500195 (2015).

268. Egger, D. A., Kronik, L. & Rappe, A. M. Theory of hydrogen migration in organic-inorganic halide perovskites. *Angewandte Chemie - International Edition* **54,** 12437–12441 (2015).

269. Bertoluzzi, L. *et al.* In situ measurement of electric-field screening in hysteresis-free PTAA/$FA_{0.83}Cs_{0.17}Pb(I_{0.83}Br_{0.17})_3$/$C_{60}$ perovskite solar cells gives an ion mobility of $3 \times 10^{-7}$ $cm^2/(Vs)$, 2 orders of magnitude faster than reported for metal-oxide-contacted. *Journal of the American Chemical Society* **140,** 12775–12784 (2018).

270. Hoque, M. N. F. *et al.* Ionic and optical properties of methylammonium lead iodide perovskite across the tetragonal–cubic structural phase transition. *ChemSusChem* **9,** 2692–2698 (2016).

271. Yun, J. S. *et al.* Critical role of grain boundaries for ion migration in formamidinium and methylammonium lead halide perovskite solar cells. *Advanced Energy Materials* **6,** 1600330 (2016).

272. Sanchez, R. S. *et al.* Slow dynamic processes in lead halide perovskite solar cells. Characteristic times and hysteresis. *Journal of Physical Chemistry Letters* **5,** 2357–2363 (2014).

273. Gottesman, R. *et al.* Extremely slow photoconductivity response of $CH_3NH_3PbI_3$ perovskites suggesting structural changes under working conditions. *Journal of Physical Chemistry Letters* **5,** 2662–2669 (2014).

274. Yin, W. J., Shi, T. & Yan, Y. Unusual defect physics in $CH_3NH_3PbI_3$ perovskite solar cell absorber. *Applied Physics Letters* **104,** 063903 (2014).

275. Deng, L. L., Xie, S. Y. & Gao, F. Fullerene-based materials for photovoltaic applications: Toward efficient, hysteresis-free, and stable perovskite solar cells. *Advanced Electronic Materials* **4,** 1700435 (2017).

276. Zhu, Z. *et al.* High-performance hole-extraction layer of sol-gel-processed NiO nanocrystals for inverted planar perovskite solar cells. *Angewandte Chemie - International Edition* **53,** 12571–12575 (2014).

277. Chen, W. *et al.* Efficient and stable large-area perovskite solar cells with inorganic charge extraction layers. *Science* **350,** 944–948 (2015).

278. Mosconi, E., Meggiolaro, D., Snaith, H. J., Stranks, S. D. & De Angelis, F. Light-induced annihilation of Frenkel defects in organo-lead halide perovskites. *Energy and Environmental Science* **9,** 3180–3187 (2016).

279. Brivio, F., Butler, K. T., Walsh, A. & van Schilfgaarde, M. Relativistic quasiparticle self-consistent electronic structure of hybrid halide perovskite photovoltaic absorbers. *Physical Review B - Condensed Matter and Materials Physics* **89,** 155204 (2014).

280. Frolova, L. A., Dremova, N. N. & Troshin, P. A. The chemical origin of the p-type and n-type doping effects in the hybrid methylammonium-lead iodide (MAPbI3) perovskite solar cells. *Chemical Communications* **51,** 14917–14920 (2015).

281. Saliba, M. *et al.* Cesium-containing triple cation perovskite solar cells: Improved stability, reproducibility and high efficiency. *Energy and Environmental Science* **9,** 1989–1997 (2016).

282. Abdi-Jalebi, M. *et al.* Maximizing and stabilizing luminescence from halide perovskites with potassium passivation. *Nature* **555,** 497–501 (2018).

283. Abdi-Jalebi, M. *et al.* Potassium-and rubidium-passivated alloyed perovskite films: Optoelectronic properties and moisture stability. *ACS Energy Letters* **3,** 2671–2678 (2018).

284. Van Reenen, S., Kemerink, M. & Snaith, H. J. Modeling anomalous hysteresis in perovskite solar cells. *Journal of Physical Chemistry Letters* **6,** 3808–3814 (2015).

285. Richardson, G. *et al.* Can slow-moving ions explain hysteresis in the current-voltage curves of perovskite solar cells? *Energy and Environmental Science* **9,** 1476–1485 (2016).

286. Bisquert, J., Garcia-Belmonte, G. & Mora-Sero, I. in *Unconventional thin film photovoltaics* 57–106 (Royal Society of Chemistry, Cambridge, 2016).

287. Kim, S.-G. *et al.* Potassium ions as a kinetic controller in ionic double layers for hysteresis-free perovskite solar cells. *Journal of Materials Chemistry A* **7,** 18807–18815 (2019).

288. Kubicki, D. J. *et al.* Phase segregation in Cs-, Rb- and K-doped mixed-cation $(MA)_x(FA)_{1-x}PbI3$ hybrid perovskites from solid-state NMR. *Journal of the American Chemical Society* **139,** 14173–14180 (2017).

289. Ahn, N. *et al.* Trapped charge-driven degradation of perovskite solar cells. *Nature Communications* **7,** 13422 (2016).

290. Chen, S. *et al.* Mobile ion induced slow carrier dynamics in organic-inorganic perovskite $CH_3NH_3PbBr_3$. *ACS Applied Materials and Interfaces* **8,** 5351–5357 (2016).

291. Tan, Z.-K. *et al.* Bright light-emitting diodes based on organometal halide perovskite. *Nature Nanotechnology* **9,** 687–692 (2014).

292. Yuan, M. *et al.* Perovskite energy funnels for efficient light-emitting diodes. *Nature Nanotechnology* **11,** 872–877 (2016).

293. Wang, N. *et al.* Perovskite light-emitting diodes based on solution-processed self-organized multiple quantum wells. *Nature Photonics* **10,** 699–704 (2016).

294. Yang, X. *et al.* Efficient green light-emitting diodes based on quasi-two-dimensional composition and phase engineered perovskite with surface passivation. *Nature Communications* **9,** 570 (2018).

295. Lin, K. *et al.* Perovskite light-emitting diodes with external quantum efficiency exceeding 20 per cent. *Nature* **562,** 245–248 (2018).

296. Cho, H., Kim, Y.-H. H., Wolf, C., Lee, H.-D. D. & Lee, T.-W. W. Improving the stability of metal halide perovskite materials and light-emitting diodes. *Advanced Materials* **30,** 1704587 (2018).

297. Vashishtha, P. & Halpert, J. E. Field-driven ion migration and color instability in red-emitting mixed halide perovskite nanocrystal light-emitting diodes. *Chemistry of Materials* **29,** 5965–5973 (2017).

298. Yi, C. *et al.* Entropic stabilization of mixed A-cation ABX3 metal halide perovskites for high performance perovskite solar cells. *Energy and Environmental Science* **9,** 656–662 (2016).

299. Geyer, S. M., Scherer, J. M., Moloto, N., Jaworski, F. B. & Bawendi, M. G. Efficient luminescent down-shifting detectors based on colloidal quantum dots for dual-band detection applications. *ACS Nano* **5,** 5566–5571 (2011).

300. Pering, S. R. *et al.* Azetidinium lead iodide for perovskite solar cells. *Journal of Materials Chemistry A* **5,** 20658–20665 (2017).

301. De Marco, N. *et al.* Guanidinium: A route to enhanced carrier lifetime and open-circuit voltage in hybrid perovskite solar cells. *Nano Letters* **16,** 1009–1016 (2016).

302. Kubicki, D. J. *et al.* Formation of stable mixed guanidinium-methylammonium phases with exceptionally long carrier lifetimes for high-efficiency lead iodide-based perovskite photovoltaics. *Journal of the American Chemical Society* **140,** 3345–3351 (2018).

303. Kieslich, G., Sun, S. & Cheetham, A. K. Solid-state principles applied to organic–inorganic perovskites: New tricks for an old dog. *Chem. Sci.* **5,** 4712–4715 (2014).

304. Ferdani, D. W. *et al.* Partial cation substitution reduces iodide ion transport in lead iodide perovskite solar cells. *Energy & Environmental Science* **12,** 2264–2272 (2019).

305. Zou, S. *et al.* Stabilizing cesium lead halide perovskite lattice through Mn(II) substitution for air-stable light-emitting diodes. *Journal of the American Chemical Society* **139,** 11443–11450 (2017).

306. Das Adhikari, S., Guria, A. K. & Pradhan, N. Insights of doping and the photoluminescence properties of Mn-doped perovskite nanocrystals. *The Journal of Physical Chemistry Letters* **10,** 2250–2257 (2019).

307. Bera, S. *et al.* Limiting heterovalent B-Site doping in $CsPbI_3$ nanocrystals: Phase and optical stability. *ACS Energy Letters* **4,** 1364–1369 (2019).

308. Hou, S., Gangishetty, M. K., Quan, Q. & Congreve, D. N. Efficient blue and white perovskite light-emitting diodes via manganese doping. *Joule* **2,** 2421–2433 (2018).

309. Gangishetty, M. K., Sanders, S. N. & Congreve, D. N. $Mn^{2+}$ doping enhances the brightness, efficiency, and stability of bulk perovskite light-emitting diodes. *ACS Photonics* **6,** 1111–1117 (2019).

310. Cortecchia, D. *et al.* Defect engineering in 2D perovskite by Mn(II) doping for light-emitting applications. *Chem* **5,** 2146–2158 (2019).

311. Pitarch-Tena, D., Ngo, T. T., Vallés-Pelarda, M., Pauporté, T. & Mora-Seró, I. Impedance spectroscopy measurements in perovskite solar cells: Device stability and Noise reduction. *ACS Energy Letters* **3,** 1044–1048 (2018).

312. Bisquert, J. *Nanostructured energy devices: Equilibrium concepts and kinetics* 352 (CRC Press, 2015).

313. Almora, O., Guerrero, A. & Garcia-Belmonte, G. Ionic charging by local imbalance at interfaces in hybrid lead halide perovskites. *Applied Physics Letters* **108,** 043903 (2016).

314. Schoonman, J. The ionic conductivity of pure and doped lead bromide single crystals. *Journal of Solid State Chemistry* **4,** 466–474 (1972).

315. Liu, W. *et al.* $Mn^{2+}$-doped lead halide perovskite nanocrystals with dual-color emission controlled by halide content. *Journal of the American Chemical Society* **138,** 14954–14961 (2016).

316. Domanski, K. *et al.* Not all that glitters is gold: metal-migration-induced degradation in perovskite solar cells. *ACS Nano* **10,** 6306–6314 (2016).

317. Seo, H. K. *et al.* Efficient flexible organic/inorganic hybrid perovskite light-emitting diodes based on graphene anode. *Advanced Materials* **29,** 1605587 (2017).

# Summary

Solar power is the most promising energy source to play a key role in the transition to clean energy worldwide. Scaling solar energy by the required margin requires continuous development towards new concepts and higher efficiencies. Metal halide perovskites have proven their potential for low-cost and highly efficient solar cells and are arguably one of the most promising materials for next-generation tandem solar cells in combination with silicon. Tandem solar cells could increase power-conversion efficiencies at low costs and provide an entry point for perovskites into the mass market.

PART I: EFFICIENCY POTENTIAL UNDER REALISTIC CONDITIONS

The performance of solar cells is typically assessed using standard test conditions assuming a temperature of 25 °C and an incident solar spectrum that mimics a sunny summer day in the northern hemisphere (AM1.5G). However, the actual usable energy yield is strongly dependent on realistic operation conditions and the location of deployment. We have developed a model to predict the performance of next-generation solar cells under realistic operating conditions, described in **Chapter 1**, which is the foundation of the first part of this thesis. The model allows to predict changes in the performance of realistic solar cells upon changes in temperature, solar spectrum, and irradiance by including device- and material-specific parameters.

In **Chapter 2** we analyse the variation of solar spectra measured throughout an entire year in two locations with distinctively different climate conditions. We find a broad distribution of measured solar spectra for different weather conditions, seasons, and times of day. We use the measured outdoor illumination conditions to analyse their effect on the limiting efficiency of different tandem solar cell configurations and show that limiting efficiencies are above 41% for all tandem configurations even at non-ideal climate conditions. We furthermore show that different tandem configurations place different constraints on the choice of band gaps and that their efficiencies are strongly influenced by spectral and temperature changes, with the monolithically-integrated series tandem being most affected as it is subject to current matching.

While in the previous chapter we use ideal subcells, in **Chapter 3** we proceed by quantifying the performance potential of perovskite/silicon tandem solar cells

from realistic subcells under measured outdoor illumination conditions. We show quantitatively that the optimisation of the nonradiative recombination, parasitic resistances, and optical losses of the perovskite solar cell have the potential for an absolute efficiency increase of perovskite/silicon tandem solar cells of 3 to 4% each. When improving the perovskite solar cell to its optimum, we find that the efficiency of silicon solar cells can be improved by up to 14% absolute when used in a tandem configuration with perovskites.

In **Chapter 4** we show that using bifacial silicon solar cells can further increase the efficiency of perovskite/silicon tandem solar cells by 5 to 6% absolute. We find that bifacial perovskite/silicon tandem solar cells allow for a wide range of perovskite band gaps to be used in the monolithically-integrated series tandem configuration by carefully designing their surroundings. In addition, we find that the stability of the series tandem against changing solar spectra is improved by the use of a bifacial silicon solar cell, as the current-matching constraints are partially relaxed. As a result, both the series tandem and the four-terminal tandem configurations offer efficiency potentials above 42% under realistic operating conditions.

**Chapter 5** discusses a promising alternative to tandem solar cells – the singlet fission photon multiplier. In contrast to tandem solar cells, the photon multiplier can be easily integrated into existing solar cell technologies without modification of the underlying solar cell. We show that the exciton multiplication process singlet fission can be used to reduce thermalization losses in conventional silicon solar cells, by modulating the incoming solar spectrum. We simulate the performance of such a photon multiplier in combination with a variety of silicon solar cells under realistic operation conditions. We find that the photon multiplier has the potential to increase the efficiency of silicon solar cells by up to 4.2% absolute even at realistic operation conditions, with little dependence on the location of deployment.

### Part II: Quantifying ion migration in metal halide perovskites

Ion migration in perovskites leads to device degradation and changes the properties of the device during operation, both undesirable for applications. The understanding of ion migration is crucial for the fabrication of stable and efficient perovskite devices. We have pioneered a technique based on time-resolved capacitance measurements to quantify mobile ions in perovskite-based devices such as solar cells and light-emitting diodes, which forms the basis for the second part of this thesis.

In **Chapter 6** we show how measuring the capacitance in both the frequency and the time domain can be used to study ionic dynamics within perovskite devices, quantifying activation energy, diffusion coefficient, sign of charge, concentration, and the length of the ionic double layer. We furthermore show how time-dependent

capacitance measurements can be used to distinguish between effects caused by electronic defect states and mobile ions.

In **Chapter 7** we quantify mobile ions in the prototype metal halide perovskite, $MAPbI_3$. We show that both cations ($MA^+$) and halides ($I^-$) migrate, but with very different diffusion coefficients ($10^{-12}$ and $10^{-9}$ $cm^2$ $s^{-1}$, respectively). Only the migration of the cations is slow enough to explain the often-observed current-voltage hysteresis in solar cells from $MAPbI_3$. We find that the concentration of mobile cations ($10^{16}$ $cm^{-3}$) is significantly higher than the concentration of mobile halides ($10^{15}$ $cm^{-3}$) and the activation energy for mobile halides is highly reproducible for different devices with 0.29 eV, while the activation energy of mobile cations depends strongly on device fabrication.

Record-efficiency perovskite solar cells are made from a mixture of cations and halides. In **Chapter 8** we investigate ion migration in these mixed-cation mixed-halide perovskites in different device architectures. We observe no evidence of mobile cations, suggesting that cation migration is impeded in these mixed perovskites. We furthermore find that the activation energy (0.28 eV) and concentration ($10^{15}$ $cm^{-3}$) of mobile halide ions are similar to those in $MAPbI_3$ perovskites. However, the diffusion coefficient is reduced by one to two orders of magnitude compared to $MAPbI_3$ ($10^{-11}$ to $10^{-10}$ $cm^2$ $s^{-1}$). In contrast to $MAPbI_3$, our results indicate that the migration of halides is the cause of the current-voltage hysteresis in mixed perovskites. We furthermore show that potassium passivation does not affect the activation energy, but reduces the density of mobile ions by one order of magnitude by removing excess halides from the bulk. The lower mobile ion concentration leads to an improved stability and reduces photo-induced halide segregation.

In **Chapter 9** we investigate the effect of the partial substitution of lead by manganese on mobile ions in perovskite light-emitting diodes. We find that manganese substitution has only minor effects on the density ($10^{15}$ $cm^{-3}$) and diffusion coefficient ($10^{-11}$ $cm^2$ $s^{-1}$) of mobile halides. The activation energy for halide migration, however, increases twofold from 0.14 to 0.30 eV upon manganese substitution due to the smaller ionic radius of manganese compared to lead, contracting the perovskite lattice. As a result, we assume that the amount of mobile ions migrating into the contact layers and the amount of ions migrating from the contact layers into the perovskite bulk are reduced, which leads to an increase in the stability of the device.

Overall, the first part of this thesis provides realistic estimates of the efficiency potential of next-generation solar cell technologies under realistic outdoor operation conditions to estimate their maximum annual energy yield. Our results provide

quantitative insights on how the reduction of dominant loss channels improves the efficiency of next-generation solar cells, paving the way for future efficiency improvements. The second part of this thesis offers quantitative insights into the effect of different additives and perovskite compositions on ion migration in perovskite-based devices. These findings will guide future investigations on ion migration and move the research on stable perovskite-based devices from an empirical approach towards a rational development.

# Samenvatting

Zonne-energie is de meest veelbelovende energiebron om wereldwijd een belangrijke rol te spelen in de transitie naar schone energie. Om het gebruik van zonne-energie op te schalen naar de benodigde hoeveelheid zijn nieuwe concepten en zonnecellen met hogere efficiëntie nodig. Metaalhalide perovskieten hebben een grote potentie om goedkope en zeer efficiënte zonnecellen op te leveren, en worden gezien als een van de meest veelbelovende materialen voor de nieuwe generatie tandemzonnecellen, in combinatie met siliciumzonnecellen. Deze tandemzonnecellen zijn efficiënter in het omzetten van licht in elektriciteit, relatief goedkoop, en vormen een toegangspunt voor de grootschalige productie van perovskieten.

### Deel I: Potentiële efficiëntie onder realistische omstandigheden

Zonnecellen worden normaliter getest onder standaardomstandigheden, waarbij een temperatuur van 25 °C en een zonnespectrum dat kenmerkend is voor een zonnige zomerdag op het noordelijk halfrond (AM1.5G) worden aangenomen. Echter is de bruikbare energieopbrengst van een zonnecel afhankelijk van realistische omstandigheden en de locatie waarop deze gebruikt wordt. Wij hebben een model ontwikkeld om de energieopbrengst van nieuwe generatie zonnecellen te voorspellen onder realistische omstandigheden. Dit model staat beschreven in **hoofdstuk 1**, en vormt het fundament van het eerste deel van dit proefschrift. Met dit model kunnen we voorspellen hoe veranderingen in temperatuur, het zonnespectrum en lichtsterkte de energieopbrengst van realistische zonnecellen beïnvloeden, gebruik makende van parameters specifiek voor een type materiaal of zonnecel.

In **hoofdstuk 2** analyseren we de variatie van zonnespectra die gedurende één jaar gemeten zijn op twee locaties met een totaal verschillend klimaat. We zien dat de gemeten zonnespectra zeer uiteenlopend zijn, afhankelijk van de weersomstandigheden, seizoenen en het tijdstip van de dag. Deze gemeten zonnespectra worden vervolgens gebruikt om te berekenen wat de efficiëntie is van verschillende typen tandemzonnecellen, en observeren dat deze minstens 41% is, zelfs onder niet-ideale klimaatomstandigheden. Verder laten we zien dat de keuze van de optimale bandkloof afhankelijk is van de configuratie van de tandemzonnecel, en dat de energieopbrengst sterk beïnvloed wordt door veranderingen in het spectrum van de zon en de temperatuur. De tandemzonnecel in een monolithisch geïntegreerde se-

rieschakeling wordt hierdoor het meest beïnvloed, omdat hierbij de stroomsterkte van beide subcellen overeen moet komen voor minimale verliezen.

Terwijl we in het voorgaande hoofdstuk ideale sub-zonnecellen aannamen, gaan we in **hoofdstuk 3** verder met het kwantificeren van de potentiële energieopbrengst van perovskiet-silicium tandemzonnecellen met realistische sub-zonnecellen, wederom gebruik makende van gemeten zonnespectra. We laten kwantitatief zien dat het optimaliseren van de niet-stralende recombinatie, parasitaire weerstand en optische verliezen van de perovskietzonnecel de absolute efficiëntie van de perovskiet-silicium tandemzonnecel elk met 3 tot 4%-punt kan verhogen. Als de perovskietzonnecel nog verder verbeterd wordt, zou de efficiëntie van siliciumzonnecellen zelfs met 14%-punt verhoogd kunnen worden middels een tandemconfiguratie met perovskietzonnecellen.

In **hoofdstuk 4** laten we zien dat dubbelzijdige siliciumzonnecellen de efficiëntie van perovskiet-silicium tandemzonnecellen met 5 tot 6%-punt kan verhogen. Een andere bevinding is dat in dubbelzijdige perovskiet-silicium tandemzonnecellen in een monolithisch geïntegreerde serieschakeling een scala aan perovskietbandkloofwaardes gebruikt kan worden door de omgeving zorgvuldig te ontwerpen. Verder observeren we dat het gebruik van een dubbelzijdige siliciumzonnecel een serie geschakelde tandemzonnecel stabieler maakt tegen wisselende zonnespectra, omdat er minder beperkingen zijn door subcellen die verschillende stroomsterktes genereren. Ten gevolge hiervan hebben zowel de serie geschakelde tandemzonnecel als de tandemconfiguratie met vier aansluitingen een potentiele efficiëntie van meer dan 42% onder realistische omstandigheden.

In **hoofdstuk 5** bespreken we een veelbelovend alternatief voor tandemzonnecellen – fotonenvermenigvuldiging door singletsplitsing. In tegenstelling tot tandemzonnecellen kan fotonenvermenigvuldiging eenvoudig geïntegreerd worden in bestaande zonneceltechnologieën zonder dat de onderliggende zonnecel aangepast hoeft te worden. We laten zien dat het vermenigvuldigen van excitonen door singletsplitsing het zonnespectrum verandert, en zodoende gebruikt kan worden om warmteverliezen in conventionele siliciumzonnecellen te verminderen. We simuleren de energieopbrengst van de combinatie van zo'n fotonenvermenigvuldiger met een variëteit aan siliciumzonnecellen onder realistische omstandigheden. We zien dat de fotonenvermenigvuldiger de potentie heeft om de efficiëntie van siliciumzonnecellen met 4.2 %-punt te verbeteren, en dat dit nauwelijks afhankelijk is van de locatie.

## DEEL II: HET KWANTIFICEREN VAN IONMIGRATIE IN METAALHALIDE PEROVSKIETEN

Migratie van ionen in perovskieten resulteert in degradatie van de zonnecel en veranderingen in diens eigenschappen: beiden zijn ongunstig voor toepassingen. Begrip van deze ionmigratie is cruciaal voor het fabriceren van stabiele en efficiënte perovskietzonnecellen. Wij zijn pionier geweest in het ontwikkelen van een techniek die gebaseerd is op tijdsopgeloste capaciteitsmetingen, waarmee we mobiele ionen in bijvoorbeeld zonnecellen of leds kunnen kwantificeren, wat de basis vormt van het tweede gedeelte van dit proefschrift.

In **hoofdstuk 6** laten we zien hoe het meten van de elektrische capaciteit in zowel het frequentie- als het tijdsdomein gebruikt kan worden om de dynamiek van ionen de bestuderen in perovskietzonnecellen. Hierbij worden de activeringsenergie, de diffusiecoëfficiënt, het teken van de lading, de concentratie en de lengte van de ionen dubbellaag gekwantificeerd. Verder laten we zien hoe tijdsopgeloste capaciteitsmetingen gebruikt kunnen worden om effecten veroorzaakt door elektronische defecten en mobiele ionen van elkaar te onderscheiden.

In **hoofdstuk 7** kwantificeren we mobiele ionen in het prototype metaalhalide perovskiet: $MAPbI_3$. We observeren dat zowel kationen ($MA^+$) en haliden ($I^-$) migreren, echter met zeer uiteenlopende diffusiecoëfficiënten (van respectievelijk $10^{-12}$ en $10^{-9}$ $cm^2s^{-1}$). Enkel de migratie van de kationen is langzaam genoeg om de hysterese te verklaren die vaak geobserveerd wordt in de stroom-spanningskarakteristieken van $MAPI_3$-zonnecellen. We zien dat de concentratie van mobiele kationen ($10^{16}$ $cm^{-3}$) significant hoger is dan de concentratie van mobiele haliden ($10^{15}$ $cm^{-3}$) en dat de activeringsenergie voor mobiele haliden een zeer reproduceerbare waarde heeft van 0.29 eV, terwijl de activeringsenergie voor mobiele kationen van de fabricatie afhangt.

De perovskietzonnecellen met de hoogste efficiëntie worden gemaakt van een mengsel van kationen en haliden. In **hoofdstuk 8** onderzoeken we ionmigratie in dit type perovskieten met een kation- en halidemengsel in verschillende structuren. We observeren geen mobiele kationen, wat suggereert dat de kationmigratie wordt onderdrukt in perovskieten met dit kationmengsel. Verder observeren we dat zowel de activeringsenergie (0.28 eV) als de concentratie ($10^{15}$ $cm^{-3}$) van mobiele halideionen dezelfde waarde hebben als in de $MAPbI_3$ perovskieten. De diffusiecoefficient ($10^{-11}$ à $10^{-10}$ $cm^2s^{-1}$) is echter één à twee ordegroottes kleiner dan voor $MAPbI_3$. In tegenstelling tot $MAPbI_3$ suggereren onze resultaten dat de hysterese in stroomspanningskarakteristieken van gemengde perovskieten wordt veroorzaakt door de migratie van haliden. Verder zien we dat passivering met kalium de activeringsenergie niet beïnvloedt maar wel de concentratie van mobiele ionen met één orde-

grootte verlaagt, door het overschot aan aan haliden uit de bulk te verwijderen. De lagere concentratie mobiele ionen verbetert de stabiliteit en vermindert de lichtgeïnduceerde halidesegregatie.

In **hoofdstuk 9** onderzoeken we het effect van het gedeeltelijk vervangen van lood door mangaan op de mobiele ionen in perovskietleds. We observeren dat deze mangaansubstitutie slechts een marginaal effect heeft op de concentratie ($10^{15}$ $cm^{-3}$) en diffusiecoëfficiënt ($10^{-11}$ $cm^2s^{-1}$) van mobiele haliden. De activeringsenergie voor halidemigratie verdubbelt echter van 0.14 naar 0.30 eV dankzij de mangaansubstitutie doordat mangaan een kleinere ionstraal heeft dan lood, wat een reductie van het perovskietrooster tot gevolg heeft. We nemen aan dat ten gevolge hiervan minder mobiele ionen van de perovskiet naar de contactlagen migreren en *vice versa*, wat de stabiliteit van de led verbetert.

Samenvattend, laat het eerste gedeelte van dit proefschrift een realistische schatting zien van de potentiële efficiëntie van de volgende generatie zonnecellen onder realistische omstandigheden, waarmee de maximale jaarlijkse energieopbrengst ingeschat kan worden. Onze resultaten geven inzicht in hoe het onderdrukken van dominante nadelige processen de efficiëntie van de volgende generatie zonnecellen kan verbeteren, en maken dus vrij baan voor het verder verbeteren van deze volgende generatie zonnecellen. Het tweede gedeelte van dit proefschrift geeft kwantitatieve inzichten in de effecten van verschillende additieven en perovskietsamenstellingen op de ionmigratie in perovskietdiodes. Deze bevindingen geven richting aan vervolgonderzoek naar ionmigratie en maken het onderzoek naar perovskietdiodes niet langer empirisch, maar rationeel gedreven.

# List of publications

This thesis is based on the following publications:

- M.H. Futscher and B. Ehrler, Efficiency limit of perovskite/Si tandem solar cells. *ACS Energy Letters* **1**, 863-868 (2016) (**Chapter 1 & Chapter 2**).
- M.H. Futscher and B. Ehrler, Modelling the performance limitations and prospects of perovskite/Si tandem solar cells under realistic operation conditions. *ACS Energy Letters* **2**, 2089-2095 (2017) (**Chapter 1 & Chapter 3**).
- M.H. Futscher, G. Coletti, A.R. Burgers, L.J. Geerlings, D. Zhang, S.C. Veenstra, A. Louwen, W. Van Sark, S. Luxembourg and B. Ehrler, Efficiency potential of bifacial perovskite/silicon tandem solar cells under realistic operation condition, in preparation (**Chapter 4**).
- M.H. Futscher and B. Ehrler, The potential of singlet fission photon multipliers as an alternative to silicon-based tandem solar cells. *ACS Energy Letters* **3**, 2587-2592 (2018) (**Chapter 5**).
- M.H. Futscher, M.K. Gangishetty, D.N. Congreve and B. Ehrler, Quantifying mobile ions in perovskite-based devices with temperature-dependent capacitance measurements: frequency versus time domain. under review (**Chapter 6**).
- M.H. Futscher, J.M. Lee, L. McGovern, L.A. Muscarella, T. Wang, M.I. Haider, A. Fakharuddin, L. Schmidt-Mende and B. Ehrler, Quantification of ion migration in $CH_3NH_3PbI_3$ perovskite solar cells by transient capacitance measurements. *Materials Horizons* **6**, 1497-1503 (2019) (**Chapter 7**).
- M.H. Futscher, K. Ji, L. McGovern, S. Sanchez, S.D. Stranks and B. Ehrler, Potassium passivation reduces the concentration of mobile ions in triple-cation mixed-halide perovskites, in preparation (**Chapter 8**).
- M.H. Futscher, M.K. Gangishetty, D.N. Congreve and B. Ehrler, Manganese doping stabilizes perovskite light-emitting diodes by reducing ion migration, in preparation (**Chapter 9**).

Other publications by the author:

- M.H. Futscher, T. Schultz, J. Frisch, M. Ralaiarisoa, E. Metwalli, M.V. Nardi, P. Müller-Buschbaum and N. Koch, Electronic properties of hybrid organic/inorganic semiconductor pn-junctions. *Journal of Physics: Condensed Matter* **31**, 064002 (2018).

- A. Karani, L. Yang, S. Bai, M.H. Futscher, H.J. Snaith, B. Ehrler, N.C. Greenham, D. Di, Perovskite/colloidal quantum dot solar cells: theoretical modelling and monolithic structure. *ACS Energy Letters* **3**, 869-874 (2018).

- M.H. Futscher, M. Philipp, P. Müller-Buschbaum and A. Schulte, The role of backbone hydration of poly(N-isopropyl acrylamide) across the volume phase transition compared to its monomer. *Scientific Reports* **7**, 17012 (2017).

- J.M. Lee, M.H. Futscher, L.M. Pazos-Outón and B. Ehrler, Highly transparent singlet fission solar cell with multistacked thin metal contacts for tandem applications. *Progress in Photovoltaics: Research and Applications* **25**, 936-941 (2017).

- L.M. Pazos-Outón, J.M. Lee, M.H. Futscher, A. Kirch, M. Tabachnyk, R.H. Friend and B. Ehrler, A silicon-singlet fission tandem solar cell exceeding 100% external quantum efficiency with high spectral stability. *ACS Energy Letters* **2**, 476-480 (2017).

- J. Zhang, M.H. Futscher, C. Cho, A. Sadhanala, A.J. Pearson, B. Kan, X. Wan, N.C. Greenham, Y. Chen, B. Ehrler, R.H. Friend, A.A. Bakulin, Sequentially deposited versus conventional nonfullerene organic solar cells: interfacial trap states, vertical stratification, and exciton dissociation, *Advanced Energy Materials*, 1902145 (2019).

- M. Xiao, D. Shen, M.H. Futscher, B. Ehrler, K.P. Musselman, W.W. Duley and Y.N. Zhou, Threshold switching in single nanobelt device emulating artificial nociceptor, *Advanced Electronic Materials*, 1900595 (2019).

# Acknowledgements

I am very grateful to many people who helped, encouraged, and supported me during my PhD. After all, it is the people you meet and connect with who transform a PhD into the experience of a lifetime.

First of all I would like to thank Bruno Ehrler for giving me the opportunity to work in such a wonderful environment. It was a great journey and I learned a lot from you. You led me from beginning to end, with a lot of passion, always supportive, and with lots of ideas. I particularly appreciate your constant innovative thinking, both for scientific challenges and for managing the group. You really are a role model for future scientists.

Furthermore, I would like to thank all current and former members of the Hybrid Solar Cells Group – Andrea Pollastri, Andrew Pun, Arnoud Jongeling, Benjamin Daiber, Christian Dieleman, Eline Hutter, Elio Monaco, Emil Kensington, Fabian Ecker, Isabel Koschany, Jumin Lee, Joris Bodin, Koen van den Hoven, Le Yang, Linda van der Waart, Loreta Muscarella, Lucie McGovern, Luis Pazos-Óuton, Maarten Mennes, Marc Duursma, Maria Minone, Marnix Ackermans, Merlijn Kersten, Merlinde Wobben, Mischa Hillenius, Ruby de Hart, Ruirt Bosma, Roan van Leeuwen, Silvia Ferro, Stefan Tabernig, Talia Martz-Oberlander, Tianyi Wang, and Toon Maassen. Thanks to all of you, I was able to grow as a scientist and as a person. I enjoyed our time together inside and outside AMOLF, in the lab, during lunch breaks, at conferences, and during our many outings. There are some people who deserve special mention: Benjamin, even though our research projects have always been somewhat out of phase, I have always enjoyed discussing work-related and non-work-related aspects over a coffee or beer. Christian, thank you for many interesting conversations and for cheering up the lab with your whistling. Eline, it was great fun working together with you, you truly enriched our group. Thanks also for the translation of the summary into Dutch. Jumin, for sharing all the knowledge of sample fabrication and for the many opportunities to enjoy Korean food and movies. Lucie, it was great to see you coming back after a successful Master's thesis. I enjoyed working with you and hopefully will continue to do so in the future. Loreta, for the many occasions in which you helped me with the fabrication of perovskite solar cells. Marc, for all the indispensable help in the lab. Without your help, everything would take much longer. Silvia, for being such

a great office mate. Tianyi, it was a pleasant coincidence to meet you again, after having already been in the same group in Munich.

Thanks to all the members of the Center for Nanophotonics for many inspiring discussions. Especially Albert Polman for the creation of the LMPV program within the Center for Nanophononics, which makes AMOLF a world-renowned location for excellent photovoltaic research. For constructive feedback on manuscripts I thank Eric Johlin, Esther Alarcón Lladó, Mark Knight, and Sander Mann, but above all Erik Garnett, who has offered his advice countless times.

As a young scientist, having a mentor by your side is crucial. Also before AMOLF, I have been lucky enough to have received support and valuable advice from excellent scientists. I would like to thank Georg Maret, Ullrich Steiner, Silvia Vignolini, Peter Müller-Buschbaum, and Norbert Koch. It is thanks to all of you that I have come this far.

Big thanks to my paranymphs Giulia Giubertoni and Lukas Helmbrecht. Thank you for being by my side not only throughout the last years, but also during my defence. Giulia, I could not be happier to have shared an office with you from the very beginning. It was a lot of fun and you were one of the reasons why I liked to go to the office in the morning. I enjoyed our many conversations, even if our screens were always a bit of a barrier. I also really enjoyed the many evenings and weekend trips spent together with you and Judith. You are an amazing couple and I will miss you both very much. Lukas, I am very happy to have met you. We have shared many special moments together during these years, at one of our many dinners, weekend trips, or concerts. It is inspiring how creative and driven you are and I wish you all the happiness and success in the future that you deserve. I very much hope to stay in close contact, wherever our ways may lead us.

Being a scientist means sharing knowledge and exchanging ideas. During my PhD I was fortunate to be able to collaborate with many researchers around the world. It was a great pleasure to work together and I hope I will continue to do so in the future. Thanks to Arfa Karani, Artem Bakulin, Henry Snaith, Jiangbin Zhang, Jovana Milić, Kevin Musselman, Luis Pazos-Outón, Martin Stolterfoht, Michael Grätzel, Ming Xiao, and Vincent Le Corre. I furthermore want to say thank you to: Atse Louwen and Wilfried van Sark for providing us with data to simulate real-world climate conditions. Bart Geerlings, Dong Zhang, Gianluca Coletti, Sjoerd Veenstra, Stefan Luxembourg, and Teun Burgers for discussions on bifacial tandem solar cells. Dan Congreve and Mahesh Gangishetty for providing us with many glowing samples. Azhar Fakharuddin, Irfan Haider, and Lukas Schmidt-Mende for sending us perovskite solar cells. Sandy Sanchez for teaching us how to fabricate high-efficiency perovskite solar cells. Kangyu Ji and Sam Stranks for a constant supply of samples. And all other scientist I met along the way.

Amsterdam and all the people I have met here will always have a special place in my heart. Special thanks to Kévin Cognée, for being such a good friend. The italian crew, Alessandro Antoncecchi, Federica Burla, Giorgio Oliveri, Nicola Gritti, and Marco Saltini, for many evenings with lots of good food and wine. Mario Avellaneda and Olga Filina, thank you for convincing us to move into the same building as you. It has always been a lot of fun to spend time with you. Olesia Sacharova and Thijs Jansen, I will greatly miss having you as neighbours but I know that we will always keep in touch. Thijs, let me know when you are up for the next extreme hike. There are many more people worth mentioning here, including Agata Szuba, Andrea Cordaro, Annemarie Berkhout, Biplab Patra, Carolyn Moll, Cristina Sfiligoj, Giada La Gala, Jenny Kontoleta, Jian-Yao Zheng, Laura Canil, Lorenzo De Angelis, Mark Aarts, Mathijs Rozemuller, Nasim Tavakoli, Oleg Selig, Parisa Khoram, Ruslan Röhrich, Sarah Brittman, Sebastian Öner, Susan Rigter, Sven Askes, Tom Veeken, Verena Neder, and many more who I hope will excuse my forgetfulness. Thanks also to all my friends from Constance, who repeatedly challenged me with marathons or ridiculously long hikes, and to all my friends from Vienna, who I wish I could see more often. There is never a dull moment with you. Our Tarock evenings are some of my favourite memories.

Thanks to the strong and loving support of my parents. My special thanks go to my mother, Brigitte Futscher, for always being there for me and believing in me. I am sorry I had to live this far away to achieve my goals. Many thanks also for all the effort you put into drawing the cover for this thesis, which has become really beautiful.

Finally, I would like to thank my wonderful wife Laura Futscher. Thank you for moving to this flat and rainy country with me, just to find out that life here is actually pretty great. Laura, you have contributed so much to help me achieve my goals, I cannot thank you enough. Thank you very much for your love and for always supporting me, encouraging me, and cheering me up. I look forward to mastering future challenges together as a team.

# About the author

Moritz Hieronymus Futscher was born in Vienna, Austria on June 27, 1989. In 2012 he obtained his Bacherlor's degree in physics from the University of Konstanz, Germany. During his Bachelor's studies he spent five months at the University of Cambridge, England, where he wrote his Bachelor's thesis about gyroid structured optical metamaterials under the supervision of Prof. Ullrich Steiner and Prof. Georg Maret.

After a brief period working at Porsche's research and development centre in Weissach, Germany, he studied condensed matter physics at the Technical University of Munich. During his Master's studies he spent one year at the Humboldt-University of Berlin to write his Master's thesis on the energy-level alignment at hybrid inorganic/organic semiconductor interfaces under the supervision of Prof. Norbert Koch and Prof. Peter Müller-Buschbaum. In 2016 he obtained his Master's degree (with distinction).

He then started working as a PhD student in the Hybrid Solar Cells group at AMOLF in Amsterdam, the Netherlands, under the supervision of Dr. Bruno Ehrler, the results of which are presented in this thesis.